Strong Correlation Effects in Atmospheric Pressure Plasmas

by

Marco D. Acciarri

A dissertation submitted in partial fulfillment
of the requirements for the degree of
Doctor of Philosophy
(Nuclear Engineering and Radiological Sciences)
in The University of Michigan
2024

Doctoral Committee:

Associate Professor Scott Baalrud, Chair
Professor John Foster
Associate Professor Brian Kiedrowski
Professor Mark Kushner
Dr. Christopher Moore, Sandia National Laboratory

Marco D. Acciarri

acciarri@umich.edu

ORCID iD: 0000-0003-2768-1259

To my Nonno, Giuseppe

ACKNOWLEDGEMENTS

Writing this dissertation marks the end of my university journey. When I began my university studies 10 years ago, I could never have imagined all the experiences and learning I would encounter along the way. Filled with dreams and hopes, I embarked on a path that, through various setbacks, successes, fortunate and unfortunate events, and above all, immense sacrifice, has led me to this point - to graduate with my Ph.D. from the NERS department at the University of Michigan. I will forever be grateful for having had the opportunity to complete my studies at this university and under the guidance of Professor Baalrud, who has significantly influenced my professional career.

I would like to express my profound gratitude to my advisor, Professor Baalrud. Your unwavering support, even during my most challenging times, is something I will always cherish. The opportunity to study at the University of Michigan under your guidance has opened a world of possibilities for me. Your patience, empathy, mentoring, and enthusiasm for exploring fundamental physics problems have been essential throughout my PhD journey. You have not only been a role model as a researcher and professional but also pushed me to deepen my understanding of complex physics problems. The lessons I have learned under your tutelage will undoubtedly benefit my career and personal growth for years to come. I am also immensely grateful to Christopher Moore for countless hours of discussions about my research, his guidance, constant feedback, and unwavering support. Without his assistance, my PhD would not have been possible. I would like to thank Sandia National Laboratories and the

Department of Energy for the support of my research throughout my PhD journey.

I would also like to thank professors Yue-Ying Lau, John Foster and Mark Kushner. Having the opportunity to take your classes had a pivotal role in my academic studies. The passion and effort with which you teach and communicate your knowledge to students is something I have always been amazed with. Taking your classes gave me a deeper understanding into plasma physics and its applications than what I've ever aspired to.

I also wish to thank my past and present group members, whose camaraderie made this experience enjoyable and rewarding. Lucas Beving, Louis Jose, Julia Marshall, James Welch, Julian Kinney, Lucas Babati, Moises Enriquez and Ryan Park, provided constructive feedback and inspiring ideas. I am fortunate to have had such an exceptional group of peers to work with. I would also like to thank Jarett LeVan. Working with you has been an honor, and having the privilege to witness the emergence of a future plasma scientist is something I will always cherish.

I would like to extend my heartfelt thanks to my friends around the globe whose virtual conversations supported me throughout this journey, making me feel connected to Argentina and less isolated during these years. Special thanks to Lisandro, Alan, Leandro, Paulo and Camila.

Last but certainly not least, I would like to thank my family. Dad and Mom, you taught me to dream big and that with perseverance, hard work, and determination, anything is possible. No matter the challenges of the past or those that may come, the values and lessons you imparted are the greatest legacy a son could ever receive. Our phone calls over the years have been a pillar of strength, encouraging me never to give up. I am proud to be the first member of the Acciarri family to earn a Ph.D., along with many other achievements that only you know about. I am also grateful to my sister Ornella, for your patience and for listening to my lengthy voice messages when I needed to vent, and to my brother Mauro, for all your support and love. To

everyone, thank you! And now, I can proudly say, I've done it!

TABLE OF CONTENTS

DEDICATION ii

ACKNOWLEDGEMENTS iii

LIST OF FIGURES x

LIST OF TABLES xvii

ABSTRACT xix

CHAPTER

I. Introduction 1

1.1 Background 1
1.1.1 Discharges at atmospheric pressure 2
1.1.2 Fast gas heating 4
1.1.3 Simulation techniques used for atmospheric pressure plasmas 6
1.2 Strong correlations 12
1.2.1 Strongly coupled interactions at atmospheric pressure 13
1.2.2 Disorder induced heating 15
1.2.3 Diffusion 17
1.2.4 PIC simulations 19

II. Simulation Techniques 24

2.1 Molecular dynamics 24
2.1.1 Basics of molecular dynamics 25
2.1.2 Interaction potentials 26
2.1.3 The particle particle particle mesh method 27
2.1.4 Equations of motion 27
2.1.5 Thermostating and energy conserving simulations . 27
2.1.6 Temperature calculation 28

2.1.7 Monte Carlo collision method 29
2.1.8 Molecular dynamics simulations of atmospheric pressure plasmas 30
2.2 Global model 31
2.3 Particle in cell 33
2.3.1 Monte Carlo collision method 38

III. Coulomb coupling influences ion and neutral temperatures in atmospheric pressure plasmas 39

3.1 MD simulations setup 39
3.2 Molecular dynamics results 42
3.3 Disorder induced heating 44
3.4 Ion-neutral temperature relaxation 48
3.5 Three-body recombination 51
3.6 Model for maximum and equilibrium ion temperature. 53
3.7 Comparison with experiments 56
3.8 Arbitrary ionization dynamics 58
3.8.1 Setup 59
3.8.2 Results 61
3.8.3 Comparison with experiment 63
3.9 Effect of rotational degrees of freedom in molecular plasmas . 65
3.9.1 Setup 66
3.9.2 MD results 68
3.10 General model for DIH and temperature evolution 71
3.10.1 Setup 72
3.10.2 MD results 72
3.10.3 Model and discussion 73

IV. Global model for a nanosecond pulsed discharge in atmospheric N_2 with disorder induced heating 77

4.1 Global model 77
4.2 Reaction set for molecular nitrogen 78
4.3 Setup 86
4.4 Results at atmospheric pressure 87
4.4.1 Varying the reduced electric field 95
4.5 Results at 10 atmospheres 98
4.5.1 Varying the reduced electric field 103
4.6 Implications of disorder induced heating in plasma chemistry 106

V. Influence of strong Coulomb coupling on diffusion in atmospheric pressure plasmas 108

5.1 Theoretical model 109

5.1.1 Theoretical framework . . . 109
5.1.2 Neutral-neutral collisions . . . 111
5.1.3 Ion-neutral collisions . . . 112
5.1.4 Ion-ion collisions . . . 112
5.1.5 Disorder induced heating . . . 114
5.1.6 Diffusion coefficients . . . 115
5.2 Molecular dynamics simulations . . . 120
5.2.1 Validation of the MCC + MD simulation setup . . . 123
5.2.2 Calculation of the ion diffusion coefficient . . . 125
5.3 Molecular dynamics results . . . 128
5.4 Pressure dependence . . . 129

VI. When should PIC simulations be applied to atmospheric pressure plasmas? Impact of correlation heating . . . 134

6.1 Simulation setup . . . 135
6.1.1 Molecular dynamics . . . 135
6.1.2 Particle in cell . . . 136
6.2 Disorder-induced heating . . . 136
6.2.1 Molecular dynamics results . . . 136
6.2.2 PIC: influence of grid resolution . . . 138
6.2.3 PIC: influence of macroparticle weight . . . 140
6.2.4 Grid heating and influence of interpolation scheme 147
6.2.5 Reduced dimensions . . . 151

VII. Artificial Correlation Heating in PIC simulations . . . 153

7.1 Artificial correlation heating . . . 153
7.1.1 Macroparticle coupling strength . . . 153
7.1.2 Parameter space . . . 155
7.2 PIC simulations . . . 161
7.2.1 Artificial correlation heating . . . 162
7.3 ACH model . . . 166
7.4 Discussion . . . 168
7.4.1 Limit of fine grid resolution . . . 168
7.4.2 Effect of grid resolution . . . 169
7.4.3 Effect of shape function order . . . 172
7.4.4 Numerical instability produced by ACH and ionization 173
7.4.5 Artificial correlation heating in reduced dimensions 177
7.4.6 Limit of applicability of the PIC method and stability criteria . . . 177

VIII. Conclusion . . . 180

APPENDIX 186

BIBLIOGRAPHY 191

LIST OF FIGURES

Figure

1.1 Overview of different atmospheric pressure gas discharges spanning a range of more than 10 orders of magnitude in electron density. TD stands for Townsend discharge. Illustration extracted from [1]. . . . 3

1.2 Comparison of the typical timescales of the possible mechanisms of fast neutral gas heating observed. The disorder induced heating and ion-neutral temperature relaxation mechanisms affect the ion and neutral temperatures respectively in faster timescales compared to the previously studied mechanisms. The timescales here assume atmospheric pressure and typical ionization fractions [2]. 6

1.3 Coupling parameter space for ion-ion, ion-neutral and neutral-neutral interactions for an Ar gas at room temperature and different pressures and ionization fractions. 14

2.1 Illustration of the PIC method. Fields are solved in a grid and then interpolated to the positions of macroparticles. Then the equations of motions are solved and the charges are interpolated back to the grid. 35

3.1 Ion and neutral final temperatures for different r_ϕ values. 41

3.2 Evolution of the ion and neutral temperatures during the discharge at atmospheric pressure for different ionization fractions. 43

3.3 Ion kinetic energy (K_i), neutral kinetic energy (K_n) and total energy E_T for a discharge at atmospheric pressure and an ionization fraction of $x_i = 0.01$. Each energy is normalized by the number of ions (N_i), neutral atoms (N_n) and total number of particles N respectively and the kinetic energy at room temperature $T_0 = 300\ K$. Large fluctuations were observed in the ion kinetic energy due to the oscillations in the Coulomb potential energy after the DIH. 43

3.4 After an instant ionization pulse, ions can be at distances much smaller compared to a_{ii} leading to large repulsion forces. 45

3.5 Ion-ion radial distribution function $g(r)$ at different timesteps during the simulation of a partially ionized Ar plasma with an ionization fraction of $x_i = 0.01$. The ion-ion radial distribution function corresponds to an OCP at the same equilibrium Γ_{ii} showing that the ions are strongly coupled and the ion-ion interactions are not screened by the presence of neutral atoms. In each simulation, the $g(r)$ was obtained after computing an average over all the ions in the simulation and 100 consecutive time steps that corresponded to a time window of $t \times \omega_{pi} = 0.05$. An ensemble average was also computed using data from 20 different simulations. 46
3.6 Evolution of the Coulomb coupling parameter Γ_{ii} during the discharge at different ionization fractions. 48
3.7 Ion-neutral momentum transfer cross section at different relative velocities, obtained for the charge induced dipole potential used in the simulations. 50
3.8 Evolution of the ion temperature for a discharge with $x_i = 0.01$ along with the model described in equations (3.2)–(3.4). 51
3.9 Evolution of the temperature for a discharge with a ionization fraction $x_i = 0.01$ for different r_ϕ values. 52
3.10 Ion-neutral three-body recombination rate for a discharge with a ionization fraction $x_i = 0.01$ for different r_ϕ values. For the case $r_\phi = 0.133$ the bound states fraction is approximately zero. 53
3.11 Variation of the maximum ion temperature and equilibrium temperature with the ionization fraction from the MD simulations and the model. 55
3.12 The Coulomb coupling parameter at equilibrium is smaller than the coupling parameter at room temperature without accounting for DIH. At small ionization fractions $\Gamma_{ii}^{\mathrm{eq}}(T^{\mathrm{eq}}, x_i)$ converges to $\Gamma_{ii}(T_0, x_i)$ where T_0 is the room temperature. 55
3.13 (a) Ionization fraction profiles used in the MD simulations. (b) Evolution of ion and neutral temperatures from MD simulations for each ionization fraction profile shown in (a). Continuous lines represent the ion temperature while dashed lines represent the neutral gas temperature. A vertical dashed line marks the instant at which ionization stops for the cases of gradual ionization. 62
3.14 Evolution of the neutral gas temperature from molecular dynamics, using the gradual ionization fraction profiles shown in figure 3.13(a) and from a nanosecond pulsed discharge in atmospheric air [3]. . . . 65
3.15 Illustration of the disorder-induced heating process. Ionization transforms neutral gas into a nonequilibrium plasma. Coulomb repulsion causes the ions to separate on a picosecond timescale, causing significant translational heating. Collisions then distribute this energy across neutral and rotational degrees of freedom until they reach an equilibrium. The collision relaxation timescale near atmospheric pressure is often characteristic of nanoseconds. 68

3.16 Simulated time-evolution of the temperature components of an N_2 plasma at a 0.30 ionization fraction. Lines correspond to the ion translational temperature (blue), ion rotational temperature (orange), neutral molecule rotational temperature (green), and neutral molecule rotational temperature (red). 70
3.17 Simulated and predicted temperatures of N, N_2, and N_4 plasma using the approximate and precise formulation from [4] with the ion-ion g(r) computed from MD. These models are based on the same principle described in previous sections, conversion from potential to kinetic energy due to DIH. 70
3.18 Change in total kinetic energy density (with respect to $t = 0$) for N, N_2, and N_4. This data comes from simulations at an ionization fraction of 0.30. 71
3.19 Ion-ion radial distribution function right after ionization and after DIH. The peak at small distances after ionization correspond to the newly created ions. 73
3.20 Evolution of ion (T_i) and neutral gas (T_n) temperatures from a molecular dynamics simulation using the numerical setup described in [5] but with a final ionization fraction of 20% and having only 40 ionization substeps. 74
3.21 Integral $I^* = \int_0^\infty d\tilde{r}\ \tilde{r}\,[g(\tilde{r}) - 1]$ for different values of the macroparticle coupling parameter Γ_{ee}^w and fit $I^*(\Gamma) = a/(b + \Gamma)^c + d$ with parameters $a = 0.6032$, $b = 0.0372$, $c = 0.1549$ and $d = -0.9917$. . . 76
4.1 a) Gaussian voltage pulse and reduced electric field and b) electron temperature and deposited power per unit volume. 88
4.2 Evolution of molecular nitrogen ion densities in ground and excited states. 89
4.3 Evolution of electron, atomic ion and total molecular ion densities over time in a) linear and b) log scale. 90
4.4 Evolution of ground and excited states of a) molecular and b) atomic nitrogen. 91
4.5 Evolution of ion and neutral gas temperatures as function of time. . 93
4.6 Rate of increase dT/dt for a) ion and b) neutral gas temperatures from different contributions. 95
4.7 a) Final fractional dissociation δ and b) final electron density with and without DIH as function of $E^{\max}/N_0$. 97
4.8 a) Electron and b) gas temperatures with and without DIH as function of $E^{\max}/N_0$. 98
4.9 a) Evolution of Gaussian voltage pulse and reduced electric field and b) electron temperature and deposited power per unit volume as function of time with and without DIH at 10 atmospheres. 100
4.10 a) Evolution of ion and neutral gas temperatures and b) evolution of charged species densities with and without DIH at 10 atmospheres. 101
4.11 Rate of increase of a) ion and b) neutral gas temperatures with and without DIH at 10 atmospheres. 103

4.12 a) Fractional dissociation and b) electron density as function of the reduced electric field at an initial neutral gas pressure of 10 atmospheres. 105
5.1 Coulomb coupling parameter and equilibrium temperature at atmospheric pressure for different ionization fractions. The temperature used to compute Γ_{ii} is the equilibrium temperature from equation (3.8). 115
5.2 Ratio between the ion-ion and ion-neutral collision frequencies in a pressure-ionization fraction parameter space for an Ar plasma. Ion-ion collisions are expected to determine the diffusion rate when this ratio is large. 116
5.3 Ion diffusion coefficient (green solid line) as a function of ionization fraction. Also shown are the ion diffusion coefficient assuming room temperature (purple dotted line), which neglects the DIH effect, the ion-neutral (blue dash-dotted line) and ion-ion (black dashed line) interdiffusion coefficients. The ion diffusion coefficient obtained from the MD simulations is shown in red dots. 118
5.4 Ion-ion interdiffusion coefficient obtained using the Chapman-Enskog solution of the mean force kinetic theory (black dashed line) and using the traditional Landau-Spitzer solution. There is a clear divergence of the diffusion coefficient in the Landau-Spitzer solution as the argument of the Coulomb logarithm approaches zero. 119
5.5 Neutral diffusion coefficient at atmospheric pressure for a broad range of ionization fractions (red solid line). Also shown are the neutral diffusion coefficient ignoring DIH (black dashed line), and the neutral-ion (purple dotted) and neutral-neutral (blue dashed line) interdiffusion coefficients. 120
5.6 Convergence test for the total ion diffusion coefficient at an ionization fraction of 10^{-9} with different timesteps Δt. 122
5.7 Evolution of the ion temperature for a discharge at atmospheric pressure and an ionization fraction of $x_i = 10^{-2}$ using an MD+MCC simulation setup (black line) and a MD-only simulation (red line). The MD+MCC module correctly reproduces the dynamics and equilibrium at a lower computational cost than MD only. 124
5.8 Ion radial distribution function at equilibrium from the MD+MCC simulations at different ionization fractions (colored lines). The radial distribution function of an OCP at the corresponding equilibrium Γ_{ii} parameter (black lines). 125
5.9 (a) Velocity autocorrelation function of ions $Z(t)/Z(0)$ for different ionization fractions and (b) integral $\widetilde{D}(t) = \frac{1}{3}\int_0^t Z(t')dt'$ for different ionization fractions. The ion self diffusion coefficient was taken as the plateau value of $\widetilde{D}(t)$. 127
5.10 Equilibrium temperature for different pressures and ionization fractions computed using equation (3.8). This accounts for disorder induced heating and ion-neutral temperature relaxation. 130

5.11 Ion diffusion coefficient predicted from the model of section 5.1 for different pressures and ionization fractions. The dashed lines represent the diffusion coefficients at room temperature while the solid lines correspond to the case where disorder induced heating is accounted for and the equilibrium temperature is computed from equation (3.8). 132
5.12 Neutral diffusion coefficient at different pressures and ionization fractions. The dashed lines represent the diffusion coefficients at room temperature while the complete lines correspond to the case where disorder induced heating is accounted for and the equilibrium temperature from equation (3.8) is used. 133
6.1 Evolution of the ion temperature obtained with a 3D3V PIC simulation with a grid spacing of $\Delta x/a_{ii} \approx 0.042$ and from an MD simulation for the same initial conditions and density. 137
6.2 Evolution of the ion temperature for an ion density of $n_i = 2.5 \times 10^{24}$ m^{-3} and initial room temperature obtained from MD and using the PIC method for different grid spacing. 139
6.3 Ion temperature of the first peak (at $t \approx 1.5\ \omega_{pi}^{-1}$) for different grid spacing values $\Delta x/a_{ii}$. The maximum ion temperature converges to the expected physical value for $\Delta x/a_{ii} \leq 0.1$. 139
6.4 Evolution of the ion temperature using a grid spacing of $\Delta x/a_{ii} \approx 0.042$ for different macroparticle weights w. 140
6.5 Change in the ion temperature obtained with PIC simulations at different macroparticle weights. The change in temperature obtained with the scaling law $\Delta T_i^w = w^{2/3}\Delta T_i$ is shown for comparison. . . . 141
6.6 Illustration of the distribution of macroparticles in PIC simulations for (top) weakly vs. (bottom) strongly coupled plasmas assuming a grid spacing of approximately the Debye length. 142
6.7 Pair correlation function $g(r)$ for different macroparticle weights at equilibrium taking as reference the physical average interparticle spacing (a) and taking as reference the average macroparticle spacing a_{ii}^w (b). The pair correlation function of an OCP at the equilibrium Γ_{ii} is shown for comparison. 145
6.8 (a) Evolution of the ion temperature and grid spacing $\Delta x/\lambda_{D_i}$ for an ion density of 2.5×10^{24} m^{-3}, unity macroparticle weight and average number of macroparticles per cell $N_c = 0.00023$. (b) Evolution of the total, electrostatic and kinetic energies over time. 149
6.9 (a) Evolution of the ion temperature obtained from PIC simulations with different shape functions for the first 100 ion plasma periods, and (b) the first 3 plasma periods. The grid resolution is $\Delta x/a_{ii} \approx 0.51$ and $\Delta x/\lambda_{Di} \approx 3.13$ and the ion density is 2.5×10^{24} m^{-3}. Increasing the order of the shape function reduces the growth rate of the observed grid heating and DIH. 151
7.1 Evolution of the electron temperature for the first few electron plasma periods for different grid spacing. The electron density is 1.25×10^{23} m^{-3} and the macroparticle weight is 1000. 156

7.2 Evolution of the macroparticle coupling strength between electrons in a PIC simulation where ACH is observed. The macroparticle Γ_{ee}^{w} decreases to a value of approximately 1.5 after $1.5\omega_{pe}^{-1}$. A grid resolution of $0.3\lambda_{De}$ was used. 156
7.3 Artificial correlation heating limit curves for different macroparticle weights. The allowed operating region for PIC simulations is located on the left side of each curve. 158
7.4 Limiting curve for ACH region from the model described in equation (7.3) and numerical results from 3D-PIC simulations. 159
7.5 Evolution of the electron temperature during the first $3\omega_{pe}^{-1}$ of each simulation for an electron density of 2.5×10^{19} m^{-3}, an initial electron temperature $T_e = 3$ eV and an initial grid resolution of $\Delta x/\lambda_{De} = 0.5$ for different macroparticle weights. 164
7.6 Illustration of the distribution of macroparticles in PIC simulations for (a) $w \gtrsim 1$, $\Gamma_{ee}^{w} < 1$ and $a_{ee}^{w} \ll \Delta x$ and (b) $w \gg 1$, $\Gamma_{ee}^{w} > 1$ and $a_{ee}^{w} \gtrsim \Delta x$ assuming a grid spacing of approximately the Debye length. The color intensity of each cell represents the local charge density. For $w \gtrsim 1$ the charge density is uniformly distributed within the grid for a uniform spatial configuration of macroparticles. However, for $w \gg 1$ the charge is localized in the few cells where macroparticles are located. Therefore, there is an artificially enhanced repulsive electric field that is resolved by the grid. This causes macroparticles to separate from each other in order to minimize the overall potential energy. 165
7.7 Maximum electron temperature obtained from the set of simulations with parameters indicated in Table 7.3. The maximum electron temperature increases with the electron density and macroparticle weight due to the corresponding increase in the initial Γ_{ee}^{w} value. 168
7.8 a) Maximum electron temperature obtained from the set of PIC simulations run with the parameters shown in Table 7.4. Labels indicate the product $n_e w^2$. b) Dimensionless electron temperature $\tilde{T}_e$ as a function of the grid spacing. 171
7.9 Radial distribution function obtained from PIC simulations run at different grid resolutions for an electron density of $n_e = 2.5\times10^{23}$ m^{-3} and a macroparticle weight of 1000. 173
7.10 Maximum electron temperature obtained from PIC simulations for an electron density of $n_e = 2.5 \times 10^{23}$ m^{-3}, a macroparticle weight $w = 1000$, and varying the grid resolution and the shape function order. 174

7.11 Evolution of: a) the electron temperature, b) electron density, c) ionization rate, d) grid resolution compared to the average distance between macroparticles, and e) grid resolution compared to the electron Debye length, for the PIC simulations described in Table 7.5. Simulations with a macroparticle weight large enough to satisfy the $\Gamma_{ee}^{w} > 1$ criterion are observed to be subject to ACH, which induces a runaway process that increases the electron density faster than an exponential curve. When the macroparticle weight is increased from 10^3 to 10^5 the ionization rate increases several orders of magnitude due to ACH and the runaway heating process. 175
7.12 Limiting curves for the PIC method in the electron temperature vs $n_e w^2$ parameter space. Each curve was obtained with a different grid resolution $\Delta x/\lambda_{De}$ ranging from 0.1 to 5. The ACH region lies on the right side of each curve. 178
7.13 Diagram illustrating the general procedure that should be used to choose PIC input parameters $(n, T, \Delta x/\lambda_D, w)$ in order to avoid ACH. 179
A.1 Numerical charge induced dipole potential for different values of r_ϕ compared to the charge induced dipole potential. 188
A.2 Fraction of ion-neutral and neutral-neutral bound states for different r_ϕ values. 189
A.3 a) Ion-neutral and b) neutral-neutral minimum distance distribution for $r_\phi = 0.046 a_{\text{in}}$ at an ionization fraction of 0.5. 190

LIST OF TABLES

Table

3.1 Parameters used for the molecular dynamics simulations. The time step value was $\Delta t \times \omega_{pi} = 5 \times 10^{-4}$ in all cases. 41
3.2 Comparison of the measured neutral gas temperature to the predicted values accounting for disorder induced heating and ion neutral temperature relaxation. 57
4.1 Electronic levels of N_2, N included in the reaction set. The energy is given relative to the ground state. The main difference with [6] is that here we incorporate the $N_2(a^1\Pi_g)$ and $N_2(E^3\Sigma_g^+)$ states. A total of 19 different species are included in the model. 81
4.2 Electron Impact excitation of N_2 82
4.3 Electron Impact Ionization of N_2 83
4.4 Electron impact excitation of N_2 ions 83
4.5 Electron impact excitation of atomic N 84
4.6 Electron Impact Dissociation of N_2 and N_2^+ 85
4.7 Electron impact ionization of atomic N 85
4.8 Associative and Penning ionization 85
4.9 Quenching 85
4.10 Electron - neutral elastic scattering 86
4.11 Coulomb collisions 86
4.12 Charge exchange 86
5.1 Parameters used for the MD-MCC simulations. The number of ions was $N_i = 5000$ and the total number of timesteps was 3×10^5 for all simulations. 123
7.1 Grid spacing and average number of macroparticles per cell for the numerical results shown in figure 7.1. 155
7.2 Parameters utilized in the PIC simulations shown in Fig. 7.5. The initial grid resolution was set as $\Delta x/\lambda_{De} = 0.5$. 164
7.3 Parameters used in the PIC simulations shown in Fig. 7.7. The initial grid resolution was set as $\Delta x/a_{ee}^w = 0.1$ which corresponds to an average number of macroparticles per cell of $N_c = 2.35 \times 10^{-4}$. . 169
7.4 Parameters used to study the effect of the grid resolution on ACH shown in Fig. 7.8. 172

7.5 Parameters used in the PIC simulations to study the effect of ACH combined with ionization as shown in Fig. 7.11. Here, the simulation domain and cell size Δx remain constant during each simulation. . . 176

ABSTRACT

Molecular dynamics simulations are used to model ion and neutral temperature evolution in atmospheric pressure plasmas. Results show that ion-ion interactions are strongly coupled at ionization fractions as low as 10^{-5} and that the temperature evolution is influenced by effects associated with the strong coupling. Specifically, disorder-induced heating (DIH) is found to rapidly heat ions on a timescale of the ion plasma period ($\sim$ 1 ps) after an ionization pulse. This is followed by the collisional relaxation of ions and neutrals, which cools ions and heats neutrals on a longer ($\sim$ns) timescale. The sequence of DIH and ion-neutral temperature relaxation suggests a new mechanism for ultrafast neutral gas heating. A model for DIH is developed and integrated into a global plasma chemistry model for a nanosecond pulsed nitrogen discharge. It is found that when full ionization is reached, DIH increases the overall temperature by 20% at one atmosphere and by 60% at ten atmospheres. Furthermore, it is found that DIH indirectly influences the electron temperature through electron-ion Coulomb collisions and thus enhances electron impact inelastic processes such as dissociation and ionization.

Ion diffusion in atmospheric pressure plasmas is examined in the context of strong coupling. Three regimes are identified. At low ionization fractions ($x_i \lesssim 10^{-6}$), standard weakly correlated ion-neutral interactions set the diffusion rate. At moderate ionization fractions ($10^{-6} \lesssim x_i \lesssim 10^{-2}$) there is a transition from ion-neutral to ion-ion collisions setting the diffusion rate. In this regime, the effect of strong

Coulomb coupling in ion-ion collisions is accounted for by applying the mean force kinetic theory. At high ionization fractions ($x_i \gtrsim 10^{-2}$), strongly correlated ion-ion collisions dominate and the plasma is heated substantially by DIH. Model predictions are tested using molecular dynamics simulations, which included a Monte Carlo collision routine to simulate the effect of ion-neutral collisions at the lowest ionization fractions. The model and simulations show good agreement over a broad range of ionization fractions. The results provide a model for ion diffusion, on a wide range of ionization fractions and pressures, solely considering the elastic contribution to the diffusion coefficient - as an illustration of how strong Coulomb coupling influences diffusion processes in general.

Molecular dynamics simulations are used to test when the particle-in-cell (PIC) method applies to atmospheric pressure plasmas. It is found that PIC applies only when the plasma density and macroparticle weight are sufficiently small because of two effects associated with correlation heating. First, PIC is not well suited to capture DIH because doing so requires using a macroparticle weight of one and a grid that well resolves the physical interparticle spacing. These criteria render PIC intractable for macroscale domains and long timescales due to grid heating. The second effect is a numerical error due to Artificial Correlation Heating (ACH), like DIH it is caused by the Coulomb repulsion between particles, but differs in that it is a numerical effect caused by a macroparticle weight larger than one. Here, we found that avoiding ACH requires that the macroparticle coupling strength be smaller than one $\Gamma^w < 1$, where $\Gamma^w \equiv \Gamma w^{2/3}$, $\Gamma = Z^2e^2/(4\pi\epsilon_o a k_B T)$ is the physical coupling strength and w is the macroparticle weight. A comprehensive model of ACH is developed that incorporates electron density, temperature, macroparticle weight, and grid resolution. It is then tested, delineating the boundaries of the PIC method's applicability and offering a predictive framework for ACH. Moreover, this work explores a runaway heating process induced by ACH in the presence of ionization, which can lead to numerical

instability.

CHAPTER I

Introduction

1.1 Background

Atmospheric pressure plasmas, in particular cold atmospheric pressure plasmas (CAPP), have been widely implemented and commercialized for numerous applications including the inactivation of various pathogens in medicine [7], food industry [8], agriculture [9], water purification [10], CO_2 conversion [11], plasma assisted ignition (PAI)[12, 13], and plasma assisted combustion (PAC) [12, 13], showing promising results and an increasing interest in those industries. CAPP technology presents several advantages over other plasma technologies including operational simplicity, low running cost, and environmental friendliness, since no vacuum chamber is needed and the reactor is frequently open [1, 7]. The increasing interest has led to an intensive effort to understand the main mechanisms responsible for plasma dynamics and its correlation with reactive species delivery [14, 15, 16, 17, 18]. However, still some effort should be paid to provide a deeper insight into the basic physics mechanisms, including the ones responsible for fast neutral gas heating [3, 19, 20, 21, 22, 23, 24, 25, 26].

At atmospheric and higher pressures, direct energy transfer from the electric field to ions is negligible, with electrons being primarily heated by the electric field. The electrons then transfer energy to heavy particles through ionization, excitation, dissociation of molecules, and elastic collisions. Typical electron temperatures range from

1 to 3 eV. In atomic gases, energy transfer to heavy particles is mainly through elastic collisions, while in molecular gases, vibrational excitation predominates within this temperature range. The efficiency of energy transfer from the electric field to electrons is significantly higher than the collisional energy transfer between electrons and heavy particles due to the large mass difference, resulting in gas temperatures much lower than electron temperatures [27].

This highly non-equilibrium behaviour, where electrons are much hotter than heavy species, promotes chemical reactions of interest making CAPPs of special interest for multiple applications. In particular, non-thermal atmospheric pressure plasmas can induce chemical reactions in various gas mixtures without significantly heating them, thus keeping energy consumption relatively low. The desired chemical effect is achieved by efficient production of reactive species resulting from the collision of high-energy electrons with neutral species [27]. If a large ionization degree is achieved at atmospheric pressure, Coulomb collisions between electrons and ions start to dominate and both species reach similar temperatures. Under this condition, the plasma is said to be at a local thermodynamic equilibrium (LTE), as is common in arc discharges [28].

1.1.1 Discharges at atmospheric pressure

Various types of plasma discharges can be generated at atmospheric pressure, each with distinct properties and applications [1, 27, 28, 29, 30]. Figure 1.1 illustrates the characteristic gas temperature and electron density of different discharges at atmospheric pressure.

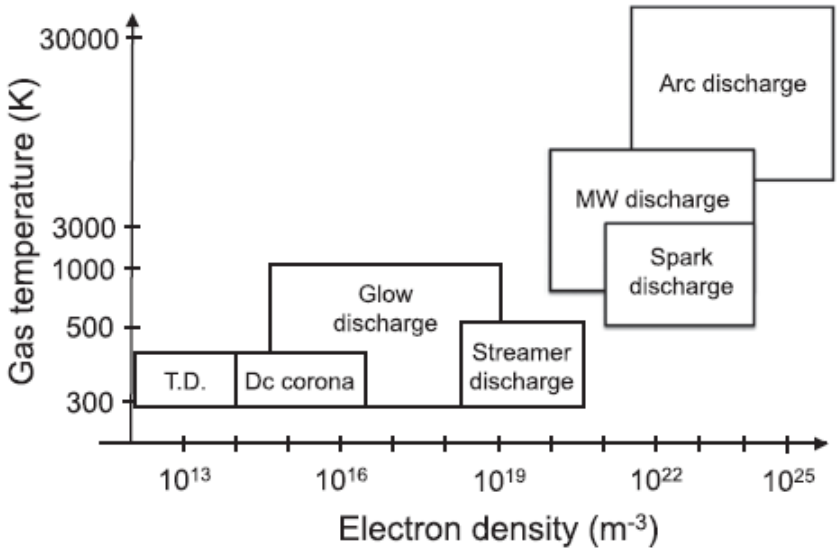

Figure 1.1: Overview of different atmospheric pressure gas discharges spanning a range of more than 10 orders of magnitude in electron density. TD stands for Townsend discharge. Illustration extracted from [1].

The main different types of discharges at atmospheric pressure include streamers, sparks and arcs which can be generated with nanosecond pulsed discharges. These discharges are initiated by very short, high-voltage pulses between electrodes. Streamer discharges in this context occur when the pulse ionizes the air to create a conductive path, which does not necessarily bridge the electrodes completely. This form can evolve into a spark discharge if the ionized channel extends and makes a direct connection between electrodes, allowing a more substantial current to flow and releasing more energy. Further escalation of this process can lead to an arc discharge, where the discharge becomes continuous due to sustained ionization and high conductivity in the plasma channel, characterized by very high current and thermal energy release. The ability to transition between these states within nanosecond pulsed discharges allows for precise control over the discharge characteristics. Applications of nanosecond pulsed discharges include plasma-assisted combustion and flow control, where precise control over plasma properties is essential. In these applications, different gas heating mechanisms become of special interest, which is described in the following

section.

1.1.2 Fast gas heating

Fast gas heating refers to a rapid increase in gas temperature commonly observed in non-equilibrium low-temperature plasmas at or above atmospheric pressure [3, 19, 21, 22, 23, 26, 31, 32]. It is commonly thought to stem from the electron kinetic energy via the relaxation of electronically excited states of atoms and molecules [21, 31], or from the dissociation of molecules [20, 33]. In plasma assisted combustion, the abrupt temperature increase induces an acceleration of combustion chemistry, thus shortening the ignition delay time [31]. Therefore, control over gas heating is pivotal for successful ignition [3]. In plasma aerodynamics, the primary effect of a plasma discharge on flow is often linked to gas heating in the discharge area, underscoring the significance of an accurate description of fast gas heating [34, 35]. Employing various discharges for plasma flow control, the most efficient actions generally involve the rapid release of thermal energy at specific points within the discharge area [21, 31]. Each of these examples highlight the need to understand the mechanisms underlying fast gas heating and the timescales on which they operate.

Although ion temperatures are difficult to measure in atmospheric pressure plasmas, measurements have been made of neutral gas temperatures that are elevated well above ambient room temperature [3, 19, 20, 21, 22, 23, 24, 25, 26]. Several mechanisms of neutral gas heating are known. Examples of the typical timescales are shown in figure 1.2. One is energy transfer from electron-neutral elastic collisions [32], which is typically expected to occur at timescales of 100's of ns. Other mechanisms that can transfer energy from electrons to neutral atoms/molecules include energy transfer between vibrationally excited states in molecules [36, 37], energy transfer from vibrational to translational states [36, 37, 38], electron-ion recombination processes [23] followed by ion-neutral elastic collisions, electron impact dissociation reactions [21]

and quenching of electronically excited molecules by oxygen atoms [22]. In fact, there are some examples in which one or more of these mechanisms appear to fully explain the measured neutral gas temperature. These include electron-neutral elastic heating on timescales of 100s of nanoseconds [24] and vibrational to translational relaxation on timescales of 10s of microseconds [25], among others [21, 22, 26].

Gas heating mechanisms in low-temperature plasmas have been extensively studied in the past [3, 19, 20, 21, 22, 23, 24, 25, 26, 32, 33, 36, 37, 38]. In air, electronically excited states contribute significantly to gas heating through dissociative excitation or quenching of electronically excited nitrogen molecules, as identified by Popov in 2011 [21]. Specifically, dissociation reactions due to electron impact on O_2 and N_2 molecules, and quenching processes involving electronically excited N_2 molecules by oxygen atoms, play a crucial role [21, 33]. Vibrationally excited states also contribute to gas heating due to non-thermal electron impact excitation, storing energy in the vibrational modes of nitrogen molecules, which is then released through vibration-translation (VT) and vibration-vibration (VV) relaxations [22, 36, 37, 38]. Energy exchange through electron-neutral elastic collisions further enhances fast gas heating in plasma discharges once the ionization fraction is high enough [32].

Moreover, the kinetic model presented by Popov (2011) emphasizes the significant role of dissociation reactions by electron impact and the quenching of electronically excited molecules in fast gas heating. At reduced electric fields (E/N) above 200 Td, the main contribution to gas heating in nitrogen-oxygen mixtures arises from these processes. Key reactions include the quenching of $N_2(C^3\Pi_u)$ by O_2, quenching of $N_2(B^3\Pi_g)$ by O_2, dissociation of N_2 by electron impact, quenching of excited $O(^1D)$ atoms by N_2, dissociation of O_2 by electron impact, and quenching of $N_2(A^3\Sigma_u^+)$ and $N_2(a'^1\Sigma_u^-)$ by O_2 [21]. These processes result in significant energy release and gas heating. For instance, quenching of $N_2(A^3\Sigma_u^+)$ by O_2 leads to the formation of vibrationally excited N_2 and dissociation of O_2, significantly contributing to gas

heating. This model highlights that approximately 30% of the discharge power is converted to fast heating of nitrogen-oxygen mixtures, with the efficiency depending on the oxygen content and the reduced electric field [21]. These findings provide a firm theoretical and experimental basis for understanding gas heating mechanisms in non-equilibrium atmospheric pressure plasmas.

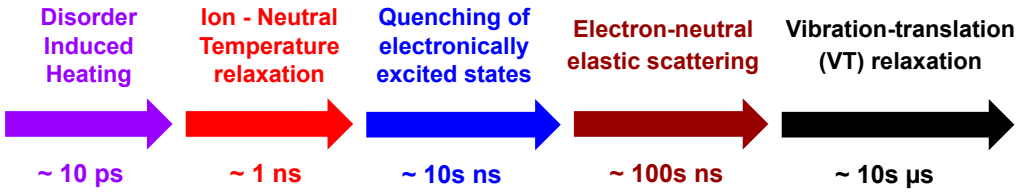

Figure 1.2: Comparison of the typical timescales of the possible mechanisms of fast neutral gas heating observed. The disorder induced heating and ion-neutral temperature relaxation mechanisms affect the ion and neutral temperatures respectively in faster timescales compared to the previously studied mechanisms. The timescales here assume atmospheric pressure and typical ionization fractions [2].

1.1.3 Simulation techniques used for atmospheric pressure plasmas

The most used simulation techniques for low temperature plasmas and in particular, atmospheric pressure plasmas are 0D global models, fluid simulations and the particle-in cell method described in the following sections.

1.1.3.1 0D Global models

A global model in plasma chemistry is a method used to simulate the behavior of plasmas by considering the entire system as a single, well-mixed volume without resolving spatial variations. This modeling technique simplifies the plasma dynamics by averaging the properties over the entire reactor volume, thus reducing the complexity of the simulations and making it computationally less demanding.

The core of a global model consists of solving a set of rate equations for the densities of various species involved in the plasma. These equations account for the production and loss processes of species due to various reactions, such as ionization,

recombination, excitation, and dissociation. For example, the model presented by Minesi et al. in 2023 includes these processes in the context of nanosecond pulsed discharges in atmospheric pressure air [6]. Most of gas heating modeling has been conducted using 0D global models [21, 22, 31]. Global models include as input parameters initial densities and energy distribution functions for species as well as corresponding rate coefficients and cross sections, pressure and reduced electric field. Some of these parameters are typically derived from experimental data or more detailed kinetic models such as solving the Boltzmann equation [39]. Chapter II describes a global model developed in this work. When spatial variations need to be accounted for, the global model can be included in a fluid simulation as described in the following section.

1.1.3.2 Fluid simulations

Multiple problems of interest in low temperature plasmas have phenomena with time and length scales that can differ by several orders of magnitude. These problems, can be solved with a reasonable computational cost by coupling the plasma chemistry kinetics with fluid dynamics. This approach requires to have a good understanding of the kinetic mechanisms as well as transport properties such as diffusion coefficients and thermal conductivity, since they are input parameters for such models [40].

As described by Tochikubo and Komuro (2021) [41], in the fluid model, the transport of species is described by the continuity equation for charged and neutral species

$$\frac{\partial n_k}{\partial t} + \nabla \cdot \Gamma_k = S_k, \tag{1.1}$$

where n_k, Γ_k, and S_k denote the number density, flux, and source term of the k-th species, respectively. The flux of the k-th charged species is generally described by

the drift–diffusion approximation as

$$\Gamma_k = n_k \mathbf{u}_k = \text{sign}(q_k) n_k \mu_k \mathbf{E} - D_k \nabla n_k, \tag{1.2}$$

where $\mathbf{u}_k$, q_k, μ_k, and D_k denote the mean velocity, charge, mobility, and diffusion coefficient of the k-th species, respectively, and $\mathbf{E}$ is the electric field [42]. The drift-diffusion approximation is valid at pressures above 10 mTorr and at reduced electric field below 500 Td. Furthermore, the number density of charged species should be much less than the number density of the background gas, hence the discharge must be weakly ionized. The plasma must also be collisional which means that the mean free path between electrons and the background gas must be much less than the characteristic dimension of the system. The treatment of the background neutral gas however requires the Navier Stokes equations, in order to include convective transport effects. The flux for the k-th neutral species Γ_k is described using only the diffusion term as:

$$\Gamma_k = -D_k \nabla n_k. \tag{1.3}$$

The source term S_k for charged species in equation 1.1 represents the creation and annihilation of species through chemical reactions, including electron impact ionization, electron attachment, and recombination between positively and negatively charged species. Because the reaction rate coefficients for electron impact reactions are dependent on the electron energy distribution function (EEDF), it is essential to account for the EEDF when calculating the density conservation equations.

To incorporate the effects of the EEDF, two typical models are employed. The first model is the local field approximation (LFA). In this approach, the electron mobility, diffusion coefficient, and electron impact reaction coefficients—such as the rate coefficients for ionization, attachment, excitation, and dissociation—are expressed as functions of the local reduced electric field, E/N, by solving the Boltzmann equation.

The second model also solves the Boltzmann equation but expresses the electron mobility, diffusion coefficient, and electron impact reaction coefficients as functions of the mean electron energy [41]. The local mean electron energy $\bar{\epsilon}$ in eV is obtained by solving the conservation equation of electron energy density ω_e, which is defined as the product of electron density n_e and mean electron energy $\bar{\epsilon}$, $\omega_e = n_e\bar{\epsilon}$, as

$$\frac{\partial \omega_e}{\partial t} = -\nabla \cdot \Gamma_\omega - \nabla \cdot (\mathbf{E} \cdot \Gamma_e) - \sum_k \epsilon_k \nu_k n_e - \nu_m \frac{2m}{M} \omega_e \tag{1.4}$$

where Γ_ω and Γ_e are the electron energy density flux and electron particle flux, respectively; m and M are the mass of the electron and parent gas, respectively; ν_m is the electron momentum transfer collision frequency; ϵ_k and ν_k are the threshold energy and collision frequency, respectively, for the k-th type of inelastic collision. Equation 1.4 accounts for changes in the electron energy density due to electron energy flux, electron particle flux, inelastic collisions with heavy species and elastic collisions and it assumes an electron mean energy much larger than the mean energy of the collision partners. The electron energy density flux is written as

$$\Gamma_\omega = -\frac{5}{3}\omega_e \mu_e \mathbf{E} - \frac{5}{3} D_e \nabla \omega_e, \tag{1.5}$$

where the first term represents the energy flux due to drift produced by the electric field and the second term the diffusion of energy due to gradients in the electron energy density.

Finally, electric potential is determined self-consistently with the charged species densities by solving the Poisson equation

$$\nabla \cdot (\epsilon_0 \nabla \phi) = -e(n_e - n_+ + n_-) \tag{1.6}$$

where e, ϵ, and ϕ are the unit charge, vacuum electric permittivity, and potential,

respectively, with the relation $\mathbf{E} = -\nabla\phi$. Subscripts + and − denote a positive ion and negative ion, respectively.

While fluid models can be useful for different atmospheric pressure plasmas applications at a reasonable computational cost, some problems require kinetic simulations tools. In kinetic simulations, one or more species are treated as particles and the corresponding equations of motion are solved self consistently with charge densities and collision dynamics. A commonly used kinetic simulation method is the particle-in-cell method described in the following section.

1.1.3.3 Particle in cell simulations

The Particle-In-Cell (PIC) method is a commonly used computational approach in plasma modeling [43, 44, 45] that is primarily characterized by its use of numerical macroparticles. These macroparticles serve as aggregates of physical particles, allowing the method to simulate macroscopic scales effectively. In a PIC simulation, the equations of motion of macroparticles are solved self consistently with the electric field produced by solving the Poisson equation for the instantaneous charge density locally on a grid. The PIC method requires a series of numerical conditions to ensure validity. First, the Debye length must be adequately resolved to prevent artificial "grid heating" [44, 46]. Second, a sufficiently large number of macroparticles per cell must be maintained to ensure a statistically representative model of the plasma. In addition, the Courant-Friedrichs-Lewy (CFL) condition must be met to resolve the corresponding plasma frequency. This condition is a stability criterion that determines the maximum allowable time step for numerical integration. Specifically, the time step must be small enough to ensure that a particle does not travel more than one cell length in a single time step, thus maintaining the stability and accuracy of the simulation [44]. Adherence to these guidelines enables the PIC method to make kinetic simulations tractable and to simulate entire plasma devices with a reasonable

computational cost. This method is described with more details in chapter II.

The PIC method is pivotal in understanding and modeling low-temperature plasmas, including those at atmospheric pressure. It is often integrated with Monte Carlo Collisions (MCC), providing a robust tool for investigating the complex dynamics of plasma discharges from a kinetic standpoint. The MCC method is a numerical approach in particle simulations that models particle collisions by randomly sampling outcomes based on cross-sectional data, effectively capturing the statistical nature of particle interactions [44]. This capability is especially crucial in non-equilibrium plasmas, where electron energy distributions are typically non-Maxwellian. For instance Klich et al. (2022) used a hybrid PIC/MCC simulation to investigate radio-frequency (RF) atmospheric pressure plasma jets (APPJs) in the non-neutral regime [47]. Additionally, Donkó et al. (2021) described the application of the eduPIC code, an educational PIC/MCC simulation tool, in modeling capacitively coupled RF plasmas, demonstrating detailed plasma characteristics at atmospheric pressure [48].

Moreover, PIC simulations have been extensively used to model streamer discharges at atmospheric pressure, characterized by fast-propagating ionization waves. Chanrion and Neubert (2008) developed a 2D axi-symmetrical PIC-MCC code to study the propagation of streamers in air, providing critical insights into the role of photoionization and the conditions necessary for the formation of runaway electrons [49]. Kolobov and Arslanbekov (2016) highlighted the importance of adaptive mesh refinement (AMR) in PIC simulations, specifically for high-pressure gas breakdown and streamer development, showing that cell-based AMR significantly enhances the efficiency and accuracy of simulations [50]. Teunissen and Ebert (2016) utilized a 3D PIC-MCC model with adaptive mesh refinement to investigate the inception of nanosecond pulsed discharges around a sharp anode in nitrogen/oxygen mixtures at atmospheric pressure, highlighting the impact of photoionization and space charge on discharge development [51]. The versatility and detailed insights offered by PIC simu-

lations are indispensable for advancing the understanding of low-temperature plasmas and their applications, as continuous improvements in computational resources enable more complex and accurate models of plasma behavior under various conditions.

1.2 Strong correlations

Strong coupling refers to interactions in which the average potential energy of interacting particles [$\phi_{ss'}(r = a_{ss'})$, where $a_{ss'}$ is the average distance between particles of species s and s'] exceeds their average kinetic energy ($k_B T_{ss'}$), i.e. $\Gamma_{ss'} \gtrsim 1$, where s and s' are the species involved in the interaction and,

$$\Gamma_{ss'} = \frac{\phi_{ss'}(r = a_{ss'})}{k_B T_{ss'}}, \tag{1.7}$$

where $T_{ss'} = (T_s + T_{s'})/2$ is a mean temperature characterizing the two interacting species. For example, the Coulomb potential for ion-ion interactions is $\phi_{ii} = (Ze)^2/4\pi\epsilon_0 a_{ii}$ and the ion-ion Coulomb coupling parameter is $\Gamma_{ii} = (Ze)^2/(4\pi\epsilon_0 a_{ii} k_B T_i)$.

A weakly coupled plasma is characterized by the dominance of kinetic energy over potential energy, meaning the average potential energy between particles is much less than their thermal energy. This leads to weak interactions where long-range Coulomb forces are screened by the Debye length, and the plasma parameter Λ (which represents the number of particles in a Debye sphere) is much greater than one. As a result, weakly coupled plasmas can be described accurately by classical kinetic theory and the Boltzmann equation, focusing on small-angle collisions and employing approximations like the standard Coulomb logarithm in the Landau-Spitzer formula.

Conversely, strongly coupled plasmas have a higher interaction strength where the potential energy between particles is comparable to or greater than their kinetic energy. This results in significant particle correlations and large-angle collisions, which invalidate the weak coupling assumptions. Also, many-body interactions are a char-

acteristic of strong coupling. This has major implications in transport coefficients like diffusion, thermal conductivity and viscosity and particle dynamics. In this regime, models need to account for strongly coupled physics, often requiring first principles molecular dynamics simulations or advanced theoretical approaches to capture the plasma dynamics accurately [52, 53, 54, 55].

1.2.1 Strongly coupled interactions at atmospheric pressure

In most CAPPs, ions are expected to be in equilibrium with the neutral gas near room temperature, while electrons have a much higher temperature on the order of eV or several eV. A consequence is that the hotter electrons are characterized by a weakly coupled regime ($\Gamma_{ee} \ll 1$), while the much cooler ions can be strongly coupled ($\Gamma_{ii} \gtrsim 1$) if the ionization fraction is large enough.

For a partially ionized plasma with one gas species, neutral-neutral, ion-neutral and ion-ion interactions are included using the Lennard-Jones, charge induced dipole and Coulomb potentials respectively [56]

$$\phi_{\mathrm{LJ}}(r) = 4\epsilon \left[\left(\frac{\sigma}{r}\right)^{12} - \left(\frac{\sigma}{r}\right)^{6} \right], \tag{1.8}$$

$$\phi_{\mathrm{ind}}(r) = -\frac{q^2}{8\pi\epsilon_0}\frac{\alpha_{\mathrm{R}} a_0^3}{r^4}, \tag{1.9}$$

and

$$\phi(r) = \frac{q^2}{4\pi\epsilon_0}\frac{1}{r}, \tag{1.10}$$

where $\epsilon = 120k_B$, $\sigma = 0.34$ nm, and $\alpha_{\mathrm{R}} = 11.08$ for Ar [56] and a_0 is the Bohr radius. Considering an Ar plasma at room temperature and variable ionization fraction and pressure, the coupling parameter associated with each interaction can be computed from equations (1.7)–(1.10), using $a_{in} = (3/4\pi n_{in})^{1/3}$ where $n_{in} \approx x_i n_i + x_n n_n$ to estimate the average interparticle spacing between ions and neutrals. Here, $x_i = n_i/n$ and $x_n = n_n/n$ are the ion and neutral concentrations, n_i and n_n are the ion and

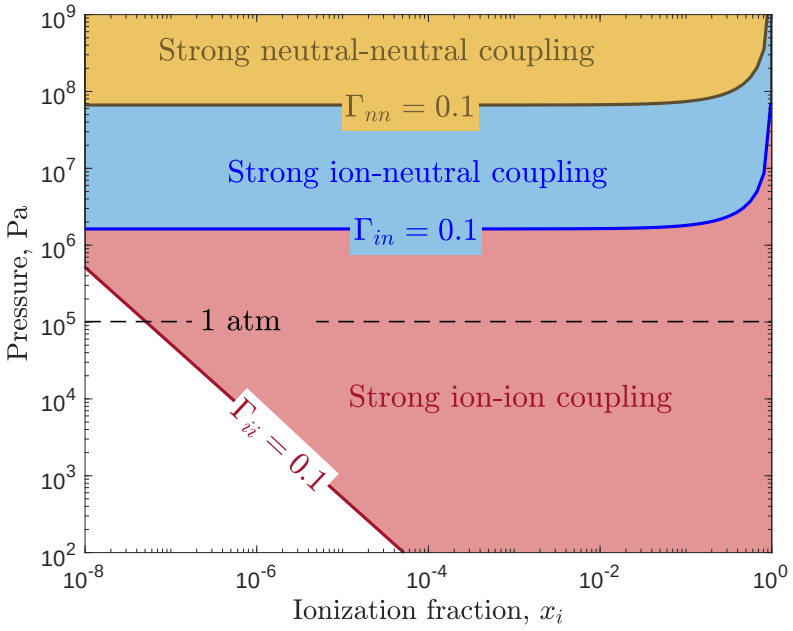

Figure 1.3: Coupling parameter space for ion-ion, ion-neutral and neutral-neutral interactions for an Ar gas at room temperature and different pressures and ionization fractions.

neutral densities, and $n = n_i + n_n$ is the total density. The pressure and ionization fraction at which the transition from a weakly to a strongly coupled regime occurs is estimated from the limit $\Gamma = 0.1$, which is the condition where the Boltzmann equation is known to break down [57, 58].

As shown in figure 1.3, at small ionization fractions and pressures below atmospheric pressure, none of the interactions are strongly coupled. However, by increasing the ionization fraction or the pressure, it is possible to find a strong ion-ion coupling region. In fact, the figure shows that ion-ion interactions at many CAPP conditions are expected to be strongly coupled. In particular, where the ionization fraction is greater than 10^{-6} such as streamer, spark and arc discharges as shown in figure 1.1. If the pressure is increased above $\approx$ 10 atm, a strong ion-neutral coupling regime is reached. Further increases in pressure can lead to a strong neutral-neutral coupling regime at around 1000 atm.

Since the ion-ion Coulomb coupling parameter exceeds 0.1 in many CAPPs ap-

plications, the binary ion-ion collision picture and hence the Boltzmann equation are not expected to apply. In this strongly coupled regime, many-body collisions dominate the interactions between ions and a simulation technique that accounts for strong coupling effects is necessary for modeling such plasmas when ion dynamics are important.

1.2.2 Disorder induced heating

Strongly coupled plasmas are influenced by physical effects that fundamentally differ from those governing weakly coupled plasmas. An example is disorder-induced heating [59]. This arises in strongly coupled systems when the potential energy landscape associated with interactions between particles changes in such a way that particles move to a lower potential energy configuration, releasing kinetic energy in the form of heat. One way that this can occur is through the ionization of a neutral gas. When short-range atomic interactions change to long-range Coulomb interactions, ions reconfigure to a more ordered state due to their mutual repulsion. The more ordered state has a lower potential energy than the initial state (immediately after ionization) because ions spread further apart from one another. The decrease in potential energy in this reconfiguration is compensated by an increase in kinetic energy. Disorder-induced heating is not important in weakly coupled plasmas because the kinetic energy gained in the reconfiguration is small compared to the initial kinetic energy. However, it can be a dominant effect in strongly coupled plasmas. For example, DIH caused by ionization has been measured and studied in detail in ultracold neutral plasmas [59, 60, 61, 62].

This work shows that ionization can cause DIH in atmospheric pressure plasmas as well, and that it can be a dominant effect that determines both the ion and neutral temperature evolution. Using Molecular Dynamics (MD) simulations, we show that immediately after ionization ions have a coupling strength much larger than one,

with Γ_{ii} ranging from approximately 5 to 25 for simulations when the ionization fraction ranges from 0.01 to 0.7, corresponding to ion densities from 2.5×10^{23} m^{-3} to 1.75×10^{25} m^{-3}. Ions then rapidly heat over a timescale of approximately one ion plasma period (ω_{pi}^{-1}, where $\omega_{pi} = \sqrt{e^2 n_i / \epsilon_o m_i}$ is the ion plasma frequency) to a condition where $\Gamma_{ii} \approx 1$. This typically corresponds to a ~ps timescale. This can raise the ion temperature several times, depending on the ionization fraction. After DIH, ions thermally equilibrate with neutrals via elastic scattering, causing them to cool and the neutral gas to heat. The cooling causes ions to return to a more strongly coupled state. Depending on the ionization fraction, the neutral heating can be substantial, leading to neutral temperatures that are several times room temperature. Ion-neutral thermal equilibration typically takes hundreds to thousands of ion plasma periods, corresponding to a ~ns timescale. In addition to the simulations, a model is developed to describe the main features of the ion and neutral temperature evolution. These results are described with more details in chapter III. Then, in chapter IV, the developed model is implemented in a plasma chemistry global model to compare different sources of fast gas heating with disorder induced heating in N_2 nanosecond pulsed discharges at 1 atm and 10 atm. It is observed that while DIH is not the dominant heating mechanism, when full ionization is reached, it can increase the temperature on the order of 20% and 60% at 1 and 10 atm. In particular, when DIH becomes relevant, the electron density is large enough such that thermalization occurs and both electrons and ions are at equilibrium with each other. Finally, while DIH is not the main heating mechanism in the mentioned pressure range, it can indirectly influence the plasma chemistry by reducing the energy transfer from electrons to ions and thus, increasing the rates of electron impact inelastic processes including dissociation and ionization.

1.2.3 Diffusion

The transport of ionized reactive species in atmospheric pressure plasmas is one of the main mechanisms of interest and is governed by mobility and diffusion processes. Furthermore, the transport of reactive species in general is relevant for many of the mentioned applications from medicine to plasma assisted ignition and combustion. For example, in plasma assisted ignition, diffusion of reactive nitrogen and oxygen species (RONS) can influence the ignition process and flame propagation, reducing the ignition delay time by orders of magnitude and increasing the flame propagation velocity [13, 63]. In plasma assisted combustion, the relative timescales between diffusion and advection of fuel and reactive species and the combustion reaction rates can influence the combustion efficiency [64]. Another example is diffuse plasmas: while constriction into filaments is likely to happen in atmospheric pressure plasmas, Li et al [65] showed that ambipolar diffusion plays a significant role as a possible mechanism to generate cost efficient atmospheric diffuse plasma jets for biomedical decontamination and materials processing applications. Similarly, Tang et al [66] showed that ambipolar diffusion plays a key role in the onset of diffuse direct-current glow discharges at atmospheric pressure. Finally, in CO_2 conversion by plasma technology, modelling the different plasma discharges with fluid simulations requires diffusion coefficients as one of many input parameters in order to account for spatial variations due to transport in the plasma [67].

It is clear that diffusion processes play a key role in a variety of plasma devices at atmospheric pressure and above. An underappreciated aspect in modeling the diffusion rate in these plasmas is that ions can be in a regime of strong Coulomb coupling, since ions are expected to be be strongly correlated ($\Gamma_{ii} > 1$) in atmospheric pressure discharges, particularly at larger ionization fractions ($x_i \gtrsim 10^{-5}$). Standard models of diffusion in plasmas are based on the Boltzmann kinetic equation [68], which applies to the weakly correlated regime $\Gamma_{ii} \ll 1$, and therefor are not applicable.

In this work, we propose a model for diffusion that accounts for strong ion-ion correlations at atmospheric pressure discharges over a wide range of ionization fractions. The model is an application of the recently developed mean force kinetic theory [52], which has previously been applied to fully ionized plasma, to the case of partially ionized atmospheric pressure plasma. We show that the total ion diffusion coefficient exhibits three regimes: (1) At small ionization fraction ($x_i \lesssim 10^{-6}$), corresponding to ion densities of $n_i \lesssim 10^{20}$ m^{-3}, ion diffusion is dominated by weakly coupled ion-neutral collisions, as usually modeled based on the Boltzmann equation [69, 70, 71]. (2) For moderate ionization fractions ($10^{-6} \lesssim x_i \lesssim 10^{-2}$), corresponding to ion densities ranging from $n_i \approx 10^{20} - 10^{24}$ m^{-3}, ion-ion collisions are important and strong ion-ion correlations influence the diffusion processes. (3) At large ionization fraction ($x_i \gtrsim 10^{-2}$), corresponding to ion densities $n_i > 10^{24}$ m^{-3}, strongly correlated ion-ion interactions set the diffusion rate. Furthermore, the strong ion-ion correlations formed in the ionization process cause disorder-induced heating (DIH), which substantially increases the ion and neutral temperatures [2]. Here, we show that the temperature increase due to the DIH considerably increases the expected ion and neutral diffusion coefficients at atmospheric pressure and this effect becomes more pronounced at larger pressures, such as the range relevant to plasma assisted combustion [13]. We show that the plasma densities over which the ion diffusion coefficient is affected by strong Coulomb coupling are of special interest to nanosecond repetitively pulsed (NRP) discharges in the regimes of glow ($n_i \approx 10^{19} - 10^{21}$ m^{-3}) , spark ($n_i \approx 10^{21} - 10^{22}$ m^{-3}) and thermal spark ($n_i \approx 10^{25}$ m^{-3}) discharges [72].

The model was tested using MD simulations. Including both ions and neutral atoms in MD simulations can be prohibitively computationally expensive at low ionization fractions. In order to solve this problem, we incorporated a Monte Carlo collision module for ion-neutral collisions described in chapter II. This applies MCC to model ion-neutral collisions, while solving for the ion-ion interactions self-consistently,

as in standard MD simulations. This is similar to the model described in Donko *et al* [73] for electron-neutral collisions. Comparing with previous results [2], we show that the MD+MCC approach is suitable for obtaining both the dynamics and equilibrium properties of a discharge. Furthermore, the results obtained with the proposed method provides a tool to compute the ion diffusion coefficient using the Green-Kubo relations [74]. The MCC model is valid for ion-neutral interactions because they are weakly correlated at atmospheric pressure conditions, due to their short-range nature. These results are described with further details in chapter V.

1.2.4 PIC simulations

An implication of ions being strongly coupled for a wide range of ionization degrees at atmospheric pressure is that common approaches to modeling atmospheric pressure plasmas need to be reassessed. Most modeling techniques, including PIC methods and solutions of multi-fluid equations, are based on solving a Boltzmann equation or approximations of it (such as multi-fluid models obtained from taking moments of the Boltzmann equation). However, the Boltzmann equation is valid only for weakly coupled systems, such as dilute gases and plasmas. At a fundamental level, it does not treat strong coupling effects that can influence dynamics of atmospheric pressure plasmas. Disorder-induced heating is an example of this. If strong correlations are not accounted for, the ion and neutral temperatures could be mistakenly underestimated as well as transport properties.

Given the transformative impact of atmospheric pressure plasma applications, understanding and controlling the characteristics of these plasmas is of paramount importance. Accurate and efficient modeling of plasma discharges at atmospheric and higher pressures is critical for the advancement and optimization of plasma devices. Simulations, for instance, can aid in identifying optimal operating parameters like discharge voltage, power, frequency, electrode configuration, and gas mixture for

diverse applications. Consequently, it is imperative to develop reliable and efficient computational tools for simulating the behavior of cold atmospheric pressure plasmas.

1.2.4.1 PIC simulations and strongly coupled plasmas

It is found that PIC simulations are not well-suited to atmospheric pressure plasmas when the plasma density or macroparticle weight are too large because of effects associated with correlation heating. Here, we refer to "PIC simulations" in the traditional sense, not including the P3M method [74], which we consider to be a variant of MD in this work. The assumptions of the PIC method presume weak coupling between charged particles, ignoring interactions within a macroparticle and within a cell. Hence, pure PIC simulations effectively solve the Vlasov equation. In an attempt to incorporate collisions, PIC is often combined with a Boltzmann collision operator through the MCC or DSMC methods [44, 45]. It may be expected that creating a collision routine to incorporate strong correlation effects could enable the successful application of PIC in these scenarios. However, it is shown here that PIC faces inherent challenges when modeling strongly coupled plasmas that can not be remedied by the addition of a collision routine. These shortcomings stem from the requirement that PIC simulations at atmospheric pressure need to resolve very small spatial scales (here the Debye length and mean ion separation) while using macroparticles to remain practical.

In fact, a primary factor precluding the effective use of PIC in these scenarios is disorder-induced heating. Here it is shown that to correctly capture DIH within PIC simulations, it is necessary to adopt a macroparticle weight (w) of one and to resolve the physical interparticle spacing. However, adhering to these conditions renders PIC prohibitively expensive for macroscopic−scale domains, as the computational load dramatically increases. Compounding the challenge, because the average interparticle spacing between ions is larger than the Debye length λ_D, adhering to the requisite

of the Debye length resolution, the physical interparticle spacing also needs to be resolved. This leads to less than one macroparticle per cell, inducing grid heating even if the Debye length is resolved. The combination of these conditions significantly exacerbates the difficulty of employing PIC for the simulation of strongly correlated, atmospheric pressure plasmas. These results are described in chapter VI.

1.2.4.2 Artificial correlation heating

Beyond the limitations associated with strongly coupled plasmas, this study reveals a new numerical heating mechanism, termed "artificial correlation heating" (ACH), which can arise even in weakly coupled plasmas. This mechanism is analogous to the cause of DIH, as it stems from Coulomb repulsion, but distinguishes itself as a numerical effect associated with a macroparticle weight larger than one, $w > 1$. Interestingly, like DIH, ACH is also associated with a conversion of potential to kinetic energy that arises at strong coupling. However, the coupling strength involved in this case is a macroparticle coupling strength

$$\Gamma^{w}_{ss'} = \Gamma_{ss'} w^{2/3}, \tag{1.11}$$

where $\Gamma_{ss'}$ is the physical coupling strength for interactions between species s and s', derived in equation 1.11. Thus, even if the physical coupling strength is small, the macroparticle coupling strength can be large if $w \gg 1$. Chapter VI describes how equation 1.11 is derived by accounting for the effect of macroparticle weight in the numerical Coulomb coupling parameter. Avoiding ACH requires maintaining numerous macroparticles per cell, a factor that further complicates the application of the PIC method.

In the context of atmospheric pressure plasmas, ions may reach a strongly correlated regime and therefore be influenced by DIH, while electrons are expected to be

weakly coupled due to their larger temperature. This may lead to the expectation that PIC applies to the electrons. Although that can be true, we find that ACH is an important consideration if a large macroparticle weight is applied to the electrons.

Since ACH arises as a consequence of a numerically-enhanced Coulomb potential energy due to a large macroparticle weight, here we propose that in order to avoid ACH, a PIC simulation must obey a criterion that the macroparticle coupling parameter be less than one, $\Gamma^w_{ss'} < 1$, for each combination of interacting species s and s'.

Here, we will concentrate on like-particle interactions ($s = s'$), so $a_{ss'} = a_s = (3/4\pi n_s)^{1/3}$ and $T_{ss'} = T_s$ is the temperature of species s. The $\Gamma^w_{ss'} < 1$ condition limits how high a macroparticle weight can be for a given density and temperature. If this condition is not met, then the weakly coupled particles will be represented numerically as strongly coupled macroparticles, which induces ACH and can significantly raise the temperature of that species on a short timescale characteristic of the plasma period of that species $\omega_{ps}^{-1} = (\epsilon_o m_s / Z_s^2 e^2 n_s)^{1/2}$.

Acknowledging the significance of ACH, a comprehensive model is developed that incorporates density, temperature, macroparticle weight and grid resolution. Validated against PIC simulations, this model serves as a predictive tool to delineate a limit of applicability of the PIC method. It is shown that ACH provides an upper limit on the density scaled by the macroparticle weight squared, $n_s w^2$, for a fixed temperature. In addition, the consequences of violating the ACH condition ($\Gamma^w_s < 1$) are explored. In particular, the magnitude of ACH can be reduced if a large number of macroparticles are present per cell. Specifically, it is found that if ≈ 240 particles per cell are present, then the temperature rise from ACH remains small even if $\Gamma^w_s > 1$. However, this approach is not entirely satisfactory because it implies not resolving the Debye length, and therefore, grid heating occurs. This is because Γ^w_s, the Debye length λ_{Ds}, the average number of macroparticles per cell N_c and cell size

Δx are related as $\Delta x/\lambda_{Ds} = (4\pi N_c/3)^{1/3}\sqrt{3\Gamma_s^w}$. Thus, if $\Gamma_s^w > 1$ and $N_c > 1$, then the Debye length is necessarily unresolved.

Finally, it is shown that ACH can induce a runaway heating process in simulations that include ionization of a neutral gas. As the electron temperature artificially increases due to ACH, it can trigger nonphysical ionization events, further increasing the electron density and perpetuating the cycle of heating and, ultimately, resulting in numerical instability. This positive feedback loop highlights the critical need for a better understanding and careful application of the PIC method, especially when simulating plasmas with high densities and large macroparticle weights in 3D domains. These results are described in chapter VII.

CHAPTER II

Simulation Techniques

In this work, different numerical approaches have been used to study strongly coupled effects in atmospheric pressure plasmas. While highly expensive from a computational point of view, molecular dynamics is useful to study basic physics phenomena as well as to calculate transport coefficients from first principles. This method was used to study disorder induced heating as well as ion diffusion (chapters III and V respectively) and it is described in section 2.1. Secondly, the PIC method is a robust and commonly used technique for a wide range of plasma discharges. Here, a PIC simulation code is developed to study the limitations of PIC in the strongly coupled regime by comparing the results with the more first-principles MD simulations. This method is described in section 2.3 and the results are covered in chapters VI and VII. Finally, a global model is developed to study the effects of strongly coupled physics on plasma chemistry for nanosecond pulsed discharges. This method is described in section 2.2 and the results in chapter IV.

2.1 Molecular dynamics

Molecular Dynamics is a computational technique that serves as a powerful tool for studying the dynamical behavior of molecular systems, offering valuable insights into the microscopic mechanisms underlying various physical processes. The method

provides insights into the equilibrium and transport properties of classical many-body systems by solving Newton's equations of motion for a system of interacting particles over a specified time period [74]. In this section, the principles of MD are described as well as modifications incorporated into the open source software LAMMPS [75], used in this work, in order to study diffusion in strongly coupled atmospheric pressure plasmas.

2.1.1 Basics of molecular dynamics

The core idea of MD simulations is to solve for the particle dynamics from a first principles standpoint, in the sense that direct forces are calculated over individual particles by knowing the interaction potentials. While this method is not strictly first principles since it is classical, it is more accurate than other particle based methods such as PIC. The standard simulation setup involves the following steps:

1. **Initial conditions:** A sample is prepared by selecting a model system consisting of N particles. Initial positions and velocities of these particles are assigned, typically following a Maxwell-Boltzmann distribution. Particles can represent atoms, ions, electrons or even complex molecular structures.

2. **Simulation domain:** The simulation domain can be arbitrarily defined depending on the application of interest. In this work, MD simulations are run in cubic domains with periodic boundary conditions for particles and fields.

3. **Force calculation:** The forces acting on each particle are computed using interatomic potentials or force fields. Commonly used potentials include Lennard-Jones, Coulombic interactions, and more complex empirical or calculated potentials for specific species.

4. **Integration of equations of motion:** Newton's equations of motion are integrated to update the positions and velocities of the particles over discrete

time steps. Algorithms such as the Verlet integration or leapfrog methods are often employed for this purpose.

5. **Equilibration:** The system is allowed to evolve until it reaches equilibrium, where macroscopic properties like temperature and pressure stabilize.

6. **Data collection:** After equilibration, the system's properties are sampled and averaged over time to obtain meaningful physical quantities such as temperature, pressure, diffusion coefficients, and radial distribution functions.

2.1.2 Interaction potentials

In a MD simulation, the force acting on each particle is a sum of the forces due to the particle's interaction with other particles in the system. Forces are calculated from interaction potentials predefined for each pair of particles $(s, s^{'})$ in the domain. Interaction potentials are defined as a function of the intermolecular distances, however they can be classified as either short or long range potentials. Short range potentials, such as the Lennard-Jones (LJ) potential are usually treated with a cutoff distance. This is, only particles within a certain radius from a given particle are considered when calculating the force due to the LJ potential. However, long range potentials, such as the Coulomb potential are treated differently. A cutoff distance is usually defined for a long range potential in order to treat differently the contribution to the force over a particle from particles within the cutoff distance and particles at larger distances [74]. An example of this is the particle particle particle mesh method described in the following section.

2.1.3 The particle particle particle mesh method

The P3M method consists of splitting the Coulomb potential into two parts using the identity

$$\frac{1}{r} = \frac{f(r)}{r} + \frac{1 - f(r)}{r} \tag{2.1}$$

where $f(r)$ is a switching function. Hence, the P3M method is based on separating the total interaction between particles into the sum of short-range interactions (first term in equation), which are computed by direct particle particle summation, and long-range interactions (second term in equation), which are calculated by solving Poisson's equation using periodic boundary conditions. The long-range Poisson solve part consists of interpolating the charges into a grid within the domain, where the Poisson equation is solved usually using a fast Fourier transform (FFT), and then the potential is interpolated back onto the positions of each particle. By doing this, the P3M method can efficiently handle long range potentials in large simulation domains without having an O(N^2) computer associated time, since the long range part handled by an FFT has a cost of O(N log N) [45, 74].

2.1.4 Equations of motion

Once forces on each particle due to the rest of the particles in the system are calculated, Newton's equations of motion are solved for each particle on every timestep. The commonly used method is the Verlet algorithm, which is energy conserving with a local error O(Δt^4) in the position and a global error O(Δt^2) , both for position and velocity [74].

2.1.5 Thermostating and energy conserving simulations

Standard MD simulations are split into two stages as described before. First, a thermostat simulation is run which mimics a canonical ensemble by maintaining

constant the total number of particles, volume and temperature of the system (NVT stage). This stage ensures that the system is equilibrated within a temperature range defined as an input parameter. This equilibration is a necessary step before switching to an energy conserving stage where microscopic physics phenomena is studied. There are different algorithms for the NVT stage but the most commonly used is the Nosé-Hoover thermostat, which consists of extending the Hamiltonian of the system by using a coordinates transformation in the phase space in order to represent a heat bath at a constant temperature [74]. This stage imposes a temperature into the system by bringing it into thermal contact with a large heat bath. This stage is run until the temperature, as well as the potential energy in the system reach a steady state.

Once equilibrium is reached, the simulation is switched from NVT to an energy conserving stage (NVE) where E represents the total energy of the system. This stage is necessary since in our work we focus on studying the non equilibrium ion dynamics in the strongly coupled regime, in particular, the evolution of the ion temperature after ionization. In this stage, the unmodified Hamiltonian is used and equations of motion are solved using the Verlet or other energy conserving algorithm [45, 74]. In this stage, thermodynamic properties are calculated to study the system.

2.1.6 Temperature calculation

In MD simulations, temperature is derived from the kinetic energy of the particles. Using the equipartition theorem, the temperature T can be calculated as

$$\left\langle \frac{1}{2} m v^2 \right\rangle = \frac{3}{2} k_B T, \tag{2.2}$$

where m is the mass of a particle, v is its velocity, and k_B is the Boltzmann constant. This temperature is termed "kinetic" because it directly relates to the motion of the

particles. For a system in equilibrium and in the absence of non-conservative forces, this kinetic temperature aligns with the thermodynamic temperature, which is a measure of the average kinetic energy per degree of freedom in the system [74]. The kinetic temperature is used primarily because it provides a computationally straightforward and instant measure of the system's temperature, assuming equilibrium conditions. The instantaneous temperature $T(t)$ in a simulation is given by

$$T(t) = \frac{\sum_{i=1}^{N} m_i v_i^2}{k_B N_f}, \tag{2.3}$$

where N_f is the number of degrees of freedom of the system.

2.1.7 Monte Carlo collision method

To obtain macroscopic transport rates such as diffusion coefficients, MD simulations must include enough particles to represent a macroscopic sample of plasma, i.e., a fluid element. For example, for a mixture of neutrals and ions, it requires having a macroscopic volume for even the most dilute species. For low ionization fractions, a pure MD simulation for both ions and neutrals becomes far too expensive computationally. For instance, a requirement of 5000 ions at 0.1% ionization fraction translates to a requirement of 5×10^6 neutrals. On the other hand, ion-neutral and neutral-neutral interactions are expected to be weakly coupled and well described by the traditional Boltzmann kinetic equation at atmospheric pressure as described in chapter I. This justifies a hybrid simulation approach where ion-ion interactions are computed using MD, and ion-neutral interactions using the Boltzmann kinetic theory.

In order to explore ionization fractions as small as 10^{-9} without increasing the computational cost, as shown in chapter V, neutral species were modeled as a background fluid at equilibrium, as in Donko *et al* [73]. Here, ion-neutral collisions were modeled using a Monte Carlo Collision (MCC) module that we implemented

in LAMMPS source code. The MCC algorithm, similar to that in Ref. [73], is described next. Ions and the background neutral gas interact via ion-neutral momentum transfer collisions. The probability of a collision to occur during a timestep Δt is

$$P_{\text{coll}} = 1 - \exp(-n_n Q_{in}^{(1)}(u)\ u\ \Delta t), \tag{2.4}$$

where n_n is the neutral gas density, $u = |\mathbf{v}_i - \mathbf{v}_n|$ is the relative velocity between an ion and a neutral atom and $Q_{in}^{(1)}(u)$ is the momentum transfer cross section for elastic ion-neutral collisions. The relative velocity between an ion and a neutral atom is calculated by randomly choosing a velocity $\mathbf{v}_n$ from a Maxwellian distribution for the background neutral gas at a temperature T. This probability is calculated for each ion at each timestep and is compared to a uniform random number R between 0 and 1. If $P_{\text{coll}} \leq R$ the collision occurs and the rotation of the relative velocity vector after scattering through angle β is calculated from

$$\Delta\mathbf{u} = u\big[\sin(\beta)\cos(\phi)\hat{x} + \sin(\beta)\sin(\phi)\hat{y} - 2\sin^2(\beta/2)\hat{u}\big] \tag{2.5}$$

where the angles β and ϕ are determined using $\cos(\beta) = 1-2R_1$ and $\phi = 2\pi R_2$, where R_1 and R_2 random numbers uniformly distributed over the interval $[0, 1]$. Thus, ion-neutral collisions are considered isotropic. The random number generator used was based on the Mersenne twister algorithm proposed by Matsumoto and Nishimura (1998) [76]. Conservation of momentum implies that $\Delta\mathbf{v}_i = (m_{in}/m_i)\Delta\mathbf{u}$, where $m_{in}/m_i = 1/2$ for same species collisions. Hence, the post collision ion velocity is given by $\mathbf{v}_i(t + \Delta t) = \mathbf{v}_i(t) + \Delta\mathbf{u}/2$.

2.1.8 Molecular dynamics simulations of atmospheric pressure plasmas

In this work, molecular dynamics simulations are used as a first principle method to study the strongly coupled ion dynamics in atmospheric pressure plasmas. Chapter

III shows the results obtained from MD simulations using the LAMMPS open source software. Both ion and neutral species are simulated as particles with the respective interaction potentials for partially ionized atmospheric pressure plasmas. Then, chapter V focuses on the calculation of the ion diffusion coefficient from MD simulations over a wide range of ionization fractions, treating ions as particles and neutrals as a background fluid. In these simulations, ion-neutrals collisions are incorporated using the MCC method described before.

2.2 Global model

The global model described in this section is used in chapter IV to study nanosecond pulsed discharges in atmospheric pressure plasmas. The main approximations consist of assuming electrons have a Maxwellian distribution at a temperature T_e, as well as ions at T_{ion} and the neutral gas at T_{gas}. While this is a good approximation for ions and neutral atoms/molecules, it can significantly differ from the physical EEDF at low ionization fractions. However, the goal of this work is to focus on the ionization dynamics and gas heating into regimes where large ionization fractions are achieved, in particular larger than 1%. In this regime, the EEDF is expected to be Maxwellian [6].

In a global model, each reaction can be expressed as

$$\sum_i \nu_i n_{\text{reac},i} \rightarrow \sum_i \nu_i^{'} n_{\text{prod},i} \tag{2.6}$$

where ν_i and $\nu_i^{'}$ are the stoichiometric coefficients and $n_{\text{reac},i}$ and $n_{\text{prod},i}$ are the number densities of reactants and products respectively. The rate of change of each species density is given by

$$\frac{dn_j}{dt} = \sum_{\text{r}} (\nu_{r,j}^{'} - \nu_{r,j}) k_r(T) \prod_i n_{reac,i}^{\nu_i} \tag{2.7}$$

where n_j is the density of species j and k_r(T) is the reaction rate coefficient of reaction r, which depends on the electron or gas temperature depending on the reaction. Here, the reaction rate of reaction r can be defined as $R_r = k_r(T) \prod_i n_{\text{reac},i}^{\nu_i}$.

The rate of change of the electron temperature is given by,

$$\begin{aligned}\frac{d}{dt}\left(\frac{3}{2}n_e k_B T_e\right) = \frac{n_e}{m_e}\frac{e^2E^2}{\nu_e^{\text{tot}}} - \sum_{\text{elastic}} R_i \left(\frac{2m_e}{M_i}\right)\frac{3}{2}k_B(T_e - T_{\text{gas}}) \\ - \sum_{\text{elastic}} R_i \left(\frac{2m_e}{M_i}\right)\frac{3}{2}k_B(T_e - T_{\text{ion}}) - \sum_{\text{inelastic}} R_i \Delta\epsilon_i\end{aligned} \tag{2.8}$$

where E is the electric field, k_B the Boltzmann constant, m_e the electron mass, n_e the electron density, M_i the mass of atom/ion i, molecule or ion in elastic collision j, R_i the rate of reaction of reaction i, $\Delta\epsilon_i$ the electron energy lost in reaction i and ν_e^{tot} is the total electron collision frequency with heavy species including ions and neutral particles $\nu_e^{tot} = \sum_{neutrals} k_{en}(T_e)n_n + \sum_{ions} k_{ei}(T_e)n_i$, where k_{ei} is simply the product of the electron-ion Coulomb collision frequency and ion density. While at low pressures or low ionization fractions only electron-neutral collisions are accounted for, here collisions with ions are included in order to not get unphysically large reduced electric fields at large ionization fractions where Coulomb collisions dominate [6].

The rate of change of neutral gas temperature can be calculated as

$$\begin{aligned}\frac{d}{dt}\left(\frac{3}{2}n_{\text{gas}} k_B T_{\text{gas}}\right) = &\sum_{\text{CE}_i}\frac{3}{2}R_i k_B(T_{\text{ion}} - T_{\text{gas}}) - \sum_i R_i \Delta H_i \\ &+ \sum_{\text{elastic}} R_i \left(\frac{2m_e}{M_i}\right)\frac{3}{2}k_B(T_e - T_{\text{gas}})\end{aligned} \tag{2.9}$$

where n_{gas} is the total number density of neutral atoms and molecules and ΔH_i is the change in enthalpy of the reaction i. The first term (CE_i) corresponds to heating due to charge exchange collisions. The term $-\sum_i R_i \Delta H_i$ includes gas heating due to quenching and dissociation. In addition to this equation, ion-neutral temperature relaxation is accounted for with a model described in chapter III.

Finally, the rate of change of the ion temperature is calculated as

$$\frac{d}{dt}\left(\frac{3}{2}n_i k_B T_{\text{ion}}\right) = -\sum_{\text{CE}_i}\frac{3}{2}R_i k_B(T_{\text{ion}} - T_{\text{gas}}) + \sum_{\text{elastic}} R_i\left(\frac{2m_e}{M_i}\right)\frac{3}{2}k_B(T_e - T_{\text{ion}}) \tag{2.10}$$

in addition to the DIH model and ion-neutral temperature relaxation described in chapter III.

Each rate coefficient is obtained from the integration of the corresponding cross section and a Maxwellian distribution at T_e or T_{gas} unless the rate coefficient was known [42]. The rate coefficient for electron collisions with heavy particles is calculated as

$$k(T_e) = \int_0^\infty F(\epsilon)\left(\frac{2\epsilon}{m_e}\right)^{1/2}\sigma(\epsilon)d\epsilon \tag{2.11}$$

where $F(\epsilon)$ is the real EEDF and σ the corresponding cross section. Note that $F(\epsilon) = f(\epsilon)\epsilon^{1/2}$ where $f(\epsilon)$ is the commonly used energy equivalent energy distribution function. In this work, $f(\epsilon)$ is assumed to be a Maxwellian. The rate coefficient for collisions between heavy particles is calculated as

$$k(T) = \left(\frac{1}{\pi m^*}\right)^{1/2}\left(\frac{2}{k_B T}\right)^{3/2}\int_0^\infty \sigma(\epsilon)\exp\left(\frac{-\epsilon}{k_B T}\right)\epsilon d\epsilon \tag{2.12}$$

where $m^* = m_1 m_2/(m_1 + m_2)$ is the reduced mass and m_1 and m_2 are the masses of the heavy species.

2.3 Particle in cell

To develop a better understanding of what the influence of strong coupling effects are in different simulation techniques, an in house developed electrostatic PIC code was developed. This code was used to study under what conditions disorder induced

heating can be correctly obtained from PIC simulations and how these constraints compare with traditional PIC simulations of weakly coupled plasmas. These PIC simulations were bench-marked against molecular dynamics. This section describes the basics of PIC simulations and the code developed that is used to obtain the results shown in chapters VI and VII.

In the PIC method, numerical macroparticles represent aggregates of w individual physical particles in the system, where w is the weight of each macroparticle. The equations of motion of macroparticles are solved to update positions and velocities on each timestep, self consistently with the charge density in the domain. To achieve this, charges are interpolated from macroparticles to a grid, where the Poisson equation is solved. Then the electric field is calculated on the grid and interpolated back to the position of each macroparticle. The electric field on each macroparticle is then used to calculate the force acting on each macroparticle [44]. The combined use of macroparticles with large weights and calculating forces on particles by interpolating from the electric field on a grid, helps to significantly reduce the computational cost when compared to MD simulations, which helps extend traditional PIC simulations to device scale modeling. The PIC method is illustrated in figure 2.1.

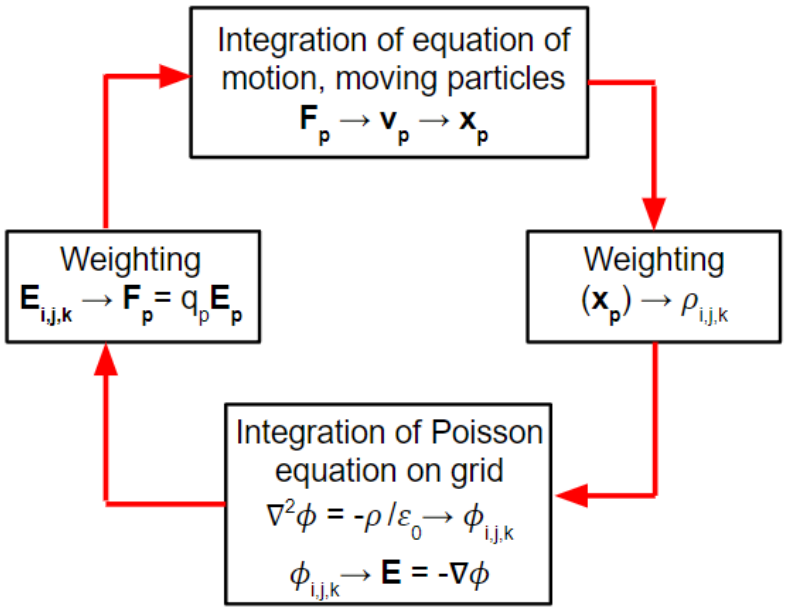

Figure 2.1: Illustration of the PIC method. Fields are solved in a grid and then interpolated to the positions of macroparticles. Then the equations of motions are solved and the charges are interpolated back to the grid.

The code developed in this work adheres to the conventional method of interpolating particle charges onto a structured uniform grid using shape functions. Subsequently, field equations are solved, and the resulting fields are interpolated back to the particle positions to integrate the equations of motion. This process is repeated throughout each iteration of the PIC simulation [44].

For the Poisson equation solver, the charge density was computed using the ion density and a uniform background neutralizing electron density to ensure stability

$$\rho(\mathbf{r}) = e\left(Zn_i(\mathbf{r}) - n_e\right), \tag{2.13}$$

where ρ is the charge density, Z is the ion charge state, n_i is the ion density and n_e is the background electron density assumed to be constant and equal to $\int_V n_i(\mathbf{r})d^3r/V$ where V is the volume of the simulation domain. The Poisson equation for the electrostatic potential was then solved using the spectral method. That is, by applying

the Fourier transform and solving the consequent algebraic equation for the electric potential in the k-space,

$$\nabla^2\phi(\mathbf{r}) = \frac{-\rho(\mathbf{r})}{\epsilon_0} \tag{2.14a}$$

$$\phi_{\mathbf{k}} = \frac{\rho_{\mathbf{k}}}{\epsilon_0 k^2} \tag{2.14b}$$

$$F^{-1}\left(\phi_{\mathbf{k}}\right) = \phi(\mathbf{r}) \tag{2.14c}$$

where ϕ is the electrostatic potential, ϵ_0 is the vacuum permittivity and F^{-1} is the inverse Fourier transform. The electric field components were obtained by numerically differentiating the electric potential among each direction using finite central differences of order $O(2)$ and periodic boundary conditions. No external electric fields were included.

Interpolation of the particle charges to the grid and the electric field from the grid to the particle positions was performed using the "scatter" and "gather" operations

$$\rho_{i,j,k} = \sum_{p=1}^{N_i} \frac{Ze}{\Delta V_{i,j,k}} \prod_{d=1}^{3} W^{(n)}\left(\frac{(\mathbf{r}_{i,j,k} - \mathbf{r}_p)\cdot\hat{\mathbf{e}}_d}{\Delta x_d}\right) \tag{2.15}$$

and

$$\mathbf{E}(\mathbf{r}_p) = \sum_{i,j,k} \mathbf{E}_{i,j,k} \prod_{d=1}^{3} W^{(n)}\left(\frac{(\mathbf{r}_{i,j,k} - \mathbf{r}_p)\cdot\hat{\mathbf{e}}_d}{\Delta x_d}\right) \tag{2.16}$$

where (i,j,k) are the indices of an arbitrary node in the domain, $\Delta V_{i,j,k} = \prod_{d=1}^{3} \Delta x_d$ is the volume of the cell within the nodes (i,j,k) and $(i+1, j+1, k+1)$, $W^{(n)}$ is the shape function of order n, $\mathbf{r}_{i,j,k}$ is the position of the node (i,j,k), $\mathbf{r}_p$ is the position of the ion p and $\mathbf{E}_{i,j,k}$ is the electric field at the node (i,j,k). The implemented shape functions ranged from order 2 to order 6. For instance, the shape function of order 2

is given as follows:

$$W^{(2)}(x) = \begin{cases} 1 - |x| & \text{for } 0 \leq x \leq 1, \\ 0 & \text{otherwise.} \end{cases} \tag{2.17}$$

A shape function of order 2 is utilized unless otherwise indicated.

The shape functions of order 4 and 6, used for the analysis on grid heating detailed in chapter VI are provided below [77]. The order-4 shape function is

$$W^{(4)}(x) = \begin{cases} \frac{2}{3} - |x|^2 + \frac{|x|^3}{2} & \text{for } 0 \leq |x| \leq 1, \\ \frac{1}{6}(2 - |x|)^3 & \text{for } 1 \leq |x| \leq 2, \\ 0 & \text{otherwise ,} \end{cases} \tag{2.18}$$

and the order-6 shape function is

$$W^{(6)}(x) = \begin{cases} \frac{1}{60}(33 - 30|x|^2 + 15|x|^4 - 5|x|^5) & \text{for } 0 \leq x \leq 1, \\ \frac{1}{120}(51 + 75|x| - 210|x|^2 + 150|x|^3 - 45|x|^4 + 5|x|^5) & \text{for } 1 \leq x \leq 2, \\ \frac{1}{120}(3 - |x|)^5 & \text{for } 2 \leq |x| \leq 3, \\ 0 & \text{otherwise.} \end{cases} \tag{2.19}$$

Integration of the equations of motion was conducted using the Verlet algorithm. The Poisson equation solver through a 3D−FFT, interpolation operations, and integration of equation of motion were implemented in CUDA−C kernels through the open source library Cupy and called from python.

In chapter VII, the present PIC code is modified to study artificial correlation heating of electrons. For these simulations, ions are considered a background non interacting species and electrons are modeled as particles.

2.3.1 Monte Carlo collision method

In chapter VII an ionization module is included to study the possibility of a positive feedback loop between artificial correlation heating and electron-impact ionization. This is done by including a Monte Carlo collision routine [44]. In this part of the work, a background neutral uniform Xe gas is included at an initial density given by $n_n = n_g - n_e$, where n_g corresponds to the ideal gas density at atmospheric pressure and room temperature. Then, in each iteration and for each electron in the simulation, the probability of ionization is computed as $P = 1 - \exp\left(-n_n \sigma_{\mathrm{Xe}} v_e \Delta t\right)$, where σ_{Xe} is the corresponding electron impact ionization cross section for Xe [78] and v_e is the electron speed. Then, this probability is compared to a random number R from a uniform distribution between 0 and 1. If $R < P$, then the ionization occurs and a new electron is added at a random position in the simulation domain with a velocity sampled from a Maxwellian distribution at the initial electron temperature. After repeating this process for each electron, the background gas density is updated, subtracting from n_n the increase produced in n_e, following the balance $n_n = n_g - n_e$.

CHAPTER III

Coulomb coupling influences ion and neutral temperatures in atmospheric pressure plasmas

3.1 MD simulations setup

Molecular dynamics simulations were carried out using the open-source software LAMMPS [75] as described in section 2.1. Since electrons are much hotter than ions and are weakly coupled, they are treated as a background non-interacting species when modeling ion and neutral dynamics. Thus, they were not included in the simulation. This is similar to the one-component plasma model [79], which is known to provide an accurate description of ions in the presence of weakly coupled (comparatively hot) electrons, such as in ultracold neutral plasmas [80]. Short (neutral-neutral), medium (ion-neutral) and long (ion-ion) range interactions were modeled using the potentials defined in equations (1.8)–(1.10).

Since the charge induced dipole potential is attractive, particles can interact at arbitrarily short spatial scales. In order to avoid the rare occurrence of close interactions that require a very short timestep to resolve, a repulsive core term was added to the charge-induced dipole potential from expression (1.9)

$$\phi_{\text{ind}}(r) = \frac{q^2}{8\pi\epsilon_0}\frac{\alpha_R a_0^3}{r^4}\left(\frac{r_\phi^8}{3r^8} - 1\right), \tag{3.1}$$

where r_ϕ is the radius at which the repulsive core acts. It was desired to choose r_ϕ to be small enough to minimize the occurrence of non-physical force values, but large enough to decrease the computational cost due to the smaller timestep requirement. This is similar to what has been done in MD simulations of ultracold neutral plasmas [81, 82]. The effect of the repulsive core also depends on the simulation setup. For simulations conducted at thermodynamic equilibrium, we found that the value of r_ϕ sets the number of ions that attach to neutrals; as shown in the Appendix A. However, this work concentrates on non-equilibrium simulations where r_ϕ is only a numerical convergence parameter needed to avoid closely orbiting particles. The reason why r_ϕ is not important in the non-equilibrium simulations is that ion-neutral three-body recombination is slow compared to the DIH and ion-neutral relaxation timescales that we focus on. For the non-equilibrium simulations we chose $r_\phi = 0.133a_{\text{in}}$ (here a_{in} was estimated as $\approx a_{\text{nn}}$ for $x_i < 0.5$ and $\approx a_{\text{ii}}$ for $x_i > 0.5$). This is the smallest value at which we can avoid closely orbiting particles and non-physical force values; see Appendix A and figure 3.1. A convergence test was conducted varying r_ϕ from $0.133a_{\text{in}}$ to $0.5a_{\text{in}}$ at an ionization fraction of $x_i = 0.5$ (figure 3.1) showing that the ion and neutral temperature at the end of the simulation (after ion-neutral relaxation) is independent of r_ϕ when $r_\phi < 0.25a_{\text{in}}$.

In order to study the evolution of a non-equilibrium discharge, a neutral Ar gas at room temperature and atmospheric pressure was simulated until equilibrium was reached. This stage of the simulation was run with a Nosé-Hoover thermostat (NVT ensemble) applied [74]. Then, a fraction of the particles were instantly ionized and a NVE (microcanonical) simulation was run including the ion-neutral, neutral-neutral and ion-ion interactions. This simulation setup was repeated for different ionization fractions. The timestep used was $5\times10^{-4}\omega_{pi}$ and the NVE simulation was run until the equilibrium was reached. The number of particles was varied such that the minimum number of ions in the system was 2500 and the number of neutral atoms was scaled

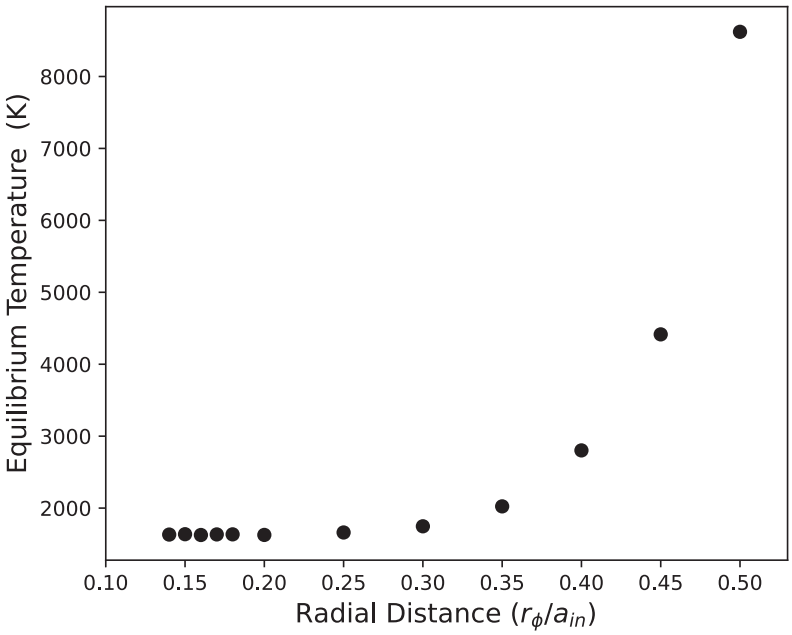

Figure 3.1: Ion and neutral final temperatures for different r_ϕ values.

in order to achieve the desired ionization fraction in each simulation. The simulation domain size was scaled with the total number of particles in order to maintain the desired gas density. The simulation domain was a three-dimensional box with periodic boundary conditions. The ionization fraction, total number of particles, time step and length of simulation used for each simulation are specified in table 3.1.

Table 3.1: Parameters used for the molecular dynamics simulations. The time step value was $\Delta t \times \omega_{pi} = 5 \times 10^{-4}$ in all cases.

Ionization Fraction (x_i)	Number of Particles	Plasma Frequency (ω_{pi}) $\times 10^{12}$ (rad/s)	Length of Simulation ($t_f \times \omega_{pi}$)
0.01	250000	0.1046	150
0.1	25000	0.3308	500
0.3	10000	0.5731	650
0.5	10000	0.7398	800
0.7	10000	0.8754	1000

3.2 Molecular dynamics results

As shown in figure 3.2, the evolution of the ion temperature can be divided into three stages. First, a rapid increase in the ion temperature was observed over the first ion plasma period of the simulation. This is thought to be due to disorder induced heating. This stage generates fluctuations in the ion temperature that persist for several plasma periods; as shown in figures 3.2 and 3.3. Secondly, ion-neutral temperature relaxation was observed with a timescale characterized by the ion-neutral collision frequency. Finally, a gradual heating of both ions and neutrals is observed over a much longer timescale due to three-body recombination of ions and neutrals (this is difficult to view in figure 3.2, but is demonstrated more clearly below).

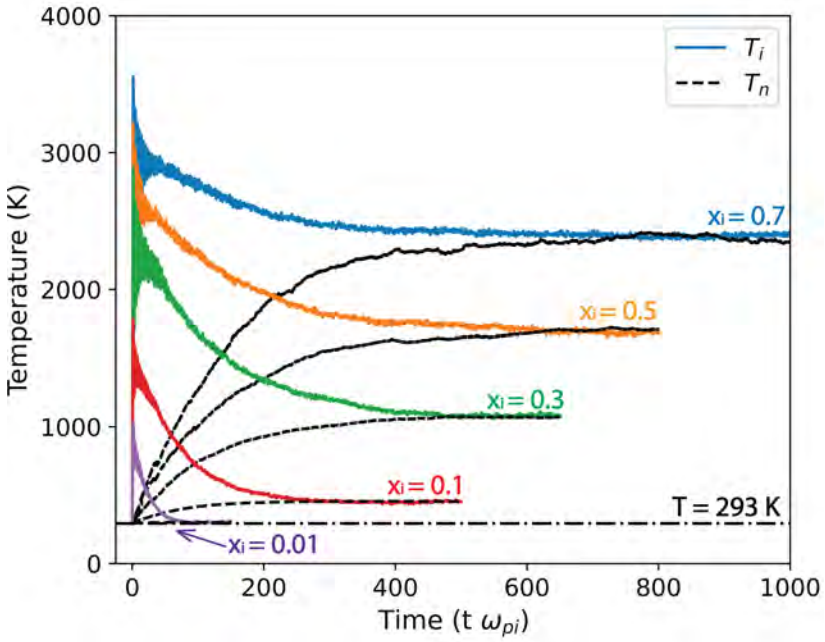

Figure 3.2: Evolution of the ion and neutral temperatures during the discharge at atmospheric pressure for different ionization fractions.

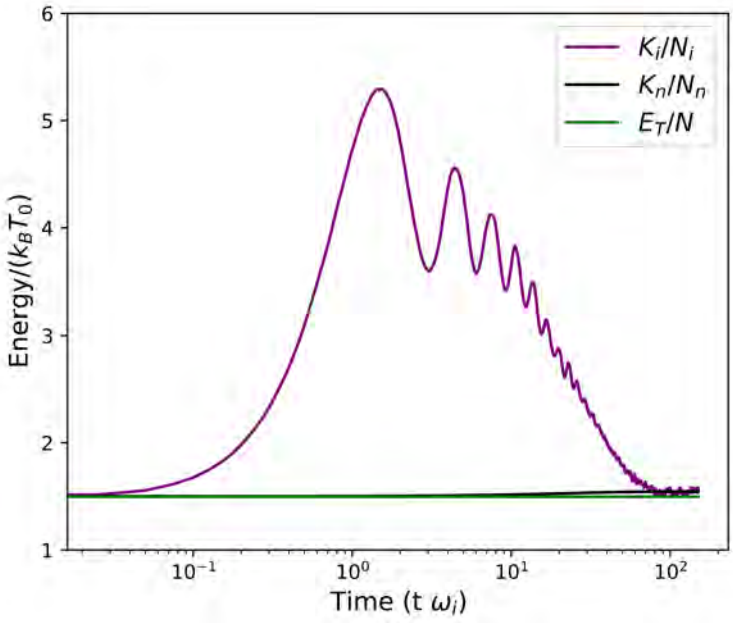

Figure 3.3: Ion kinetic energy (K_i), neutral kinetic energy (K_n) and total energy E_T for a discharge at atmospheric pressure and an ionization fraction of $x_i = 0.01$. Each energy is normalized by the number of ions (N_i), neutral atoms (N_n) and total number of particles N respectively and the kinetic energy at room temperature $T_0 = 300\ K$. Large fluctuations were observed in the ion kinetic energy due to the oscillations in the Coulomb potential energy after the DIH.

3.3 Disorder induced heating

Before the ionization pulse is applied, the initial distribution of positions of neutral atoms corresponds to the equilibrium state of a gas interacting via the short-range Lennard-Jones potential. Therefore, ionization creates many ions separated by distances that are much smaller than the average distance between ions $a_{ii} = (3/4\pi n_i)^{1/3}$ where n_i is the ion density. Since the interaction between ions is governed by the Coulomb potential, which is a long range potential, this leads to a large repulsive force between ion pairs that brings ions apart, as illustrated in figure 3.4.

The separation of ions corresponds to the formation of a correlated state. This can be quantified by the radial distribution function $[g(r)]$, which is defined by setting $n_o g(r) 4\pi r^2 dr = N(r)$, where $N(r)$ is the total number of particles in a spherical shell of radius r and thickness dr centered on a chosen particle. Here, $n_o = N/V$ is the average number of particles (N) in a volume (V); i.e., it is the uniform background number density. When $g(r) = 1$ for all distances r, the system is in an uncorrelated state. Figure 3.5 shows that just after ionization the ion positions correspond to the weakly correlated state of the neutral gas they were formed from. Correlations quickly develop as ions spread apart over the timescale of an ion plasma period. This is indicated by the void of particles that forms from distances $r = 0$ to approximately $r = a_{ii}$. Such a void, which is sometimes referred to a Coulomb hole in plasmas, is a characteristic property of a strongly coupled system. Another characteristic is a peak near the average nearest neighbor distance (a_{ii}), which is also observed at times later than one ion plasma period.

A simple estimate for the magnitude and timescale of DIH can be obtained by considering the motion of a typical ion. In the limit that the initial configuration is random in space, and the final distribution is perfectly ordered (a lattice), ions will move an average distance of approximately $a_{ii}/2$. The electrostatic potential change in moving from a position $r_1 = a_{ii}/2$ to $r_2 = a_{ii}$ is $\Delta\phi = \phi_2 - \phi_1 = -eZ/(4\pi\epsilon_0 a_{ii})$. This will

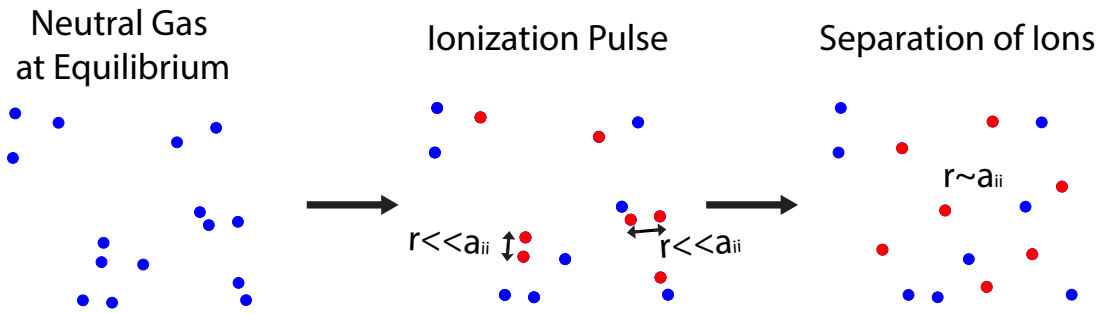

Figure 3.4: After an instant ionization pulse, ions can be at distances much smaller compared to a_{ii} leading to large repulsion forces.

decrease the total potential energy of the ions by a factor of $\Delta \mathrm{U} \approx -Z^2e^2/(4\pi\epsilon_0 a_{ii})$. Since energy is conserved during the NVE simulation, this leads to a corresponding increase in the ion kinetic energy $\Delta \mathrm{K} = -\Delta \mathrm{U} \approx Z^2e^2/(4\pi\epsilon_0 a_{ii})$. For ionization fractions above approximately 10^{-4}, the initial value of Γ_{ii} based on room temperature (when the ionization pulse is applied) is considerably larger than 1, so the change in the ion kinetic energy due to DIH is much greater than the kinetic energy before the pulse. Estimating the temperature after DIH as $\frac{3}{2}k_BT \approx \Delta \mathrm{K}$, the Coulomb coupling parameter from equation (1.7) is $\Gamma_{ii} \approx 1.5$. In all cases simulated, DIH is observed to increase the ion temperature until a critical value of approximately $\Gamma_{ii} = 1.9$ is reached; see figure 3.6. This is quite close to the estimate of 1.5. The value of the temperature directly after DIH is the maximum value observed, $T_i^{\max}$, as ions subsequently cool due to collisional relaxation with neutrals.

The timescale for DIH can be estimated from the time it takes an ion to move from a position $r_1 = a_{ii}/2$ to $r_2 = a_{ii}$ due to the Coulomb repulsion of a nearby ion. Considering Newton's equation of motion, $md^2x/dt^2 = eE$ and approximating $d^2x/dt^2 \sim \Delta x/\Delta t^2 \sim (a_{ii}/2)/\Delta t^2$, and $eE \sim e^2/(4\pi\epsilon_o a_{ii}^2)$, the characteristic timescale for this process is the ion plasma period $\Delta t \approx \omega_{pi}^{-1}$. This also agrees well with the simulations, where the maximum ion temperature is reached approximately $1.5\omega_{pi}^{-1}$ after the ionization pulse; see figure 3.6.

Disorder induced heating has been previously observed in ultracold neutral plas-

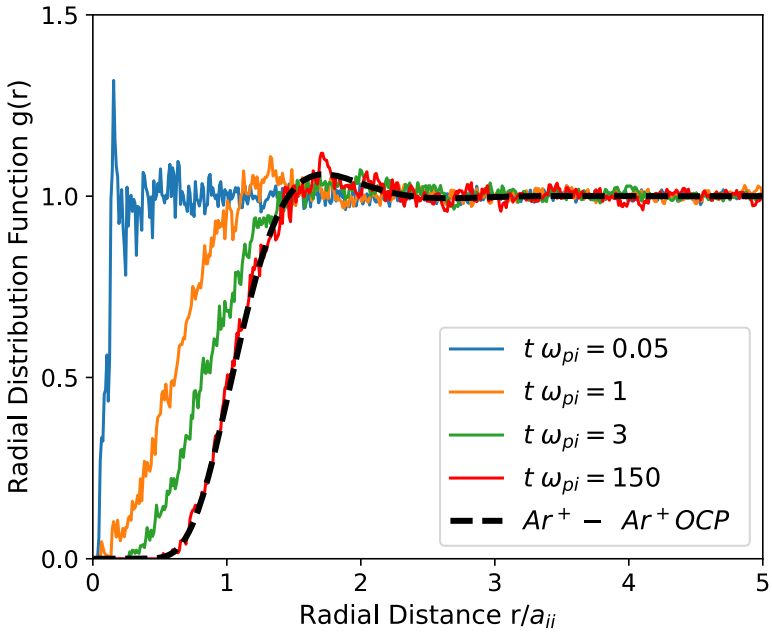

Figure 3.5: Ion-ion radial distribution function $g(r)$ at different timesteps during the simulation of a partially ionized Ar plasma with an ionization fraction of $x_i = 0.01$. The ion-ion radial distribution function corresponds to an OCP at the same equilibrium Γ_{ii} showing that the ions are strongly coupled and the ion-ion interactions are not screened by the presence of neutral atoms. In each simulation, the $g(r)$ was obtained after computing an average over all the ions in the simulation and 100 consecutive time steps that corresponded to a time window of $t \times \omega_{pi} = 0.05$. An ensemble average was also computed using data from 20 different simulations.

mas formed by photoionizing laser-cooled atoms [60]. Immediately after ionization ions have a very small kinetic energy since the neutral gas they are formed from was at millikelvin temperature. However, they have significant excess potential energy since the ionization has changed the potential energy landscape to that associated with long-range interactions. As the excess potential energy is converted into kinetic energy the ions heat to a state where $\Gamma_{ii} \approx 1$ over a timescale of $1\omega_{pi}^{-1}$, just as described above. The process observed here is essentially the same. One important difference is that the ionization pulse in an atmospheric pressure plasma typically only partially ionizes the gas, whereas near total ionization is common in an ultracold neutral plasma.

An implication is that DIH is only expected to be important if the ionization fraction is high enough. Heating occurs only when the initial ion state (just after ionization) satisfies $\Gamma_{ii} > 1$. Otherwise, the kinetic energy gained by DIH is small compared to the initial kinetic energy. Furthermore, the basic mechanism isn't expected to apply since the ions remain in a weakly coupled disordered state even after ionization. Assuming ions are born from neutral gas at room temperature, $\Gamma_{ii} > 1$ requires that $x_i \gtrsim 10^{-4}$. Thus, at room temperature atmospheric pressure gas conditions, DIH is expected to occur only if the ionization fraction is larger than one part in ten thousand $x_i \gtrsim 10^{-4}$.

After DIH, ions overshoot their equilibrium positions leading to oscillations of the Coulomb potential energy near the ion plasma frequency. Since the total energy is conserved during the NVE simulation and the ions are strongly coupled after the DIH, those oscillations translate to observable kinetic energy fluctuations. This is shown in figure 3.3 from the simulation with an ionization fraction of 0.01. Such fluctuations are only noticeable in the strongly coupled regime, where the ion kinetic energy is comparable to the Coulomb potential energy ($\Gamma \approx 1$). These fluctuations were observed to damp over a period of time between $2\omega_p^{-1}$ and $50\omega_p^{-1}$ depending

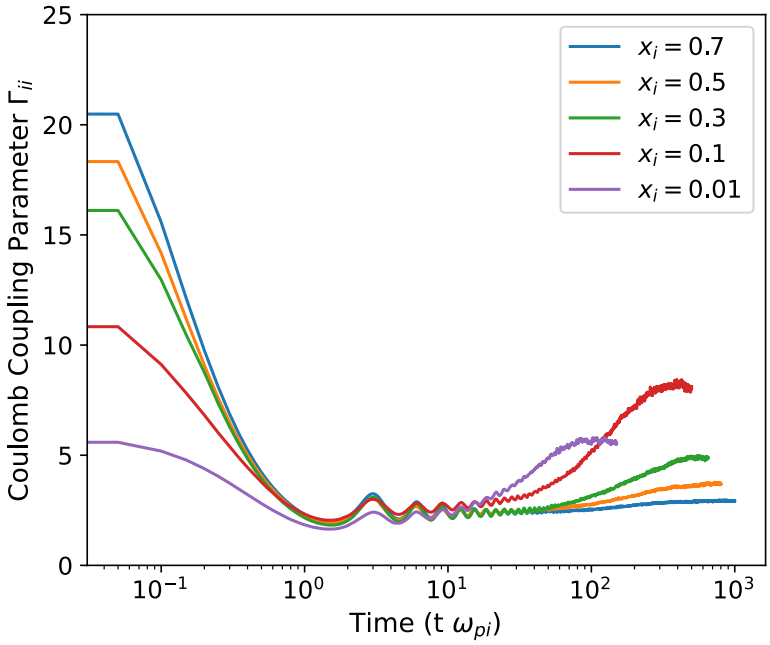

Figure 3.6: Evolution of the Coulomb coupling parameter Γ_{ii} during the discharge at different ionization fractions.

on the ionization fraction; see figure 3.2. The presence of large fluctuations in the ion temperature after DIH has also been observed in ultracold neutral plasmas experiments [60] and MD simulations [81]. While this section described DIH in the context of an instant ionization pulse, section 3.8 extends the analysis to an arbitrary ionization dynamics.

3.4 Ion-neutral temperature relaxation

After disorder-induced heating, ion and neutral temperatures equilibrate due to ion-neutral collisions. This causes the ions to cool and the neutrals to heat by an amount and at a rate that depends on the ionization fraction. Ion cooling increases the ion-ion coupling strength, as shown in figure 3.6. This leads to an ion-ion coupling strength that is larger than one, $\Gamma_{ii} > 1$, after the ion and neutral temperatures relax for all ionization fractions simulated. It is also noteworthy that fast neutral heating can be significant, especially when the ionization fraction is high. Neutral heating is

a common observation in atmospheric pressure plasma experiments [19, 21, 22, 23].

Ion-neutral temperature relaxation was modeled using standard methods based on the Boltzmann equation [83]. The cross section for ion-neutral interactions was computed based on two-body collisions interacting through the charge-induced dipole potential from equation (3.1). The Boltzmann-based approach is expected to be valid since the ion-neutral interaction is in a weakly coupled regime; see figure 1.3. The resulting temperature relaxation rate is described by

$$\frac{dT_i}{dt} = -\frac{3}{2}\nu_{in}(T_i - T_n), \tag{3.2}$$

$$\frac{dT_n}{dt} = \frac{3}{2}\nu_{ni}(T_i - T_n), \tag{3.3}$$

and

$$\nu_{ss'} = \frac{4n_{s'}\bar{v}_{ss'}}{3}\int_0^\infty dg \;\; Q^{(1)}_{ss'}(g)g^5e^{-g^2}. \tag{3.4}$$

Here, T_i and T_n are ion and neutral temperatures respectively, $\nu_{ss'}$ is the energy transfer collision frequency between the species s and s', $g = u/\bar{v}_{ss'}$ where u is the relative velocity and $\bar{v}^2_{ss'} = 2k_BT_s/m_s + 2k_BT_{s'}/m_{s'}$, where m_s and $m_{s'}$ are both the Ar mass, and $Q^{(1)}_{ss'}$ is the momentum transfer cross section

$$Q^{(1)}_{ss'} = 2\pi\int_0^\infty [1 - \cos(\chi)]bdb, \tag{3.5}$$

where

$$\chi = \pi - 2b\int_{r_0}^\infty \frac{dr/r^2}{\sqrt{1 - \frac{b^2}{r^2} - \frac{2\phi_{in}(r)}{m_{ss'}u^2}}} \tag{3.6}$$

is the scattering angle. Here, b is the impact parameter, r_0 is the distance of closest approach obtained from the largest root of the denominator in equation (3.6), r is the radial distance, $m_{ss'}$ is the reduced mass, u is the relative velocity and ϕ_{in} is the charge induced dipole potential from equation (3.1) with $r_\phi = 0.133a_{in}$ computed

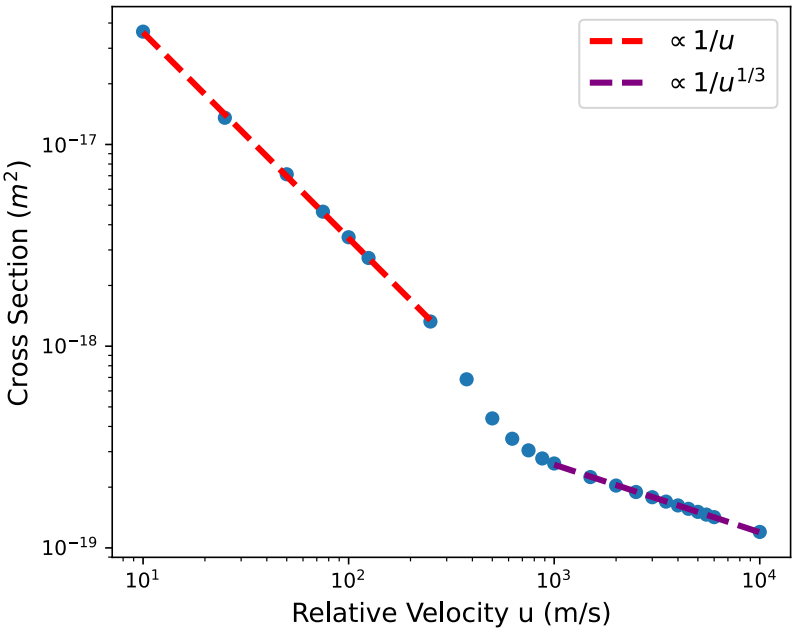

Figure 3.7: Ion-neutral momentum transfer cross section at different relative velocities, obtained for the charge induced dipole potential used in the simulations.

from equation (3.5). The ion-neutral momentum transfer cross section obtained is shown in figure 3.7.

The evolution of the ion temperature obtained using equations (3.2)–(3.4) is shown in figure 3.8 for the discharge at an ionization fraction of 0.01. Here, the initial temperature used in the model was taken from the value of the MD simulations after DIH. The predictions show good agreement with the MD simulations in both the equilibrium temperature as well as the relaxation time. At other ionization fractions, the equilibrium temperature increases with ionization fraction due to smaller neutral atom densities and due to the larger ion temperature achieved due to the DIH. The equilibrium temperature was higher than room temperature and the corresponding coupling parameter was smaller compared to the the initial value of Γ_{ii} with the exception of the smallest ionization fraction of 0.01, where the large neutral density led to an equilibrium temperature similar to room temperature; see figure 3.2.

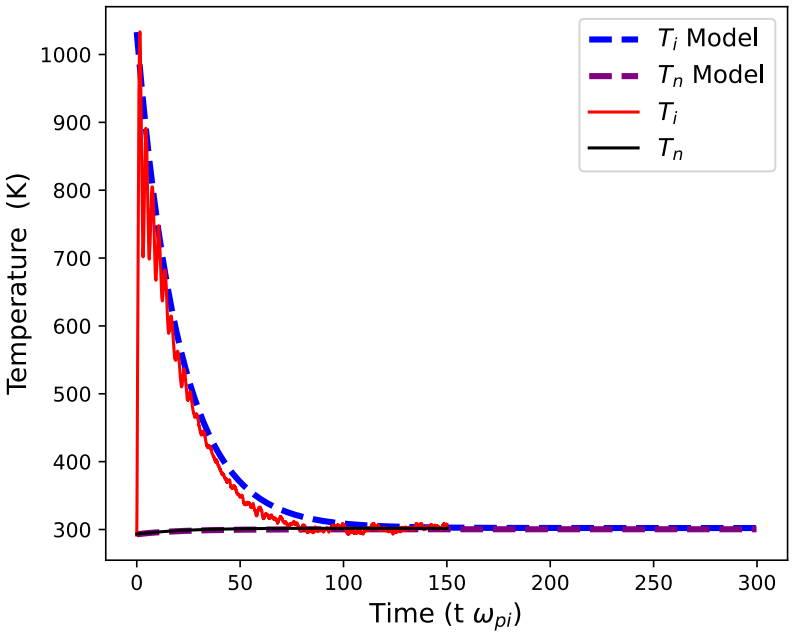

Figure 3.8: Evolution of the ion temperature for a discharge with $x_i = 0.01$ along with the model described in equations (3.2)–(3.4).

3.5 Three-body recombination

As described in section 3.1, r_ϕ was used as a numerical convergence parameter in the non-equilibrium simulations and the temperature evolution over the timescale of DIH and ion-neutral equilibration was independent of r_ϕ. However, as shown in Appendix A, for $r_\phi/a_{in} < 0.133$ neutral particles start to orbit ions, which forms bound states that can cause heating over a much longer timescale than the DIH or ion-neutral relaxation. In order to compare these time scales, we repeated the non-equilibrium simulation on a longer time scale with different values of r_ϕ/a_{in}. Simulations at an ionization fraction of $x_i = 0.01$ and r_ϕ/a_{in} values of 0.100 and 0.090 were carried out with a total simulation time of $t \times \omega_{pi} = 4000$ and compared with a simulation at the same ionization fraction but using $r_\phi/a_{in} = 0.133$. As shown in figure 3.9, the simulations show a similar ion temperature evolution immediately after the ionization pulse, including DIH followed by ion-neutral temperature relaxation through collisions. However, at $t \times \omega_{pi} \approx 50$, bound states start to form when $r_\phi/a_{in} < 0.133$,

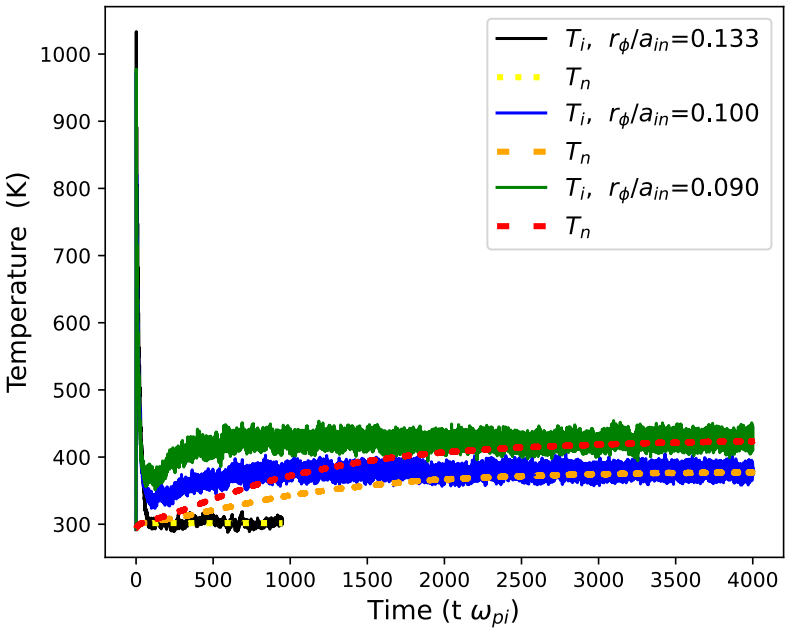

Figure 3.9: Evolution of the temperature for a discharge with a ionization fraction $x_i = 0.01$ for different r_ϕ values.

which increases the ion temperature when compared to the same simulation with $r_\phi/a_{in} = 0.133$. This is due to particles becoming trapped in the potential well of the charge-induced dipole potential, which exchanges a reduction in the potential energy with an increase in the kinetic energy. The increase of the fraction of ion-neutral bound states over time is shown in figure 3.10 for both r_ϕ/a_{in} values. The recombination fraction was determined from a histogram of nearest neighbor positions, as described in appendix A. The additional heating due to the ion-neutral three-body recombination causes the temperature to increase by approximately 75 K and 125 K, reaching a value near 375 K and 425 K at $t \times \omega_{pi} = 4000$ for r_ϕ/a_{in} values of 0.100 and 0.090 respectively. This corresponds to a time at which 97% of ions have at least one neutral atom orbiting them. It was observed that the timescale of the ion-neutral three-body recombination is much longer than ion-neutral temperature relaxation; $\sim 1000\omega_{pi}^{-1}$ corresponds to $\sim$ 100s ns.

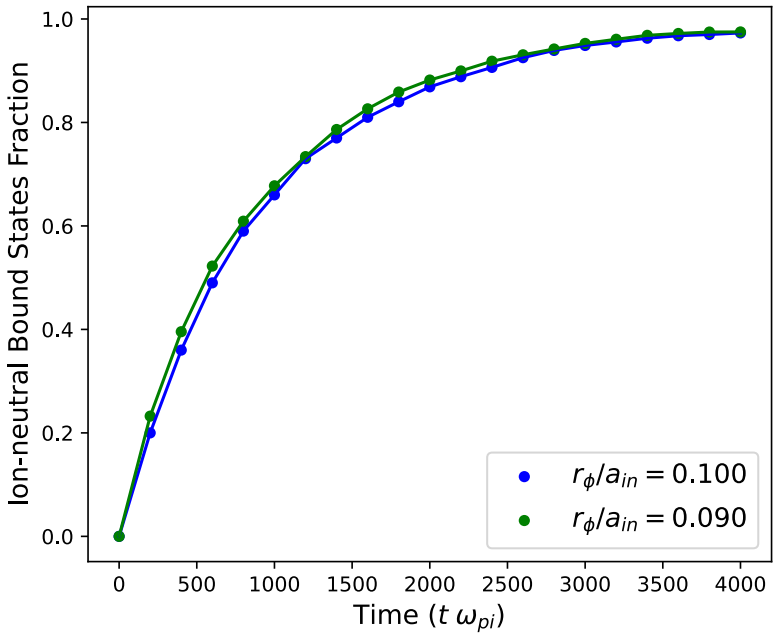

Figure 3.10: Ion-neutral three-body recombination rate for a discharge with a ionization fraction $x_i = 0.01$ for different r_ϕ values. For the case $r_\phi = 0.133$ the bound states fraction is approximately zero.

3.6 Model for maximum and equilibrium ion temperature.

The maximum and equilibrium ion temperatures can be estimated using simple energy conservation arguments. Since the increase in the ion temperature is due to DIH, where the ions travel a distance $\approx\ a_{ii}$ over a plasma period ω_p^{-1}, the maximum ion temperature corresponds to that which makes the ion-ion coupling parameter approximately unity. Utilizing the simulation result that $\Gamma_{ii} \approx 1.91$ at the peak temperature and equation (1.7), the maximum ion temperature is estimated to be

$$T_i^{\max} = \frac{1}{1.91}\frac{Z^2e^2}{4\pi\epsilon_0 k_B}\frac{1}{a_{ii}} \tag{3.7}$$

where $a_{ii} = (3/4\pi x_i n)^{1/3}$ is the average interparticle spacing between ions. The maximum ion temperature estimated with the equation (3.7) shows good agreement with the results obtained from the MD simulations, as shown in figure 3.11.

If we assume that the total kinetic energy is conserved after DIH until thermo-

dynamic equilibrium is reached, it is possible to write a simple energy equation to obtain the equilibrium temperature $T_{\rm eq}$, i.e., the temperature after ion-neutral thermal equilibration,

$$T_{\rm eq} = x_i \, T_i^{\rm max} + (1 - x_i) \, T_n(t = 0) \tag{3.8}$$

where T_n is the neutral atom temperature at the beginning of the simulation, x_i is the ionization fraction and $T_i^{\rm max}$ is the maximum ion temperature obtained with equation (3.7). As shown in figure 3.11, the values of $T_{\rm eq}$ and $T_i^{\rm max}$ obtained using the model show good agreement with MD simulations over a broad range of ionization fractions. Furthermore, the expected coupling parameter with and without accounting for the DIH can be calculated by using the correct equilibrium temperature and the room temperature respectively, as shown in figure 3.12. The values predicted for $\Gamma_{ii}^{\rm eq}$ show good agreement with the results from the MD simulations. It is noticeable how the coupling parameter at equilibrium is smaller than what would be predicted using room temperature, since the DIH increases the equilibrium temperature of the system at large ionization fractions. However, at small ionization fractions the values for $\Gamma_{ii}(T_0, x_i)$ and $\Gamma_{ii}^{\rm eq}(T_{\rm eq}, x_i)$ match due to the large neutral density compared to the ion density.

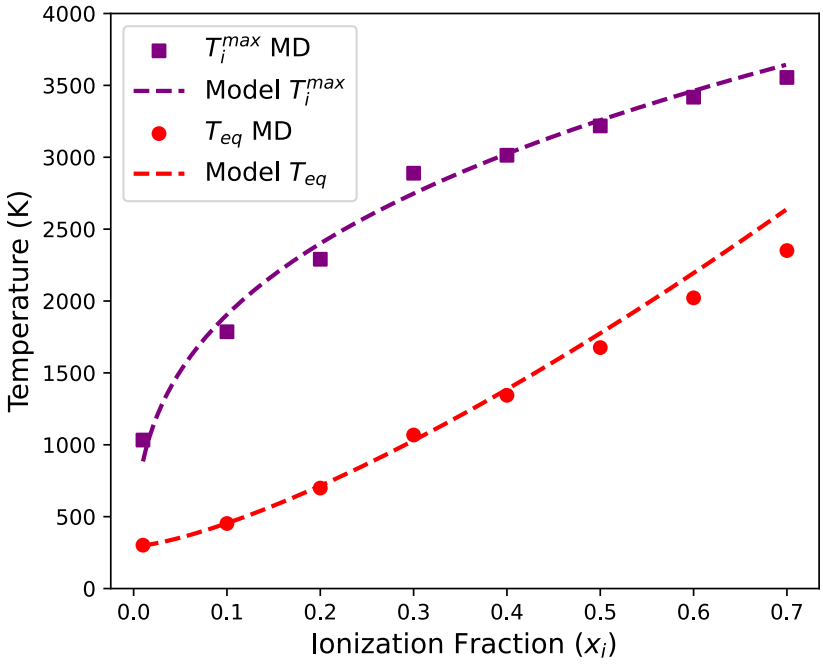

Figure 3.11: Variation of the maximum ion temperature and equilibrium temperature with the ionization fraction from the MD simulations and the model.

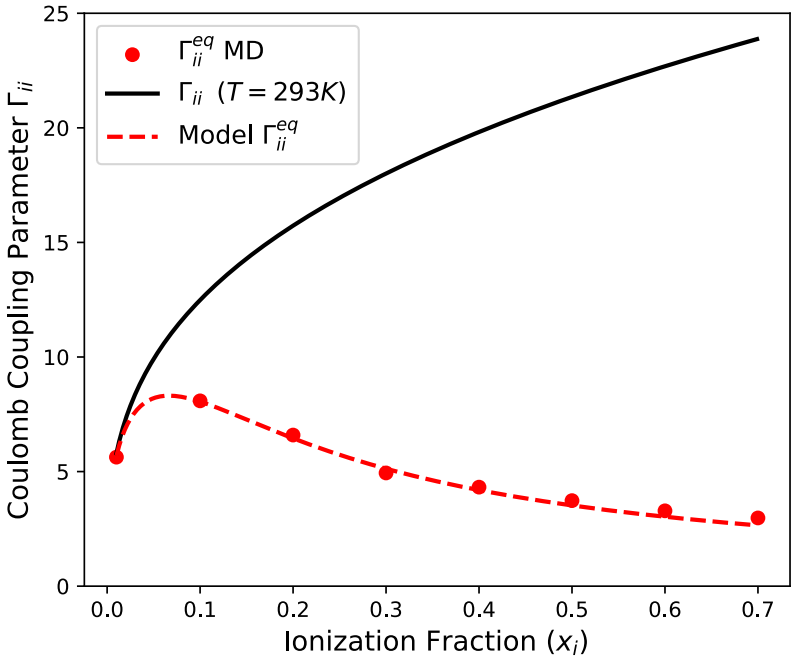

Figure 3.12: The Coulomb coupling parameter at equilibrium is smaller than the coupling parameter at room temperature without accounting for DIH. At small ionization fractions $\Gamma_{ii}^{\mathrm{eq}}(T^{\mathrm{eq}}, x_i)$ converges to $\Gamma_{ii}(T_0, x_i)$ where T_0 is the room temperature.

3.7 Comparison with experiments

Previous measurements have observed considerable neutral gas heating in ns pulsed spark discharges at atmospheric pressure. For example van der Horst *et al* measured a neutral gas temperature of 750 K at at time 1 μs after ignition in a N_2/H_2O mixture [32]. They also showed that the pressure due to the discharge increased to 3 bar and the corresponding ionization fraction was $x_i = 0.16$. Using the model for the equilibrium temperature from equation (3.8) and the pressure and ionization fraction measured in [32], we calculate an expected ion-neutral equilibrium temperature of 765 K with a relaxation time of 2.6 ns. This temperature agrees quite closely with the experimental measurement. The original reference suggested that the gas heating may be due to elastic collisions between electrons and N_2. For the conditions of this experiment, the energy transfer time due to elastic collisions is approximately 0.5 μs, which is near the time at which the temperature was measured. Measurements at a shorter timescale might reveal the degree to which DIH may contribute to the observed heating.

DIH is predicted to occur over the first 13 ps after ignition for the pressure and ionization fraction measured in [32]. The subsequent ion-neutral temperature relaxation occurs over 2.6 ns after the ignition. The noticeable separation of timescales shows that a better time resolution for experiments could help to identify the responsible heating mechanisms.

A Lo et al showed that in pulsed discharges in air at atmospheric pressure [3] the neutral gas temperature at the end of the streamer phase in the center of the discharge was approximately 1200 K and the electron density at the same time and location was 9.2×10^{18} cm^{-3}. Assuming quasineutrality and using our model for an initial temperature of 300K and the corresponding total ion density, the gas temperature after the DIH and ion-neutral temperature relaxation (which occurs in a timescale smaller than the duration of the streamer phase) is predicted to be 1250 K. This

Table 3.2: Comparison of the measured neutral gas temperature to the predicted values accounting for disorder induced heating and ion neutral temperature relaxation.

Gas composition	Total ion density (m^{-3})	Measured gas temperature (K)	Predicted gas temperature (K)	Reference
N_2	4×10^{24}	750	765	[32]
air	9.2×10^{24}	1200	1250	[3]
air	4×10^{25}	4800	5000	[26]

agrees well with the experimental measurement.

Finally, we note that not all measurements of neutral gas heating appear to be explained solely by DIH and additional heating mechanisms might contribute significantly to the heating observed in some cases. N Minesi et al. [26] studied a fully ionized atmospheric pressure plasma in a thermal spark with an electron density of $\sim 4 \times 10^{19}$ cm^{-3}. These measured a neutral gas temperature of 48000 K from the relative emission intensity of N^+ excited states, after 10 ns. Using our model for an initial temperature of 300 K and the measured density the predicted neutral gas temperature is only 5000 K, which does not agree with the observed increase in the temperature. This suggests that the DIH is not a dominant effect and other mechanisms are responsible for the very large neutral gas heating in this experiment. It is also possible that the experimentally derived temperature from the relative emission intensity, which assumes a Saha-Boltzmann distribution in equilibrium with the electrons, significantly overestimates the actual gas temperature as the excited states are often not in equilibrium with the electron temperature in gas discharges [84].

Table 3.2 summarizes these comparisons between the model and experiments. The results presented here suggest that the DIH and subsequent ion-neutral relaxation should be considered as a possible mechanism for the observed neutral heating in multiple experiments where high ionization fractions are achieved.

3.8 Arbitrary ionization dynamics

The sequence of disorder-induced heating (picosecond) and ion-neutral temperature relaxation (nanosecond) suggests a new mechanism for ultrafast neutral gas heating. Previous sections considered only the case of an instantaneous ionization pulse, whereas the ionization pulse extends over nanoseconds in many experiments. Here, molecular dynamics simulations are used to analyze the evolution of ion and neutral gas temperatures for a gradual ionization over several nanoseconds. The results are compared with published experimental results from a nanosecond pulsed discharge, showing good agreement with a measurement of fast neutral gas heating in the streamer phase.

Results show that since DIH is a consequence of conservation of energy, from a thermodynamics standpoint, the total increase in temperature does not depend on the ionization rate. Instead, it relies solely on the initial and "final" potential configurations of the system, which are determined from the ionization fraction and pressure of the discharge. These findings offer a refined understanding of the underlying mechanisms, showing that when ionization occurs on a nanosecond timescale or slower, the evolution of the neutral gas temperature due to DIH closely follows the ion density profile.

In order to validate these predictions, MD simulation results for a gradual ionization ramp case are compared with experimental measurements of neutral gas temperature in an atmospheric pressure air nanosecond pulsed discharge from Lo *et al.* [3]. The good agreement between the simulated evolution of the neutral gas temperature and experimental measurements suggests that DIH followed by ion-neutral temperature relaxation has a significant influence on neutral gas heating in these experiments. A conclusion is that DIH should be considered alongside atomic reaction-based mechanisms for fast gas heating. This novel gas heating mechanism stands out as the fastest reported to date.

3.8.1 Setup

Molecular dynamics simulations were run using the open-source software LAMMPS [75]. The configuration employed builds upon that described in previous section 3.1, but with the assumption of gradual ionization. Partially ionized monatomic N gas was simulated instead of Ar with Lennard Jones parameters $\epsilon = 99.8k_B$, $\sigma = 0.3667$ nm (equation 1.8), and $\alpha_{\mathrm{R}} = 7.5$ (equation 1.9) for N [42]. The P3M method was used to simulate ion-ion interactions. [74] A separation distance of $r_c = 10\ a_{ii}$ was selected for differentiating the short and long-range parts of the Ewald summation, and a cutoff distance of 5σ was applied for the Lennard-Jones potential. To prevent close interactions that require a short timestep due to the attractive charge-induced dipole potential, we used a repulsive core with radius r_ϕ. As shown in section 3.5 a choice of $r_\phi \approx 0.133\ a_{\mathrm{in}}$ at atmospheric pressure blocks the three-body recombination that is unable to be simulated in a classical MD simulation. Three-body recombination is physically expected to influence plasma dynamics on a longer timescale than is considered here [2]. A cutoff distance of $5a_{\mathrm{in}}$, where a_{in} represents the average ion-neutral spacing, was used for the ion-neutral direct-force calculations.

To study the evolution of a non-equilibrium discharge with an arbitrary ionization rate, a neutral monatomic N gas at room temperature and atmospheric pressure was simulated until equilibrium was reached as delineated in [2]. This stage of the simulation was run with a Nosé-Hoover thermostat (NVT ensemble) followed by an NVE simulation once room temperature was reached [74]. The NVE simulation included neutral-neutral, ion-neutral, and ion-ion interactions with the potentials detailed in equations 1.8, 1.9, and 1.10. In this stage, the ion density $n_i(t)$ was an input parameter. The timestep used was $5 \times 10^{-4}(\omega_{pi}^{\max})^{-1}$, where $\omega_{pi}^{\max}$ is the maximum plasma frequency corresponding to the maximum ion density $n_i^{\max}$. The total number of particles was 50,000. The simulation domain was a three-dimensional box with periodic boundary conditions, and the volume was set to ensure that at the initial room tem-

perature and with 50,000 atoms, the total gas density was approximately 2.5×10^{25} m^{-3}, corresponding to atmospheric pressure.

Here, we compare our MD simulations with a nanosecond pulsed discharge experiment conducted in atmospheric air, as reported by Lo et al. [3]. The experimental setup involved the generation of a discharge via a positive high-voltage pulse applied to pin-to-pin electrodes over a duration of 15 ns. Within this time frame, a streamer phase emerged, propagating between the electrodes, which subsequently transitioned into a spark phase characterized by low voltage and high current. Optical emission spectroscopy measurements indicated an ultra-fast gas heating, reaching temperatures up to 1200 K at 15 ns post-current rise [3]. In addition, the electron density was measured at the end of the streamer phase to be 9.2×10^{24} m^{-3}. Our analysis is particularly concentrated on this initial streamer phase.

To replicate these experimental conditions in the MD simulations, we employed the following method during the second NVE stage. A subset of neutral atoms was randomly ionized at intervals of every n_t timesteps, resulting in the conversion of approximately 10 neutral atoms into ions per ionization event. The value of n_t was dynamically adjusted to achieve a desired ion density profile, denoted as $n_i(t)$. It is crucial to note that we have intentionally omitted certain heating mechanisms commonly believed to contribute to gas heating in order to isolate the effect of DIH and assess its potential impact on the neutral gas temperature. Specifically, our simulations employed a monatomic nitrogen gas model, thereby neglecting dissociation processes. Furthermore, quenching of electronically excited species was not accounted for and no external electric field was included.

Figure 3.13(a) illustrates three distinct ionization profiles, $x_i(t) = n_i(t)/n$, used in the simulations: an instant ionization profile, a linear ionization profile, and an ionization profile proportional to the deposited energy measured in the experiment reported by Lo *et al.* [3]. The maximum ion density simulated was 9.2×10^{24} m^{-3}

($x_i \approx 0.368$), aligning with the maximum electron density documented in reference [3].

3.8.2 Results

Figure 3.13(b) illustrates the evolution of ion and neutral gas temperatures for each of the ionization profiles. In the cases of gradual ionization, the ion temperature exhibits a peak on a ns timescale. This is associated with ionization events that cause DIH on a timescale that is shorter than the ion-neutral relaxation timescale. Following this initial surge, the ion temperature declines as the ion and neutral temperatures approach one another on a timescale of a few nanoseconds. At later times, the ion and neutral temperatures are approximately equal, and rise at the same rate. This incremental rise is attributed to disorder-induced heating, occurring continuously with ion-neutral temperature relaxation as the neutral gas undergoes ionization during the simulation. Ionization proceeds at a much slower pace compared to DIH and the ensuing ion-neutral temperature relaxation. Therefore, both ions and neutrals elevate their temperature according to the same temperature profile, defined by the ionization fraction $x_i(t)$. The dynamics of ion and neutral temperatures contrasts with the instantaneous ionization case, assumed in section 3.3 [2], where for the same ionization fraction ions heat much faster, on a ps timescale to a maximum temperature of $\sim$ 2800 K. Then, ions cool through ion-neutral collisions, increasing the neutral gas temperature on a $\sim$ ns timescale.

It is noteworthy that the moment the ionization ceases (at 15 ns for the gradual ionization profiles) the temperatures of the ion and neutral gases align, reaching a state referred to as "equilibrium". The "equilibrium" temperature between ions and neutrals, discerned in figure 3.13(b), is measured at 1275 K and does not depend on the ionization dynamics, since all the simulated $n_i(t)$ profiles reach the same final temperature. This is in agreement with the model described in equation 3.8, which

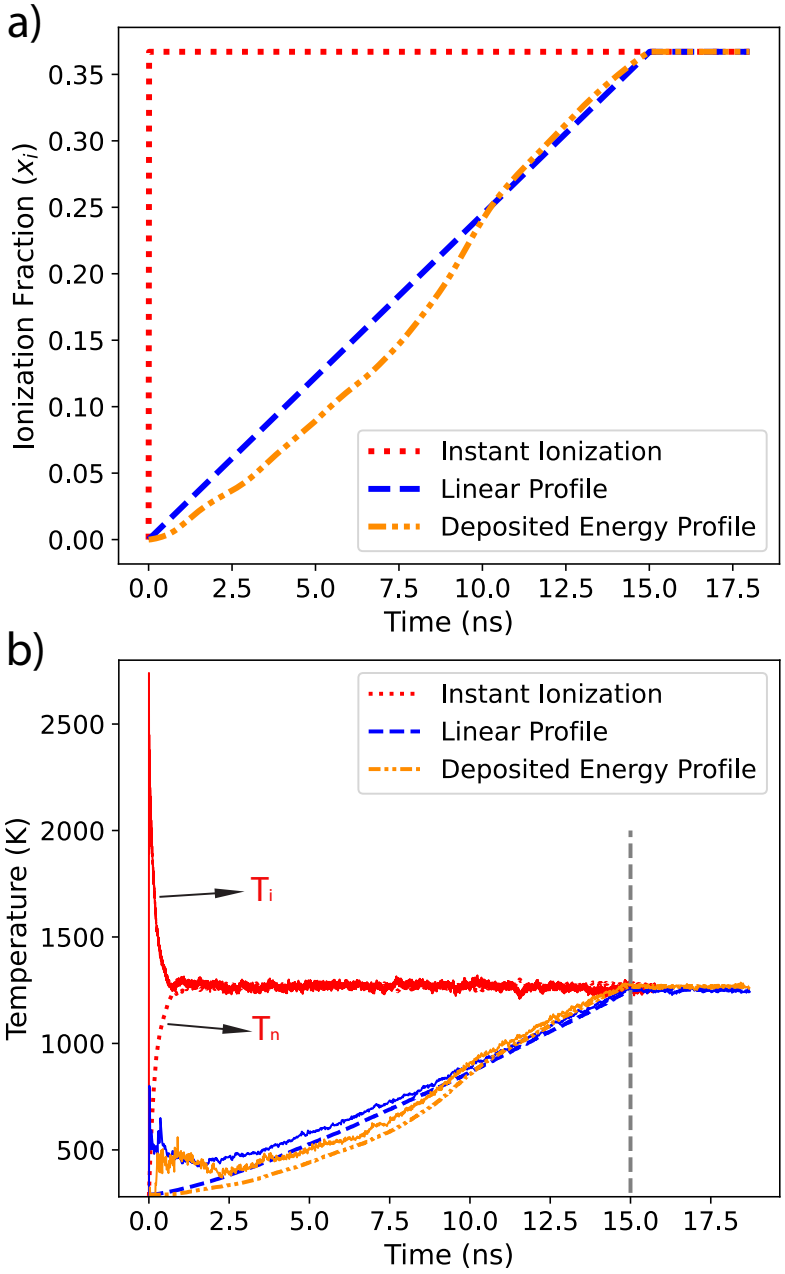

Figure 3.13: (a) Ionization fraction profiles used in the MD simulations. (b) Evolution of ion and neutral temperatures from MD simulations for each ionization fraction profile shown in (a). Continuous lines represent the ion temperature while dashed lines represent the neutral gas temperature. A vertical dashed line marks the instant at which ionization stops for the cases of gradual ionization.

forecasts an equilibrium temperature of 1272 K. Beyond the 15 ns mark, the simulations persists without alterations in the ionization degree, and no further changes in the temperature are observed. It is noteworthy that although the three different MD simulations have different ionization timescales, they all converge to the same "equilibrium" temperature. The congruence of the final temperature for all the simulations and its accord with equation 3.8 highlights that the total energy released by DIH is independent of the ionization dynamics, depending only on the initial conditions and final ionization state.

3.8.3 Comparison with experiment

Figure 3.14 presents a comparison between the neutral gas temperature obtained from MD and the published measurements from Lo *et al* [3]. Molecular dynamics results are shown for both of the gradual ionization profiles depicted in figure 3.13(b). The final "equilibrium" temperature from the MD simulations aligns well with the experimental results. The simulations also agree with the experimental measurements of the temperature evolution, extending from the initiation of the discharge up to 15 ns. Moreover, the temperature determined using an ionization profile founded on the deposited energy profile measured experimentally, demonstrates good agreement with the measured temperature [3].

It is important to highlight that the MD simulations did not incorporate heating mechanisms related to plasma chemistry, such as spontaneous dissociation or quenching of electronically excited molecules, nor did they include the external electric field or elastic electron-neutral collisions. Furthermore, the simulation domain consisted of a small periodic box with a total number of atoms and ions of 50,000, and thus excluded geometric effects. The simulation setup rests exclusively on thermodynamic arguments and it still is able to recover the experimentally observed temperature profile, including only interactions between ion and neutral atoms through the poten-

tials described in equations 1.8-1.10. Conversely, Lo *et al.*[3] attribute the detected gas heating in the streamer phase to the well-recognized quenching of electronically excited species by oxygen molecules. However, the commonly assumed mechanism is more likely to have occurred over 10's of ns and was thus a significant mechanism for spark-timescale temperature increases but not the streamer initiation-timescale heating. This suggests that DIH and ion-neutral temperature relaxation might constitute an essential ultra-fast heating mechanism, one that has been overlooked in the current analysis of cold atmospheric pressure plasmas.

In Lo *et al.* [3], the discharge transitioned into a spark after 15 ns, with the gas heating persisting over an extended timescale. This concurs with the timescale argument employed here, suggesting that while alternative heating mechanisms commonly found in partially ionized plasmas still occur, DIH can significantly influence the ion and neutral gas temperatures on a much shorter timescale and should be incorporated in future analyses.

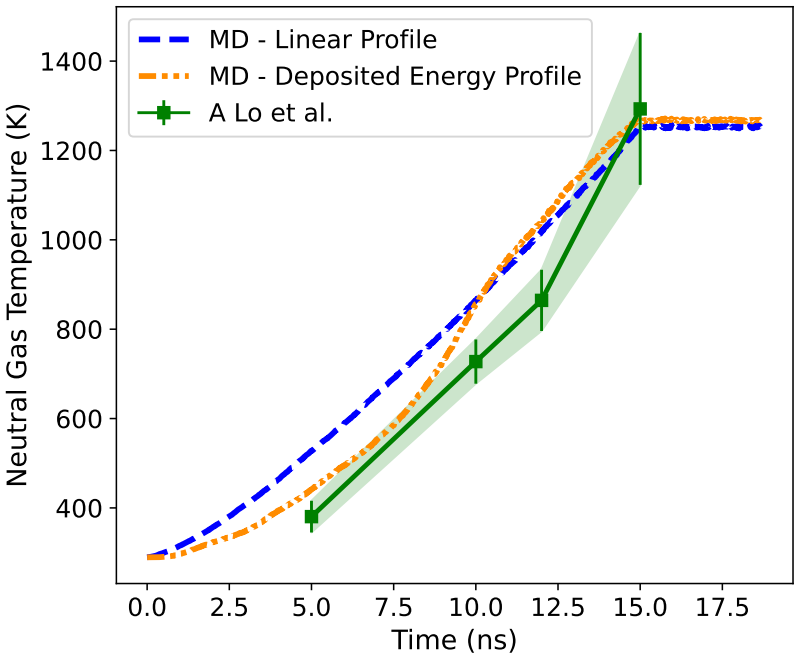

Figure 3.14: Evolution of the neutral gas temperature from molecular dynamics, using the gradual ionization fraction profiles shown in figure 3.13(a) and from a nanosecond pulsed discharge in atmospheric air [3].

3.9 Effect of rotational degrees of freedom in molecular plasmas

Previous sections described DIH in the context of atomic gases after an instant ionization pulse, here we extend these results to molecular plasmas. The work presented in this section was led by Jarett LeVan and the author of this thesis participated as a coauthor. A main finding is that the energy gained by ions in disorder-induced heating gets spread over both translational and rotational degrees of freedom on a nanosecond timescale, causing the final ion and neutral gas temperatures to be lower in the molecular case than in the atomic case [4]. However, it is important to note that in a real discharges in molecular gases, large ionization fractions are achieved after dissociation, making these results less relevant at the regimes where DIH contributes significantly to gas heating. The importance of dissociation to achieve large

ionization fractions and its influence in gas heating are described in chapter IV.

Using molecular dynamics (MD) simulations of Nitrogen gas (N_2), we find that DIH causes the ion translational temperature to rapidly increase over approximately one ion plasma period ($\approx$ 1 ps). This is followed by translational-rotational and ion-neutral relaxation processes that occur in roughly 1 ns. The latter process leads to fast neutral gas heating. A main finding is that the translational-rotational energy exchange leads to a lower total temperature resulting from DIH than in the atomic case. This is because the kinetic energy gained by ions from DIH gets distributed amongst more degrees of freedom in the molecular case. Considering N_2, the kinetic energy gain is eventually spread equally over 3 translational and 2 rotational degrees of freedom, for a total of 5. This contrasts with the 3 degrees of freedom in the atomic case. Furthermore, we confirm that this principle extends to molecules with 3 rotational degrees of freedom by simulating an N_4 molecular plasma. Despite the reduction in temperature due to the presence of rotational degrees of freedom, DIH can still cause a temperature increase on the order of thousands of Kelvin.

3.9.1 Setup

Molecular dynamics simulations were run using LAMMPS [75]. Nitrogen (N_2) molecules were modelled as rigid rotors, allowing for no vibration, and all ions were modelled as N_2^+, consisting of a neutral atom rigidly bonded to an ion. A bond length of 1.09 Å[85] was held constant using the "fix rigid" command in LAMMPS, which solves the forces and torques on each rigid body by summing the forces and torques on its constituent atoms. This approach ignores vibration, an assumption expected to be valid because the characteristic vibrational temperature of N_2 is 3374 K [86] and the temperature is far below this for the majority of the simulation. Additionally, DIH and the subsequent ion-neutral energy relaxation occur at the nanosecond timescale or less, while translational-vibrational energy exchange in N_2 occurs on a microsecond

timescale [87]. A real ionization process will certainly create excited vibrational states, but this does not affect DIH because the ion and neutral atom temperatures are too low to couple to the vibrational modes.

Electrons were left out of the simulation because their high temperature in CAPPs make them weakly coupled as described in previous chapters. In strongly coupled plasmas, treating electrons as a non-interacting background species yields accurate ion and neutral dynamics, as commonly done in the one-component plasma (OCP) model [88]. Chemical effects were also left out as they are beyond the scope of this chapter, however they will be discussed in chapter IV.

Interactions were modelled on a per-atom basis, with the ion-ion, ion-neutral, and neutral-neutral interaction potentials given by the Coulomb, charge-induced dipole, and Lennard-Jones potentials described in equations 1.10, 3.1, 1.8 with $\epsilon = 99.8k_B$, $\sigma = 0.3667$ nm, and $\alpha_R = 7.5$ for N_2.

This section will focus on data from the N_2 simulations. However, for comparison's sake, simulations of N and N_4 were also run. The atomic nitrogen simulations were run in the exact same fashion as the previous sections and in [2]. In the N_4 simulations, N_4 was modelled using an open-chain geometry as described by Glukhovtsev and Laiter [89]; a structure which, importantly, has three rotational degrees of freedom. All N_4 ions were modelled as N_4^+, with one of the two middle atoms ionized and a modified LJ coefficient $\epsilon = 29.0k_B$ was used in order to prevent significant neutral gas correlations.

To start the simulations, 10,000 molecules of neutral gas was evolved under the influence of a thermostat until equilibrium at room temperature was reached. Then, a fraction of the molecules were instantly ionized and an NVE (microcanonical) simulation was run with timestep $\Delta t = 5 \times 10^{-4}\omega_{pi}^{-1}$, a value found to be sufficiently small for conserving energy. Molecule positions and velocities were output once every plasma period and used to calculate translational and rotational temperatures.

The simulation domain was a 3-dimensional box with periodic boundary conditions. Three simulations for each of N, N_2, and N_4 were run at every tenth ionization fraction from 0.10 to 0.70. Data was averaged across the three trials to minimize statistical deviation.

3.9.2 MD results

The averaged time-evolution of the component temperatures from a particular set of simulations, N_2 at a 0.30 ionization fraction, can be seen in figure 3.16. This plot shows results of the NVE stage simulation and $t = 0$ refers to the time immediately following ionization. A sharp spike can be seen in the translational temperature of N_2^+, reaching its peak after 2.22 ps (1.52 ω_{pi}^{-1}). This is disorder-induced heating. Molecules, upon being ionized, structurally rearrange themselves until they reach their state of minimal potential energy, increasing their translational kinetic energy in the process. This heating is followed by collisional relaxation, during which the N_2^+ translational temperature equilibrates with the rest of the degrees of freedom in the simulation over the course of one nanosecond, ultimately reaching an equilibrated temperature of 732 K. Figure 3.15 shows an illustration of this process.

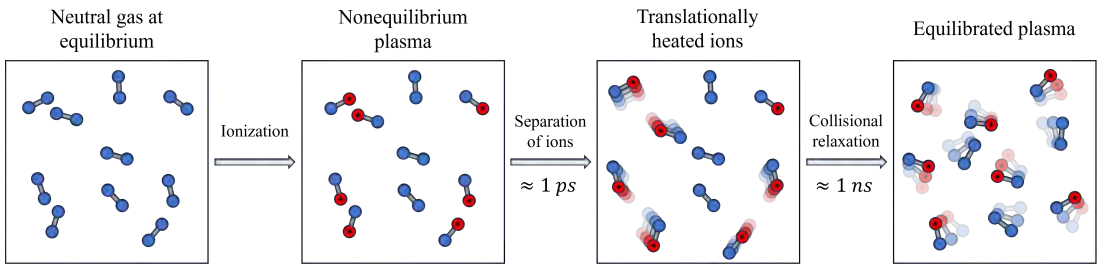

Figure 3.15: Illustration of the disorder-induced heating process. Ionization transforms neutral gas into a nonequilibrium plasma. Coulomb repulsion causes the ions to separate on a picosecond timescale, causing significant translational heating. Collisions then distribute this energy across neutral and rotational degrees of freedom until they reach an equilibrium. The collision relaxation timescale near atmospheric pressure is often characteristic of nanoseconds.

Simulations of each gas type, N, N_2, and N_4, followed a similar time-evolution to

figure 3.16. Ion translational temperatures always peaked after 1.5 plasma periods, consistent with the atomic ion case [2], and equilibration always occurred in roughly one nanosecond. However, they all produced differing equilibrium temperatures. We found the equilibrium temperature scales with the ionization fraction $x_i^{4/3}$, again consistent with section 3.6. This is caused by an increased ion density and thus an increased chance of two ions being generated in close enough proximity to gain an energy exceeding the initial thermal energy as they repel.

It is also observed that the equilibrated temperature is inversely proportional to the number of degrees of freedom present, implying $T_{eq,N} > T_{eq,N_2} > T_{eq,N_4}$, as shown in figure 3.17. This comes as a direct consequence of the equipartition theorem. Figure 3.18 shows that, for a given ion density, N, N_2, and N_4 plasmas convert the same amount of potential energy to kinetic energy. However, in N_4, this energy must be spread across 6 degrees of freedom (3 translational and 3 rotational), while it is spread across just 5 in N_2 and 3 in N. It is clear, then, that DIH models must consider the number of active degrees of freedom.

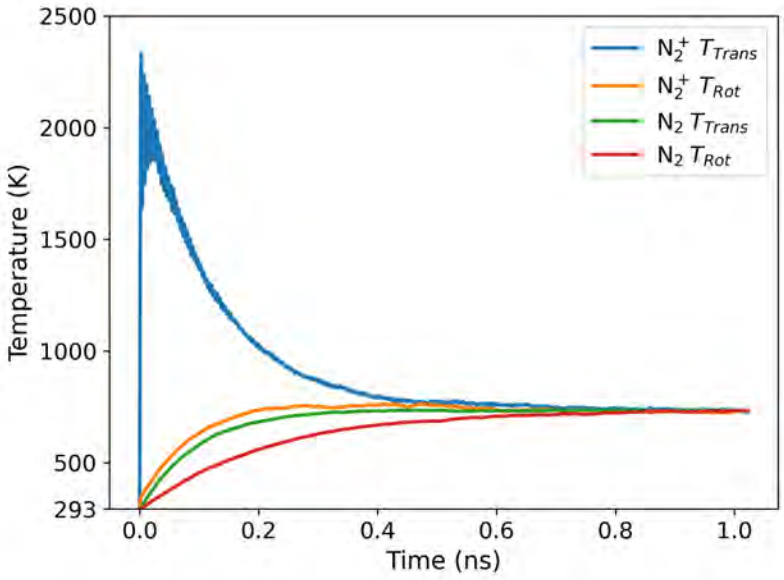

Figure 3.16: Simulated time-evolution of the temperature components of an N_2 plasma at a 0.30 ionization fraction. Lines correspond to the ion translational temperature (blue), ion rotational temperature (orange), neutral molecule rotational temperature (green), and neutral molecule rotational temperature (red).

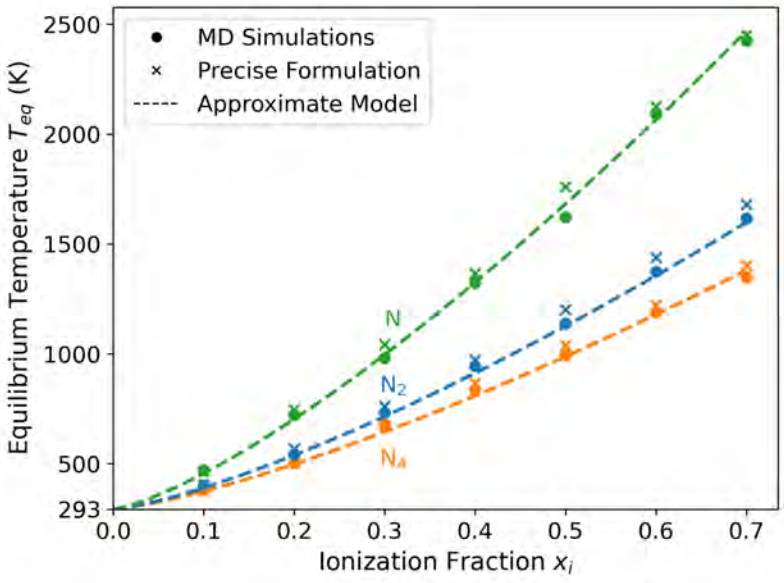

Figure 3.17: Simulated and predicted temperatures of N, N_2, and N_4 plasma using the approximate and precise formulation from [4] with the ion-ion g(r) computed from MD. These models are based on the same principle described in previous sections, conversion from potential to kinetic energy due to DIH.

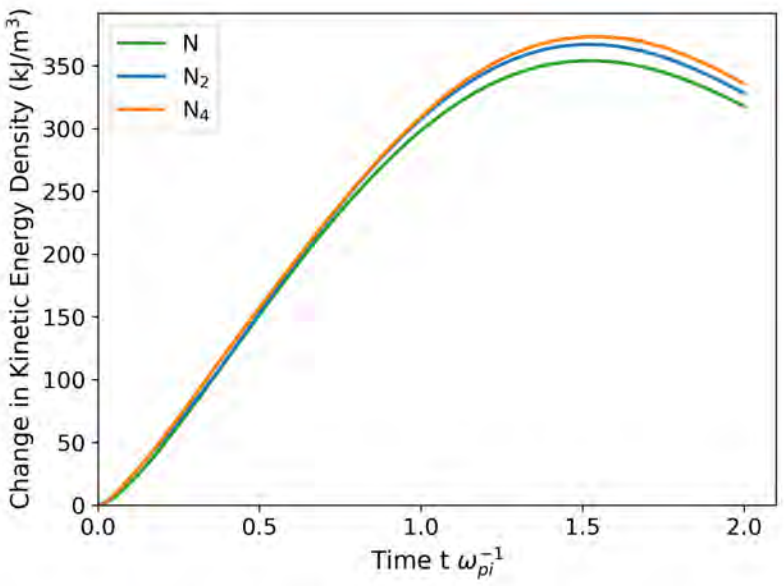

Figure 3.18: Change in total kinetic energy density (with respect to $t = 0$) for N, N_2, and N_4. This data comes from simulations at an ionization fraction of 0.30.

3.10 General model for DIH and temperature evolution

While a model based on conservation of energy to estimate the increase in ion and neutral gas temperatures due to DIH was described in section 3.6 [2], it is limited to the instant ionization case. This section describes a generalized model for DIH in the context of an arbitrary ionization dynamics, and validates it against molecular dynamics simulations. Subsequently, this model is incorporated into a global plasma chemistry model for a nanosecond pulse discharge in atmospheric N_2 in chapter IV.

The importance of developing a general model for DIH under an arbitrary ionization dynamics lies in how plasmas discharges are modeled. Most nanosecond pulsed discharges are studied using plasma chemistry global models, as described in section 2.2. In these models, the evolution of the gas and ion temperatures are solved by integrating equations 2.9 and 2.10 over time. Hence, it is necessary to have a model for DIH that can be easily integrated in a numerical algorithm where equations 2.9 and 2.10 are solved.

3.10.1 Setup

The molecular dynamics setup used consists in what is described in section 3.8.1 but with a smaller number of ionization steps. Here, only 40 ionization steps are used to showcase the difference in timescale between DIH and the ion-neutral temperature relaxation. This is done in order to illustrate how the model for DIH is implemented. A linear ionization rate is assumed with a final ionization fraction of 20% after 5 ns, then the simulation continues for 1.5 ns without additional ionization. Hence, the ionization fraction increases by 0.5% on each ionization step and the time between ionization steps is 0.125 ns. The timestep used for the MD simulation was $10^{-3}/\omega_{pi}^{max}$, where ω_{pi}^{max} is the ion plasma frequency at the maximum ion density, after 5 ns. The total number of particles was 50000 and the parameters used for the charged induced dipole and Lennard Jones potential are given in section 3.8.1 for atomic nitrogen.

3.10.2 MD results

In a discharge with an arbitrary but gradual ionization rate, DIH occurs continuously as ions are created from the background neutral gas. To illustrate this, figure 3.19 shows the ion-ion radial distribution function g(r), right after ionization and after 1.5 the inverse of the ion plasma frequency, once DIH happens in one of the ionization steps. As observed, there is a small peak at a short distance after ionization, which corresponds to the newly created ions at random positions. After DIH happens, the newly created ions separate from the ions closest to them and the system evolves to the lowest potential configuration increasing the kinetic energy. The g(r) after DIH corresponds to a one component plasma at the corresponding coupling strength [2].

Figure 3.20 shows the evolution of ion and neutral gas temperatures from molecular dynamics using the described setup. The choice of doing 40 ionization steps was done to showcase how DIH happens every time an ionization step occurs. The ion temperature follows two stages between ionization steps. First, a rapid increase due

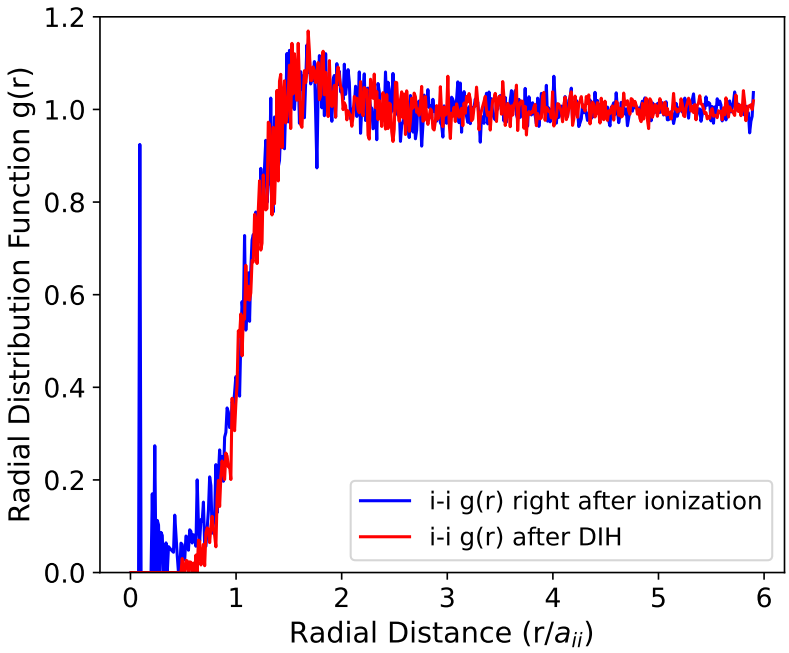

Figure 3.19: Ion-ion radial distribution function right after ionization and after DIH. The peak at small distances after ionization correspond to the newly created ions.

to DIH on a timescale given by the instantaneous value of $1.5\omega_{pi}^{-1}$, followed by an ion-neutral temperature relaxation through collisions, as described in previous sections. This process is repeated until the final ionization fraction is reached. The neutral gas temperature however, continuously increases due to collisions with ions until equilibrium is reached with the ion temperature after the last ionization step. Doing the ionization steps numerically more gradually, while maintaining the same ionization rate, would not change the rate of increase of the neutral gas temperature in this case. Hence, the model that is described in the following section also applies to the limit where the same timestep is used for ionization and temperature relaxation.

3.10.3 Model and discussion

In order to model DIH it is necessary to capture the change in the ion-ion g(r) between each ionization event and the subsequent DIH. In addition, this is followed by ion-neutral collisions that cool ions and heat neutrals, thus, the model can be

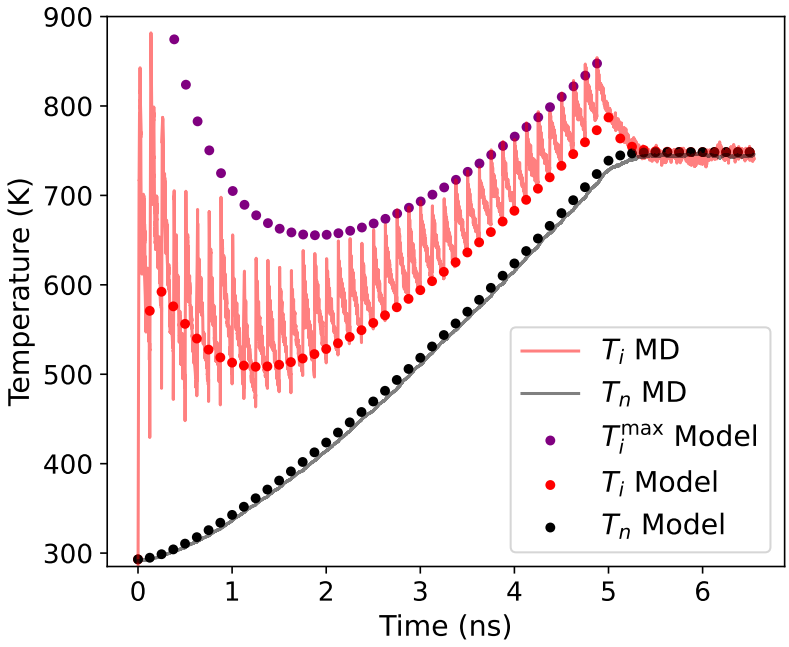

Figure 3.20: Evolution of ion (T_i) and neutral gas (T_n) temperatures from a molecular dynamics simulation using the numerical setup described in [5] but with a final ionization fraction of 20% and having only 40 ionization substeps.

separated in two stages, DIH and ion-neutral relaxation through collisions. Hence, the calculation of the change in potential energy between the two described states of ions, after ionization and after DIH, is necessary. From statistical mechanics, the change in potential energy of ions in the system between two consecutive states where ionization happened is given by

$$\Delta PE_{ii}^{k+1} = 2\pi n_i^{k+1} x_i^{k+1} \int_0^\infty dr r^2 \phi_c(r) \left[\tilde{g}_{ii}^{k+1} - g_{ii}^{'k}\right] \tag{3.9}$$

where k and k+1 corresponds to the two instants of time, after ionization and after DIH, $\tilde{g}_{ii}^{k+1}$ is the ion-ion radial distribution function after DIH and $g_{ii}^{'k}$ after ionization, $\phi_c(r)$ is the Coulomb potential and x_i the ionization fraction.

The radial distribution function right after ionization, $g_{ii}^{'k}$ can be expressed as a function of the ion-ion radial distribution function g_{ii}^k and the ion-neutral distribution

function g_{in}^k right before ionization

$$g_{ii}^{\prime k} = \frac{x_i^k}{x_i^{k+1}} g_{ii}^k + \frac{\Delta x_i^k}{x_i^{k+1}} g_{in}^k. \tag{3.10}$$

Using equation 3.10, the change in potential energy can be rewritten as

$$\Delta PE_{ii}^{k+1} = \frac{e^2}{2\epsilon_0} n^{k+1} (a_{ii}^{k+1})^2 \left[I^*(\Gamma_{ii}^{min}) - \left(\frac{x_i^k}{x_i^{k+1}} \right) I^*(\Gamma_{ii}^k) - \left(\frac{\Delta x_i^k}{x_i^{k+1}} \right) I^*(g_{in}^k) \right] \tag{3.11}$$

where $I^*(\Gamma_{ii}) = \int_0^\infty dr r \left(g(r) - 1\right)$, with g(r) the OCP radial distribution function for Γ_{ii} and $I^*(g_{in}^k) = \int_0^\infty dr r \left(g_{in}^k(r) - 1\right)$. The radial distribution function $g_{in}^k(r)$ can be approximated as a step function at $r = 0.133 a_{in}$, with a_{in} the average interparticle distance between ion-neutral pairs, since ion-neutral interactions are weakly coupled and the distance at which $g_{in}^k(r)$ becomes 1 corresponds to hard core radius used in equation 3.1 [2]. Figure 3.21 shows a fit to $I^*(\Gamma_{ii})$,

$$I^*(\Gamma) = \frac{a}{(b + \Gamma)^c} + d \tag{3.12}$$

with parameters $a = 0.6032$, $b = 0.0372$, $c = 0.1549$ and $d = -0.9917$. Then, to calculate the change in the ion temperature due to DIH one needs to solve

$$\tilde{T}_i^{k+1} = \left(\frac{x_i^k}{x_i^{k+1}} \right) T_i^k + \left(\frac{\Delta x_i^k}{x_i^{k+1}} \right) T_n^k - \frac{2}{3k_B} \Delta PE_{ii}^{k+1} \tag{3.13}$$

iteratively on to find $\tilde{T}_i^{k+1}$. After each DIH step, the ion-neutral temperature relaxation must be calculated at the corresponding time between k and k+1, starting with an ion temperature given by $\tilde{T}_i^{k+1}$ and a neutral temperature of T_n^k. The ion-neutral temperature relaxation is done by solving equations 3.2 and 3.3 until temperatures T_i^{k+1} and T_n^{k+1} are calculated. This process is repeated every time there is an increase in n_i due to ionization.

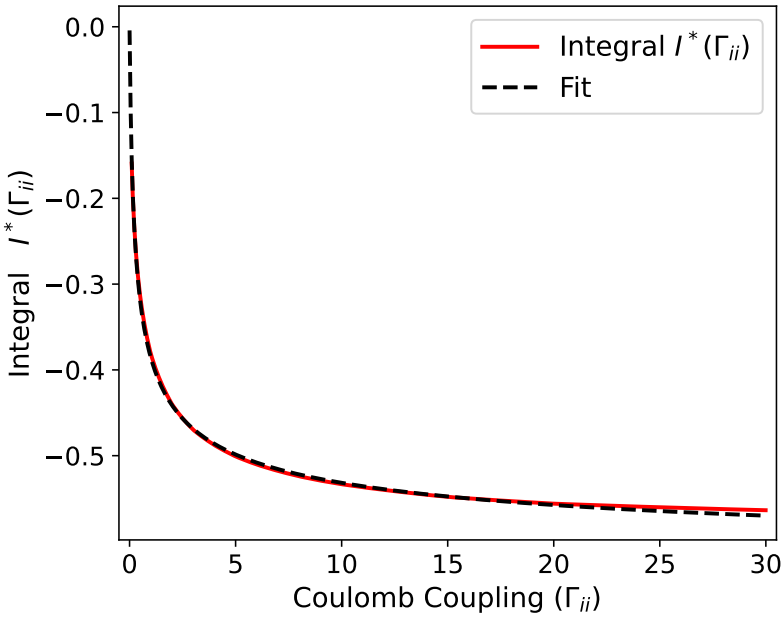

Figure 3.21: Integral $I^* = \int_0^\infty d\tilde{r}\ \tilde{r}\,[g(\tilde{r}) - 1]$ for different values of the macroparticle coupling parameter Γ_{ee}^w and fit $I^*(\Gamma) = a/(b+\Gamma)^c + d$ with parameters $a = 0.6032$, $b = 0.0372$, $c = 0.1549$ and $d = -0.9917$.

The ion and neutral gas temperatures calculated with the model are shown in figure 3.20. In addition, the maximum ion temperature, after each DIH stage ($\tilde{T}_i^{k+1}$) is shown. The model described for DIH and ion-neutral temperature relaxation shows a good agreement with the temperatures obtained from molecular dynamics. The following chapter integrates this model into a global plasma chemistry model of a nanosecond pulsed discharge.

CHAPTER IV

Global model for a nanosecond pulsed discharge in atmospheric N_2 with disorder induced heating

4.1 Global model

This chapter introduces a comprehensive model integrating disorder induced heating in a global plasma chemistry model to examine nanosecond pulse discharges in atmospheric nitrogen. While traditional global models have focused predominantly on mechanisms such as dissociation and excitation of molecular nitrogen, this work extends the modeling framework to include DIH, offering a detailed exploration of its role alongside other fast gas heating mechanisms. It is observed that while dissociation remains a dominant heating mechanism at high reduced electric fields, DIH additionally increases the temperature by 20% after reaching full dissociation and ionization at atmospheric pressure. Furthermore, if the initial pressure of the neutral gas is increased to 10 atmospheres, DIH increases the overall temperature by 60% after reaching full ionization. It is also observed that when the reduced electric field is not large enough to fully ionize the gas, but large enough such that the total ion density makes DIH relevant, electrons lose less energy to ions through collisions due to the larger ion temperature, increasing the rate of inelastic processes. Hence, when DIH is included in the model, it indirectly helps to increase the dissociation

and ionization degrees. This effect becomes more important as the pressure increases above one atmosphere. These results indicate that while DIH is not the predominant source of gas heating in atmospheric pressure plasmas, it can be non negligible and indirectly influence the plasma chemistry. This indicates that DIH could potentially have major implications in discharges at higher pressures and should be included in global models for such conditions.

4.2 Reaction set for molecular nitrogen

The reaction set used in this work is based to what is described by Minesi *et al* [72] for an atmospheric air nanosecond pulsed discharge global model with the difference that here, all the reactions involving oxygen are removed and quenching reactions relevant for gas heating mechanisms are incorporated. In addition, the energy released due to dissociation of molecular nitrogen is accounted for in order to include possible gas heating mechanisms. It is important to remark that, vibrational states are not included with the exception of $N_2(A^3\Sigma)$(v=1-10), which are grouped into the $N_2(A^3\Sigma)$ excited state [6, 90]. This approximation was made in order to simplify the reaction set, however, it reduces the possible number of dissociation and ionization pathways and thus, gas heating mechanisms. Future work should include a more complete reaction set to include additional possible dissociation pathways in order to have a more accurate gas heating analysis. Here, we only focus on having a simple but first comparison between different chemistry-related gas heating mechanisms and DIH and its influence in the overall plasma chemistry at and above atmospheric pressure.

In the reaction set used in this work, for electron-heavy reactions, the rate coefficient is a function of the electron temperature. For heavy-heavy reactions, the rate coefficient is a function of the gas temperature with the exception of charge exchange where the rate coefficient is calculated using the ion temperature. The rate coefficients are calculated assuming a Maxwellian distribution at the corresponding temperature

as described in chapter II. The approximation of a Maxwellian EEDF is valid for atmospheric N_2 and air nanosecond pulsed discharges at ionization fractions above 1% as described in [6, 91]. The cross-section of electron-impact excitation of N_2 to $N_2(A^3\Sigma_u^+)$ is the sum of the cross-sections to the $N_2(A, v = 1-10)$ levels taken from [6, 90]. The $N_2(B^3\Pi_g, B^3\Sigma_u^-, W^3\Delta_u)$ states are lumped together in the $N_2(B)$ state, using the cross-sections of [92] as described by [6]. Differently than in [6], $N_2(C^3\Pi_u, E^3\Sigma_g^+)$ states are not grouped. In addition, instead of grouping $N_2(a'^1\Sigma_u^-, a^1\Pi_g, w^1\Delta_u)$ singlet states in the $N_2(a')$ state [6], here we only group $N_2(a'^1\Sigma_u^-, w^1\Delta_u)$ into $N_2(a')$ and we track separately the $N_2(a^1\Pi_g)$ state because their dissociation cross-sections differ by one order of magnitude. The electronic excitation of N_2(A, B, C, a',a^1, E) by electron impact as well as the transitions between the N_2^+(X, A, B, C) states by electron impact are taken from [93]. The ionization cross-sections of N_2(X) to N_2^+(X, B), were estimated in [94]. The ionization cross-sections of N_2(A, B, a', a^1, C, E) are taken from [93]. The dissociation cross-section of N_2 ground state, is taken from [95, 96], whereas the dissociation cross-sections of the electronically excited states are from [93]. In electron-impact dissociation of any electronic state of N_2, the fragments are N(^{4}S) and N(^{2}D) [95, 96]. We neglect the formation of excited electronic states of N^+. A summary of the electronic levels of N_2 and N modeled in the present reaction set is given in table 4.1. In this model, the N_2 dissociation and ionization by electron-impact are state-specific and more details are given in table 4.6 with the cross sections taken from [93]. The quenching of N_2 excited states is taken from the work of Popov [22] and provided by Mark Zammit at Los Alamos. It was shown in [22] that this set reproduces the ultrafast heating observed in [20] and [33, 97]. Electron impact excitation and ionization of N are taken from [98, 99]. Penning and associative ionization of N_2 reactions are included from [100]. The present reaction set does not include spontaneous emission from N_2 excited states and photo ionization of molecular nitrogen.

In order to account for gas heating mechanisms, the energy released ($\Delta H < 0$) in the electron impact dissociation reactions as well as quenching of N_2 excited states is accounted for. In the case of dissociation, since some of the excited states are lumped together, ΔH is calculated as a weighted average based on the dissociation cross sections from each of the grouped excited states. Tables 4.6 and 4.9 show the dissociation and quenching reactions with the respective ΔH values. Additional gas heating mechanisms are included, as described in chapter II, due to charge exchange and momentum transfer collisions between neutrals and ions. In order to have a more complete reaction set, additional dissociation pathways should be included, in particular from vibrational excited states.

While this reaction set and the global model implemented in this work, described in chapter II, do not include reverse rates it is important to remark that when full ionization is achieved in experiments at atmospheric pressure, the plasma is expected to be at LTE. This means that the results obtained in this chapter could change in terms of the relative population of excited states and final ionization degree. However, the current analysis is focused on a simple comparison between DIH and already studied gas heating mechanisms. Future work, should include the model for DIH presented in this work in a more accurate global model with a more complete reaction set. In addition, the reaction set described here is used at one and ten atmospheres of initial pressure. However, for pressures larger than one atmosphere, three body reactions should be included. In addition to the mentioned approximations, this work does not include any diffusion loses or gas flow, since we only consider very short nanosecond pulses focusing on the ionization dynamics and disorder induced heating.

Table 4.1: Electronic levels of N_2, N included in the reaction set. The energy is given relative to the ground state. The main difference with [6] is that here we incorporate the $N_2(a^1\Pi_g)$ and $N_2(E^3\Sigma_g^+)$ states. A total of 19 different species are included in the model.

State	**Configuration**	**E (eV)**
$N(^4S^\circ)$	$2s^2 2p^3$	0
$N(^2D^\circ)$	$2s^2 2p^3$	2.38
$N(^2P^\circ)$	$2s^2 2p^3$	3.575
$N(^4P)$	$2s^2 2p^3(^3P)3s$	10.33
$N(^2P)$	$2s^2 2p^3(^3P)3s$	10.68
$N(^4P)$	$2s^2 2p^4$	10.92
$N(^2S^\circ)$	$2s^2 2p^2(^3P)3p$	11.60
$N(^4D^\circ)$	$2s^2 2p^2(^3P)3p$	11.75
$N_2(X^1\Sigma_g^+)$		0
$N_2(A^3\Sigma_u^+)$		6.23
$N_2(B^3\Pi_g)$		7.40
$N_2(a'^1\Sigma_u^-)$		8.55
$N_2(a^1\Pi_g)$		8.89
$N_2(C^3\Pi_u)$		11.06
$N_2(E^3\Sigma_g^+)$		11.88
$N_2^+(X^2\Sigma_g^+)$		0
$N_2^+(A^2\Pi_u)$		1.13
$N_2^+(B^2\Sigma_u^+)$		3.16
$N_2^+(C^2\Sigma_u^+)$		8.02

Table 4.2: Electron Impact excitation of N_2

#	Reaction
1	$e + N_2 \rightarrow e + N_2(A^3\Sigma)(v=0\text{-}4)$
2	$e + N_2 \rightarrow e + N_2(A^3\Sigma)(v=5\text{-}9)$
3	$e + N_2 \rightarrow e + N_2(A^3\Sigma)(v=10)$
4	$e + N_2 \rightarrow e + N_2(B^3\Pi)$
5	$e + N_2 \rightarrow e + N_2(a^1\Pi)$
6	$e + N_2 \rightarrow e + N_2(a'^1\Sigma)$
7	$e + N_2 \rightarrow e + N_2(C^3\Pi)$
8	$e + N_2 \rightarrow e + N_2(E^3\Sigma)$
9	$e + N_2(A^3\Sigma) \rightarrow e + N_2(B^3\Pi)$
10	$e + N_2(A^3\Sigma) \rightarrow e + N_2(a'^1\Sigma)$
11	$e + N_2(A^3\Sigma) \rightarrow e + N_2(a^1\Pi)$
12	$e + N_2(A^3\Sigma) \rightarrow e + N_2(C^3\Pi)$
13	$e + N_2(A^3\Sigma) \rightarrow e + N_2(E^3\Sigma)$
14	$e + N_2(B^3\Pi) \rightarrow e + N_2(a'^1\Sigma)$
15	$e + N_2(B^3\Pi) \rightarrow e + N_2(a^1\Pi)$
16	$e + N_2(B^3\Pi) \rightarrow e + N_2(C^3\Pi)$
17	$e + N_2(B^3\Pi) \rightarrow e + N_2(E^3\Sigma)$
18	$e + N_2(a'^1\Sigma) \rightarrow e + N_2(a^1\Pi)$
19	$e + N_2(a'^1\Sigma) \rightarrow e + N_2(C^3\Pi)$
20	$e + N_2(a'^1\Sigma) \rightarrow e + N_2(E^3\Sigma)$
21	$e + N_2(a^1\Pi) \rightarrow e + N_2(C^3\Pi)$
22	$e + N_2(a^1\Pi) \rightarrow e + N_2(E^3\Sigma)$
23	$e + N_2(C^3\Pi) \rightarrow e + N_2(E^3\Sigma)$

Table 4.3: Electron Impact Ionization of N_2

#	Reaction
24	$e + N_2 \rightarrow e + e + N_2^+$
25	$e + N_2(A^3\Sigma) \rightarrow e + e + N_2^+$
26	$e + N_2(B^3\Pi) \rightarrow e + e + N_2^+$
27	$e + N_2(C^3\Pi) \rightarrow e + e + N_2^+$
28	$e + N_2(a'^1\Sigma) \rightarrow e + e + N_2^+$
29	$e + N_2(a^1\Pi) \rightarrow e + e + N_2^+$
30	$e + N_2(E^3\Sigma) \rightarrow e + e + N_2^+$
31	$e + N_2 \rightarrow e + e + N_2^+(A^2\Pi_u)$
32	$e + N_2 \rightarrow e + e + N_2^+(B^2\Sigma_u^+)$
33	$e + N_2 \rightarrow e + e + N_2^+(C^2\Sigma_u^+)$
34	$e + N_2(A^3\Sigma) \rightarrow e + e + N_2^+(A^2\Pi_u)$
35	$e + N_2(A^3\Sigma) \rightarrow e + e + N_2^+(B^2\Sigma_u^+)$
36	$e + N_2(A^3\Sigma) \rightarrow e + e + N_2^+(C^2\Sigma_u^+)$
37	$e + N_2(B^3\Pi) \rightarrow e + e + N_2^+(A^2\Pi_u)$
38	$e + N_2(B^3\Pi) \rightarrow e + e + N_2^+(B^2\Sigma_u^+)$
39	$e + N_2(B^3\Pi) \rightarrow e + e + N_2^+(C^2\Sigma_u^+)$
40	$e + N_2(C^3\Pi) \rightarrow e + e + N_2^+(A^2\Pi_u)$
41	$e + N_2(C^3\Pi) \rightarrow e + e + N_2^+(B^2\Sigma_u^+)$
42	$e + N_2(C^3\Pi) \rightarrow e + e + N_2^+(C^2\Sigma_u^+)$
43	$e + N_2(a'^1\Sigma) \rightarrow e + e + N_2^+(A^2\Pi_u)$
44	$e + N_2(a'^1\Sigma) \rightarrow e + e + N_2^+(B^2\Sigma_u^+)$
45	$e + N_2(a'^1\Sigma) \rightarrow e + e + N_2^+(C^2\Sigma_u^+)$
46	$e + N_2(a^1\Pi) \rightarrow e + e + N_2^+(A^2\Pi_u)$
47	$e + N_2(a^1\Pi) \rightarrow e + e + N_2^+(B^2\Sigma_u^+)$
48	$e + N_2(a^1\Pi) \rightarrow e + e + N_2^+(C^2\Sigma_u^+)$

Table 4.4: Electron impact excitation of N_2 ions

#	Reaction
49	$e + N_2^+ \rightarrow e + N_2^+(A^2\Pi_u)$
50	$e + N_2^+ \rightarrow e + N_2^+(B^2\Sigma_u^+)$
51	$e + N_2^+ \rightarrow e + N_2^+(C^2\Sigma_u^+)$
52	$e + N_2^+(A^2\Pi_u) \rightarrow e + N_2^+(B^2\Sigma_u^+)$
53	$e + N_2^+(A^2\Pi_u) \rightarrow e + N_2^+(C^2\Sigma_u^+)$
54	$e + N_2^+(B^2\Sigma_u^+) \rightarrow e + N_2^+(C^2\Sigma_u^+)$

Table 4.5: Electron impact excitation of atomic N

#	Reaction
55	$e + N \rightarrow e + N(^2D^0)$
56	$e + N \rightarrow e + N(^2P^0)$
57	$e + N \rightarrow e + N(^4P)$
58	$e + N \rightarrow e + N(^2P)$
59	$e + N \rightarrow e + N(2s^2 2p^4)$
60	$e + N \rightarrow e + N(^2S^0)$
61	$e + N \rightarrow e + N(^4D^0)$
62	$e + N(^2D^0) \rightarrow e + N(^2P^0)$
63	$e + N(^2D^0) \rightarrow e + N(^4P)$
64	$e + N(^2D^0) \rightarrow e + N(^2P)$
65	$e + N(^2D^0) \rightarrow e + N(2s^2 2p^4)$
66	$e + N(^2D^0) \rightarrow e + N(^2S^0)$
67	$e + N(^2D^0) \rightarrow e + N(^4D^0)$
68	$e + N(^2P^0) \rightarrow e + N(^4P)$
69	$e + N(^2P^0) \rightarrow e + N(^2P)$
70	$e + N(^2P^0) \rightarrow e + N(2s^2 2p^4)$
71	$e + N(^2P^0) \rightarrow e + N(^2S^0)$
72	$e + N(^2P^0) \rightarrow e + N(^4D^0)$
73	$e + N(^4P) \rightarrow e + N(^2P)$
74	$e + N(^4P) \rightarrow e + N(2s^2 2p^4)$
75	$e + N(^4P) \rightarrow e + N(^2S^0)$
76	$e + N(^4P) \rightarrow e + N(^4D^0)$
77	$e + N(^2P) \rightarrow e + N(2s^2 2p^4)$
78	$e + N(^2P) \rightarrow e + N(^2S^0)$
79	$e + N(^2P) \rightarrow e + N(^4D^0)$
80	$e + N(2s^2 2p^4) \rightarrow e + N(^2S^0)$
81	$e + N(2s^2 2p^4) \rightarrow e + N(^4D^0)$
82	$e + N(^2S^0) \rightarrow e + N(^4D^0)$

Table 4.6: Electron Impact Dissociation of N_2 and N_2^+

#	Reaction	ΔH (eV)
83	$e + N_2 \rightarrow e + N + N(^2D^0)$	-0.90
84	$e + N_2(A^3\Sigma) \rightarrow e + N + N(^2D^0)$	-0.72
85	$e + N_2(B^3\Pi) \rightarrow e + N + N(^2D^0)$	-0.84
86	$e + N_2(a'^1\Sigma) \rightarrow e + N + N(^2D^0)$	-3.05
87	$e + N_2(C^3\Pi) \rightarrow e + N + N(^2D^0)$	-0.43
88	$e + N_2(E^3\Sigma) \rightarrow e + N + N(^2D^0)$	-2.78
89	$e + N_2(a^1\Pi) \rightarrow e + N + N(^2D^0)$	-2.45
90	$e + N_2^+ \rightarrow e + N(^2D^0) + N^+$	-0.34
91	$e + N_2^+(A^2\Pi_u) \rightarrow e + N(^2D^0) + N^+$	-1.34
92	$e + N_2^+(B^2\Sigma_u^+) \rightarrow e + N(^2D^0) + N^+$	-0.96
93	$e + N_2^+(C^2\Sigma_u^+) \rightarrow e + N(^2D^0) + N^+$	-0.96

Table 4.7: Electron impact ionization of atomic N

#	Reaction
94	$e + N \rightarrow e + e + N^+$
95	$e + N(^2D^0) \rightarrow e + e + N^+$
96	$e + N(^2P^0) \rightarrow e + e + N^+$
97	$e + N(^4P) \rightarrow e + e + N^+$
98	$e + N(^2P) \rightarrow e + e + N^+$
99	$e + N(2s_2p_4) \rightarrow e + e + N^+$
100	$e + N(^2S^0) \rightarrow e + e + N^+$
101	$e + N(^4D^0) \rightarrow e + e + N^+$

Table 4.8: Associative and Penning ionization

#	Reaction
102	$N(^2D^0) + N(^2P^0) \rightarrow e + N_2^+$
103	$N(^2P^0) + N(^2P^0) \rightarrow e + N_2^+$
104	$N_2(a'^1\Sigma) + N_2(a'^1\Sigma) \rightarrow e + N_2 + N_2^+$
105	$N_2(a'^1\Sigma) + N_2(A^3\Sigma) \rightarrow e + N_2 + N_2^+$

Table 4.9: Quenching

#	Reaction	ΔH (eV)
106	$N_2(A^3\Sigma) + N_2(A^3\Sigma) \rightarrow N_2(B^3\Pi) + N_2$	-4.99
107	$N_2(A^3\Sigma) + N_2(A^3\Sigma) \rightarrow N_2(C^3\Pi) + N_2$	-1.31
108	$N_2(B^3\Pi) + N_2 \rightarrow N_2 + N_2$	-7.35
109	$N_2(B^3\Pi) + N_2 \rightarrow N_2(A^3\Sigma) + N_2$	-1.18
110	$N_2(C^3\Pi) + N_2 \rightarrow N_2(a'^1\Sigma) + N_2$	-2.63
111	$N_2(a'^1\Sigma) + N_2 \rightarrow N_2(B^3\Pi) + N_2$	-1.05

Table 4.10: Electron - neutral elastic scattering

#	Reaction
112	$e + N_2 \rightarrow e + N_2$
113	$e + N_2(A^3\Sigma) \rightarrow e + N_2(A^3\Sigma)$
114	$e + N_2(B^3\Pi) \rightarrow e + N_2(B^3\Pi)$
115	$e + N_2(C^3\Pi) \rightarrow e + N_2(C^3\Pi)$
116	$e + N_2(a'^1\Sigma) \rightarrow e + N_2(a'^1\Sigma)$
117	$e + N_2(E^3\Sigma) \rightarrow e + N_2(E^3\Sigma)$
118	$e + N_2(a^1\Pi) \rightarrow e + N_2(a^1\Pi)$
119	$e + N \rightarrow e + N$
120	$e + N(^2D^0) \rightarrow e + N(^2D^0)$
121	$e + N(^2P^0) \rightarrow e + N(^2P^0)$
122	$e + N(^4P) \rightarrow e + N(^4P)$
123	$e + N(^2P) \rightarrow e + N(^2P)$
124	$e + N(2s_2p_4) \rightarrow e + N(2s_2p_4)$
125	$e + N(^2S^0) \rightarrow e + N(^2S^0)$
126	$e + N(^4D^0) \rightarrow e + N(^4D^0)$

Table 4.11: Coulomb collisions

#	Reaction
127	$e + N^+ \rightarrow e + N^+$
128	$e + N_2^+ \rightarrow e + N_2^+$
129	$e + N_2^+(A^2\Pi_u) \rightarrow e + N_2^+(A^2\Pi_u)$
130	$e + N_2^+(B^2\Sigma_u^+) \rightarrow e + N_2^+(B^2\Sigma_u^+)$
131	$e + N_2^+(C^2\Sigma_u^+) \rightarrow e + N_2^+(C^2\Sigma_u^+)$

Table 4.12: Charge exchange

#	Reaction
132	$N_2^+ + N_2 \rightarrow N_2 + N_2^+$

4.3 Setup

The numerical setup is described in chapter II, including momentum transfer collisions between ion and neutral species based on the model described in chapter III, as well as disorder induced heating for ion species with the model described in 3.10. The initial condition consist in an electron and N_2^+ ion population of 10^{20}

m^{-3} and a N_2 neutral gas density of 2.5×10^{25} m^{-3} in the ground state. In the case of simulations at 10 atmospheres, these densities are scaled accordingly. The timestep used is 0.1 and 0.01 ps at 1 and 10 atmospheres respectively. The discharge is assumed to happen in a pin to pin electrode configuration with a separation of 1.2 mm, similar to [6]. The initial ion and gas temperature is 300K and the initial electron temperature is 0.1 eV. The applied voltage has a Gaussian shape with a variable amplitude, a FWHM of 3 ns and a mean of 3.5 ns at atmospheric pressure, and 10 times smaller FWHM and μ at 10 atmospheres.

4.4 Results at atmospheric pressure

Figure 4.1 shows a) the applied voltage and reduced electric field for a simulation at atmospheric pressure and b) the electron temperature and deposited power per unit volume with and without including the model for DIH described in section 3.10. The reduced electric field is calculated accounting for the effective electron mobility, which includes both electron-ion and electron-neutral collisions since at large ionization fractions Coulomb collisions dominate. For this applied pulse, a difference between the voltage and reduced electric field curves is observed due to dissociation of molecular nitrogen. The profile of the deposited power is similar to what is experimentally observed in [6] for air with a similar voltage pulse. It is important to note that here, the Gaussian pulse is just an approximation and in actual experiments, the voltage drops slower after reaching its maximum value, leading to a finite reduced electric field that continues to heat electrons after full ionization is reached [6].

As shown in figure 4.1 b), the electron temperature rapidly increases to approximately 4 eV and then inelastic collisions decrease it until full ionization is reached and electrons are at equilibrium with ions [91]. The final electron temperature is 20% higher when DIH is turned on. This is because electrons lose less energy to ions due to the larger ion temperature compared to when DIH is turned off. Hence, while

DIH only affects ions in a direct way, it can affect both neutral (see chapter III) and electron temperatures through collisions.

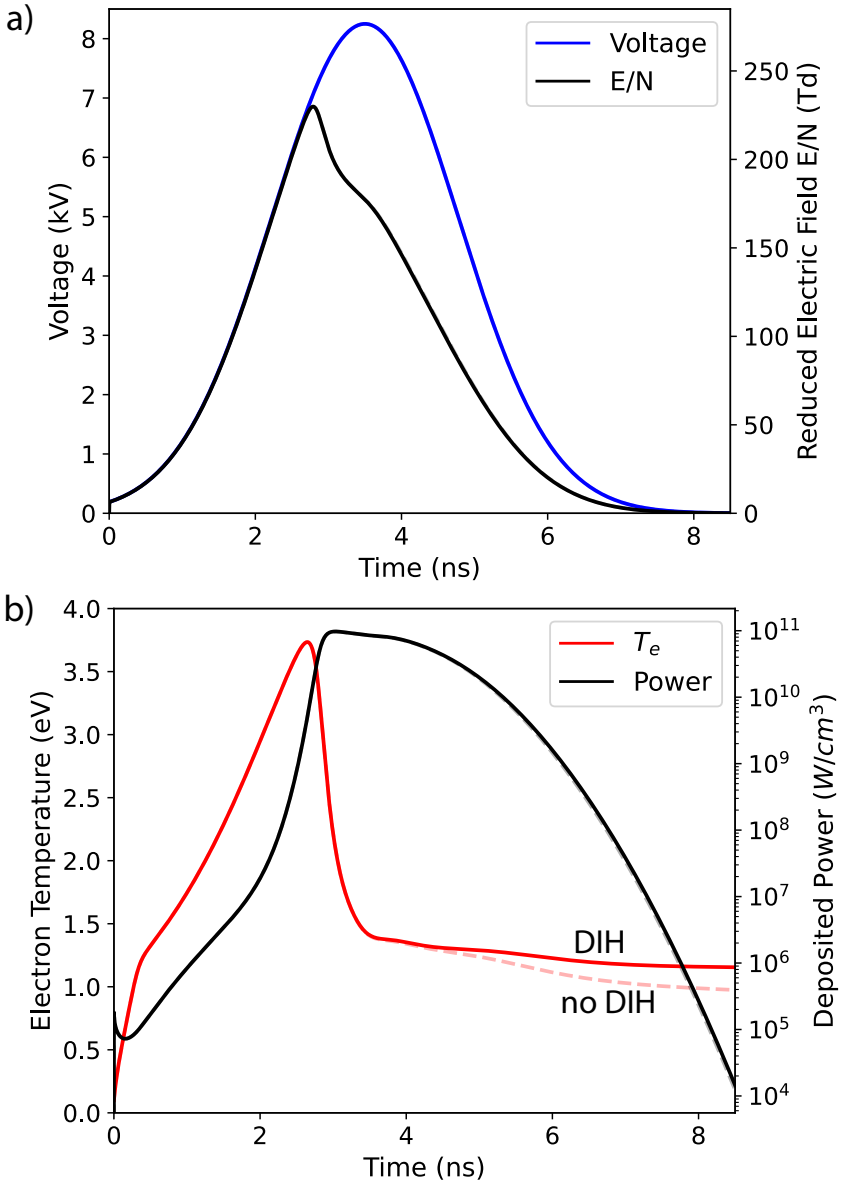

Figure 4.1: a) Gaussian voltage pulse and reduced electric field and b) electron temperature and deposited power per unit volume.

Figure 4.3 shows the evolution of the electron, atomic ion and total molecular ion densities over time in a) linear and b) log scale. Molecular ions are dominant up to 2.5 ns in the discharge, then dissociation of molecular nitrogen and ionization of atomic nitrogen becomes more important, significantly increasing the atomic ion

density. After 3 ns, molecular ions are dissociated and atomic ions become the dominant species. It is observed that during the transient, the case with DIH turned on presents a faster increase in ionization and a slightly larger atomic ion density and smaller molecular ion density. The reason why this happens is that DIH heats ions reducing the temperature difference with electrons. This smaller temperature difference between electrons and ions means that electron-ion Coulomb collisions leads to a smaller change in the electron temperature. This increases the rate coefficients of the inelastic collisions including dissociation and ionization with respect to the case without DIH. Figure 4.2 shows the time evolution of the molecular ions. A rapid increase of the excited states (A,B,C) is observed between 2 and 2.5 ns. Then, the electron density and temperature are large enough to dissociate these states. When DIH is turned on, the density of the excited states B and C decrease faster due to the higher electron temperature and density.

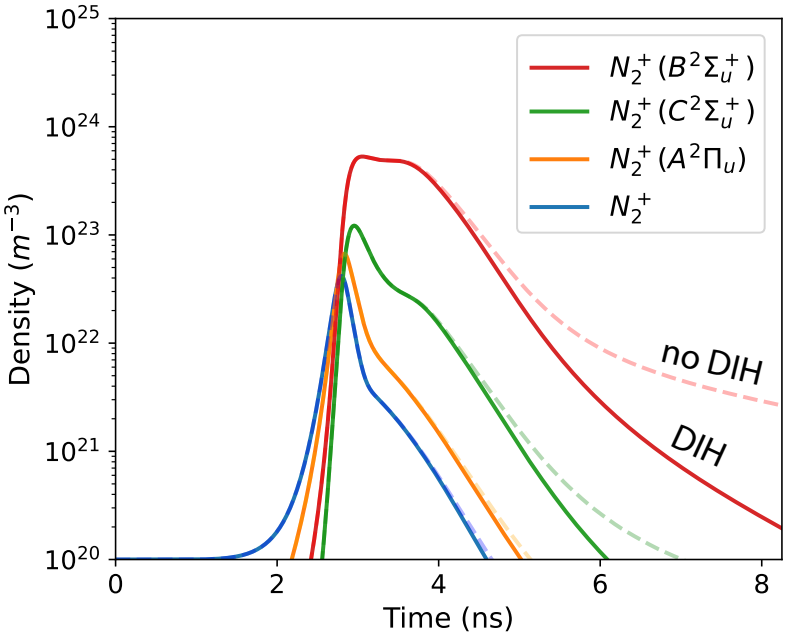

Figure 4.2: Evolution of molecular nitrogen ion densities in ground and excited states.

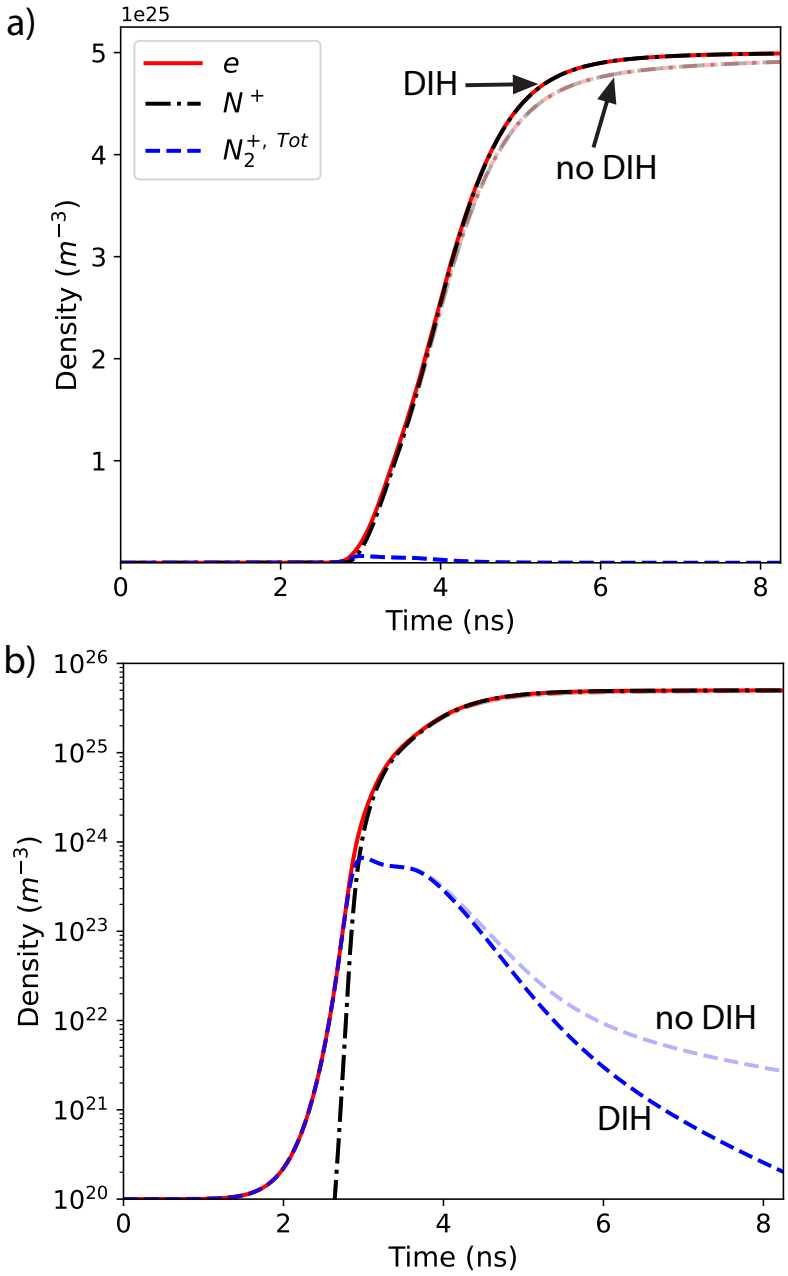

Figure 4.3: Evolution of electron, atomic ion and total molecular ion densities over time in a) linear and b) log scale.

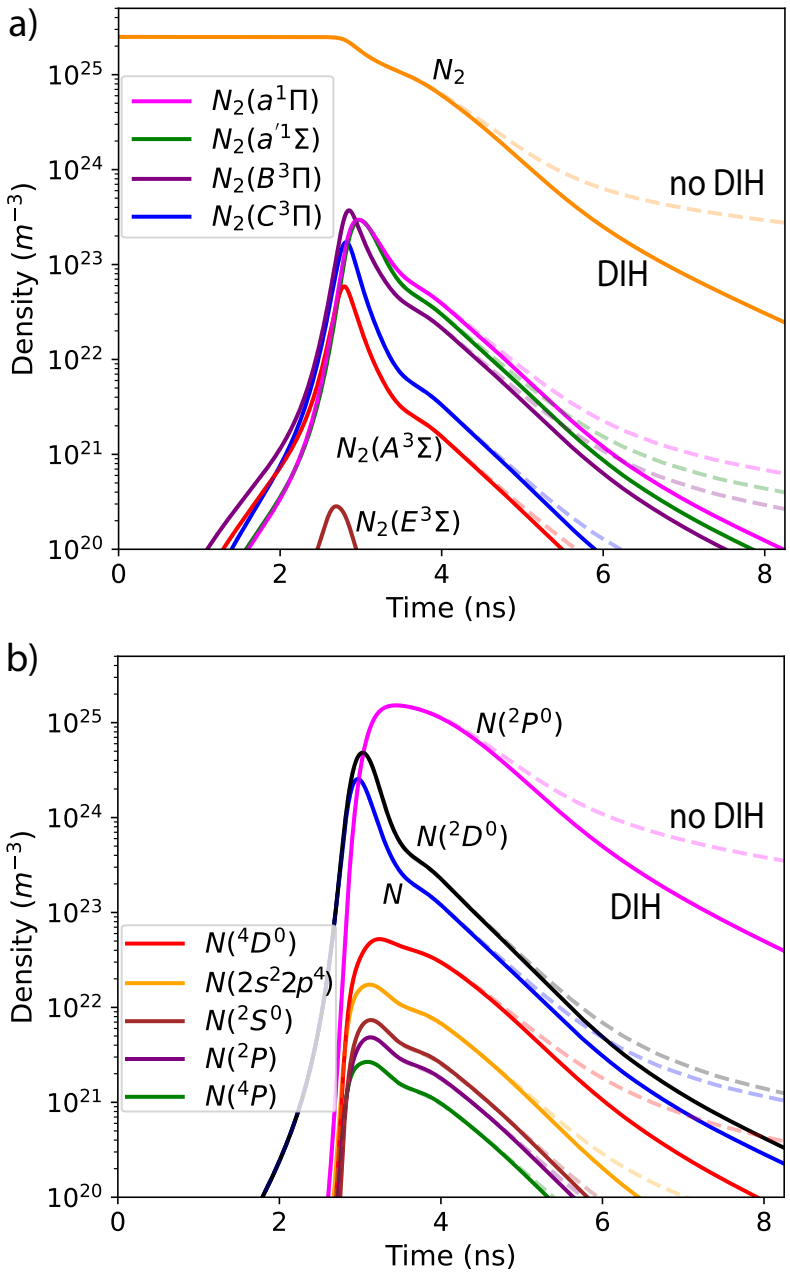

Figure 4.4: Evolution of ground and excited states of a) molecular and b) atomic nitrogen.

Figure 4.4 a) shows the evolution over time of the ground and excited states of molecular nitrogen. The total molecular nitrogen density remains constant for up to 2.5 ns in the discharge until it decreases due to dissociation. The ground state of N_2 is the dominant species over the excited states. In the same timescale there is

a build up of concentration of the excited states with $N_2(a^1, a', B)$ being the most important ones, followed by dissociation after 2.5 ns. The increase in the population of the excited states of N_2 follows the same profile as the increase in the molecular ion densities, indicating that the ionization pathway of N_2 happens mostly through electron impact of the excited states. The highest energy level $N_2(E^3\Sigma)$ has the lowest concentration, due to the smaller electron impact excitation cross section [93]. Similarly, figure 4.4 b) shows the evolution over time of the ground and excited states of atomic nitrogen. The present model includes seven different excited states of atomic nitrogen as shown in tables 4.1 and 4.5. There is an abrupt increase in the density of both ground and excited states of N around 2.5 ns, due to the large dissociation rate observed in the same timescale. The dominant species is $N(^2P^0)$, which corresponds to the second excited state of atomic nitrogen. The model used in this work includes multiple electron impact excitation and ionization pathways of atomic nitrogen, which is fundamental to explain large ionization fractions and full ionization at atmospheric pressure as demonstrated in [6, 91]. For both molecular and atomic nitrogen species, when DIH is included, the concentrations decrease faster at longer times due to the higher electron temperature and density as described before.

Figure 4.5 shows the evolution of the ion and neutral gas temperatures with and without DIH. As expected from MD simulations described in chapter III, at atmospheric pressure both ion and neutral species are practically at equilibrium on a ns timescale and any change in one of the temperatures is going to be rapidly equilibrated through collisions with the other species. A rapid increase in both temperatures is observed at around 3 ns, due to both DIH and dissociation. When DIH is turned on, the ion and gas temperatures are approximately 20% larger at the end of the simulation. This is in accordance with what is observed in the evolution of the electron temperature shown in figure 4.1 since, full ionization is reached and the electron ion equilibration timescale is shorter than the duration of the pulse, leading to thermal-

ization [91]. This thermalization occurs due to the large electron-ion elastic collision frequency at such high electron densities.

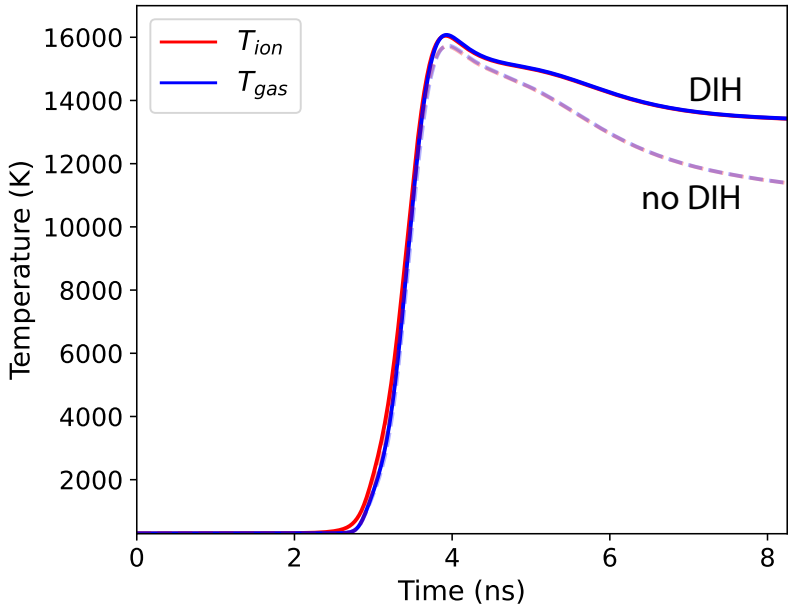

Figure 4.5: Evolution of ion and neutral gas temperatures as function of time.

The different contributions to the rate of increase of the ion temperature are shown in figure 4.6 a). The major contribution to the ion temperature comes from elastic collisions with electrons, followed by disorder induced heating. Again, this is due to the large electron ion collision frequency once the ion and electron densities become significant ($\geq 10\%$). Charge exchange collisions have a negligible effect on both ion and neutral gas temperatures. The main energy loss mechanism for ions is elastic collisions with the neutral species. Figure 4.6 b) shows the different contributions to the rate of change of the neutral gas temperature. The most important heating mechanism for the neutral gas up to 4 ns into the discharge is elastic collisions with ions, followed by dissociation. Here it is important to remark that dissociation is the dominant mechanism that directly heats neutrals, since the gas temperature increase due to collisions with ions indirectly comes from a combination of ion heating due to electron-ion collisions and DIH. After 4 ns, a reverse process is observed, where

neutral species lose energy due to collisions with ions. This is due to the decrease in the ion temperature due to collisions with electrons, since electrons lose energy due to electron impact dissociation of N_2 and they are at equilibrium with ions due to the large electron density. It is important to remark that at large ionization fractions, quenching becomes irrelevant as a source of gas heating, being orders of magnitude below dissociation and elastic collisions between neutrals and ions. Furthermore, elastic collisions between electrons and neutral species do not contribute significantly to gas heating. Finally, the difference between including DIH or not is that when DIH is turned on, there is a larger rate of gas heating due to dissociation since electrons have more available energy which increases the dissociation rates as well as other inelastic processes.

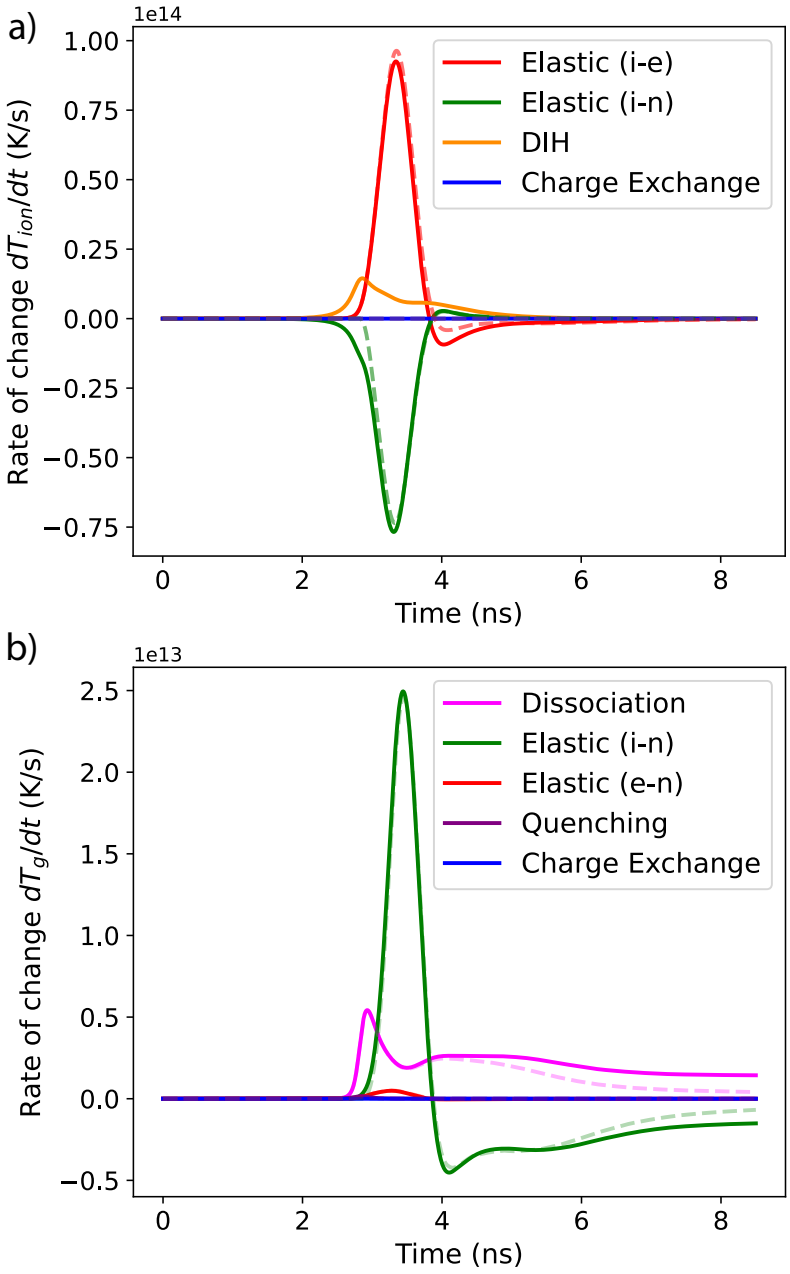

Figure 4.6: Rate of increase dT/dt for a) ion and b) neutral gas temperatures from different contributions.

4.4.1 Varying the reduced electric field

Here, the amplitude of the applied voltage pulse is changed such that it results in different reduced electric fields in the simulations. Figure 4.7 shows a) the final fractional dissociation δ and b) the final electron density with and without DIH as

function of $E^{\max}/N_0$ where $E^{\max}$ is the electric field that corresponds to the voltage pulse amplitude and N_0 is the initial total gas density. The difference between with and without DIH is that DIH helps to slightly increase the dissociation and ionization fractions. This happens because when DIH becomes relevant ($x_i \geq 10\%$), ions are at equilibrium with electrons and any increase in the ion temperature due to DIH increases the available energy of electrons for different inelastic collisions with the neutral gas, including dissociation and ionization. While this difference is not significant at atmospheric pressure the following section shows that at larger pressure it becomes more important due to the scaling of DIH with the total ion density.

Figure 4.8 shows the electron and gas temperatures as function of the reduced electric field with and without DIH. At large ionization fractions the temperatures are at equilibrium due to the large electron density. Between 200 and 250 Td, there is not a significant change in the electron and gas temperature, since all the additional power goes to inelastic processes, including dissociation and ionization 4.7. At near full ionization DIH increases the final temperature by approximately 20%.

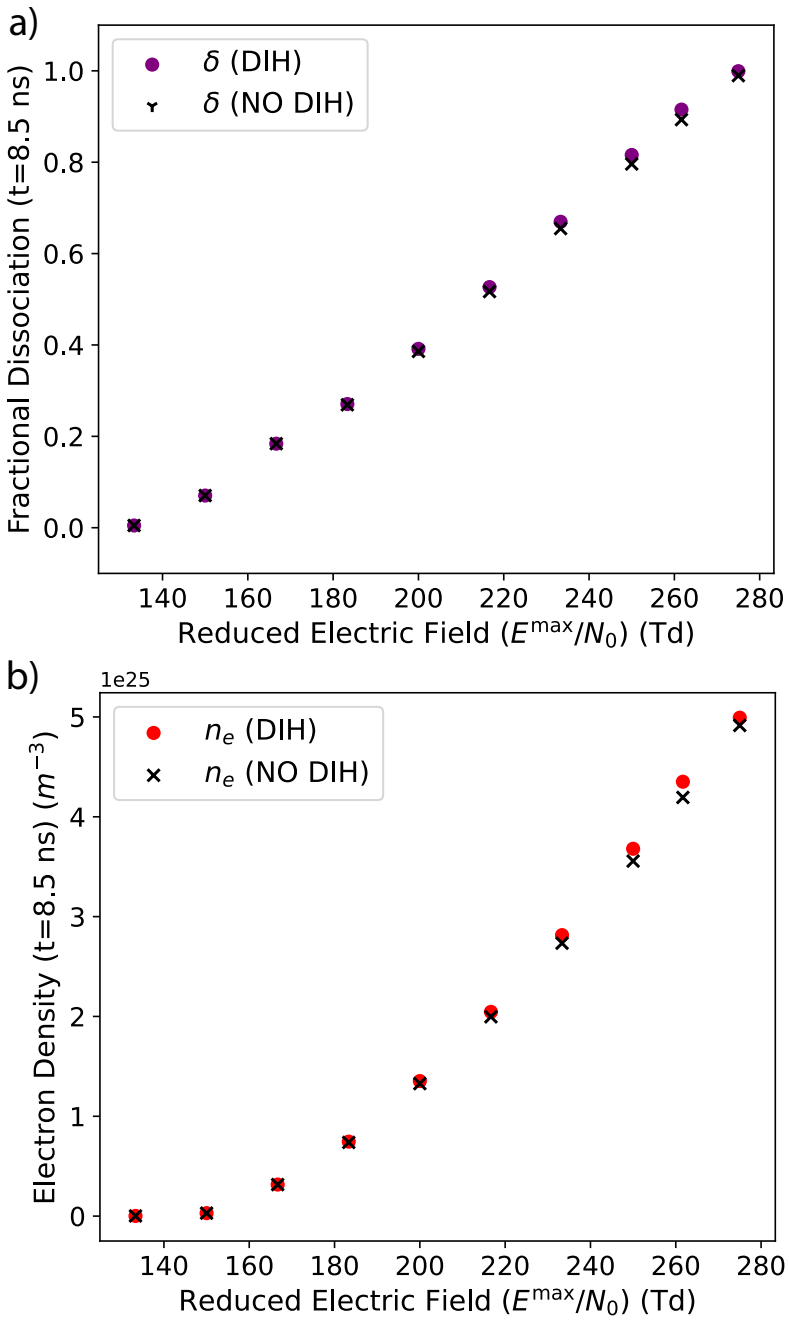

Figure 4.7: a) Final fractional dissociation δ and b) final electron density with and without DIH as function of $E^{\max}/N_0$.

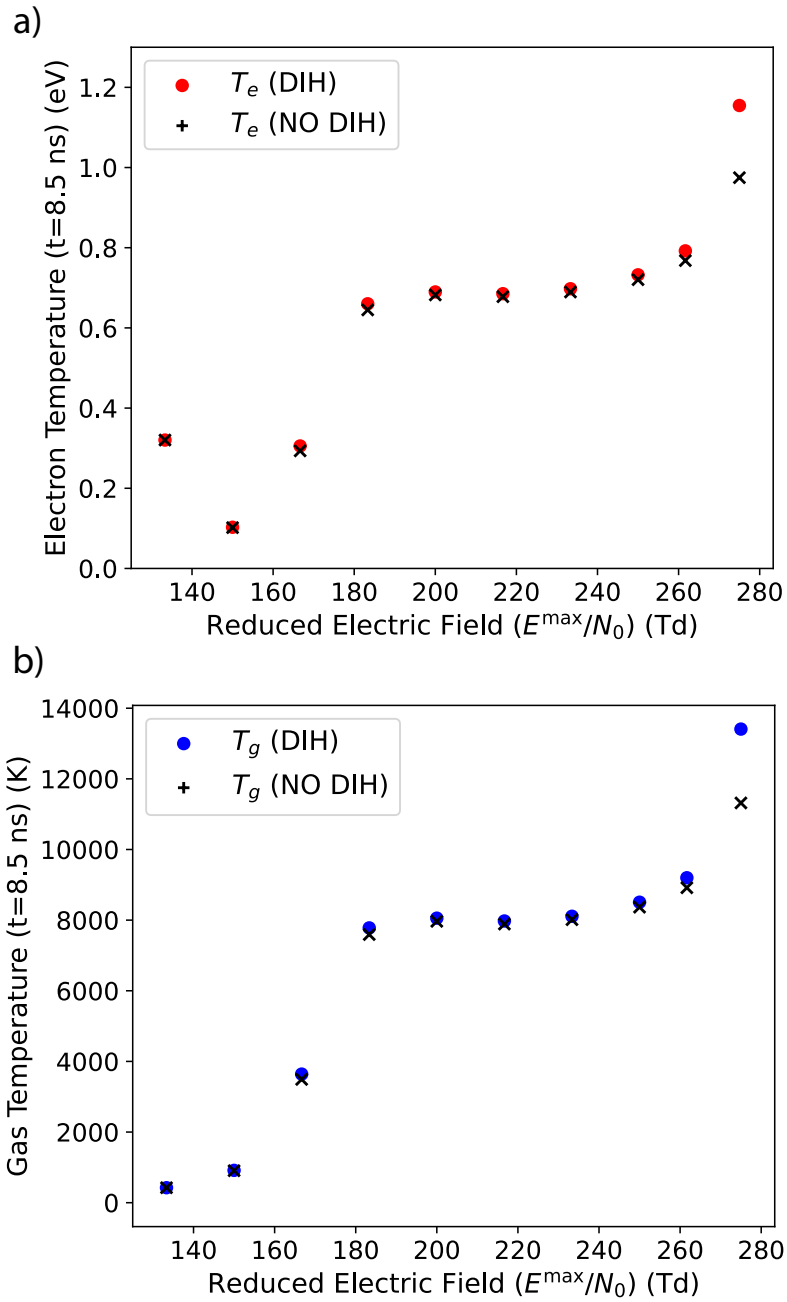

Figure 4.8: a) Electron and b) gas temperatures with and without DIH as function of E^{max}/N_0.

4.5 Results at 10 atmospheres

While the reaction set used in this work does not include three body reactions that can be important at larger pressures, our objective here is to give a simple comparison

between DIH and gas heating mechanisms as well as its potential influence in plasma chemistry. Here we show that, due to the scaling of disorder induced heating with the ion density, it becomes more important at pressures above one atmosphere. Figure 4.9 a) shows the Gaussian voltage pulse and the reduced electric field at ten atmospheres. Since both the amplitude of the pulse and initial pressure are increased by a factor of 10 when compared to atmospheric pressure, the reduced electric field has the same profile. The difference between the voltage pulse and the reduced electric field is due to dissociation of molecular nitrogen. Figure 4.9 b) shows the evolution of the electron temperature and deposited power per unit volume with and without disorder induced heating. As shown, when DIH is turned on, the final temperature is 60% larger. This difference is substantially larger than what was observed at atmospheric pressure. This is because when full ionization is reached at a larger pressure, the final total ion density is 10 times larger and DIH scales with a power of 1/3 of the ion density. This is, the energy released per ion by DIH increases with the total ion density; see section 3.6.

Figure 4.10 a) shows the evolution of the ion and gas temperatures. When DIH is turned on, the final temperature is 60% larger, the same temperature increase is seen the electron temperature because fast thermalization is induced by the elastic electron–ion collisions [91]. Figure 4.10 b) shows the evolution of electron, atomic ion and total molecular ion densities. When DIH is turned on, full ionization is reached faster, due to the excess energy that helps to increase the dissociation and ionization rates. Here, the difference is more noticeable than at atmospheric pressure, due to the scaling of DIH with the ion density.

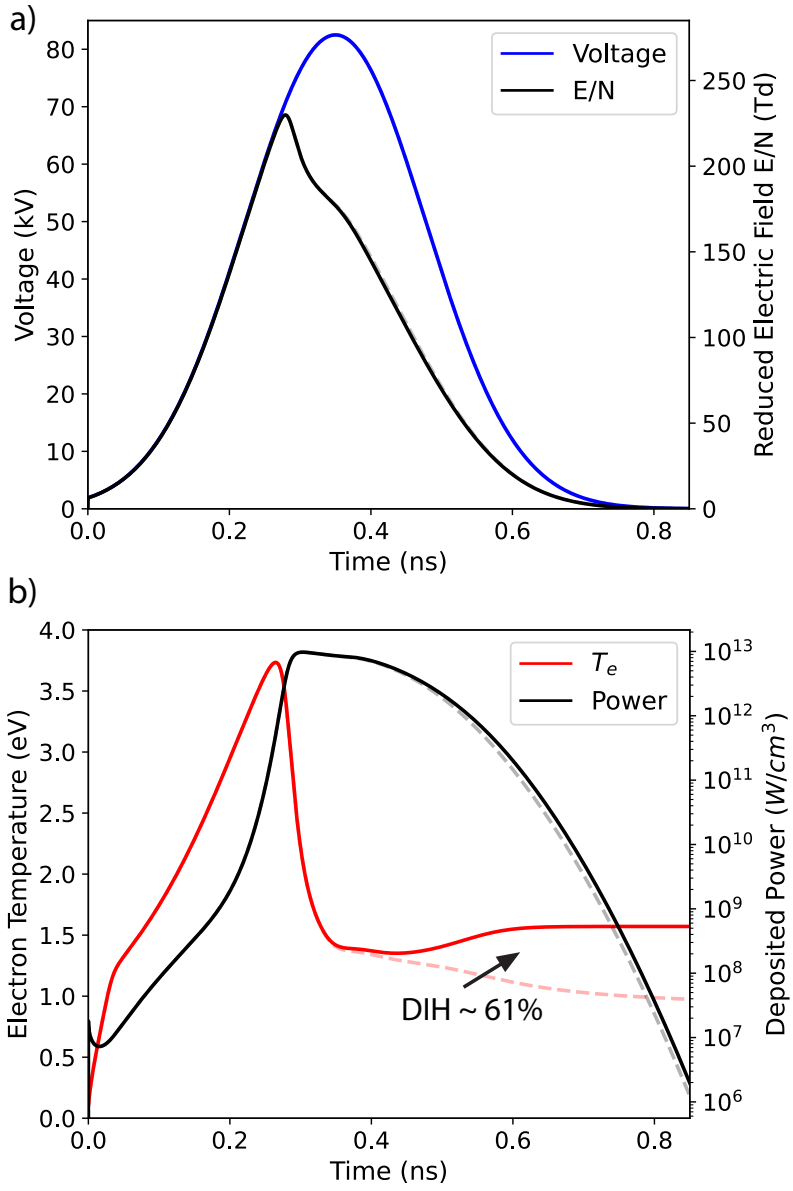

Figure 4.9: a) Evolution of Gaussian voltage pulse and reduced electric field and b) electron temperature and deposited power per unit volume as function of time with and without DIH at 10 atmospheres.

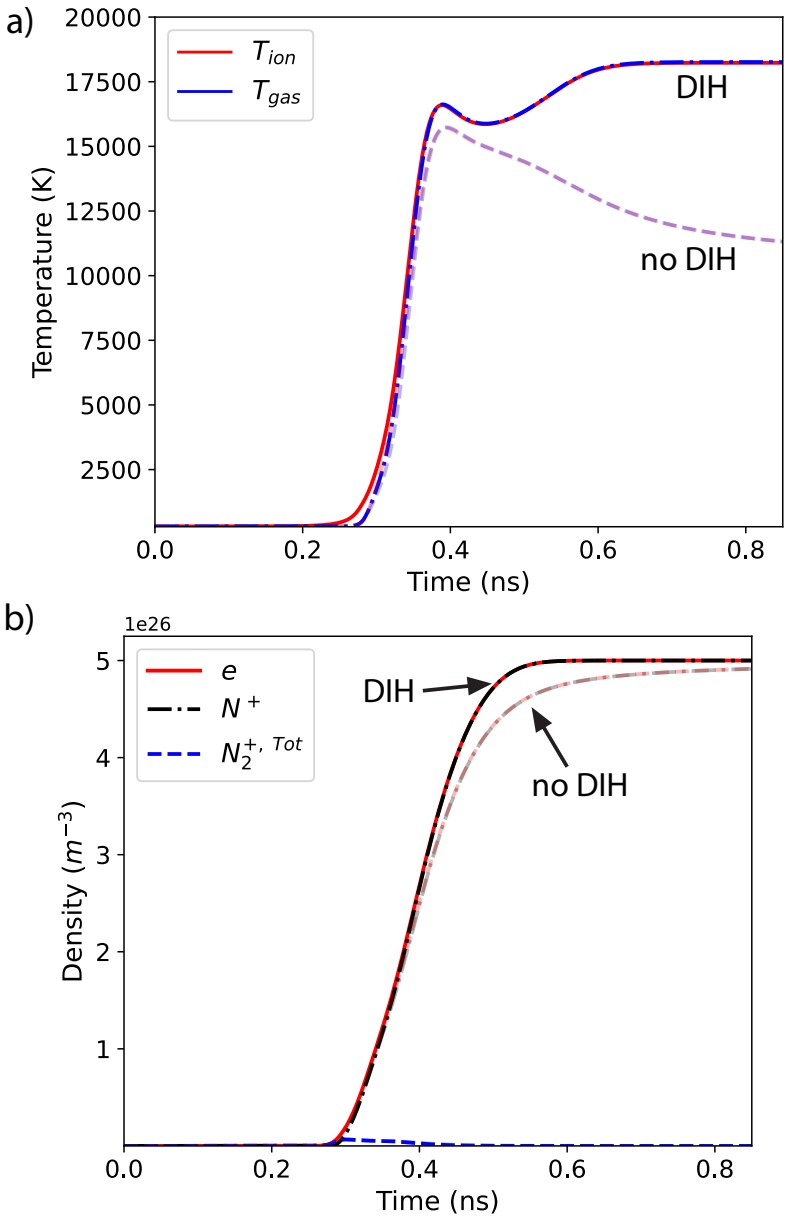

Figure 4.10: a) Evolution of ion and neutral gas temperatures and b) evolution of charged species densities with and without DIH at 10 atmospheres.

The rate of increase of ion and neutral gas temperatures are shown in figures 4.11 a) and b) respectively. The main contribution to the ion temperature increase is due to elastic electron-ion collisions, as was observed at atmospheric pressure. However, DIH contributes significantly more due to the larger ion density. The main energy loss mechanism for ions is elastic collisions with the neutral gas. Charge

exchange collisions have a negligible effect on the ion temperature. The neutral gas temperature increases predominantly due to elastic collisions with ions up to 0.4 ns. Then, ions lose energy to electrons through elastic collisions, which reverses the rate of change of the gas temperature. The main direct source of gas heating is dissociation, which is enhanced when DIH is turned on due to the larger electron temperature and thus electron impact dissociation rates. This difference is more noticeable than at atmospheric pressure due to the scaling of DIH with the ion density. As at atmospheric pressure, the contribution of quenching to the neutral gas heating is also negligible at 10 atmospheres, since electrons have enough energy in this particular case to significantly increase the dissociation and ionization fraction. Hence, the molecular nitrogen excited states don't live long enough to release energy due to quenching. This is contrary to what happens at significantly lower pressures or ionization fractions [21].

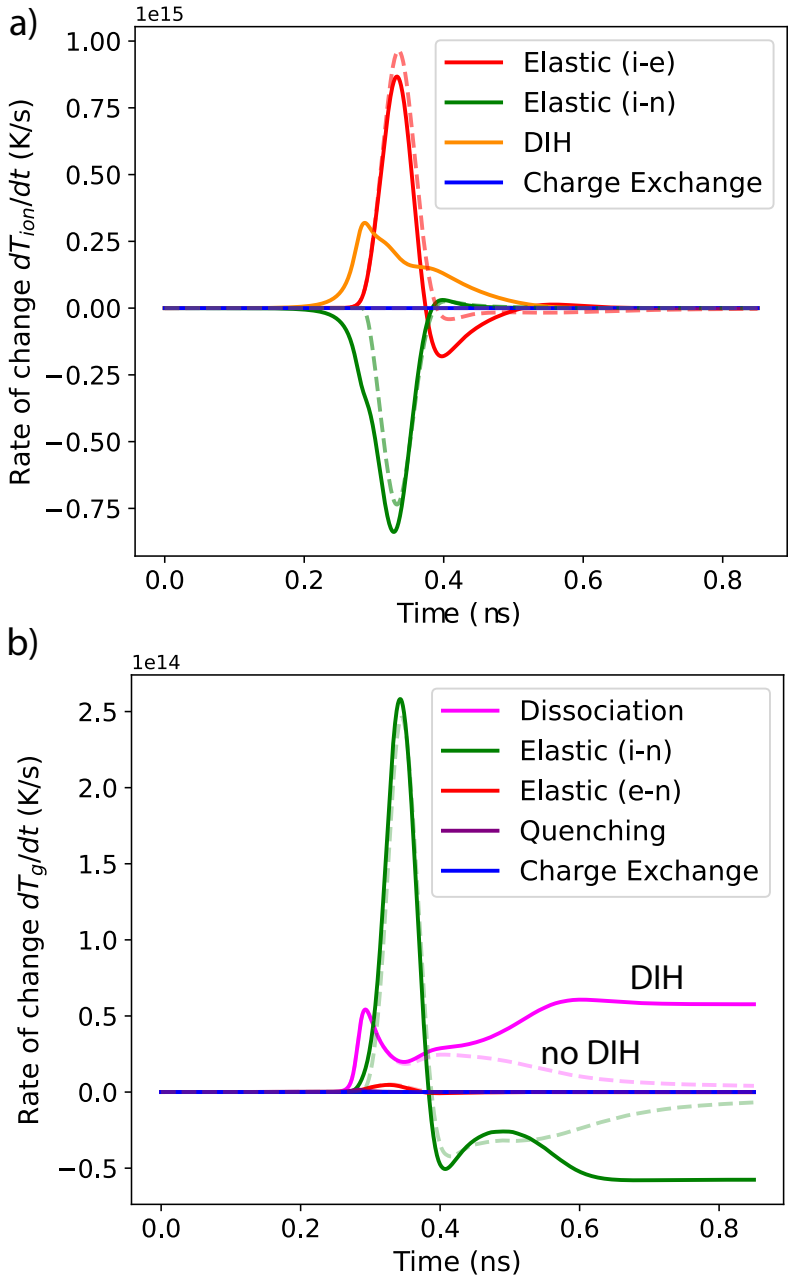

Figure 4.11: Rate of increase of a) ion and b) neutral gas temperatures with and without DIH at 10 atmospheres.

4.5.1 Varying the reduced electric field

Figure 4.12 shows the final value of a) fractional dissociation and b) electron density as a function of the reduced electric field with and without DIH. When compared to the atmospheric pressure case, here the difference is more noticeable in particular

between 220 and 260 Td. In this range of reduced electric fields, DIH combined with thermalization due to the large electron density, provides a mechanism for enhanced dissociation and ionization. This effect increases with pressure due to the scaling of DIH with the ion density. Therefore, it is expected to increase and become even more important at larger pressures.

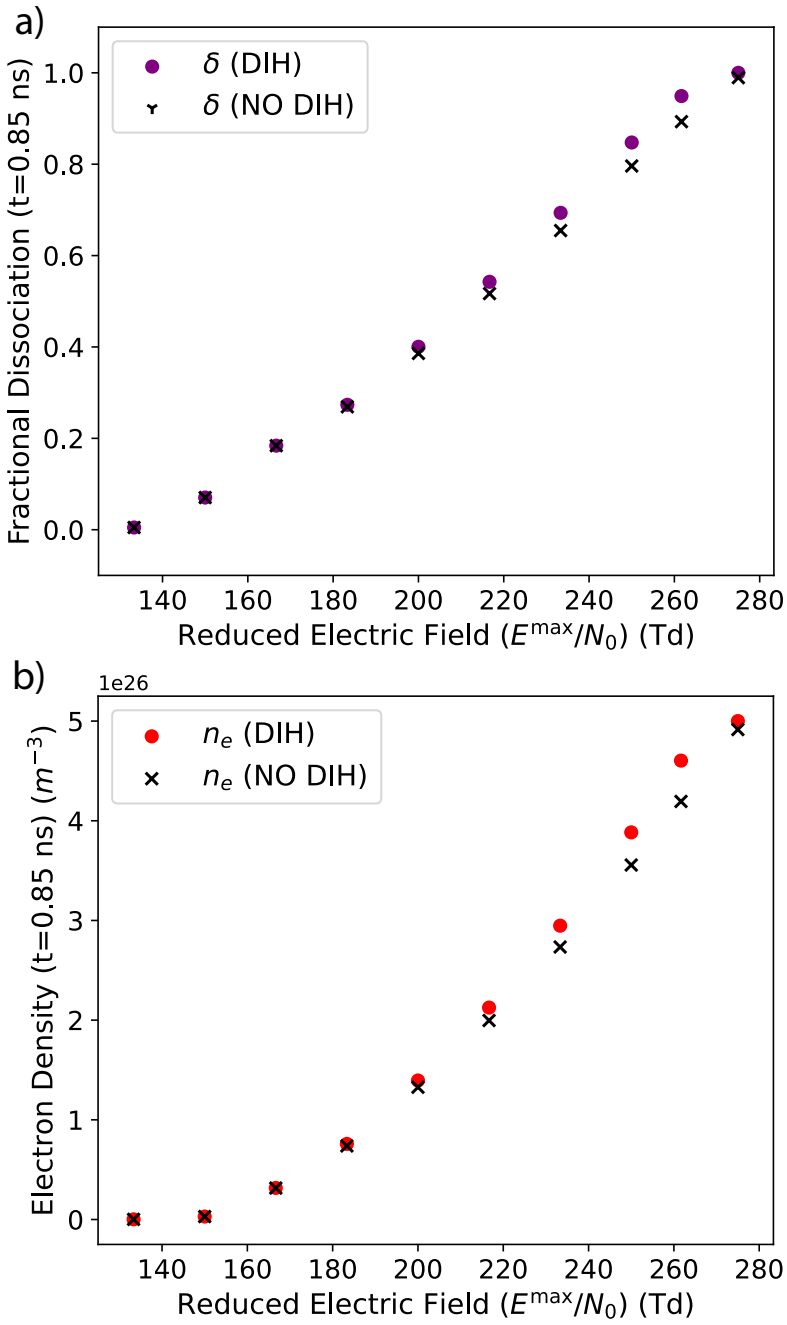

Figure 4.12: a) Fractional dissociation and b) electron density as function of the reduced electric field at an initial neutral gas pressure of 10 atmospheres.

4.6 Implications of disorder induced heating in plasma chemistry

The main takeaway is that disorder induced heating is important when the ionization fraction reaches values above 10% at atmospheric and larger pressures. DIH can significantly affect the final temperature, especially at larger pressures since it scales with the ion density to a power of 1/3. In the same regime, thermalization between electrons and ions occurs rapidly due to the large elastic collision frequency [91]. This makes DIH influence the electron temperature indirectly, providing a physical mechanism that enhances the rate coefficients of electron impact inelastic processes such as dissociation and ionization. Thus, DIH can potentially influence the plasma chemistry in an indirect way in this regime. It is important to remark that the energy released per ion due to DIH increases with the ion density, while the energy released due to dissociation of molecules or quenching does not depend on the pressure. This means that the relative importance of DIH to the already well studied gas heating mechanisms [21] increases as the pressure gets larger. This statement maintains as long as the neutral-neutral and ion-neutral interactions are weakly coupled which has a limitation as the pressure increases above 1000 atmospheres; see figure 1.3. Hence, the potential influence of DIH on the plasma chemistry can have a sweet spot at intermediate pressures between one atmosphere and 1000 atmospheres.

Finally, the analysis presented in this work concentrated on molecular nitrogen. While DIH does not depend on the chemistry in a direct way since it only depends on the overall increase in the total ion density, its relative importance to other heating mechanisms as well as its potential influence on the plasma chemistry does depend on the gas composition. As an example, molecular oxygen requires less energy to dissociate compared to nitrogen and discharges with noble gases can have completely different excitation and ionization pathways and required energies. Hence, DIH could

be more important in gases where less energy is lost in inelastic processes.

CHAPTER V

Influence of strong Coulomb coupling on diffusion in atmospheric pressure plasmas

Ion diffusion in atmospheric pressure plasmas is examined and particular attention is paid to the fact that ion-ion interactions can be influenced by strong Coulomb coupling. Three regimes are identified. At low ionization fractions ($x_i \lesssim 10^{-6}$), standard weakly correlated ion-neutral interactions set the diffusion rate. At moderate ionization fractions ($10^{-6} \lesssim x_i \lesssim 10^{-2}$) there is a transition from ion-neutral to ion-ion collisions setting the diffusion rate. In this regime, the effect of strong Coulomb coupling on ion-ion collisions is accounted for by applying the mean force kinetic theory. Since both ion-neutral and ion-ion interactions contribute a comparable amount to the total diffusion rate, models (such as particle-in-cell or fluid) must account for both contributions. At high ionization fractions ($x_i \gtrsim 10^{-2}$), strongly correlated ion-ion collisions dominate and the plasma is heated substantially by disorder-induced heating. The temperature increase due to disorder-induced heating strongly influences the ion diffusion rate. This effect becomes even more important, and occurs at lower ionization fractions, as the pressure increases above atmospheric pressure. In addition to ion diffusion, disorder-induced heating affects the neutral gas temperature, therefore influencing the neutral diffusion rate.

Model predictions are tested using molecular dynamics simulations, which in-

cluded a Monte Carlo collision routine to simulate the effect of ion-neutral collisions at the lowest ionization fractions. The model and simulations show good agreement over a broad range of ionization fractions. The results provide a model for ion diffusion, on a wide range of ionization fractions and pressures, solely considering the elastic contribution to the diffusion coefficient - as an illustration of how strong Coulomb coupling influences diffusion processes in general.

5.1 Theoretical model

In this section, we first summarize the approach for computing the diffusion rates based on an arbitrary potential between species s and s'. [83] Section 5.1.1 describes the calculation of the total ion and neutral diffusion coefficients from the contribution of the interdiffusion coefficients given by ion-neutral, ion-ion and neutral-neutral interactions. A method for calculating the neutral-neutral, ion-neutral, and ion-ion contributions is described in sections 5.1.2, 5.1.3, and 5.1.4 respectively. Finally, the results are applied to assess the ion-neutral and ion-ion collision frequency parameter space and the total ion and neutral diffusion coefficients for a broad range of ionization fractions at atmospheric pressure in section 5.1.6.

5.1.1 Theoretical framework

The following summarizes the results of the Chapman-Enskog solution of the Boltzmann equation to compute diffusion coefficients. Although the Boltzmann equation is not expected to apply to the strongly coupled ion-ion interaction, the same basic framework is easily adapted to the mean force kinetic theory [52, 101] that will be used to model the ion-ion component, as described in section 5.1.4. The Chapman-Enskog solution is described in textbooks [83, 102]. Here, we quote the results.

The Chapman-Enskog solution solves the Boltzmann equation as a perturbation

from equilibrium by applying a polynomial expansion of the velocity distribution function. Here, we make use of the first-order term in that expansion. At this lowest order, the total diffusion coefficient for species s in a plasma consisting of two species (s and s') is [83]

$$D_s = \left(\frac{x_s}{D_{ss}} + \frac{x_{s'}}{D_{ss'}} \right)^{-1}, \tag{5.1}$$

where $x_s = n_s/n$ is the concentration of species s, $x_{s'} = n_{s'}/n$ is the concentration of species s' and $n = n_s + n_{s'}$ is the total number density. The mobility and diffusion coefficients of charged species s are intrinsically linked. This connection is formally described by the Einstein relation: $D_s = k_B T_s \mu_s / q_s$, where μ_s is the mobility coefficient, k_B is the Boltzmann constant, and q_s and T_s are the charge and temperature of species s, respectively. In the rest of the chapter, the analysis will primarily focus on the diffusion coefficients. Here, electron interactions are not included in the analysis following the argument discussed in Ref. [2]; since electrons are much hotter than ions and neutrals, and are in the weakly coupled regime, they act as a non-interacting charge-neutralizing background. In equation (5.1), the interdiffusion coefficient between species s and s' is

$$D_{ss'} = \frac{\sqrt{\pi}}{2} \frac{x_{s'}}{\chi_{ss'} m_{ss'} \nu_{ss'}}, \tag{5.2}$$

where

$$\nu_{ss'} = \frac{4 n_{s'} \bar{v}_{ss'}}{3} \int_0^\infty d\xi \; Q_{ss'}^{(1)}(\xi) \xi^5 e^{-\xi^2}, \tag{5.3}$$

is the momentum-transfer collision frequency,

$$Q_{ss'}^{(1)} = 2\pi \int_0^\infty [1 - \cos(\beta)] b db, \tag{5.4}$$

is the momentum transfer cross section, and

$$\beta = \pi - 2b \int_{r_0}^{\infty} \frac{dr/r^2}{\sqrt{1 - \frac{b^2}{r^2} - \frac{2\phi_{ss'}(r)}{m_{ss'}u^2}}} \tag{5.5}$$

is the scattering angle. In these equations, $m_{ss'} = m_s m_{s'}/(m_s + m_{s'})$ is the reduced mass, T is the temperature (assumed to be approximately equal for ions and neutrals in the Chapman-Enskog description), $\bar{v}_{ss'}^2 = 2k_BT/m_s + 2k_BT/m_{s'}$, $\xi = u/\bar{v}_{ss'}$ and $u = |\mathbf{v} - \mathbf{v}'|$ is the relative velocity between two particles in a binary interaction. In equation (5.5), b is the impact parameter, r_0 is the distance of closest approach obtained from the largest root of the denominator, and $\phi_{ss'}(r)$ is the potential of interaction between species s and s'. The distinction between weakly correlated neutral-neutral or ion-neutral interactions and strongly correlated ion-ion interactions enters through how the interaction potential $\phi_{ss'}$ and collision enhancement factor $\chi_{ss'}$ are treated in each case, as described in sections 5.1.2, 5.1.3, and 5.1.4.

5.1.2 Neutral-neutral collisions

Neutral-neutral interactions are short-range and weakly coupled at atmospheric pressure [2]. A common model for the interatomic interaction is the Lennard-Jones potential defined in equation 1.8 [103]

$$\phi_{\mathrm{LJ}}(r) = 4\epsilon \left[\left(\frac{\sigma}{r}\right)^{12} - \left(\frac{\sigma}{r}\right)^{6} \right], \tag{5.6}$$

where ϵ is the depth of the potential well and σ is the distance at which the potential energy is zero. The accepted values for Ar are $\sigma = 3.4 \times 10^{-10}$ m and $\epsilon = k_B 120(\mathrm{K})$ [42]. A cutoff distance of 500σ. Since neutral-neutral interactions are weakly coupled, the traditional Boltzmann-based approach based on the bare interaction potential from equation (1.8) is valid and the collision enhancement factor in equation (5.2) is

negligible: $\chi_{nn} = 1$.

5.1.3 Ion-neutral collisions

Like neutral-neutral interactions, ion-neutral interactions are short-range and weakly coupled at atmospheric pressure. The bare (unscreened) charged induced dipole potential was used to model ion-neutral interactions 3.1[42]

$$\phi_{\text{ind}}(r) = \frac{q^2}{8\pi\epsilon_0}\frac{\alpha_R a_0^3}{r^4}\left(\frac{r_\phi^8}{3r^8} - 1\right), \tag{5.7}$$

where $r_\phi = 0.133a_{in}$ and $a_{in} = (3/4\pi n_{in})^{1/3}$ with $n_{in} \approx x_i n_i + x_n n_n$, is the average interparticle spacing between ions and neutrals and $\alpha_{\text{R}} = 11.08$ for Ar [56]. Here, r_ϕ is a parameter that is implemented in the MD simulations to prevent particles getting to close to one another to resolve with a finite timestep. It is chosen to be small enough so as not to influence the resulting diffusion coefficient in either the theoretical model calculations or MD simulations. The specific value of $r_\phi = 0.133a_{in}$ comes from a numerical convergence test described in [2] and in section 3.1. Here, the Boltzmann-based approach is expected to be valid since the ion-neutral interaction is in a weakly coupled regime; see Ref. [2]. In addition, since the ion-neutral interactions are weakly coupled, the collision enhancement factor in equation (5.2) is negligible: $\chi_{in} = 1$.

5.1.4 Ion-ion collisions

The Coulomb coupling parameter for ion-ion interactions can be as large as 10 at atmospheric pressure [2]. Hence, the binary collision approach of the Boltzmann equation is no longer valid and strong ion-ion correlations need to be accounted for. To model this regime, we apply the mean force kinetic theory. [52, 104] This is a recently developed generalization of the Boltzmann equation that has been shown to accurately describe collisions and the associated transport into the strongly coupled

regime (generally for $\Gamma \lesssim 20$) [105, 106, 107]. The results of this model fit within the Champan-Enskog framework described previously, but where the interaction potential in equation (5.5) is the potential of mean force

$$\phi \rightarrow w^{(2)}(r) = -k_B T \ln\left[g(r)\right]. \tag{5.8}$$

Here, $g(r)$ is the ion-ion pair correlation function. The potential of mean force represents the interaction potential between two particles at a distance r averaging all the equilibrium configurations of the other $N-2$ particles of a system. The potential of mean force is related to the pair correlation function by equation (5.8) and includes many-body effects of the background plasma including screening and correlations [52]. In order to solve for $[g(r)]$, the hypernetted chain approximation was used as a closure for the Ornstein–Zernike equation [108],

$$g(\mathbf{r}) = \exp\left[-\frac{\phi(\mathbf{r})}{k_B T} + n_i \int c(|\mathbf{r}-\mathbf{r}'|)h(\mathbf{r}')d\mathbf{r}'\right] \tag{5.9a}$$

$$\hat{h}(\mathbf{k}) = \hat{c}(\mathbf{k})[1 + n_i \hat{h}(\mathbf{k})] \tag{5.9b}$$

where $\phi(r)$ is the bare Coulomb potential, n_i is the ion density, T the temperature, $h(r) = g(r) - 1$ and $\hat{h}(\mathbf{k})$ denotes the Fourier transform of $h(r)$. The hypernetted chain approximation has been shown to be an accurate closure to model the radial distribution function for a one component plasma across different coupling regimes [104]. It is worth noting that at weak coupling the potential of mean force is the usual Debye-Hückel screened potential, but at strong coupling it differs substantially from this, including oscillatory components at nearest neighbor positions. [104] The motivation for comparing with a one component plasma arises from the observation that, in the regimes considered here, electrons and neutrals exhibit weak coupling. Consequently, ion-ion interactions can be treated as an OCP. In addition, the elevated electron temperature makes electron screening of ions negligible, permitting the application of the

bare Coulomb potential for ion-ion interactions, as observed by Shaffer *et al.* [109]

While the potential of mean force accounts for aspects of many-body effects, there is an additional enhancement of the collision frequency associated with the reduction of space that particles can occupy because ion centers cannot be closer than their physical diameter plus an additional distance due to the Coulomb repulsion [83]. This exclusion volume, characteristic of the short range correlations in ion-ion interactions, depends on the Coulomb coupling strength of the ion species. The Enskog correction factor in the interdiffusion coefficient equation (5.2) accounts for this exclusion radius surrounding individual ions associated with Coulomb repulsion [101, 110]. The Enskog correction factor for ion-ion collisions can be calculated with the virial coefficients of the thermodynamic equation of state for hard spheres,

$$\chi_{ii} = 1 + 0.6250\, b\rho + 0.2869\, (b\rho)^2 + 0.115\, (b\rho)^3 + ... \tag{5.10}$$

where $b\rho$ is the co-volume,

$$b\rho \approx \frac{1}{3}\pi n_i \overline{\sigma}^3 \tag{5.11}$$

and $\overline{\sigma}$ is the effective ion diameter, calculated as $g(r = \overline{\sigma}) = 0.87$, [110] which depends on the Coulomb coupling strength. In this work, the $g(r)$ used to calculate $\bar{\sigma}$ and χ_{ii} was modeled using the hypernetted chain approximation from equations (5.9b) and (5.9b).

5.1.5 Disorder induced heating

Figure 5.1 shows the Coulomb coupling parameter for ion-ion interactions at atmospheric pressure and different ionization degrees using the equilibrium temperature calculated with equation 3.8 which accounts for disorder induced heating. It is well known that the Boltzmann equation breaks down when $\Gamma_{ii} \gtrsim 0.1$, so strong coupling effects are expected to onset for $x_i \gtrsim 10^{-7}$ ($\approx 10^{18}$ m^{-3}) at atmospheric

pressure [57, 58].

It is important to note that the ion-neutral "equilibrium" temperature in equation (3.8) does not consider other potential heating mechanisms found in partially ionized plasmas, such as Joule heating, quenching of electronically excited states, and VT relaxation [2]. The analysis presented here can be expanded to encompass additional heating mechanisms by incorporating their respective contributions to the temperature. Here, we focus attention on the effects that are directly associated with strong Coulomb coupling.

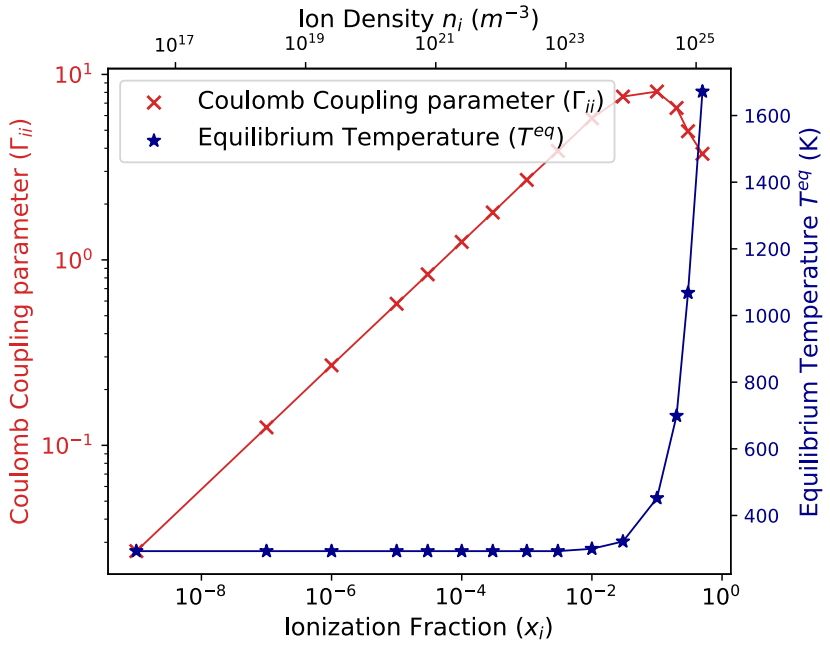

Figure 5.1: Coulomb coupling parameter and equilibrium temperature at atmospheric pressure for different ionization fractions. The temperature used to compute Γ_{ii} is the equilibrium temperature from equation (3.8).

5.1.6 Diffusion coefficients

Considering a partially ionized Ar plasma with single ion and neutral species, the ion diffusion coefficient depends on ion-neutral and ion-ion collisions, as described in equation (5.1). An estimate for which process controls the total diffusion rate is provided by the ratio between the ion-ion and ion-neutral momentum transfer collision

frequencies. This is shown for a range of gas pressure and ionization fractions in figure 5.2. The temperature used for the calculation of the collision frequencies corresponds to the equilibrium temperature from equation (3.8), which accounts for the disorder induced heating.

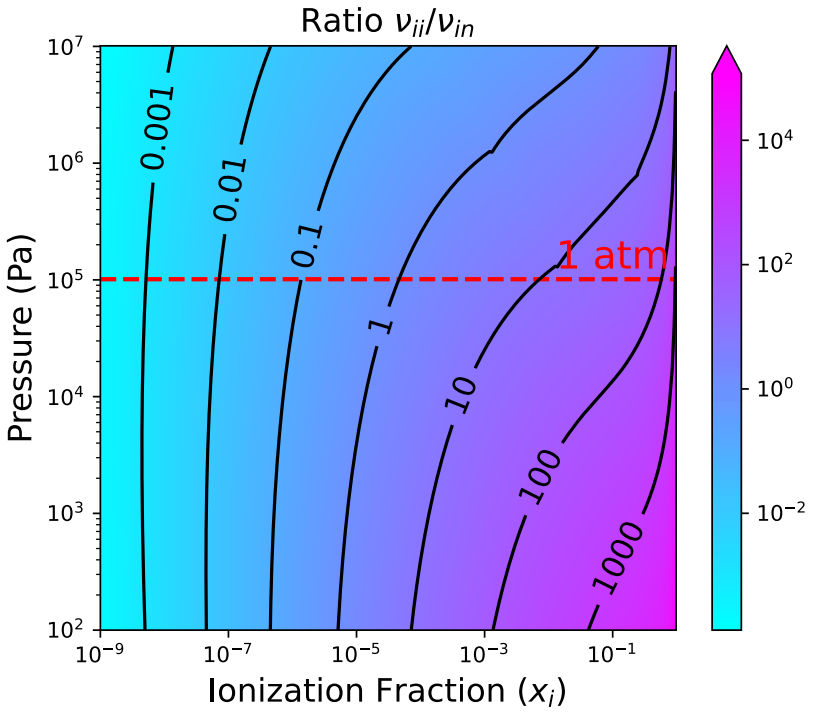

Figure 5.2: Ratio between the ion-ion and ion-neutral collision frequencies in a pressure-ionization fraction parameter space for an Ar plasma. Ion-ion collisions are expected to determine the diffusion rate when this ratio is large.

As shown in figure 5.2, ion-neutral collisions are much more frequent than ion-ion collisions at sufficiently low ionization fraction. For example, at 1 atm, ion-neutral collisions are at least 10 times more frequent than ion-ion collisions when $x_i < 10^{-6}$ ($n_i < 2.5 \times 10^{19}$ m^{-3}). In the other limit, ion-ion collisions are much more frequent than ion-neutral collisions when the ionization fraction is sufficiently large. For example, at 1 atm, ion-ion collisions are at least 10 times more frequent than ion-neutral collisions when $x_i \gtrsim 6 \times 10^{-3}$ ($n_i > 1.5 \times 10^{23}$ m^{-3}). A transition region where both types of interactions contribute to the diffusion rate is expected in the

broad intermediate region ($10^{-6} < x_i < 10^{-3}$). The figure also shows the pressure dependence of these regimes away from atmospheric pressure.

Figure 5.3 shows the ion diffusion coefficient computed from equation (5.1) at atmospheric pressure. It also shows results of the ion-neutral and ion-ion interdiffusion coefficients from equation (5.2), and the total ion diffusion coefficient ignoring the DIH effect (by assuming the temperature is room temperature). This comparison shows that three different regimes are present. First, at small ionization fractions ($x_i \lesssim 10^{-6}$) the ion diffusion coefficient converges to the ion-neutral interdiffusion coefficient, where ion-neutral collisions are dominant. Second, over an intermediate range of ionization fractions from $x_i = 10^{-6}$ to $x_i = 10^{-2}$, both ion-neutral and ion-ion collisions influence the total diffusion coefficient. Within this region, for ionization fractions larger than $x_i = 5 \times 10^{-5}$, ion collisions are more frequent and become the main contribution to the total diffusion. Finally, a third regime is observed for ionization fractions larger than $x_i > 10^{-2}$. Here, ion-ion collisions dominate and the total diffusion coefficient merges with the ion-ion interdiffusion coefficient. In this regime, DIH also causes a significant temperature increase that increases the ion diffusion coefficient substantially.

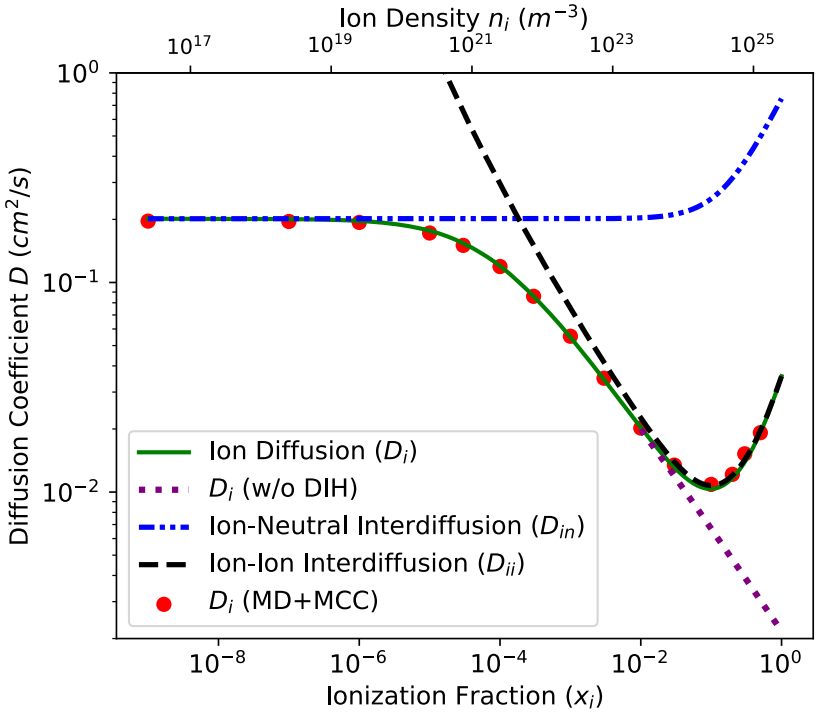

Figure 5.3: Ion diffusion coefficient (green solid line) as a function of ionization fraction. Also shown are the ion diffusion coefficient assuming room temperature (purple dotted line), which neglects the DIH effect, the ion-neutral (blue dash-dotted line) and ion-ion (black dashed line) interdiffusion coefficients. The ion diffusion coefficient obtained from the MD simulations is shown in red dots.

Figure 5.4 shows a comparison of the ion-ion interdiffusion coefficient obtained with the standard Coulomb logarithm (Landau-Spitzer) and with the mean force theory described in 5.1. For ionization fractions smaller than 10^{-6}, both interdiffusion coefficients agree because this corresponds to the weakly coupled regime (see figure 5.1). For ionization fractions larger than 10^{-5}, the interdiffusion coefficient calculated with the standard Coulomb logarithm diverges because the argument of the Coulomb logarithm (i.e., the plasma parameter) approaches 1. This signifies the well-known and dramatic breakdown of the usual plasma theory, which is based on weakly coupled assumptions. [104] On the other hand, the diffusion coefficient calculated from the mean force kinetic theory shows good agreement with the MD data over the entire range of ionization fraction, as shown in figure 5.3. This confirms that strong Coulomb

coupling influences the ion diffusion coefficient for ionization fractions larger than 10^{-6} and these strong correlations that are absent in the currently applied models need to be accounted for.

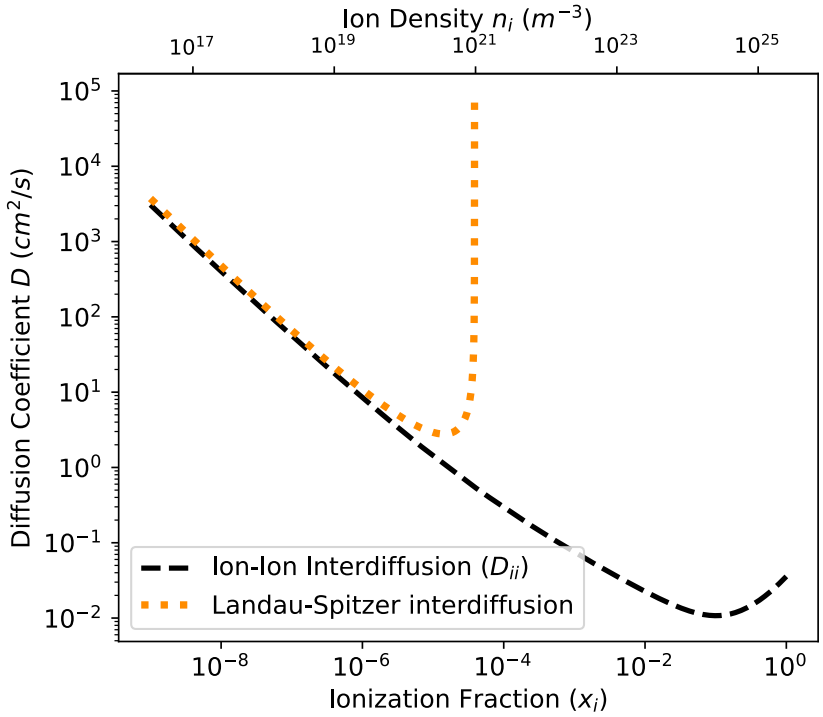

Figure 5.4: Ion-ion interdiffusion coefficient obtained using the Chapman-Enskog solution of the mean force kinetic theory (black dashed line) and using the traditional Landau-Spitzer solution. There is a clear divergence of the diffusion coefficient in the Landau-Spitzer solution as the argument of the Coulomb logarithm approaches zero.

Finally, using equation (5.1), the neutral diffusion coefficient was computed accounting for neutral-ion and neutral-neutral collisions with the equilibrium temperature from equation 3.8. Figure 5.5 shows the total neutral diffusion coefficient and its contributions due to neutral-ion and neutral-neutral collisions. The temperature increase for ionization fractions $x_i > 10^{-2}$ at atmospheric pressure is not negligible, as shown in figure 5.1. This increase affects the total neutral diffusion coefficient, leading to a considerable rise compared to the expected value without accounting for the DIH effect. These results indicate that strong ion-ion correlations can indirectly influence the neutral diffusion process through DIH, even when the interactions

between neutrals and ions, as well as between neutral species, are weakly coupled.

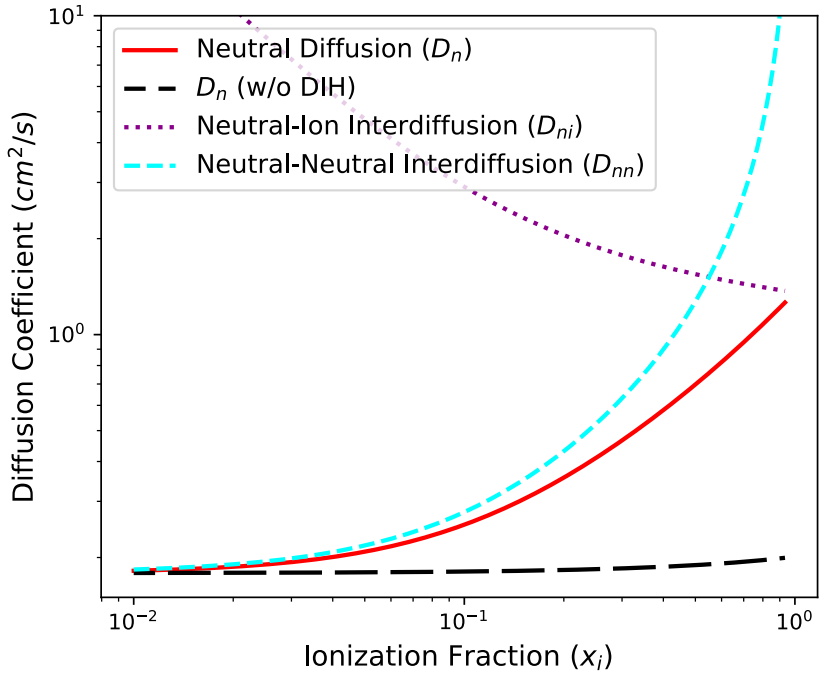

Figure 5.5: Neutral diffusion coefficient at atmospheric pressure for a broad range of ionization fractions (red solid line). Also shown are the neutral diffusion coefficient ignoring DIH (black dashed line), and the neutral-ion (purple dotted) and neutral-neutral (blue dashed line) interdiffusion coefficients.

It is crucial to elucidate that in this chapter, we contemplate a model atomic Ar characterized solely by elastic collisions, ignoring charge exchange collisions [111] and ion conversion processes [112]. Here, our focus is exclusively on the effects of strong ion-ion correlations on the ion diffusion coefficient. Subsequent inclusion of non-elastic processes is feasible in the ion-neutral interdiffusion, while employing the described model for the ion-ion interdiffusion which accounts for these strong correlations.

5.2 Molecular dynamics simulations

Molecular dynamics simulations were carried out using the open-source software LAMMPS [75]. Following the same argument from [2], electrons were assumed to be

weakly coupled due to their much larger temperature and were treated as a background non-interacting species when modeling the ion dynamics. Thus, they were not included in the simulation. Ion-ion interactions were modeled using the Coulomb potential

$$\phi_C(r) = \frac{Z^2 e^2}{4\pi\epsilon_0}\frac{1}{r} \tag{5.12}$$

where Ze is the ion charge and ϵ_0 is the vacuum permittivity. The P3M method was used to simulate ion-ion interactions. [74] A distance of $r_c = 10\ a_{ii}$, where a_{ii} is the average interparticle distance between ions, was chosen to separate short and long range parts of the Ewald summation. Ion-neutral interactions were modeled using a MCC module described in section 2.1.7.

The timestep was chosen to resolve both the ion-neutral and ion-ion collision times, as shown in table 3.1. To determine the timestep requirement in the limit of low ionization fraction, a convergence test was conducted for the ion diffusion coefficient at the lowest ionization fraction considered ($x_i = 10^{-9}$); see figure 5.6. This shows that the ion diffusion coefficient is independent of the timestep chosen for $\Delta t \nu_{in} \lesssim 10^{-3}$. In the limit where ion-ion collisions are dominant, the timestep was chosen to well resolve the ion plasma frequency.

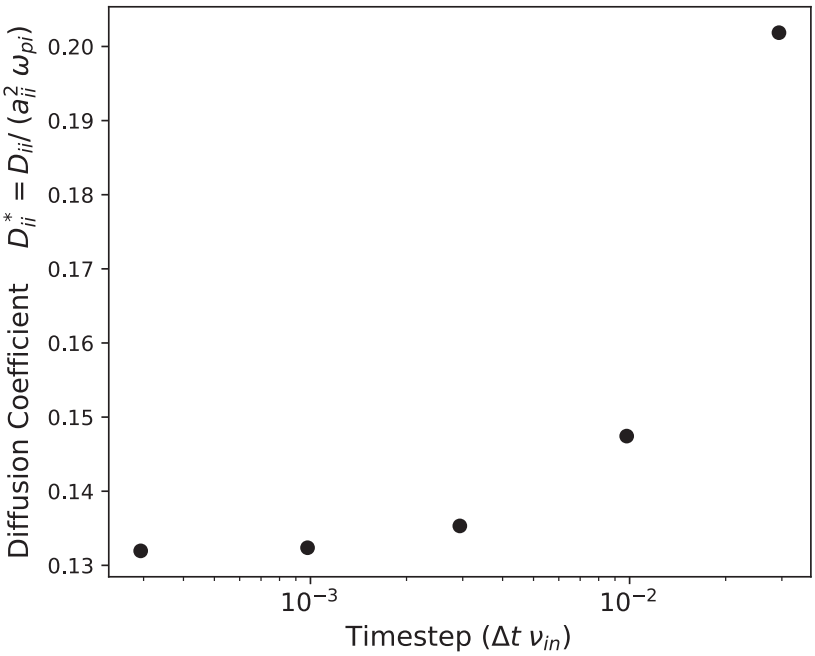

Figure 5.6: Convergence test for the total ion diffusion coefficient at an ionization fraction of 10^{-9} with different timesteps Δt.

To compute diffusion coefficients, simulations were first run in an NVE ensemble including the Monte Carlo Collision method for a one component plasma 2.1.7. Here, NVE refers to constant number of particles, volume and total energy. The NVE ensemble was run for a duration of $1000\omega_{pi}^{-1}$, when equilibrium was reached, at which point the temperature and potential energy remained constant, on average, over time. The ion and neutral gas densities used for each simulation corresponded to a fixed ionization fraction at atmospheric pressure. The neutral gas temperature used in the MCC module was calculated using equation (3.8). Once equilibrium was reached, a second NVE stage was run and the ion velocity vector was recorded every 10 timesteps for the calculation of the ion velocity auto correlation function (described in section 5.2.2). The ionization fraction, ion plasma frequency, ion-neutral collision frequency, time step and length of simulation used for each simulation are specified in table 5.1. The total number of ions in all the simulations was $N_i = 5000$ and the total number of timesteps was 3×10^5.

Table 5.1: Parameters used for the MD-MCC simulations. The number of ions was $N_i = 5000$ and the total number of timesteps was 3×10^5 for all simulations.

Ionization Fraction (x_i)	Ion-Neutral Collision Frequency (ν_{in}) $\times 10^9$ (1/s)	Plasma Frequency (ω_{pi}) (rad/s)	Length of Simulation (t_f)	Timestep (Δt) (s)
10^{-9}	3.24	3.31×10^7	2.72×10^{-8}	9.06×10^{-14}
10^{-8}	3.24	1.05×10^8	2.87×10^{-8}	9.56×10^{-14}
10^{-7}	3.24	3.31×10^8	2.72×10^{-8}	9.06×10^{-14}
10^{-6}	3.24	1.05×10^9	2.87×10^{-8}	9.56×10^{-14}
10^{-5}	3.24	3.31×10^9	2.72×10^{-8}	9.06×10^{-14}
10^{-4}	3.24	1.05×10^{10}	2.87×10^{-8}	9.56×10^{-14}
10^{-3}	3.24	3.31×10^{10}	2.72×10^{-8}	9.06×10^{-14}
10^{-2}	3.21	1.05×10^{11}	2.87×10^{-8}	9.56×10^{-14}
10^{-1}	2.98	3.31×10^{11}	9.06×10^{-9}	3.02×10^{-14}
5×10^{-1}	2.31	7.40×10^{11}	4.05×10^{-9}	1.35×10^{-14}

5.2.1 Validation of the MCC + MD simulation setup

In order to test the ion-neutral MCC model, a comparison was made between the MD+MCC setup and a simulation that used MD for all particles (ions and neutrals). An ionization fraction of $x_i = 10^{-2}$ was chosen because this is a low enough value that the presence of neutrals have a significant effect on the ion temperature evolution, but it is a high enough value that it can be simulated directly with MD at an acceptable computational cost. Additionally, it is a low enough value that the neutral temperature does not change significantly from the initial room temperature value assumed in the MCC routine. Specifically, section 3.2 showed that the maximum ion temperature due to DIH is ≈ 1030 (K) while the equilibrium temperature is similar to room temperature ≈ 300 (K) [2]. Figure 5.7 shows the evolution of the ion temperature from both simulation setups. The observed relaxation rate is nearly-identical and the maximum ion temperature is correctly resolved, showing that the MD+MCC method is able to reproduce the dynamics of the discharge obtained from the first-principles

MD simulation.

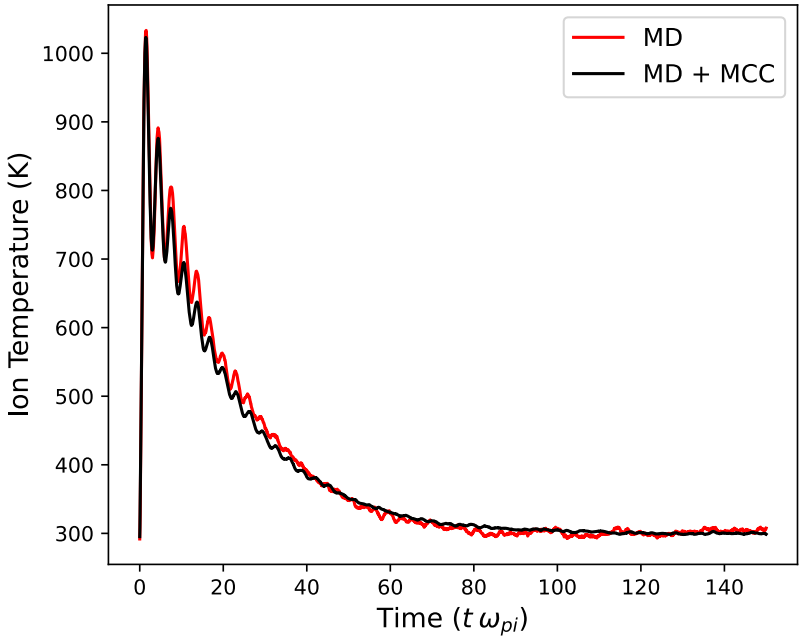

Figure 5.7: Evolution of the ion temperature for a discharge at atmospheric pressure and an ionization fraction of $x_i = 10^{-2}$ using an MD+MCC simulation setup (black line) and a MD-only simulation (red line). The MD+MCC module correctly reproduces the dynamics and equilibrium at a lower computational cost than MD only.

A second aspect of validation of the MD+MCC method was obtained by computing the radial distribution function of ions for different ionization fractions, as shown in figure 5.8. The results are compared with MD simulations of the one-component plasma (OCP) at the same equilibrium coupling parameter Γ_{ii}. The good agreement shows that ion-ion interactions are not significantly screened by the presence of neutral atoms for a broad range of ionization fractions at atmospheric pressure, which justifies the weak ion-neutral interaction assumption that is the basis of the MD+MCC method. This is, the presence of the neutral atoms does not modify how ions interact with other ions since the ion-neutral interaction is short range while the ion-ion interaction is long range. Thus, the simulation setup proposed correctly resolves both the ion dynamics and equilibrium of a partially ionized atmospheric pressure discharge.

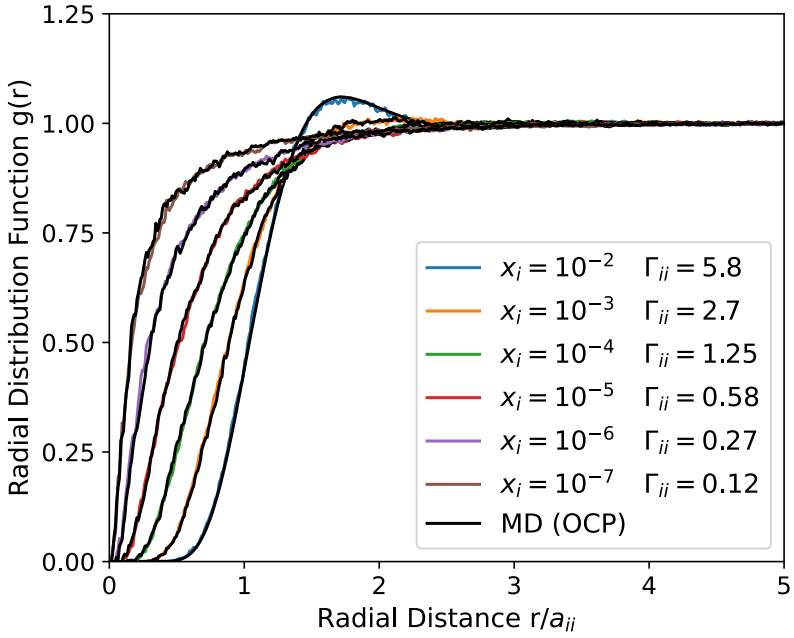

Figure 5.8: Ion radial distribution function at equilibrium from the MD+MCC simulations at different ionization fractions (colored lines). The radial distribution function of an OCP at the corresponding equilibrium Γ_{ii} parameter (black lines).

5.2.2 Calculation of the ion diffusion coefficient

The ion diffusion coefficient was computed using a standard MD method where the velocity autocorrelation function is obtained from a time-history of particle velocities at equilibrium. [74] The diffusion coefficient is then computed from the Green-Kubo relation, which is the time-integral of the velocity autocorrelation function. Velocities of all ions were recorded during the second NVE stage of the simulations and used to compute the velocity autocorrelation function,

$$Z(t, t_0) = \frac{1}{N_i} \sum_{i}^{N_i} \mathbf{v}_i(t + t_0) \cdot \mathbf{v}_i(t_0) \tag{5.13}$$

where t_0 is an initial time used to compute $Z(t, t_0)$, $\mathbf{v_i}$ is the velocity vector of ion i and the time t was taken once every 10 timesteps. A total of $N_k = 3000$ values of t_0 were used, where t_0 was taken once every 100 timesteps. In order to improve the

statistics of the velocity autocorrelation function $Z(t, t_0)$ was averaged over all N_k values of t_0 to get $Z(t)$. [74] Due to the incremental values used for t_0, the velocity autocorrelation functions exhibited an increased level of noise at the longest time t. Figure 5.9(a) shows the averaged value of $Z(t)$ for each simulation. The ion self diffusion coefficient was then computed from the Green-Kubo relation [74]

$$\widetilde{D}(t) = \frac{1}{3} \int_0^t Z(t')dt', \tag{5.14}$$

taking the limit of the integral for $t \to \infty$. Since the simulations provide only a finite time series, the ion self diffusion coefficient D was obtained from the taken as the plateau value of $\widetilde{D}(t)$ in the long time limit, as shown in figure 5.9(b).

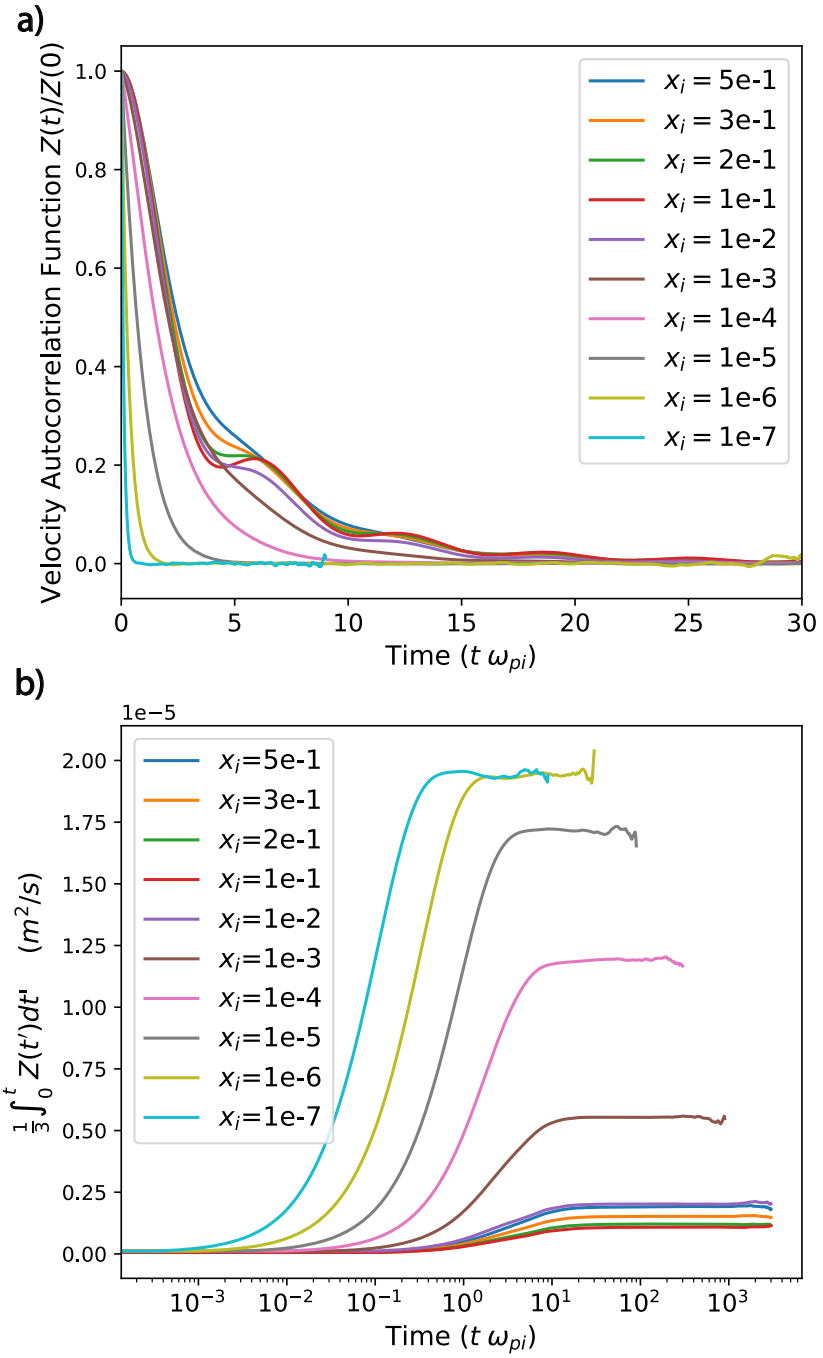

Figure 5.9: (a) Velocity autocorrelation function of ions $Z(t)/Z(0)$ for different ionization fractions and (b) integral $\widetilde{D}(t) = \frac{1}{3}\int_0^t Z(t')dt'$ for different ionization fractions. The ion self diffusion coefficient was taken as the plateau value of $\widetilde{D}(t)$.

5.3 Molecular dynamics results

Results of the velocity autocorrelation function are shown in figure 5.9. At low ionization fractions, the velocity autocorrelation function monotonically decays at an exponential rate characterized by the ion-neutral collision frequency. Since $\nu_{in} \gg \omega_{pi}$ in this limit, the decay rate is fast compared to the ion oscillation timescale. Exponential decay is expected for weakly correlated interactions, such as the ion-neutral interactions in these simulations. As the ionization fraction increases above $x_i \gtrsim 10^{-3}$, the decay rate approaches the ion plasma period and is no longer exponential, rather exhibiting non-monotonic features that are indicative of strong correlations. The change of the decay rate indicates a transition to ion-ion collisions being more frequent than ion-neutral collisions. For Coulomb coupling parameters above approximately 1, the ion-ion collision rate is expected to be approximately $0.2\omega_{pi}^{-1}$,[104] in agreement with the simulated rates. It is also noteworthy that the largest correlation features are observed for $x_i \approx 1 \times 10^{-1}$. This agrees with the predicted maximum ion-ion coupling parameter from figure 5.1, as Γ_{ii} decreases for $x_i \gtrsim 10^{-1}$ due to disorder-induced heating.

Figure 5.3 shows the ion diffusion coefficient for ionization fractions ranging from $x_i = 10^{-9}$ to $x_i = 1$. The first noticeable result is that the ion diffusion coefficient computed from the model in equation (5.1) agrees well with the results of the MD+MCC simulations. Since the simulation technique is essentially first principles, this serves as a measure of validation of the theoretical model. Furthermore, the three characteristic regimes described in the theoretical model section are be observed as a function of the ionization degree from the MD+MCC simulations as well.

The main physical relevance of these results is that diffusion coefficients, commonly used as input parameters for fluid simulations, are influenced by strong coupling effects and ion-ion interactions. Currently, it is common to model diffusion using models that are relevant only in the weakly coupled regime or only accounting for

ion-neutral collisions, even when encountering an ionization fraction where ion-ion collisions are important. Furthermore, in the regimes that correspond to glow ($n_i \approx 10^{19} - 10^{21}$ m^{-3}), spark ($n_i \approx 10^{21} - 10^{22}$ m^{-3}) and thermal spark ($n_i \approx 10^{25}$ m^{-3}) regimes of NRP discharges [72, 113], the ion diffusion coefficient needs to be calculated as we show in this work, accounting for both ion-neutral and ion-ion collisions and including the strong ion-ion correlations, in particular the disorder induced heating effect in the cases where large ionization fractions are reached.

5.4 Pressure dependence

While ions are strongly coupled at atmospheric pressure when the ionization fraction is high enough, it is natural to ask how the results extend to pressures both above and below atmospheric pressure. Figure 5.10 shows the ion-neutral equilibrium temperature computed using equation (3.8) for ionization fractions ranging from 10^{-2} to 1 and pressures ranging from 10^2 Pa to 10^7 Pa. A continuous line indicating an equilibrium temperature of 300 K separates the regions that are not affected by disorder induced heating to the regions that are. For near fully ionized plasmas, disorder induced heating affects the equilibrium temperature and becomes more significant as the pressure increases due to the larger ion density.

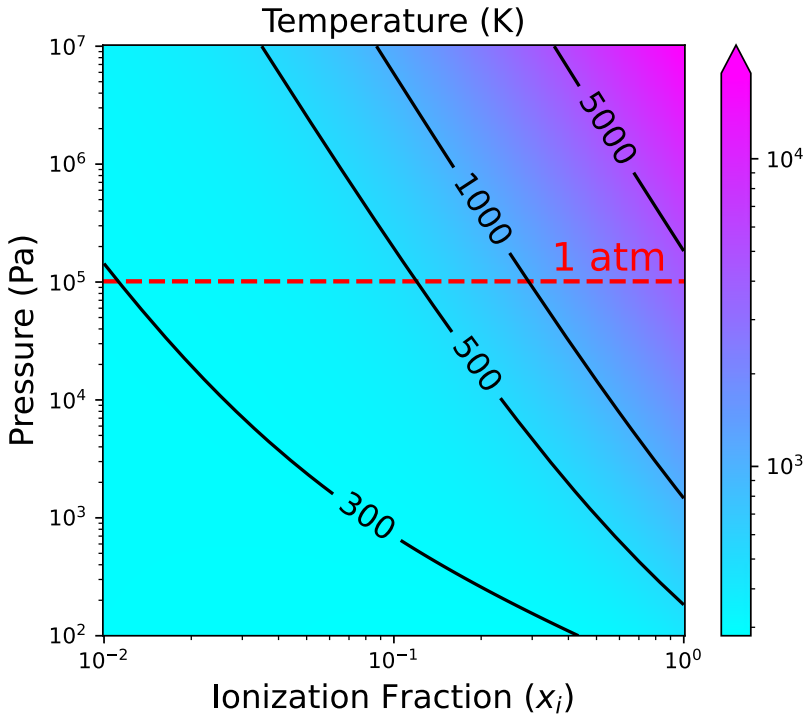

Figure 5.10: Equilibrium temperature for different pressures and ionization fractions computed using equation (3.8). This accounts for disorder induced heating and ion-neutral temperature relaxation.

For pressures up to 10 atm, ion-neutral interactions remain weakly coupled as shown in [2]. Using the method described in section 5.1, the ion diffusion coefficient was calculated as a function of the ionization fraction for pressures ranging from $10^{-3} - 10$ atm. Figure 5.11 a) shows the ion diffusion coefficient at different pressures normalized by the average interparticle spacing between ions and the ion plasma period and b) in cm^2/s. The same general trend of three distinct regimes is observed at each pressure: For the smaller ionization fractions, the main contribution to the ion diffusion is due to ion-neutral collisions. At intermediate ionization fractions, the ion diffusion exhibits a local maximum value that depends on the pressure and corresponds to the ionization fraction at which the ion-neutral and ion-ion collision frequencies equal each other. In this regime, ion-neutral and ion-ion interactions both contribute but disorder-induced heating is negligible. Finally at the largest ionization

fractions, the ion diffusion coefficient increases due to the higher equilibrium temperature produced by the disorder induced heating and ion-neutral temperature relaxation described. The main distinction as the pressure varies is the values of the ionization fraction at which these transition occur. The location of the local maximum of the diffusion coefficient associated with the intermediate regime increases with pressure, whereas the location at which disorder-induced heating onsets decreases with pressure. At 10 atm, disorder-induced heating onsets at an ionization fraction that is only slightly above the local maximum where ion-neutral and ion-ion collisions balance.

Another interesting observation is that for pressures larger than 10^{-3} atm and full ionization, the normalized diffusion coefficients converge to the same value (in units of $a_{ii}^2\omega_{pi}$). The reason this happens is that the initial Coulomb coupling parameter is larger than 1, so disorder induced heating occurs and the expected equilibrium coupling parameter is around 1.9 (as shown in [2]), for all the pressures mentioned and full ionization. Thus, each case corresponds to a fully ionized one-component plasma at $\Gamma = 1.9$, and therefore has the same value of the ion diffusion coefficient in the normalized units.

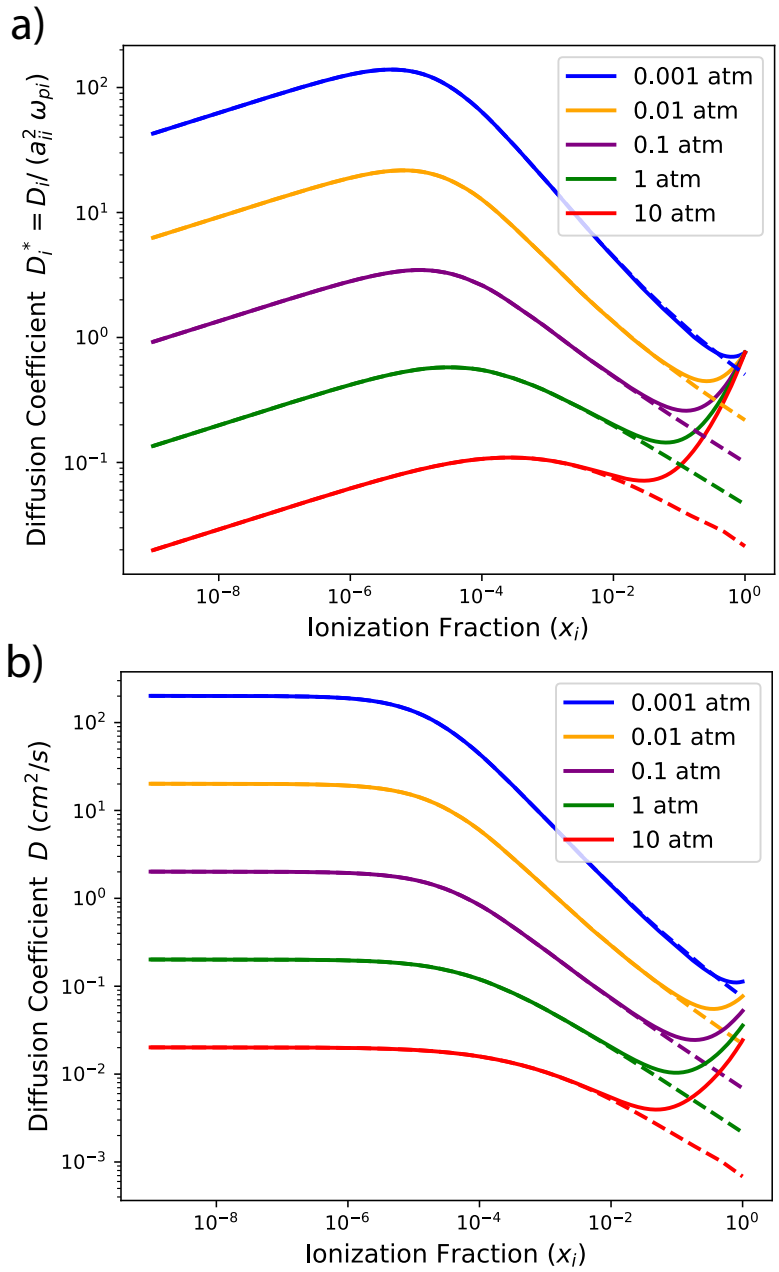

Figure 5.11: Ion diffusion coefficient predicted from the model of section 5.1 for different pressures and ionization fractions. The dashed lines represent the diffusion coefficients at room temperature while the solid lines correspond to the case where disorder induced heating is accounted for and the equilibrium temperature is computed from equation (3.8).

Figure 5.12 shows the effect of pressure on the neutral diffusion coefficient. For ionization fractions smaller than 10^{-2} and pressures below 10 atm, disorder induced

heating does not affect the equilibrium temperature. However, for ionization fractions larger than 10^{-2}, the equilibrium temperature increases above room temperature and this effect becomes more pronounced as the pressure increases, increasing the neutral diffusion coefficient. It is noteworthy that within the range of pressures and ionization fractions considered, even though neutral-neutral and ion-neutral interactions are weakly coupled, strong ion-ion coupling influences neutral diffusion rates indirectly because DIH has a significant impact on the equilibrium temperature, which, in turn, affects the neutral diffusion coefficient.

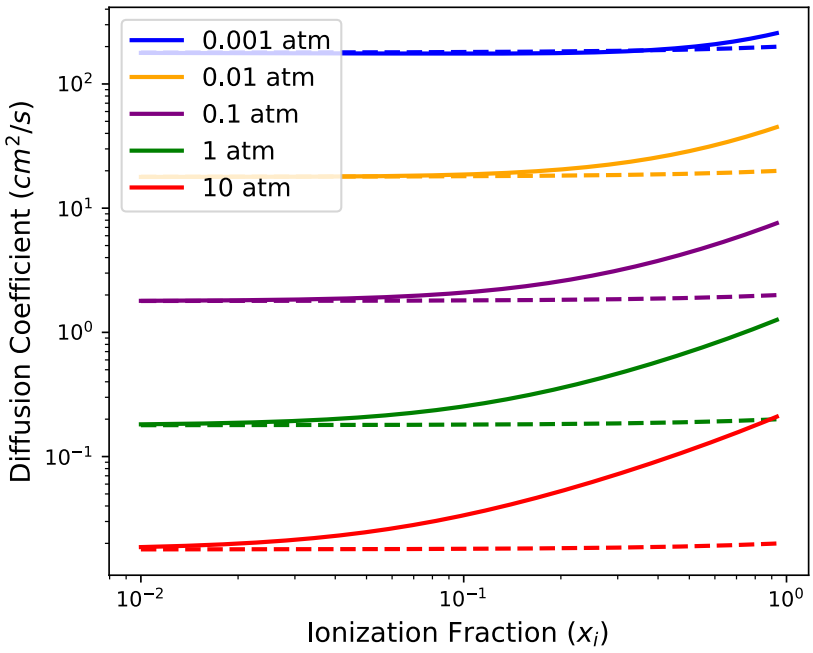

Figure 5.12: Neutral diffusion coefficient at different pressures and ionization fractions. The dashed lines represent the diffusion coefficients at room temperature while the complete lines correspond to the case where disorder induced heating is accounted for and the equilibrium temperature from equation (3.8) is used.

CHAPTER VI

When should PIC simulations be applied to atmospheric pressure plasmas? Impact of correlation heating

Accurate and efficient modeling of plasma discharges at atmospheric and higher pressures is critical for the advancement and optimization of plasma devices for multiple applications, as described in chapter I. Simulations, for instance, can aid in identifying optimal operating parameters like discharge voltage, power, frequency, electrode configuration, and gas mixture for diverse applications. Consequently, it is imperative to develop reliable and efficient computational tools for simulating the behavior of cold atmospheric pressure plasmas. The PIC method is one of the commonly used computational approach in plasma modeling [43, 44, 45]

Molecular dynamics simulations are used to test when the PIC method applies to atmospheric pressure plasmas. It is found that PIC applies only when the plasma density and macroparticle weight are sufficiently small because of disorder-induced heating. PIC is not well suited to capture DIH because doing so requires using a macroparticle weight of one and a grid that well resolves the physical interparticle spacing. These criteria render PIC intractable for macroscale domains. Furthermore, it is shown that simulations in reduced dimensions exacerbate these issues.

6.1 Simulation setup

Molecular dynamics simulations were used to test the applicability of the PIC method. The simulation domain consisted of a cubic box with periodic boundary conditions. The size of the simulation domain was calculated such that for a given number of particles, the particle density met a desired value. The basic molecular dynamics and PIC setups are described in chapter II.

6.1.1 Molecular dynamics

Since the objective of this chapter is to test the limitations of PIC simulations when ions are strongly coupled, no ion-neutral interactions were included in the MD simulations. That is, only a one-component plasma model [79] was simulated, which is known to provide an accurate description of ions in the presence of weakly coupled electrons, such as in ultracold neutral plasmas [80]. In order to study the evolution of a non-equilibrium discharge, a neutral Ar gas at room temperature and atmospheric pressure was simulated until equilibrium was reached. This stage of the simulation was run with a Nosé-Hoover thermostat applied [74] and the Lennard Jones potential [2]. Then, the entire set of particles was instantly ionized and a NVE simulation was run where ion-ion interactions were modeled using the Coulomb potential 1.10. The P3M method was used to include both short and long range contributions in ion-ion interactions. [74] A distance of $r_c = 10\ a_{ii}$ was chosen to separate short and long range parts of the Ewald summation. The timestep used was $10^{-3}\omega_{pi}$ where ω_{pi} is the ion plasma period. The number of particles was 5000. The simulated ion density was 2.5×10^{24} m^{-3} which is equivalent to the ion density of an atmospheric pressure plasma with an ionization fraction of 10%. This value was chosen as an example because DIH is significant, and it is relevant to a number experiments [3, 32]. Furthermore, a lower ion density within the strongly coupled regime could have been used and the same analysis would still apply [2].

6.1.2 Particle in cell

For the PIC simulations ions were simulated as macroparticles. The number of macroparticles was 5000, and the simulated ion density was 2.5×10^{24} m^{-3} with a timestep of $\Delta t = 10^{-3}\omega_{pi}^{-1}$. The positions of the macroparticles were initialized with a uniform random distribution and the velocities with a Maxwellian distribution at room temperature. No electron or neutral species were included since the objective of this part is to study strongly coupled ion-ion interactions in atmospheric pressure plasmas [2]. To justify not including neutral atoms, the ion-neutral collision frequency at large ionization fractions is much smaller than the ion plasma frequency which sets the timescale of DIH [2, 114]. In addition, the elevated electron temperature makes electron screening of ions negligible, as observed by Shaffer et. al. [109]. Thus, electrons are considered as a background non-interacting neutralizing species. Thus, they were not included in the simulation [2, 114]. Consequently, ion-ion interactions can be treated as an one-component plasma.

6.2 Disorder-induced heating

6.2.1 Molecular dynamics results

Figure 6.1 presents the evolution of the ion temperature over the first 10 ion plasma periods, obtained from the MD simulation described in section 6.1.1. The ion temperature rapidly increases from room temperature to a peak of ≈ 2000 K during the initial time period of $1.5\omega_{pi}^{-1}$. Throughout the evolution, the ion temperature exhibits pronounced fluctuations, a result of oscillations in the exchange of potential and kinetic energy as the system relaxes to equilibrium at a Coulomb coupling parameter larger than unity [2, 60]. The absence of ion-neutral interactions in the simulation prevents the relaxation of ion and neutral temperatures that was studied in earlier MD simulations [2]. The ion temperature shown in figure 6.1 provides a

target to obtain with PIC simulations.

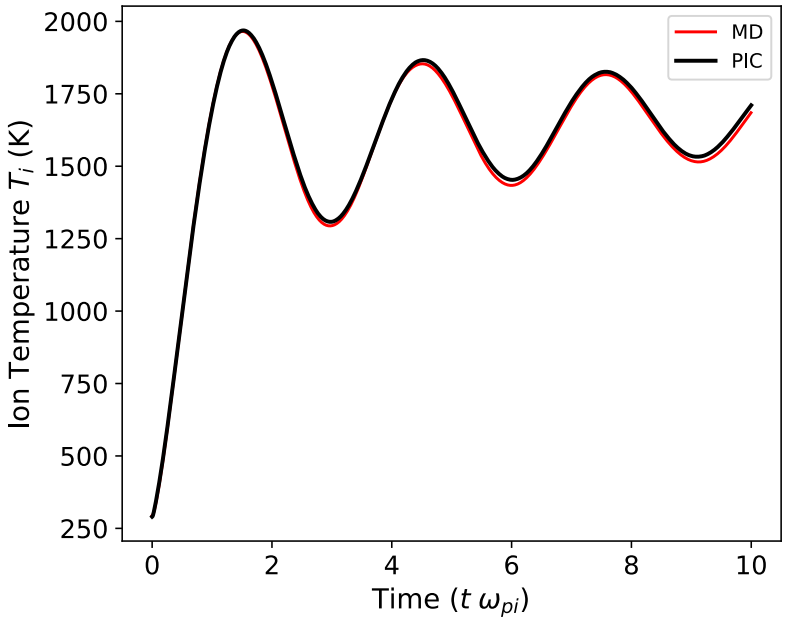

Figure 6.1: Evolution of the ion temperature obtained with a 3D3V PIC simulation with a grid spacing of $\Delta x/a_{ii} \approx 0.042$ and from an MD simulation for the same initial conditions and density.

After ionization the ions have significant excess potential energy since the interactions between particles changes from a short range (Lennard-Jones) to a long range (Coulomb) potential. Hence, ions move to their lowest potential configuration converting the excess potential energy into kinetic energy. This, combined with an initial Coulomb coupling parameter $\Gamma \approx 12$ results in the temperature increase observed in figure 6.1, known as DIH [2, 60] and described in previous chapters. After DIH, ions overshoot their equilibrium positions leading to oscillations of the Coulomb potential energy near the ion plasma frequency. Since the total energy is conserved during the MD simulation and ions are strongly coupled after DIH, those oscillations translate to observable fluctuations in ion temperature as shown in figure 6.1.

6.2.2 PIC: influence of grid resolution

Figure 6.2 presents the evolution of ion temperature from initial room temperature and a random distribution of positions for different uniform grid spacing Δx and unity macroparticle weight. At the simulated density, the expected maximum ion temperature after $t\omega_{pi} = 1.5$ is approximately 1800 K from equation (3.7). The results demonstrate that when $\Delta x/a_{ii} > 1$ and $\Delta x/\lambda_{D_i} > 1$, where λ_{D_i} is the ion Debye length, DIH is not fully observed, nor is grid heating absent. Here, DIH corresponds to the rapid initial temperature increase over $\sim 1.5\omega_{pi}^{-1}$, while grid heating is the longer-time linear increase over tens of ω_{pi}^{-1}. If $\Delta x/a_{ii} < 1$ and $\Delta x/\lambda_{D_i} > 1$, the temperature increase due to DIH aligns more closely with the expected value, but grid heating still persists. Ultimately, when both λ_{D_i} and a_{ii} are resolved, DIH is fully observed and there is an agreement with the expected temperature increase. Furthermore, the evolution of the ion temperature for the smallest grid spacing of $\Delta x \approx 0.042a_{ii}$ shows a good agreement with the target evolution obtained with MD over the $10\omega_{pi}^{-1}$ timescale, as shown in figure 6.1.

Figure 6.3 shows the maximum ion temperature, taken from the first peak of each simulation, for different grid spacing. It is clear that in order to fully capture DIH with a PIC simulation, the grid spacing must be $\Delta x \lesssim 0.1a_{ii}$. It is important to underscore that in strongly coupled plasmas, the average interparticle spacing is larger than the Debye length. Thus, resolving the Debye length to avoid grid heating requires resolving the average interparticle spacing. This implies that, on average, there are fewer particles in the simulation than grid cells, contradicting the standard practice in PIC simulations where multiple macroparticles per cell are essential to mitigate statistical noise. As an example, for a grid resolution of $\Delta x = 0.1a_{ii}$ and the simulated density, there is an average of 2.38×10^{-4} macroparticles per cell. This contrasts with the normal operation of PIC simulations of weakly coupled plasmas, where $\lambda_{D_i} \gg a_{ii}$ and the Debye length can be resolved while having multiple macroparticles per cell.

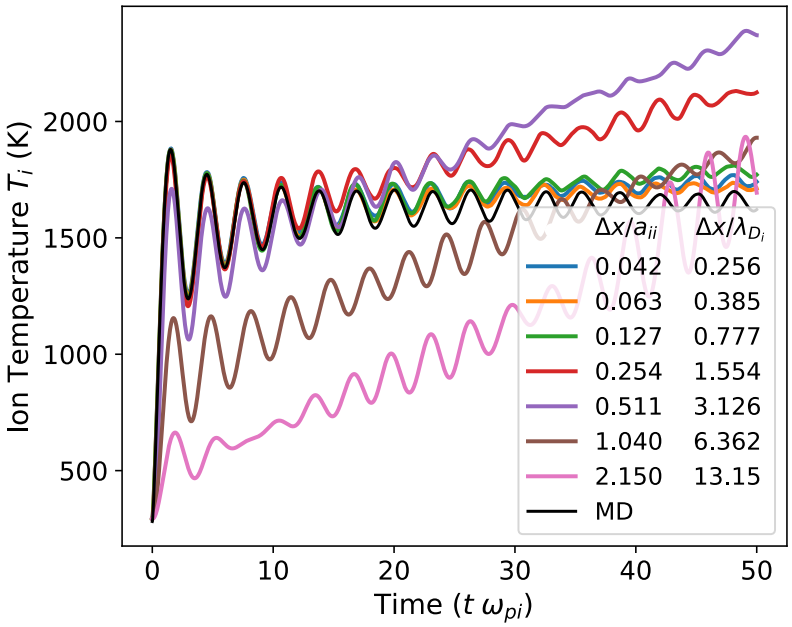

Figure 6.2: Evolution of the ion temperature for an ion density of $n_i = 2.5 \times 10^{24}$ m^{-3} and initial room temperature obtained from MD and using the PIC method for different grid spacing.

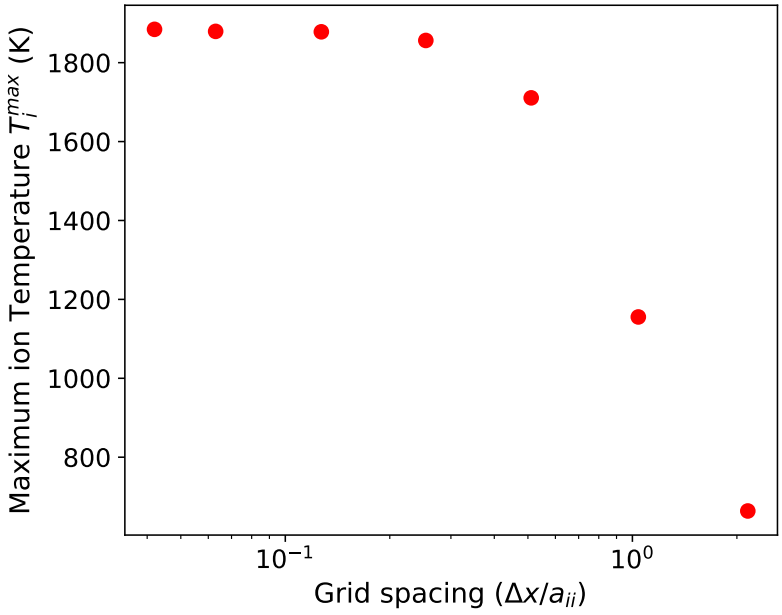

Figure 6.3: Ion temperature of the first peak (at $t \approx 1.5\ \omega_{pi}^{-1}$) for different grid spacing values $\Delta x/a_{ii}$. The maximum ion temperature converges to the expected physical value for $\Delta x/a_{ii} \leq 0.1$.

6.2.3 PIC: influence of macroparticle weight

Figure 6.4 presents the evolution of ion temperature for different macroparticle weights w, using a grid spacing of $\Delta x/a_{ii} \approx 0.042$. When $w > 1$ the observed ion temperature exceeds the expected physical value. Conversely, when $w < 1$, the observed temperature is lower. This shift in ion temperature with varying w becomes more pronounced as w is further increased or decreased from unity. The effect of the macroparticle weight on the change in the ion temperature, from room to equilibrium, is shown in figure 6.5. This highlights the tendency that temperature artificially increases rapidly with macroparticle weight.

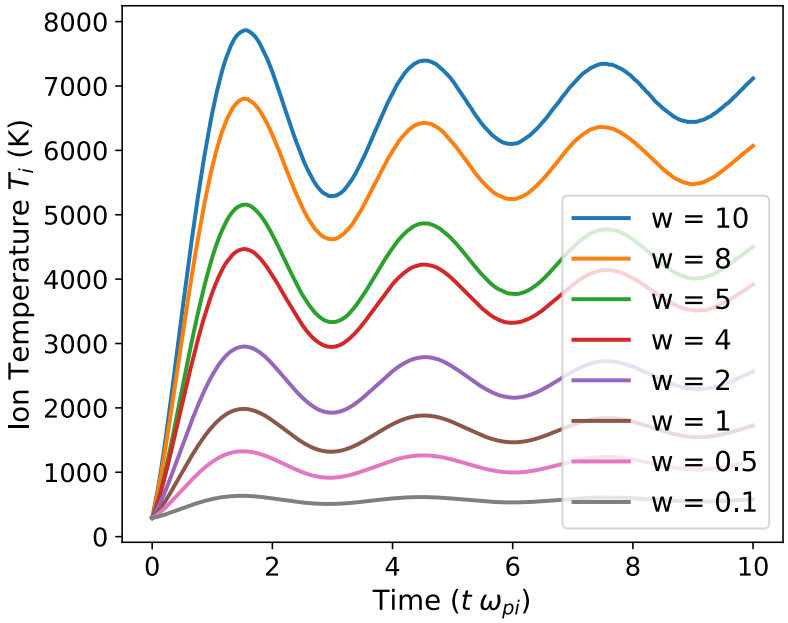

Figure 6.4: Evolution of the ion temperature using a grid spacing of $\Delta x/a_{ii} \approx 0.042$ for different macroparticle weights w.

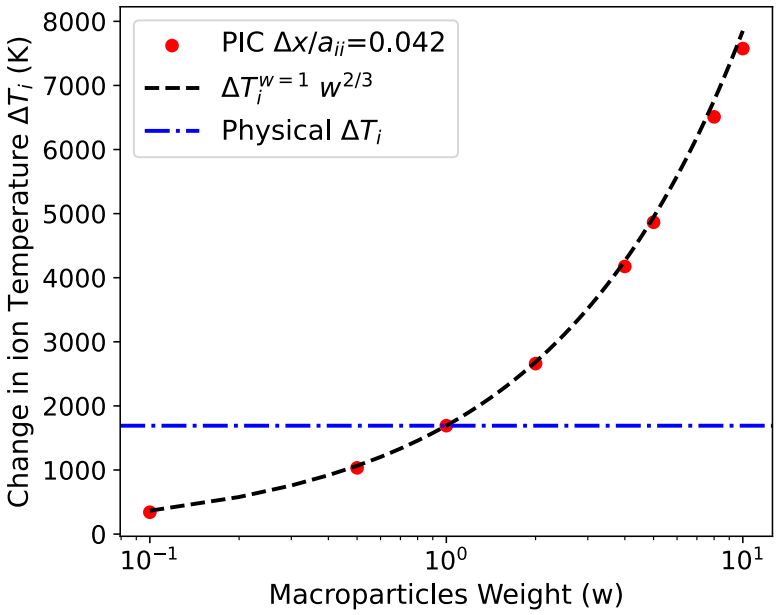

Figure 6.5: Change in the ion temperature obtained with PIC simulations at different macroparticle weights. The change in temperature obtained with the scaling law $\Delta T_i^w = w^{2/3}\Delta T_i$ is shown for comparison.

Figure 6.6 aims to provide a qualitative illustration of this influence. In standard PIC simulations of weakly coupled plasmas, the ion Debye length is much larger than the average interparticle spacing. Therefore, a large number of macroparticles is included within each cell and the resulting charge density aligns closely with the actual physical density in the computational grid. However, this is not the case in strongly coupled plasmas. Here, maintaining an average of fewer than one macroparticle per cell ($\Delta x \leq 0.1a_{ii}$) is vital for accurately resolving the strong ion-ion correlations and for obtaining a precise representation of DIH. For the same increase in particle weight, a strongly coupled simulation suffers a greater change in the density across adjacent cells when compared to a weakly coupled simulation. Raising the macroparticle weight above one results in a numerical localization of the charge density, which locally augments the electric field and subsequently elevates the overall potential energy. Conversely, lowering the macroparticle weight below one incurs the opposite effect, smoothing the charge density artificially resulting in the lower DIH observed in figure

6.4.

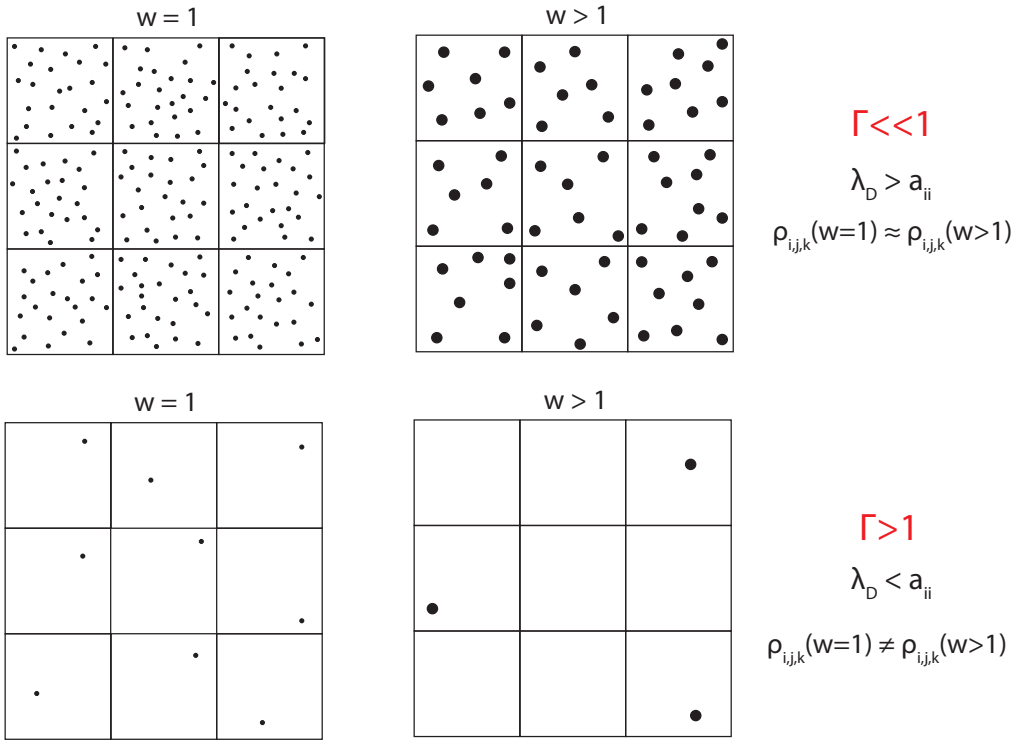

Figure 6.6: Illustration of the distribution of macroparticles in PIC simulations for (top) weakly vs. (bottom) strongly coupled plasmas assuming a grid spacing of approximately the Debye length.

Next, we consider a quantitative description of the influence of the macroparticle weight on the ion temperature. The potential energy of ions in an OCP at equilibrium can be expressed as [108]

$$\mathrm{PE} = 2\pi n_i N_i \int_0^\infty dr\; r^2 \phi(r) g(r), \tag{6.1}$$

where n_i is the ion density, N_i the number of ions, $\phi(r)$ is the interaction potential and $g(r)$ is the ion pair correlation function. It is a density profile of other particles referenced to a particle at the origin, normalized to the background density. If there is a change in the potential energy between two configurations, the corresponding

change in the ion temperature is

$$\Delta T_i = -\frac{\Delta \mathrm{PE}}{\frac{3}{2} k_B N_i}, \tag{6.2}$$

where T_i is the ion temperature. Combining expressions (6.1)-(6.2) and scaling the radial distance using the average interparticle distance between ions, the change in the ion temperature from a randomly distributed configuration in space to a final equilibrium state characterized by the pair correlation function $g(r)$ is expressed as

$$\Delta T_i = \frac{1}{3} \frac{n_i q_i^2 a_{ii}^2}{k_B \epsilon_0} \int_0^\infty d\tilde{r}\ \tilde{r}[1 - g(\tilde{r})], \tag{6.3}$$

where the pair correlation function of the initial randomly distributed configuration is taken as 1 at any radial distance and $\tilde{r} = r/a_{ii}$. Equation (6.3) can be used to estimate the change in temperature when the macroparticle weight is $w = 1$. For the more general case, $w \neq 1$, the corresponding scaling laws $n_i^w \rightarrow n_i/w$, $q_i^w \rightarrow q_i\ w$ and $a_{ii}^w \rightarrow a_{ii}\ w^{1/3}$ must be replaced in equation (6.3). The expected change in temperature for an arbitrary macroparticle weight can be expressed as

$$\Delta T_i^w = \frac{1}{3} \frac{n_i q_i^2 a_{ii}^2}{k_B \epsilon_0} w^{5/3} \int_0^\infty d\tilde{r}\ \tilde{r}[1 - g(\tilde{r})], \tag{6.4}$$

where n_i, q_i and a_{ii} are the physical values of the density, charge and average interparticle spacing respectively. Since the macroparticle temperature is the physical temperature times the macroparticle weight [$T_i^w = T_i w$], the change of the physical ion temperature is predicted to scale proportionally to $w^{2/3}$: $\Delta T_i \propto w^{2/3}$. This means that for macroparticle weights $w \neq 1$, the change in temperature due to DIH computed from PIC will differ from the physical value by a factor of $w^{2/3}$, assuming that the interparticle spacing of macroparticles is well resolved.

Figure 6.7(a) displays the pair correlation function $g(r)$, obtained by averaging

over all macroparticles between the time intervals $t\omega_{pi} = 9.5$ and $t\omega_{pi} = 10$, for different weights. The pair correlation function of an OCP at the same equilibrium temperature is included for comparison. As expected, the pair correlation function corresponding to a macroparticle weight $w = 1$ aligns well with the OCP $g(r)$ since individual physical particles are simulated. However, for $w \neq 1$, the pair correlation functions appear shifted relative to the OCP function. Not surprisingly, when the radial distance is scaled by the corresponding average macroparticle distance a_{ii}^{w}, all $g(r)$ values align with the OCP $g(r)$ at the equilibrium temperature, as shown in figure 6.7(b).

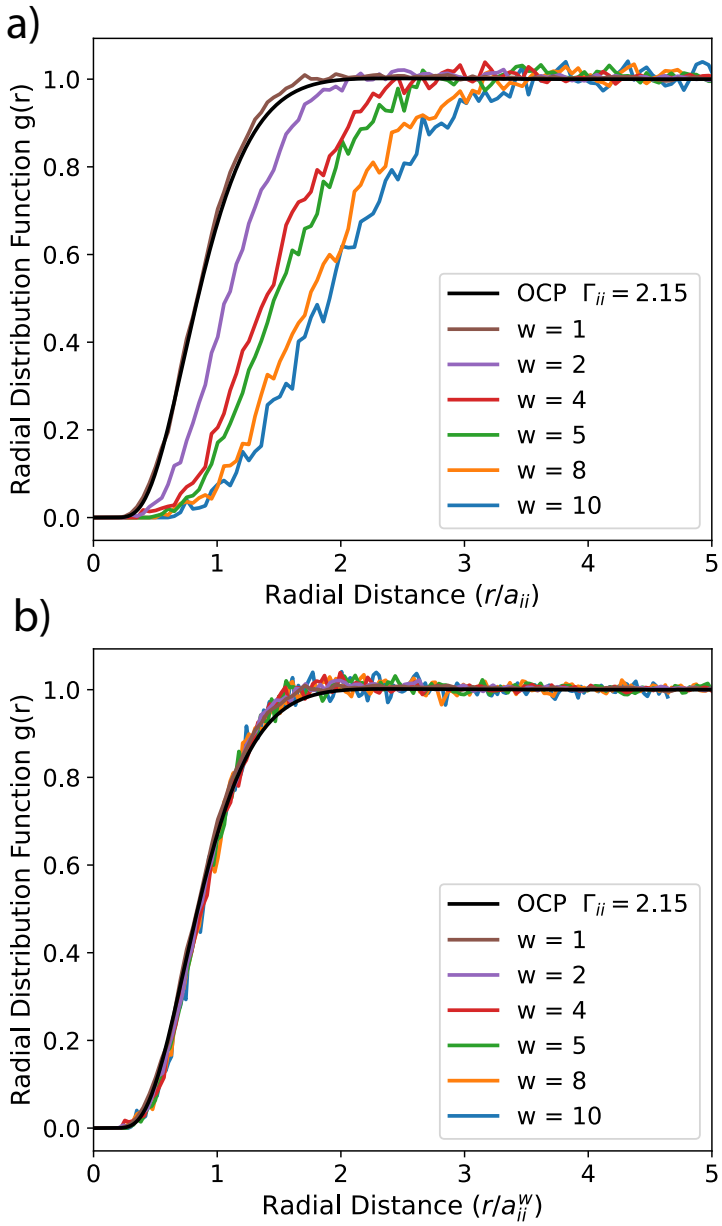

Figure 6.7: Pair correlation function $g(r)$ for different macroparticle weights at equilibrium taking as reference the physical average interparticle spacing (a) and taking as reference the average macroparticle spacing a_{ii}^{w} (b). The pair correlation function of an OCP at the equilibrium Γ_{ii} is shown for comparison.

The scaling law $\Delta T_i^w = w^{2/3}\Delta T_i$ demonstrates excellent alignment with the increase in the ion temperature obtained from PIC simulations across various macroparticle weights, as exhibited in figure 6.5. While employing macroparticles is standard in traditional PIC simulations, these findings suggest that in strongly coupled plasmas

the weight of macroparticles significantly impacts potential energy and consequently the kinetic energy and overall plasma dynamics. This effect does not physically manifest in weakly coupled plasmas, where the average Coulomb potential energy is significantly less than the kinetic energy ($\Gamma_{ii} \ll 1$), thereby facilitating the use of macroparticles.

The main takeaway of these results is that in order to capture DIH and, generally, strong correlations with PIC simulations it is necessary to resolve the average inter-particle spacing, combined with a unity macroparticle weight. Furthermore, the need to resolve such a small spatial scale adds an extra constraint to the timestep, since macroparticles should not travel a distance larger than a cell per timestep. These additional constraints make traditional PIC simulations intractable for atmospheric pressure plasmas due to the prohibitive associated computational cost. To illustrate, consider a simulation run at atmospheric pressure with an ionization fraction of 10%, and 10^6 macroparticles of unity weight. In this scenario, the simulation volume would only span an approximate length of 736 nm. Contrastingly, a simulation run under similar conditions of ionization fraction and total macroparticle count, but at a lower pressure of 1 mTorr and with a macroparticle weight of 10^7, would encompass a simulation volume with a length of approximately 14 cm - akin to the length scale of a plasma device. These discrepancies in scale underscore the limitations of PIC simulations in capturing the behavior of strongly coupled plasmas at atmospheric pressure, urging us to explore alternative computational approaches in future work. Moreover, if a fluid approach is used to model ions at atmospheric pressure and conditions relevant to the strongly coupled regime, effects such as DIH or changes in diffusion rates will be completely missed and the neutral gas temperature could be mistakenly underestimated, making the results from a simulation highly questionable due to important physics being ignored. Chapters III and IV show a solution for this problem. A possible solution for PIC simulations would be to use the P3M method instead

of traditional PIC, however to capture the correct change in the Coulomb potential the particle-particle part of P3M would require ions to have a unity macroparticle weight. While this would reduce the computational cost associated to the grid resolution, it would still make simulations of device-scale plasmas intractable due to the unity macroparticle weight.

6.2.4 Grid heating and influence of interpolation scheme

In PIC simulations, it is crucial that the grid resolution is sufficiently refined to accurately resolve the Debye length. Failure to meet this requirement can yield numerical artifacts and inaccurate simulation outcomes [44]. A well-known artifact is the numerical phenomenon of "grid heating", leading to an overestimation of the plasma temperature [46]. This artifact emerges due to the aliasing of interpolation errors that occur between the mesh quantities and macroparticles. Figure 6.2 displays the manifestation of grid heating in simulations where the ion Debye length is inadequately resolved. It is noteworthy that in strongly coupled plasmas, where $\lambda_{D_i} < a_{ii}$, avoiding grid heating by resolving the Debye length implicitly ensures the resolution of the average interparticle spacing − a prerequisite identified in this study.

Resolving the smallest Debye length eradicates grid heating in dilute plasmas. However, in the strongly coupled regime, grid heating persists. When a PIC simulation of a strongly coupled plasma resolves both the Debye length and the average interparticle distance, there is, on average, less than one macroparticle per cell. This leads to a discontinuity in the electric field every time a particle crosses a cell boundary, thereby inducing grid heating. Therefore, even when all relevant physical distances are correctly resolved, grid heating still occurs on a much longer timescale—hundreds to thousands of plasma periods. This effect is demonstrated in figure 6.8 (a), where at the onset of a simulation, $\Delta x \approx 0.6\ \lambda_{D_i}$. However, after DIH, the plasma continues to experience an increase in temperature due to grid heating on a timescale

of hundreds to thousands of plasma periods. The difference in timescales between DIH and grid heating is illustrated in figure 6.8 (b). The total energy is conserved for the first several plasma periods, where the increase in kinetic energy occurs due to a decrease in the electrostatic field energy. On a longer timescale, spanning 100s of plasma periods, the lowest potential configuration is maintained but the kinetic energy, and therefore total energy, increase due to grid heating.

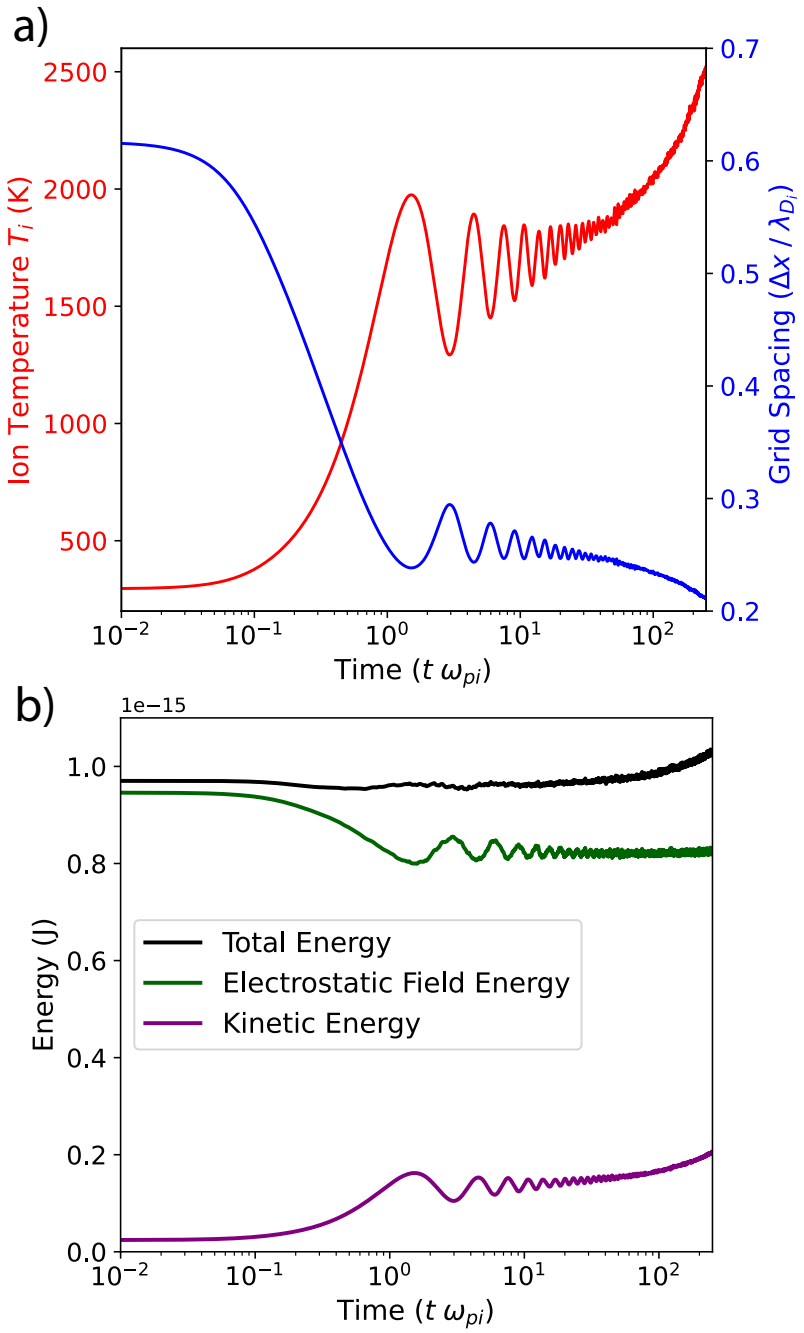

Figure 6.8: (a) Evolution of the ion temperature and grid spacing $\Delta x/\lambda_{D_i}$ for an ion density of 2.5×10^{24} m^{-3}, unity macroparticle weight and average number of macroparticles per cell $N_c = 0.00023$. (b) Evolution of the total, electrostatic and kinetic energies over time.

Recent research has explored strategies to decrease the computational cost and focus on macroscopic physical phenomena. These strategies involve reducing the

grid heating growth rate, while under resolving the Debye length through advanced energy conserving integration schemes, high-order macroparticle shape functions, and filtering methods [46, 115, 116, 117, 118, 119, 120]. These strategies, in particular high order shape functions and filtering methods, rely on the plasma being weakly coupled. While these approaches may reduce the growth rate of grid heating, it is found that it further reduces DIH.

Figure 6.9 a) shows the evolution of the ion temperature in a simulation where the grid resolution ($\Delta x/a_{ii} \approx 0.51$ and $\Delta x/\lambda_{D_i} \approx 3.13$) under resolves the ion Debye length, across different shape functions ranging from order 2 to order 6, as described in equations (2.17), (2.18) and (2.19). Consistent with existing literature, the results demonstrate that the growth rate of grid heating significantly decreases with higher order shape functions. However, in a system exhibiting strong ion-ion correlations, it is crucial to resolve the average interparticle spacing, as delineated in this study. This necessity results in an average of less than one particle per cell. Within such a framework, employing high order shape functions can result in the delocalization of the charge density, leading to an artificial reduction in the effective Coulomb coupling parameter of macroparticles. This, in turn, produces an underestimation of the electric field, which subsequently reduces the observed disorder-induced heating, as illustrated in figure 6.9 (b). This finding underscores that due to the inherent nature of strong Coulomb coupling, the charge density must remain numerically unchanged, both locally and globally to accurately represent the physical state of the plasma. This further limits the applicability of PIC simulations for plasmas where ion-ion interactions are strongly correlated.

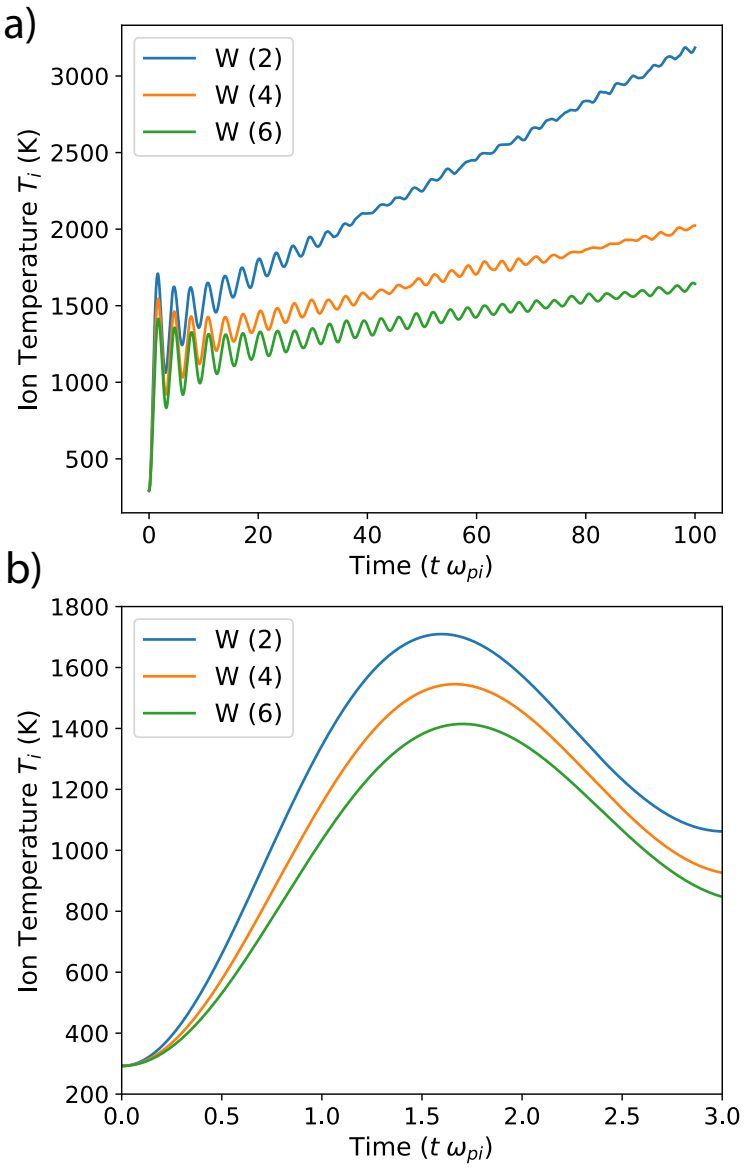

Figure 6.9: (a) Evolution of the ion temperature obtained from PIC simulations with different shape functions for the first 100 ion plasma periods, and (b) the first 3 plasma periods. The grid resolution is $\Delta x/a_{ii} \approx 0.51$ and $\Delta x/\lambda_{Di} \approx 3.13$ and the ion density is 2.5×10^{24} m^{-3}. Increasing the order of the shape function reduces the growth rate of the observed grid heating and DIH.

6.2.5 Reduced dimensions

Running PIC simulations in reduced spatial dimensions is a common approach for systems with some kind of spatial symmetry. While this approach significantly reduces the computational cost, physical quantities such as charge and particle densities,

are based on volumetric properties. The usual approximation to connect a physical volumetric density with a numerical density in reduced dimensions is to consider a constant area (or length) perpendicular to the simulation domain, allowing the calculation of a volume for each cell [48]. This approach, however, is equivalent to projecting the positions of all particles within the physical volume onto an element in the corresponding reduced dimension. While this method is acceptable in the weakly coupled regime, where interactions between individual particles are ignored and multiple macroparticles are located within each cell, it artificially reduces the interparticle distance. If a plasma is strongly coupled, that interparticle distance needs to be resolved in order to accurately capture the strong correlations. This, combined with the requirement of unity macroparticle weight described in this work, makes PIC simulations with reduced dimensions not applicable for strongly coupled plasmas.

To illustrate, for an ionization fraction of 10% at atmospheric pressure the ion density is 2.5×10^{24} m^{-3} and the corresponding average interparticle spacing in a 3D physical domain is $a_{ii} = (3/4\pi n_i)^{1/3} = 4.57 \times 10^{-9}$ m. However, if a 1D domain is used with unity macroparticle weight, the average interparticle distance in the simulation scales as $a_{ii}^{1D} = 1/n_i = 4 \times 10^{-25}$ m which is 16 orders of magnitude smaller and completely unphysical. Hence, it is clear that scaling down a problem to lower dimensions significantly affects the average interparticle spacing. This exacerbates the issues associated with applying PIC to strongly coupled plasmas.

CHAPTER VII

Artificial Correlation Heating in PIC simulations

7.1 Artificial correlation heating

In a PIC simulation, the typical use of macroparticles can alter the coupling strength for electron and ion species. This is observed when the effective coupling strength is artificially enhanced by a macroparticle weight $w > 1$, for example as detailed in section 6.2.3 and shown in figure 6.4. Consequently, a weakly coupled physical charged species can artificially transition to a strongly coupled macroparticle species. This condition, in conjunction with an average of less than one macroparticle per cell (a circumstance plausible at high plasma densities, where the Debye length is significantly decreased) instigates a novel numerical heating mechanism. This heating mechanism, similar to DIH but distinctively attributed to the macroparticle weight, is henceforth referred to as Artificial Correlation Heating (ACH).

7.1.1 Macroparticle coupling strength

When macroparticles are used, the numerical density, charge, temperature and average interparticle distance of macroparticles scale as $n_e^w \rightarrow n_e/w$, $q_e^w \rightarrow e\ w$, $T_e^w \rightarrow T_e\ w$ and $a_{ee}^w \rightarrow a_{ee}\ w^{1/3}$ respectively, where n_e, e, T_e and a_{ee} are the physical quantities for electron species and w is the macroparticle weight. To clarify, the physical temperature is an intensive quantity and it does not depend on the macroparticle

weight, however due to the scaling of the macroparticle kinetic energy with the mass, T_e^w is proportional to w [44]. Replacing these scaling laws in the equation for the Coulomb coupling parameter for electrons (1.7) we have equation 1.11,

$$\Gamma_{ee}^{w} = \frac{e^2}{4\pi\epsilon_0 a_{ee}} \frac{w^{2/3}}{k_B T_e} = \Gamma_{ee}\, w^{2/3}, \tag{7.1}$$

where Γ_{ee} represents the physical Coulomb coupling parameter of electrons. The $w^{2/3}$ factor indicates that when the macroparticle weight is significantly larger than unity, it could considerably increase the effective coupling strength between macroparticles. This in turn could artificially enhance the correlations between macroparticle electrons. Consequently, a plasma that is physically weakly coupled could be misrepresented as strongly coupled in a PIC simulation.

To illustrate, consider a plasma with an electron density of 1.25×10^{23} m^{-3} and an electron temperature of 3 eV. The electron Coulomb coupling parameter in this scenario is approximately 0.0387 which corresponds to the weakly coupled regime. If a PIC simulation is conducted with a timestep of 0.01 of the electron plasma period, a grid resolution of 0.3 the electron Debye length, and a moderate macroparticle weight w of 1000, electrons heat up significantly to a maximum temperature of 7.65 eV within 1.5 ω_{pe}^{-1} due to artificial correlation heating, as shown in figure 7.1. This nonphysical rise in the electron temperature is a consequence of a macroparticle coupling strength of approximately 3.87 (derived from equation 1.11), signifying strong coupling and thereby illustrating the potential impact of ACH. This is better observed in figure 7.2, where the evolution of the effective coupling strength between macroparticles decreases to a value of approximately 1.5 after 1.5 electron plasma periods. It is important to underscore that in a simulation with electron impact ionization collisions this process is potentially unstable, since an artificial heating of electrons could result in additional ionization that further increases the electron density and there-

$\Delta x/\lambda_{D_e}$	$\Delta x/a_{ee}^{w}$	N_c
0.3	0.088	0.00016
0.5	0.147	0.00072
0.9	0.264	0.0042
1.5	0.440	0.0194
3.0	0.881	0.1554
5.0	1.467	0.719

Table 7.1: Grid spacing and average number of macroparticles per cell for the numerical results shown in figure 7.1.

fore induces a further rise in the electron temperature due to ACH. This creates the potential for a runaway heating process.

7.1.2 Parameter space

Artificial correlation heating is observed not only because of a large, artificially enhanced, macroparticle coupling strength but also, a small number of macroparticles per cell. Hence, the artificially increased correlations between macroparticles are resolved by the grid. This is illustrated in figure 7.1, which shows that as the grid resolution increases, the maximum temperature due to ACH increases accordingly with a smaller average number of macroparticles per cell. The number of macroparticles per cell for each of these cases is shown in table 7.1. However, given an electron density and temperature, it is not possible to choose the grid resolution, macroparticle weight and number of macroparticles per cell independently. This is, the number of macroparticles per cell is an immediate consequence of the values chosen for the numerical parameters $(\Delta x/\lambda_{D_e}, w)$ given the physical values of (n_e, T_e). Hence, in scenarios where the combination of small number of macroparticles per cell and large macroparticle weight can happen, combined with a large electron density, ACH could significantly increase the electron temperature.

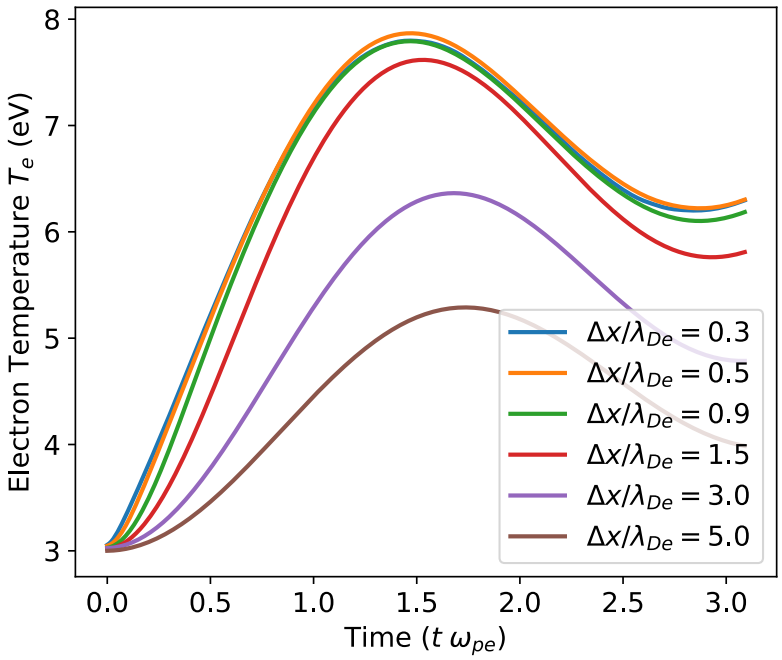

Figure 7.1: Evolution of the electron temperature for the first few electron plasma periods for different grid spacing. The electron density is 1.25×10^{23} m^{-3} and the macroparticle weight is 1000.

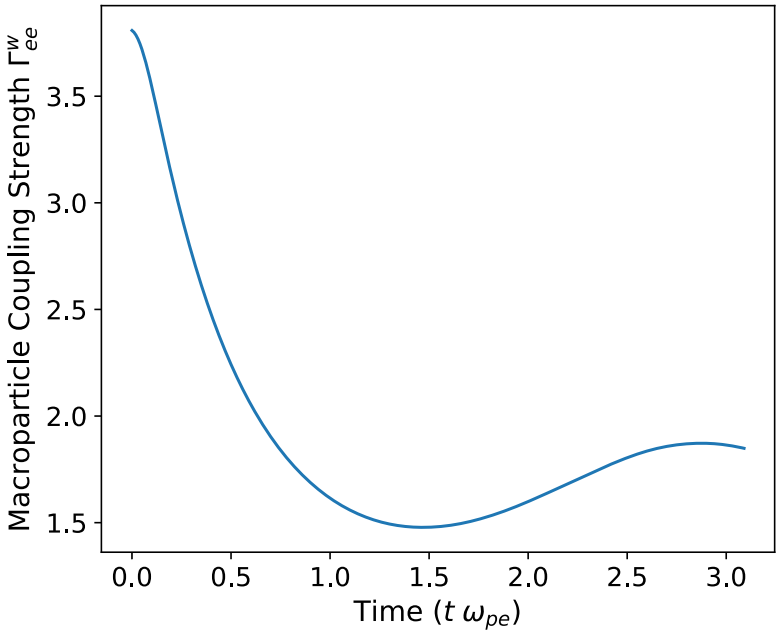

Figure 7.2: Evolution of the macroparticle coupling strength between electrons in a PIC simulation where ACH is observed. The macroparticle Γ^w_{ee} decreases to a value of approximately 1.5 after $1.5\omega_{pe}^{-1}$. A grid resolution of $0.3\lambda_{De}$ was used.

To gain a more nuanced understanding of artificial correlation heating, the following methodology was adopted. First, the grid resolution was set to $0.5\lambda_{De}$ across all simulations. A macroparticle weight was then fixed at a specific value. An initial electron temperature was selected, and different simulations were run varying the electron density until the change in T_e, $\Delta T_e = T_e^{\max} - T_e(0)$, due to ACH amounted to 5% of the initial electron temperature. Here, $T_e^{\max}$ corresponds to the electron temperature at $1.5\omega_{pe}^{-1}$. The corresponding value of n_e was recorded, and the process was repeated for different initial electron temperatures. Each data point corresponding to the set of parameters (n_e, T_e, w) represents an average across 50 simulations with different initial random seeds. This process was repeated for different macroparticle weights. Therefore, for each w, there exists a curve in the (n_e, T_e) parameter space that demarcates the limit of the applicability of PIC to restrict ACH to no more than 5% of the initial electron temperature. The region in which PIC is accurate lies to the left of the corresponding curve. Figure 7.3 shows the limiting curves for macroparticle weights of 10, 100 and 1000. As it is shown, the larger the macroparticle weight, the more limited is the density regime that can be simulated using PIC at a given temperature. This effect becomes more pronounced at smaller temperatures.

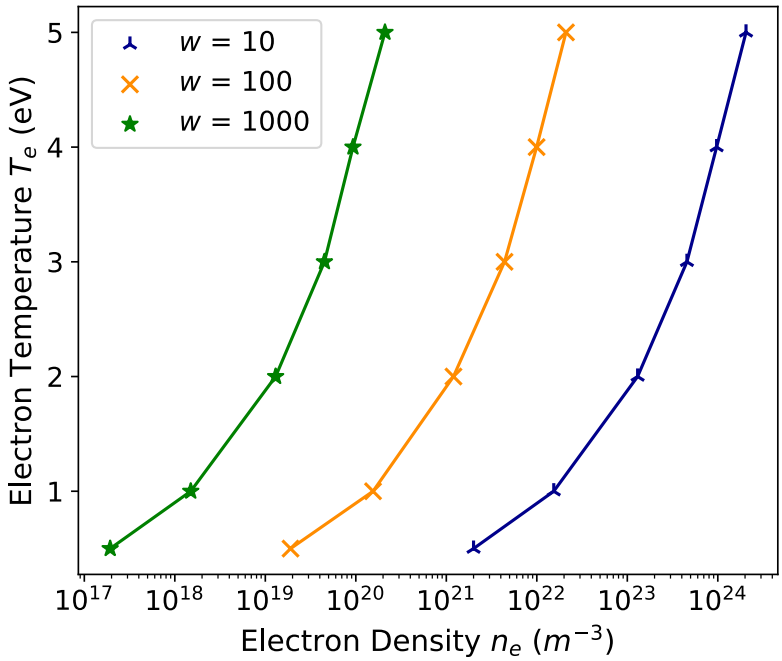

Figure 7.3: Artificial correlation heating limit curves for different macroparticle weights. The allowed operating region for PIC simulations is located on the left side of each curve.

For the results shown in figure 7.3, the input variables for the PIC simulations were (n_e, T_e, w, N_x) where N_x is the number of nodes in each direction and sets the size of the domain $L = (N_x - 1)\Delta x$. The grid spacing Δx was chosen as $\approx f\lambda_{D_e}$ where λ_{D_e} is the electron Debye length at the corresponding electron density and temperature and $f \approx 0.5$. The number of macroparticles in the domain is given by $N_e = n_e\, L^3/w$. The average number of macroparticles per cell is then $N_c = N_e/N_x^3$. Replacing the previous expressions in N_c, and assuming that $N_x \gg 1$,

$$N_c = \frac{f^3}{w} n_e \left(\frac{\epsilon_0 k_B T_e}{e^2 n_e} \right)^{3/2}. \tag{7.2}$$

Solving equation (7.2) for T_e,

$$T_e = \frac{N_c^{2/3}}{f^2} \left(\frac{e^2}{\epsilon_0 k_B} \right) (n_e w^2)^{1/3}, \tag{7.3}$$

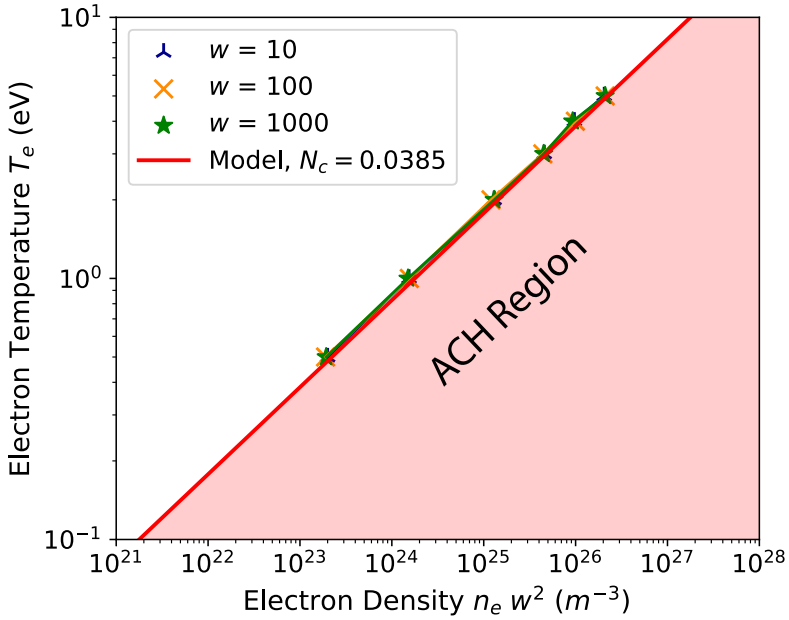

Figure 7.4: Limiting curve for ACH region from the model described in equation (7.3) and numerical results from 3D-PIC simulations.

gives an expression for the minimum electron temperature that can be simulated given the parameters $(N_c, \Delta x/\lambda_{D_e}, n_e, w)$. This minimum electron temperature directly depends on the desired number of macroparticles per cell N_c and the factor $n_e w^2$. It is observed that the chosen condition of a 5% temperature increase due to ACH, used as a criterion in the data shown in figure 7.3, is equivalent to a number of macroparticles per cell $N_c \approx 0.0385$ for all simulations. When this condition is applied to equation (7.3) with $f = 0.5$, the numerical data align with the curve defined by equation (7.3) in the $(T_e, n_e w^2)$ parameter space, as illustrated in figure 7.4.

On the right side of the limiting curve depicted in figure 7.4, artificial correlation heating significantly influences the electron temperature within a timescale dictated by the electron plasma period. In addition, on a longer timescale, grid heating arises even when the Debye length is resolved due to the use of a limited number of macroparticles per cell—a direct consequence of the specific density, temperature regimes, and macroparticle weights employed. This region is not advisable for simulations, as even partial adherence to these conditions within the simulation domain could dramatically

alter local electron dynamics. These findings considerably constrain the applicability of PIC simulations in scenarios of moderate electron temperatures and high ionization fractions or electron densities−an effect amplified by the high macroparticle weights inherent to the $n_e w^2$ scaling shown in equation (7.3). In addition, it is important to remark that ACH is not a consequence of non-energy conserving PIC schemes. ACH occurs as a consequence of the artificial increase in the Coulomb potential energy due to a large macroparticle weight. Hence, changing from a momentum-conserving to energy-conserving PIC scheme will not change the observed ACH at a given grid resolution. This is contrary to other sources of numerical heating, where for example, changing the PIC scheme can affect the growth rate of grid heating.

It is vital to emphasize that in simulations where the conditions conducive to artificial correlation heating could potentially be met, ACH initiates a positive feedback loop that enhances its effect. Specifically, once ACH occurs in simulations where ionization of a neutral gas is included, the resulting numerical increase in electron temperature can trigger nonphysical ionization events, which subsequently elevate the electron density. This in turn provokes further ACH, pushing the simulation conditions towards the right side of the diagram depicted in figure 7.4. The only way to evade ACH is by maintaining multiple macroparticles per cell. However, given certain conditions such as (n_e, T_e), a fraction of the Debye length to resolve, and a macroparticle weight, these parameters immediately determine the number of macroparticles per cell. Consequently, the ACH curve depicted in figure 7.4 represents the limit of applicability of PIC simulations for electrons. This holds true even when the physical coupling strength corresponds to the weakly coupled regime. The results shown here demonstrate that PIC simulations of typical plasmas (e.g. capacitively coupled plasmas conditions) end up requiring lower macroparticle weights than one might expect in order to maintain "many" computational particles per element if the element is sized to be roughly the Debye length.

In this chapter, we introduce a new constraint necessary to avoid ACH. This requires that the macroparticle coupling strength be smaller than one $\Gamma^w < 1$, where $\Gamma^w \equiv \Gamma w^{2/3}$, $\Gamma = Z^2e^2/(4\pi\epsilon_o a k_B T)$ is the physical coupling strength and w is the macroparticle weight. If this condition is violated, the finite macroparticle weight artificially enhances the coupling strength and causes the plasma to heat until the macroparticle coupling strength is near unity, depending on the grid resolution. A comprehensive model of ACH is developed that incorporates electron density, temperature, macroparticle weight, and grid resolution. It is then tested using PIC simulations, delineating the boundaries of the method's applicability and offering a predictive framework for ACH. Moreover, this chapter explores a runaway heating process induced by ACH in the presence of ionization, which can lead to numerical instability. A critical conclusion of this study is that the onset of ACH imposes more stringent constraints on the macroparticle weight and average number of macroparticles per cell than those typically employed in standard PIC simulations, thereby establishing a new limitation to the method's applicability.

7.2 PIC simulations

In the remaining of this chapter the simulation setup is such that in the absence of ACH, density and temperature remain constant in time. So any deviation from the initial density and temperature can be prescribed to a numerical error. The number of macroparticles used in each simulation was given by $N_e^w = n_e V/w$ where n_e is the electron density, V the volume of the simulation domain and w the macroparticle weight. The volume of the simulation domain was set by $V = L^3$ where $L = (N_x - 1)\Delta x$, N_x is the number of nodes in each direction and Δx the cell size. The simulation domain was cubic with periodic boundary conditions for fields and particles. The timestep used for all the simulations was $\Delta t = 10^{-2}\omega_{pe}^{-1}$, where $\omega_{pe} = (e^2 n_e/\epsilon_0 m_e)^{1/2}$ is the electron plasma frequency. The positions of the macroparticles were initialized

with a uniform random distribution and the velocities with a Maxwellian distribution at an initial temperature of 3 eV. No ion or neutral species were included since the objective of this part is to study artificial correlation heating of weakly coupled species, such as electrons, in a timescale given by ω_{pe}^{-1}. Thus, ions and neutrals remain stationary in the timescale of interest and are modeled as background uniform fluid. With this numerical setup, any increase of the electron temperature is attributable to a numerical error, particularly ACH or PIC heating.

In section 7.4.4, an ionization module is included to study the possibility of a positive feedback loop between ACH and electron-impact ionization. This is done by including a Monte Carlo collision routine [44] described in chapter II.

7.2.1 Artificial correlation heating

To provide a concrete example, consider a plasma with an electron density of 2.5×10^{19} m^{-3} and an electron temperature of 3 eV. In this case, the electron Coulomb coupling parameter is approximately $\Gamma_{ee} = 2 \times 10^{-3}$, indicative of a weakly coupled regime. Using a timestep of $10^{-2}\omega_{pe}^{-1}$, grid resolution $\Delta x/\lambda_{De} = 0.5$, and unity macroparticle weight ($w = 1$), no numerical heating is observed, as expected since $\Gamma_e^w \ll 1$; see Fig. 7.5. However, as the macroparticle weight is increased enough that $\Gamma_{ee}^w > 1$, significant ACH is observed despite $\Delta x/\lambda_{De} < 1$. For the particular case of $w = 10^5$, the electron temperature increases to a peak of 9 eV within $1.5\,\omega_{pe}^{-1}$. This rise in temperature is the result of a large macroparticle weight artificially increasing the coupling strength to a value of $\Gamma_{ee}^w = 4.87$, as deduced from Eq. (1.11).

The magnitude of this numerical heating is not solely attributable to the enhanced macroparticle coupling strength, but also the limited number of macroparticles per cell N_c. This is illustrated in Fig. 7.6. At a small macroparticle weight, the average number of macroparticles per cell is large enough that the distance between macroparticles is not resolved by the grid, $a_{ee}^w \ll \Delta x \approx \lambda_{De}$. Hence, the charge

density on the grid does not significantly change as particles move. However, if the macroparticle weight is increased while maintaining the cell size to resolve the Debye length, $\Delta x = 0.5\lambda_{De}$, this leads to an increased spatial resolution by the grid such that $a_{ee}^{w} \gtrsim \Delta x$. This increased grid resolution resolves the artificially enhanced repulsive electric field between macroparticles. This artificially enhanced electric field causes macroparticles to separate until the spatial configuration is such that the Coulomb potential energy is minimized, as shown in Fig. 7.6 (b). This process is similar to DIH [2], with the difference that the change in potential energy is artificially enhanced due to the large macroparticle weight and that the grid resolution influences the amount of heating that can be observed. Since the total energy is conserved in a simulation, the decrease in the potential energy leads to a significant increase in temperature, resulting in artificial heating.

The specific number of macroparticles per cell in the simulations shown in Fig. 7.5 is detailed in Table 7.2. It is crucial to note that the choice of grid resolution, macroparticle weight, and the number of macroparticles per cell are not independent variables but are related via the electron density and temperature (n_e, T_e). Specifically, the number of macroparticles in a cell $N_c = n_w \Delta x^3$, where $n_w = n/w$ is the macroparticle density, can be expressed in dimensionless form as

$$\frac{\Delta x}{\lambda_{De}} = \left(\frac{4\pi N_c}{3}\right)^{1/3} \sqrt{3\Gamma_{ee}^{w}}. \tag{7.4}$$

Simulations where a large macroparticle weight is used, such that $\Gamma_{ee}^{w} \gtrsim 1$, and the grid resolution resolves the Debye length, will inevitably lead to $N_c \ll 1$. As a consequence, the strong correlations will be resolved by the grid and ACH will be significant.

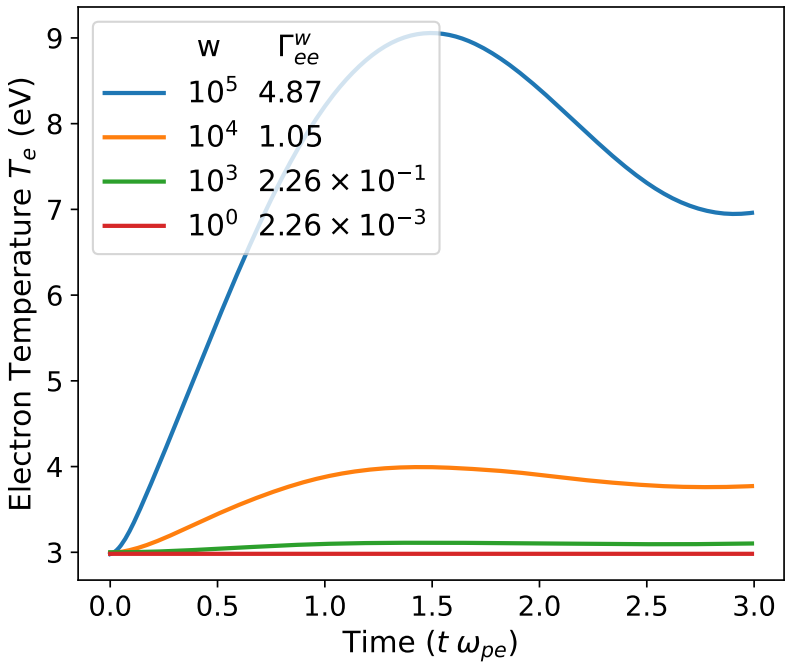

Figure 7.5: Evolution of the electron temperature during the first $3\omega_{pe}^{-1}$ of each simulation for an electron density of 2.5×10^{19} m^{-3}, an initial electron temperature $T_e = 3$ eV and an initial grid resolution of $\Delta x/\lambda_{De} = 0.5$ for different macroparticle weights.

w	N_c	Γ_{ee}^{w}	$\Delta x/a_{ee}^{w}$
1	5.34×10	2.26×10^{-3}	6.07
10^3	5.34×10^{-2}	2.26×10^{-1}	6.07×10^{-1}
10^4	5.34×10^{-3}	1.05	2.82×10^{-1}
10^5	5.34×10^{-4}	4.87	1.31×10^{-1}

Table 7.2: Parameters utilized in the PIC simulations shown in Fig. 7.5. The initial grid resolution was set as $\Delta x/\lambda_{De} = 0.5$.

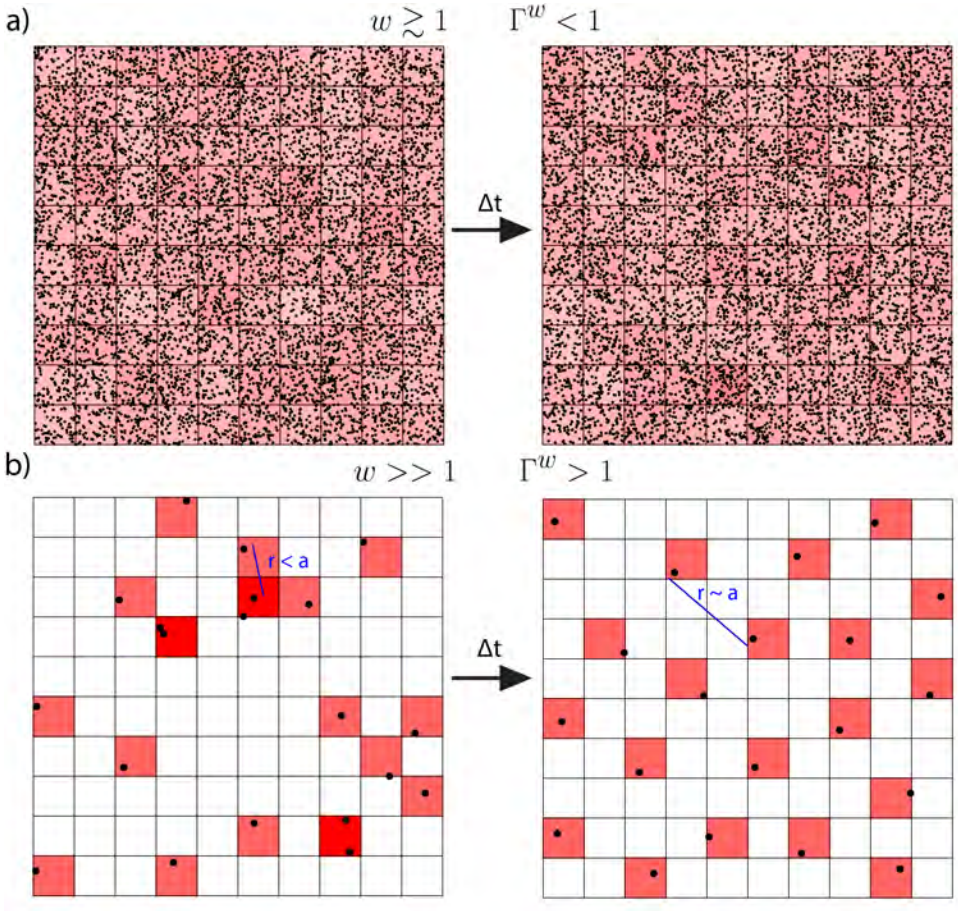

Figure 7.6: Illustration of the distribution of macroparticles in PIC simulations for (a) $w \gtrsim 1$, $\Gamma_{ee}^w < 1$ and $a_{ee}^w \ll \Delta x$ and (b) $w \gg 1$, $\Gamma_{ee}^w > 1$ and $a_{ee}^w \gtrsim \Delta x$ assuming a grid spacing of approximately the Debye length. The color intensity of each cell represents the local charge density. For $w \gtrsim 1$ the charge density is uniformly distributed within the grid for a uniform spatial configuration of macroparticles. However, for $w \gg 1$ the charge is localized in the few cells where macroparticles are located. Therefore, there is an artificially enhanced repulsive electric field that is resolved by the grid. This causes macroparticles to separate from each other in order to minimize the overall potential energy.

7.3 ACH model

Artificial correlation heating arises from macroparticles moving from an initially randomly distributed configuration to the lowest potential energy configuration, in the context of an artificially increased potential energy and a grid resolution that resolves the interparticle spacing, as shown in Fig. 7.6. The artificial increase in the potential energy arises as a consequence of a macroparticle weight larger than unity, as it was described in section 7.1. Here a theory model for ACH is described, based on the macroparticle effect on the potential energy and conservation of energy arguments. First, the potential energy is calculated from statistical mechanics. Then the change in potential energy from an initial uncorrelated state to an ordered state is calculated to predict the change in kinetic energy of macroparticles due to ACH. This model is then extended in section 7.4.2 to any grid resolution $\Delta x/a_{ee}^{w}$.

First, recall that the potential energy of electrons in an OCP system, from statistical mechanics, is given by [108]

$$\mathrm{PE} = \frac{n_e q_e^2 N_e}{2\epsilon_0} \int_0^\infty dr\ r\ g(r), \tag{7.5}$$

where N_e is the number of electrons and $g(r)$ is the electron-electron pair correlation function. The change in potential energy from the initial to final spatial configuration is then

$$\Delta\mathrm{PE} = \frac{n_e q_e^2 N_e}{2\epsilon_0} \int_0^\infty dr\ r\ \left[g^f(r) - g^0(r)\right] \tag{7.6}$$

where $g^f(r) = g(r)$ is the radial distribution function at the lowest potential configuration and $g^0(r) \approx 1$ at the initial uncorrelated state. The integral $I^* = \int_0^\infty d\tilde{r}\ \tilde{r}\,[g(\tilde{r}) - 1]$, where $\tilde{r} = r/a_{ee}$, depends exclusively on the Coulomb coupling parameter as described in chapter III and is shown in Fig. 3.21, where the smaller the coupling parameter, the smaller the change in potential energy. A fit to this integral is was

obtained using the function

$$I^*(\Gamma) = \frac{a}{(b+\Gamma)^c} + d \tag{7.7}$$

with the parameter values $a = 0.6032$, $b = 0.0372$, $c = 0.1549$ and $d = -0.9917$.

Here, the solution for $g(r)$ used to solve the integral I^* was obtained by solving the Ornstein-Zernike equation with the hypernetted chain approximation as a closure [108], as described in chapter III. The hypernetted chain approximation has been shown to be an accurate closure to model the radial distribution function for a one component plasma across different coupling regimes [104, 108, 121].

Due to conservation of energy, the change in potential energy is balanced by a change in kinetic energy

$$\Delta \text{KE} = \frac{3}{2} N_e k_B \Delta T_e = -\Delta \text{PE}, \tag{7.8}$$

where KE is the total kinetic energy. Combining Eqs. (7.6) and (7.8) and accounting for the scaling of T_e, n_e, and a_{ee} with the macroparticle weight w, the equation for the electron temperature increase due to ACH in a PIC simulation is

$$\frac{n_e q_e^2 a_{ee}^2}{2\epsilon_0} I^*(\Gamma_{ee}^{\min,w})\, w^{2/3} + \frac{3}{2} k_B \left(T_e^{\max} - T_e^0\right) = 0. \tag{7.9}$$

Here, $T_e^{\max}$ is the maximum electron temperature due to ACH and $\Gamma_{ee}^{\min,w}$ is the macroparticle coupling parameter that corresponds to this temperature. Eq. (7.9) can be solved iteratively to find a solution for $T_e^{\max}$ given the parameters n_e, w and T_e^0. It is important to underscore that the temperature $T_e^{\max}$ predicted with this model neglects the effect of the grid resolution, thus, it assumes that the average distance between macroparticles is resolved by the grid, thus $N_c \ll 1$. Modifications to account for the grid resolution are provided in Sec. 7.4.2.

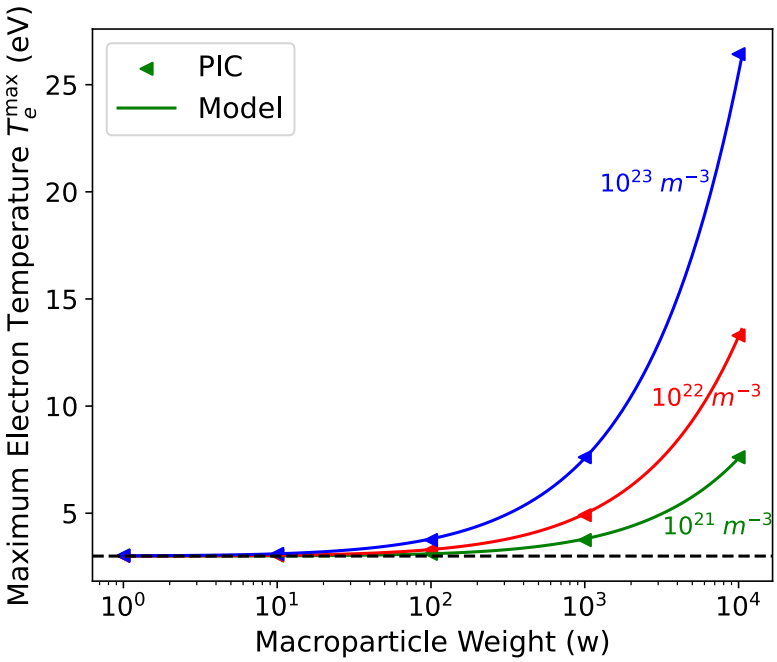

Figure 7.7: Maximum electron temperature obtained from the set of simulations with parameters indicated in Table 7.3. The maximum electron temperature increases with the electron density and macroparticle weight due to the corresponding increase in the initial Γ_{ee}^{w} value.

7.4 Discussion

7.4.1 Limit of fine grid resolution

Figure 7.7 illustrates the maximum electron temperature obtained from PIC simulations across different electron densities and macroparticle weights. Each simulation was conducted with a grid spacing of approximately $\Delta x/a_{ee}^{w} \approx 0.1$, resulting in an average of $N_c = 2.35 \times 10^{-4}$ macroparticles per cell. In this limit, the grid resolves the average distance between macroparticles. The specific parameters employed in these simulations are detailed in Table 7.3. It is clear that as the density and macroparticle weight increases, the influence of ACH on the electron temperature becomes more significant. This agrees with the fact that increasing both n_e and w increases the macroparticle coupling parameter Γ_{ee}^{w}. The theoretical model demonstrates good agreement with the PIC simulation results, showing its validity.

n_e (m^{-3})	w	Γ_{ee}^{w}	$\Delta x/\lambda_{De}$
10^{21}	1	7.74×10^{-3}	1.52×10^{-2}
	10^2	1.67×10^{-1}	7.07×10^{-2}
	10^4	3.60	3.28×10^{-1}
10^{22}	1	1.67×10^{-2}	2.24×10^{-2}
	10^2	3.60×10^{-1}	1.04×10^{-1}
	10^4	7.74	4.82×10^{-1}
10^{23}	1	3.60×10^{-2}	3.28×10^{-2}
	10^2	7.74×10^{-1}	1.52×10^{-1}
	10^4	1.67×10	7.07×10^{-1}

Table 7.3: Parameters used in the PIC simulations shown in Fig. 7.7. The initial grid resolution was set as $\Delta x/a_{ee}^{w} = 0.1$ which corresponds to an average number of macroparticles per cell of $N_c = 2.35 \times 10^{-4}$.

7.4.2 Effect of grid resolution

The results in section 7.1 indicated that the grid resolution has an impact on the temperature increase due to ACH. To further investigate this effect, a series of simulations were executed varying the grid resolution alongside different electron densities and macroparticle weights. In this set of simulations, for each combination of parameters, 20 independent simulations with different initial random seeds were conducted and the maximum temperatures were averaged. Table 7.4 show the parameters used. The outcomes, presented in Fig. 7.8 (a), reveal that an increase in cell size correlates with a reduction in ACH, which is attributed to an increase in the average number of macroparticles per cell $N_c = (3/4\pi)(\Delta x/a_{ee}^{w})^3$, as illustrated in Fig. 7.6. This increase in the cell size leads to a failure to resolve the artificially enhanced correlations, decreasing ACH.

This phenomenon is better understood by analyzing the radial distribution function obtained from PIC for a specific case of $n_e = 10^{22}$ m^{-3} and $w = 1000$, as depicted in Fig. 7.9. An increase in cell size leads to an increase in the $g(r)$ at short distances. This is a consequence of the underestimation of the Coulomb potential within a cell, inherent to the PIC method. At a threshold where $\Delta x/a_{ee}^{w} \gtrsim 7$, the $g(r)$ converges to that of an uncorrelated state and therefore ACH is effectively turned off. The nu-

merical grid used in PIC simulations makes the potential around a charged particle asymmetric. Hence, the HNC approximation no longer serves as an accurate tool to determine the $g(r)$, necessitating an alternative approach to model grid resolution effects.

Instead of modeling the grid resolution effect from the $g(r)$, a fit to the simulated temperature increase is provided. The dimensionless electron temperature $\tilde{T}_e$, defined as

$$\tilde{T}_e \equiv \frac{T_e - T_e^0}{T_e^{\max} - T_e^0}, \tag{7.10}$$

is shown in Fig. 7.8 (b). All simulations align along a single curve when the dimensionless temperature is shown as a function of grid resolution. A fitting function

$$\tilde{T}_e = \frac{1}{1 + A\,(\Delta x / a_{ee}^w)^B} \tag{7.11}$$

was applied to the simulation data, yielding coefficients $A = 0.606$ and $B = 1.767$. This fit agrees well with the simulated value. To integrate this finding into the model described in Sec. 7.3, the electron temperature influenced by ACH as a function of grid resolution can be expressed as

$$T_e\left(\frac{\Delta x}{a_{ee}^w}\right) = \frac{T_e^{\max}(n_e, T_e^0, w) - T_e^0}{1 + 0.606(\Delta x / a_{ee}^w)^{1.767}} + T_e^0. \tag{7.12}$$

Here, $T_e^{\max}$ is derived by solving Eq. (7.9) with the input parameters n_e, T_e^0, and w. As shown in Fig. 7.8 (a), the electron temperatures predicted by Eq. (7.12) closely match those observed in the PIC simulations, making the model given by Eqs. (7.9) and (7.12) a useful tool to predict ACH at any conditions and grid resolution.

It is important to underscore that avoiding ACH when $\Gamma_{ee}^w \gtrsim 1$ requires that the grid resolution be $\Delta x / a_{ee}^w \gtrsim 10$. This is equivalent to a number of particles per cell of $N_c \gtrsim 240$, a value significantly larger than what is typically required in

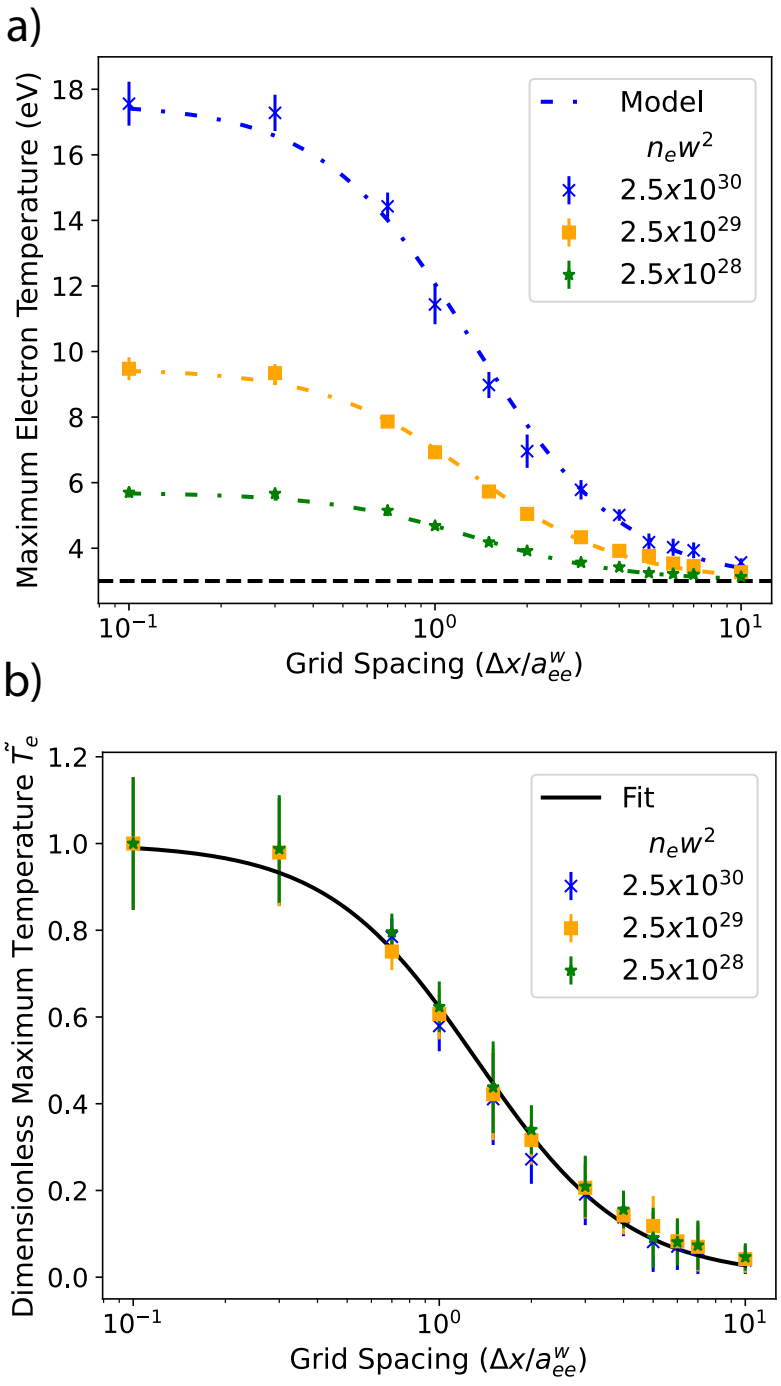

Figure 7.8: a) Maximum electron temperature obtained from the set of PIC simulations run with the parameters shown in Table 7.4. Labels indicate the product $n_e w^2$. b) Dimensionless electron temperature $\tilde{T}_e$ as a function of the grid spacing.

n_e (m^{-3}) ($2.5\times$)	w	Γ_{ee}	Γ_{ee}^w	$\Delta x/a_{ee}^w$	N_c ($2.37\times$)	$\Delta x/\lambda_{De}$
10^{20}	10^5	4.87×10^{-3}	10.50	10^{-1}	10^{-4}	0.561
				1	10^{-1}	5.61
				10	10^2	56.1
10^{23}	10^3	4.87×10^{-2}	4.87	10^{-1}	10^{-4}	0.382
				1	10^{-1}	3.82
				10	10^2	38.2
10^{24}	10^2	1.05×10^{-1}	2.26	10^{-1}	10^{-4}	0.261
				1	10^{-1}	2.61
				10	10^2	26.1

Table 7.4: Parameters used to study the effect of the grid resolution on ACH shown in Fig. 7.8.

standard PIC simulations. According to Eq. (7.4), this requirement leads to under-resolving the Debye length when $\Gamma_{ee}^w \geq 1$. Thus, avoiding ACH by reducing the grid resolution is not a viable option since not resolving the Debye length will generally lead to traditional PIC heating on timescales much longer than the plasma period. [44]. Therefore, ACH imposes an additional constraint on PIC simulations, necessitating careful consideration when modeling plasmas with large macroparticle weights.

7.4.3 Effect of shape function order

As shown in chapter VI, the order of shape functions used in a PIC simulation can affect how well correlations are resolved [122]. As the order of shape function is increased, correlations are smoothed out, effectively decreasing the artificially enhanced electric field. As a result, ACH would be expected to decrease with order of the shape function. To test how this influences ACH, the set of simulations with $n_e = 2.5 \times 10^{23}$ m^{-3} from Table 7.4 was repeated but varying the order of shape functions from 2 to 6. [77] Figure 7.10 shows the obtained maximum electron temperature for each simulation as a function of the grid resolution. It is observed that as the order of the shape function is increased, ACH does decrease. However, this effect does not make a significant enough change to justify the use of higher order shape

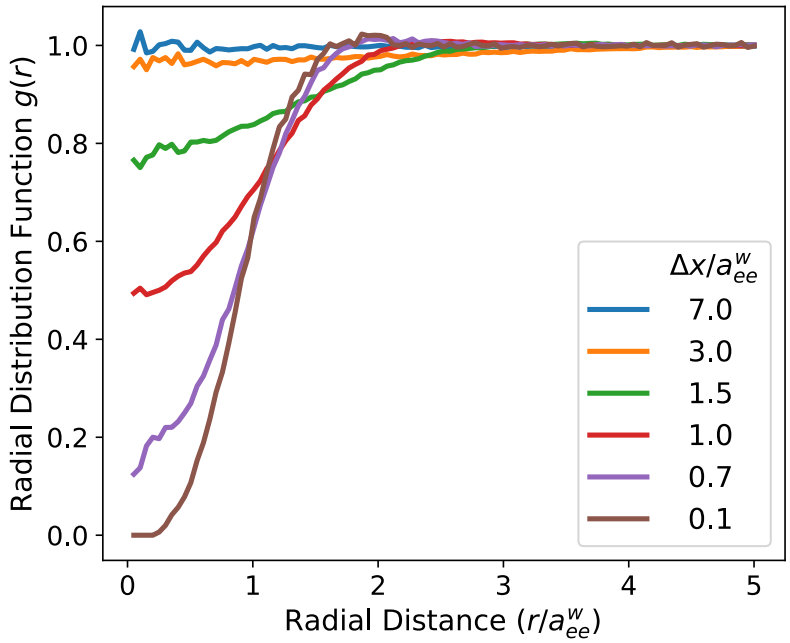

Figure 7.9: Radial distribution function obtained from PIC simulations run at different grid resolutions for an electron density of $n_e = 2.5 \times 10^{23}$ m^{-3} and a macroparticle weight of 1000.

functions to control ACH. On the contrary, as stated in the grid resolution effect analysis, increasing the cell size such that a minimum number of macroparticles per cell of $\gtrsim 240$ is reached can avoid observing ACH without an increase in computational cost. However, this last approach leads to a decrease of the grid resolution in terms of the Debye length, which can trigger PIC heating on a longer timescale.

7.4.4 Numerical instability produced by ACH and ionization

Artificial correlation heating is potentially unstable in PIC simulations when ionization of a neutral gas is included. This can happen when the bulk of the electron energy distribution function is below the peak ionization cross section energy and thus increasing the temperature will increase the ionization rate. For high temperature plasmas, O(100eV), the ionization cross section decreases with increasing energy so there should be no instability. However, for low temperature plasmas, O(1eV), the temperature rise due to ACH will significantly increase the ionization rate through

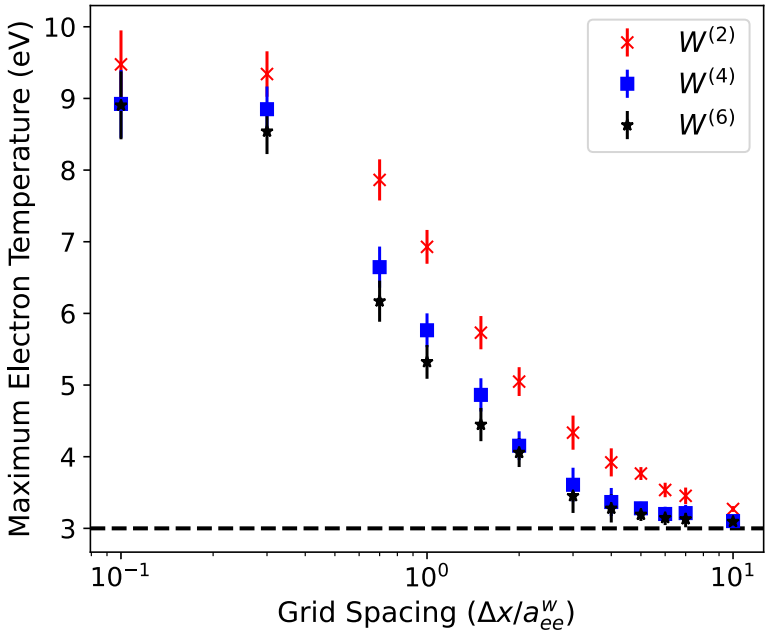

Figure 7.10: Maximum electron temperature obtained from PIC simulations for an electron density of $n_e = 2.5 \times 10^{23}$ m^{-3}, a macroparticle weight $w = 1000$, and varying the grid resolution and the shape function order.

the steep electron energy dependence of the electron-neutral impact ionization cross section in the few eV energy range; see for example Ref. [78]. The increase in the ionization rate following ACH corresponds to an artificial increase in the electron density, which then leads to more ACH, further increasing the electron temperature and potentially inducing a runaway heating process. To study the possibility of this runaway process, a set of simulations were run at an initial electron density of $n_e = 2.5 \times 10^{19}$ m^{-3}, temperature $T_e = 3$ eV and initial grid resolution $\Delta x/\lambda_{De} = 0.5$, varying the macroparticle weight from 1 to 10^5 as indicated in Table 7.5. Each simulation was repeated 20 times varying the random seed number and the results displayed are the average of all the simulations.

Figure 7.11 (a) shows the evolution of the electron temperature for each simulation over approximately 8 ps. It is clear that if the macroparticle weight is large enough that $\Gamma_{ee}^{w} > 1$, ACH significantly increases the electron temperature and that this considerably increases the ionization rate, as shown in Fig. 7.11 (c). Here, the

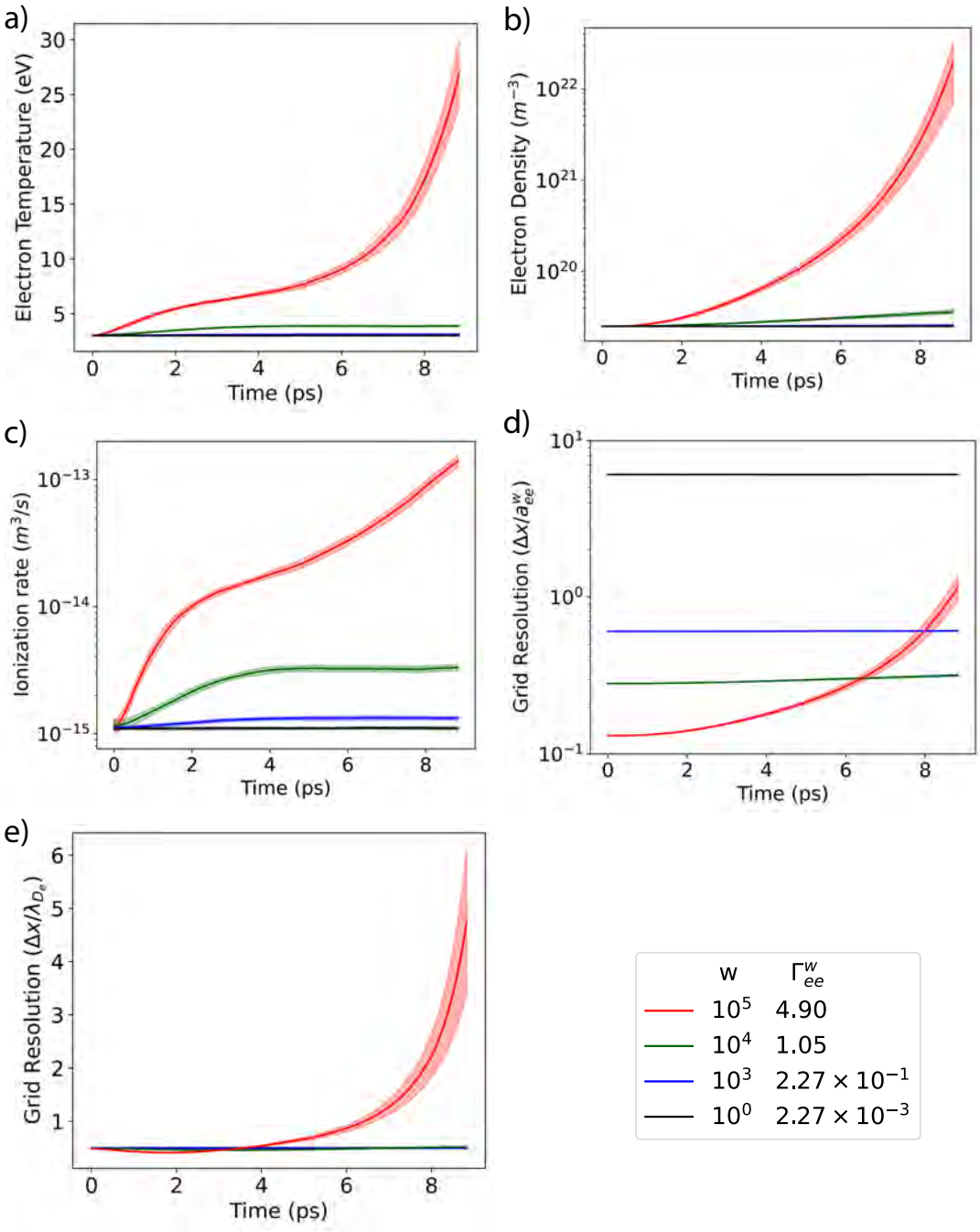

Figure 7.11: Evolution of: a) the electron temperature, b) electron density, c) ionization rate, d) grid resolution compared to the average distance between macroparticles, and e) grid resolution compared to the electron Debye length, for the PIC simulations described in Table 7.5. Simulations with a macroparticle weight large enough to satisfy the $\Gamma^w_{ee} > 1$ criterion are observed to be subject to ACH, which induces a runaway process that increases the electron density faster than an exponential curve. When the macroparticle weight is increased from 10^3 to 10^5 the ionization rate increases several orders of magnitude due to ACH and the runaway heating process.

$n_e(\mathrm{m}^{-3})$ $(2.5\times)$	Γ_{ee} $(2.3\times)$	$\Delta x/\lambda_{De}$	w	Γ_{ee}^{w}	$\Delta x/a_{ee}^{w}$	N_c $(4.9\times)$
10^{19}	10^{-3}	0.50	1.0	2.3×10^{-3}	6.1	10^{1}
			10^{3}	2.2×10^{-1}	0.61	10^{-2}
			10^{4}	1.1	0.28	10^{-3}
			10^{5}	4.9	0.13	10^{-4}

Table 7.5: Parameters used in the PIC simulations to study the effect of ACH combined with ionization as shown in Fig. 7.11. Here, the simulation domain and cell size Δx remain constant during each simulation.

ionization rate is calculated from the Xe electron-impact ionization cross section [78] and a Maxwellian distribution at the corresponding electron temperature. Comparing the curves in Fig. 7.11 (c) with macroparticle weights from 10^3 to 10^5 it is noticeable how the ionization rate can significantly increase by one or more orders of magnitude. This is reflected as an increase in the electron density with time at a faster than an exponential rate, as shown in Fig. 7.11 (b).

Since the simulation domain volume as well as the cell size Δx remains constant, increases in density and temperature affect the grid resolution. Figures 7.11 (d) and (e) show how the grid resolution changes in terms of the interparticle distance and the electron Debye length respectively. It is clear from Fig. 7.11 (d), that fixing the initial grid resolution $\Delta x/\lambda_{De} = 0.5$ but increasing the macroparticle weight improves the grid resolution in comparison with the average interparticle distance. As was demonstrated in Sec. 7.4.2, a grid that resolves a_{ee}^{w} is necessary for ACH to occur. It is also observed that for the case $w = 10^5$, the significant change in the electron density increases $\Delta x/a_{ee}^{w}$ and $\Delta x/\lambda_{De}$ over time, potentially limiting ACH after the density has built up sufficiently. It is noteworthy that this implies that if an adaptive mesh refinement method were used to maintain $\Delta x/\lambda_{De} = 0.5$, ACH would be larger than what was observed here; further increasing the temperature and, thus, electron density to values larger than what it is shown in Fig. 7.11 (a) and (b).

A conclusion is that ACH combined with ionization can lead to a runaway heating mechanism.

7.4.5 Artificial correlation heating in reduced dimensions

As described in section 6.2.5, running PIC simulations in reduced spatial dimensions is a common approach for systems with some kind of spatial symmetry. When using reduced spatial dimensions, the positions of all particles within the physical volume are projected onto an element in the corresponding reduced dimension [48]. As discussed, this method reduces the distance between numerical particles. Hence, if the physical Debye length is resolved and a lower dimensionality of a problem is simulated, the average number of macroparticles per cell is significantly increased. This considerably reduces ACH making it relevant only in 3D PIC simulations.

7.4.6 Limit of applicability of the PIC method and stability criteria

From the results obtained in this work, it is clear that ACH limits how high the electron density and macroparticle weight can be at a given electron temperature and grid resolution, and that it can be avoided if the $\Gamma^w < 1$ condition is met. However, it also shows that if the $\Gamma^w < 1$ condition is violated, the magnitude of the resulting ACH depends on the grid resolution and number of particles per cell. It is possible that a small amount of ACH is tolerable. To understand this limit of applicability of PIC simulations, the model given by Eqs. (7.9) and (7.12) was utilized to find the limiting curve defined by a 5% of electron heating due to ACH for a range of initial electron temperatures. This is, at each possible T_e and at a fixed $\Delta x/\lambda_{De}$, the model is solved for increasing values of $n_e w^2$ until a temperature increase of 5% is predicted. This defines a limiting curve for each grid resolution $\Delta x/\lambda_{De}$ at which only lower values of $n_e w^2$ can be simulated in order to avoid ACH. Figure 7.12 shows the limiting curves obtained for grid resolutions $\Delta x/\lambda_{De}$ from 0.1 to 5. As the grid

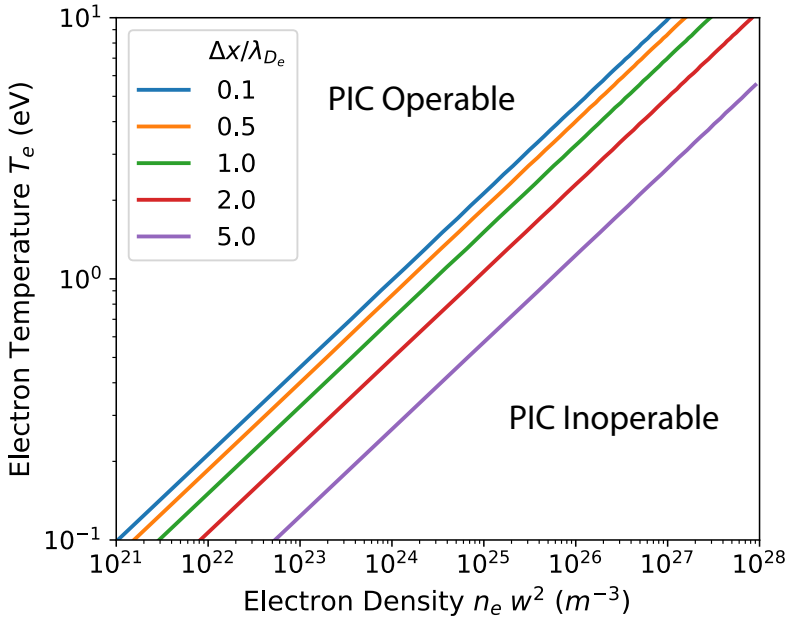

Figure 7.12: Limiting curves for the PIC method in the electron temperature vs $n_e w^2$ parameter space. Each curve was obtained with a different grid resolution $\Delta x/\lambda_{De}$ ranging from 0.1 to 5. The ACH region lies on the right side of each curve.

spacing increases, ACH becomes less important and the limiting curve shifts to higher $n_e w^2$, increasing the allowed parameter space. However, ideally the electron Debye length should be resolved in order to avoid PIC heating, this implies that there is a range of $n_e w^2$ values at each temperature that cannot be simulated using the PIC method.

Sometimes it is not imperative to resolve the Debye length and the consequent PIC heating can be controlled by using energy conserving integration schemes, as well as higher order shape functions and filtering methods [46, 115, 116, 117, 118, 119, 120]. In such cases, instead of avoiding ACH by reducing the macroparticle weight until $\Gamma_{ee}^{w} \leq 1$, it can be controlled by increasing the cell size as described in section 7.4.2. This can also be observed from Fig. 7.12, where as $\Delta x/\lambda_{De}$ is increased, the ACH limiting curve shifts to higher $n_e w^2$ values.

Figure 7.13 provides a simple procedure for ensuring that ACH remains below a tolerable level in PIC simulations. Once the input parameters (n_e, T_e, w) are chosen,

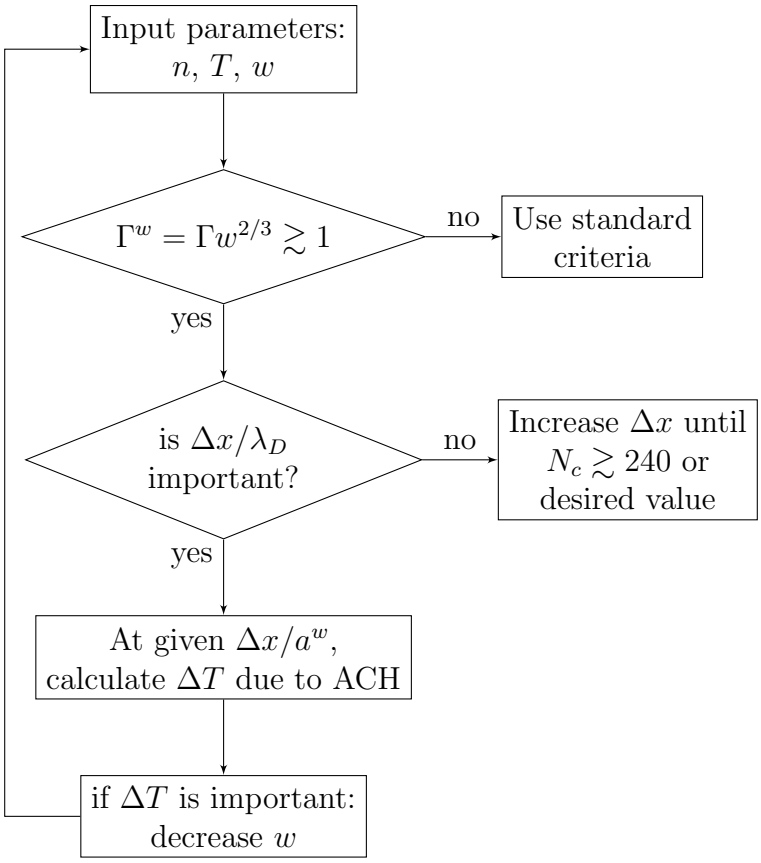

Figure 7.13: Diagram illustrating the general procedure that should be used to choose PIC input parameters $(n, T, \Delta x/\lambda_D, w)$ in order to avoid ACH.

the macroparticle coupling parameter should be calculated using Eq. (1.11). If $\Gamma_{ee}^w \leq 1$, then the standard PIC criteria can be used. However, if $\Gamma_{ee}^w \geq 1$, the remaining question to ask is if it is necessary to resolve the electron Debye length [46, 115, 116, 117, 118, 119, 120]. If the cell size Δx can be larger than the Debye length, then to avoid or control ACH Δx should be increased until $N_c \approx 240$. However, if the Debye length must be resolved, the temperature increase due to ACH can be calculated using Eqs. (7.12) and (7.9). If the expected temperature increase is significant for a particular application, then one must reduce the macroparticle weight w until ACH is reduced to a tolerable level.

CHAPTER VIII

Conclusion

The work presented in this dissertation demonstrates that ions are strongly coupled in atmospheric pressure plasmas influencing the ion and neutral gas temperatures as well as transport coefficients such as diffusion. Finally, PIC simulations are studied in the context of strong correlations.

In chapter III molecular dynamics simulations reveal that after an instant ionization pulse the ion and neutral temperatures in atmospheric pressure plasmas are influenced by an associated disorder induced heating process [2]. Disorder-induced heating is not important in weakly coupled plasmas, but can be a dominant effect in strongly coupled plasmas. It causes ions to rapidly heat to temperatures that can reach several times the background neutral gas temperature. After DIH, ions thermally equilibrate with neutrals causing them to cool and the neutrals to heat by an amount and at a rate that depends on the ionization fraction. The cooling causes ions to return to a more strongly coupled state. Due to DIH and ion-neutral temperature relaxation, the final neutral gas temperature depends on the ionization degree achieved at plasma formation. We show that at atmospheric pressure, DIH is significant for ionization fractions larger than $x_i \gtrsim 10^{-2}$ and thus, it could be important for experiments that involve nanosecond pulsed discharges, laser-produced plasmas, or other sources that achieve high ionization fractions. Furthermore, the instant ioniza-

tion approximation is relaxed to a gradual arbitrary ionization rate showing that DIH does not depend on the ionization dynamics, instead it depends on the changes in the ion density since it is a consequence of conservation of energy. Hence, DIH happens gradually as the neutral gas is ionized [5]. Additionally, DIH does not depend on the gas composition in the sense that it only depends on the total ion density. In a gradual ionization process, if the ionization fraction is large enough, DIH can significantly increase the ion temperature, then ions heat the neutral gas through collisions. A model for DIH in both instant and gradual ionization cases is developed and validated against molecular dynamics simulations.

The combination of DIH followed by ion-neutral temperature relaxation provides a new mechanism for fast gas heating that can increase the gas temperature by several thousand degrees on a nanosecond timescale. These results are of particular interest in the context of nanosecond pulsed discharges at atmospheric pressure and above. In these discharges, fast gas heating mechanisms have been traditionally studied from a plasma chemistry standpoint, including mechanisms such as dissociation and quenching of excited states [6, 21, 31, 72, 91]. In chapter IV, the model developed for DIH is integrated into a global plasma chemistry model of a nanosecond pulsed nitrogen discharge at one and ten atmospheres. Simulations show that while DIH is not the dominant heating mechanism at atmospheric pressure it can contribute for up to 20% of the final temperature if full ionization is reached. Additionally, at ionization fractions above 10% electrons and ions are at equilibrium. Hence, the energy released due to DIH indirectly influences the electron temperature, increasing the rate of inelastic processes such as dissociation and ionization. This effect becomes more important as the pressure increases since DIH scales with the total ion density. At ten atmospheres and full ionization, DIH increases the final temperature by 60%. It is important to underscore that the results studied in this work are conducted for nitrogen discharges. However, DIH could have a stronger impact in discharges with gases that have less

electron impact inelastic processes or where those processes require less energy. Finally, while the maximum pressure studied here is ten atmospheres, at larger pressures DIH could significantly affect the plasma chemistry, as long as the initial neutral gas configurations is uncorrelated.

Increasing interest has been shown in partially ionized plasmas at atmospheric pressure and above for applications ranging from CO_2 conversion [11, 67] to plasma medicine [123] and plasma assisted combustion [12, 13, 69, 70, 71]. In most of these applications, diffusion processes are of main importance in the plasma dynamics and transport of reactive species. Furthermore, one of the most used simulation techniques is multifluid models where diffusion coefficients are required as input variables. In chapter V, we show that strong Coulomb coupling effects can significantly influence diffusion processes at these conditions [114]. Considering elastic collisions, we find that the ion diffusion is characterized by three regimes as a function of the ionization degree at atmospheric pressure. First, ion-neutral collisions are dominant at small ionization fractions ($x_i < 10^{-6}$), setting the ion diffusion coefficient via weakly coupled ion-neutral interactions. A transition between ion-neutral to ion-ion collision dominated regimes occurs at a ionization fraction of $10^{-6} \lesssim x_i \lesssim 10^{-2}$. For larger ionization degrees, ion-ion collisions dominate and the the strong correlations influence the ion diffusion coefficient. These strong ion-ion correlations are accounted for using the mean force kinetic theory and including a modified Enskog correction factor for the excluded volume due to the repulsive force and large coupling strength. Furthermore, DIH is accounted for and the corresponding temperature increase at large ionization fractions ($x_i > 10^{-2}$) affects the ion diffusion coefficient as well as the neutral diffusion coefficient. This effect becomes more significant at larger pressures. Finally, a molecular dynamics Monte Carlo Collision (MD+MCC) simulation setup was implemented in LAMMPS to simulate a partially ionized Ar plasma at atmospheric pressure for ionization fractions from 10^{-9} to 1 showing a good agreement

with the theory model. This provides a tested theoretical model for diffusion that may be implemented to account for strong ion effects on diffusion in fluid simulations of atmospheric pressure plasmas.

Particle-In-Cell (PIC) simulations have been a long-standing, essential tool in plasma modeling due to their ability to make kinetic simulations accessible at device-relevant scales. Currently, there is a concerted effort to extend the application of PIC simulations to model plasmas at atmospheric pressure. In chapter VI, we show that standard PIC simulations are only applicable to weakly coupled plasmas. Furthermore, when used to model strongly coupled plasmas, such as ions at atmospheric pressure, PIC requires additional constraints to capture phenomena like disorder induced heating. Firstly, a fraction of 0.1 of the average interparticle spacing needs to be resolved in order to observe DIH, which on average results in less than one macroparticle per cell. Secondly, a unity macroparticle weight must be used. If the macroparticle weight is larger than the unity, it significantly influences the Coulomb potential energy due to a numerical localization of the electric charge, enhancing the electric field and the effective coupling strength, thus influencing the ion dynamics and temperature. These constraints considerably increase the computational cost of PIC for strongly coupled plasmas, rendering it impractical for device scale modeling.

In addition, if PIC is operated with these additional constraints, grid heating is inevitable due to the presence of less than one macroparticle per cell and high coupling strength. Attempts to reduce the growth rate of grid heating with filtering methods or high order shape functions delocalize the charge density, artificially decreasing the coupling strength of the system and influencing the ion dynamics and temperature. Moreover, it is found that PIC simulations with reduced spatial dimensions are not suitable for strongly coupled plasmas. The scaling of the physical density in 1D or 2D simulations artificially decreases the average interparticle spacing which needs to be resolved to capture the strong correlations. A primary conclusion drawn from the

presented results is that standard PIC simulations, are not suitable for strongly coupled plasmas. This places constraints on their applicability to atmospheric pressure plasmas to a sufficiently low density regime.

Chapter VII describes a novel numerical heating mechanism observed in PIC simulations, Artificial Correlation Heating. A comprehensive model for ACH is developed that incorporates variables such as electron density, temperature, macroparticle weight, and grid resolution. This model, validated against PIC simulations, maps out a new limit of the PIC method's applicability and provides a predictive tool for anticipating the influence of ACH on the electron temperature. The results can also be applied to ACH of ions in an analogous way. Its accuracy in predicting the onset and magnitude of ACH provides an instrument for a more reliable application of the PIC method in various plasma applications.

One of the key insights is understanding how ACH occurs. ACH is similar to the physical effect of DIH that arises in strongly coupled plasmas [2], but here is an artificial numerical effect that is introduced by a large macroparticle weight. Like DIH, it is caused by the Coulomb repulsion between particles, which causes them to move to the lowest potential configuration. During this spatial reordering there is a conversion of potential to kinetic energy that arises at strong coupling, with the difference that here the strong coupling is induced artificially by a large macroparticle weight.

The findings highlight that careful selection of parameters like grid resolution and macroparticle weight is crucial to avoid ACH. Moreover, the study brings to light the identification of a runaway heating process induced by ACH, particularly in simulations that include ionization. This produces a numerical instability capable of increasing the plasma density by several orders of magnitude on a short timescale, exposing the importance of identifying and avoiding ACH. The main takeaway of this study is that it describes an upper limit of applicability of the PIC method in terms

of the macroparticle weight and grid resolution. A general procedure is provided to guide on how to properly choose PIC input parameters in order to avoid or control ACH.

Future work will focus on extending the analysis presented in Chapters III and IV to higher pressures. Notably, as pressures exceed 10 atm, disorder-induced heating (DIH) could emerge as a significant and possibly dominant mechanism, impacting not only the overall temperature but also the plasma chemistry. The potential influence in the plasma chemistry arises from the anticipated high electron-ion collisionality at elevated pressures and ionization degrees. Additionally, discharges in water represent a current topic of interest within the community. In these environments, the initial neutral particles are present at densities a thousand times greater than at atmospheric pressure. While the ionization dynamics under such conditions remain poorly understood, a pivotal unresolved question is whether DIH could play a crucial role, given the potential limitations imposed by the initial correlated state of neutral particles.

APPENDIX

APPENDIX A

Equilibrium MD Simulations

An analysis was realized varying the radius r_ϕ of the charge induced dipole potential. For this analysis the simulation setup consisted of an NVT (canonical) simulation using the Nosé–Hoover thermostat, where the temperature was set to 293 K, over 1500 plasma periods. This was followed by an NVE (microcanonical) simulation for 1500 plasma periods. The timestep used varied with r_ϕ since smaller r_ϕ led to larger attractive forces and smaller timesteps were required. The timesteps used varied from $5 \times 10^{-4}\omega_p^{-1}$ to $1 \times 10^{-4}\omega_p^{-1}$ where ω_p^{-1} is the ion plasma period. The total number of particles was 10000 for all the simulations. Since the numerical charge induced dipole potential has both a repulsive and an attractive part, it presented a potential well, as shown in the figure A.1. Different radius and, therefore, minimum values of the charge induced dipole potential were explored. Once the equilibrium was reached in the NVE simulation, the distribution of minimum distances between ion-neutral and neutral-neutral pairs of particles was computed in order to study the presence of bound states. These bound states consisted of ion-neutral molecules with a spatial scale characterized by r_ϕ and $r_{LJ} \approx 2^{1/6}\,\sigma$ which corresponds to the minimum of the charge induced dipole and the Lennard Jones potentials respectively.

It was observed that for relatively small values of r_ϕ the formation of bound

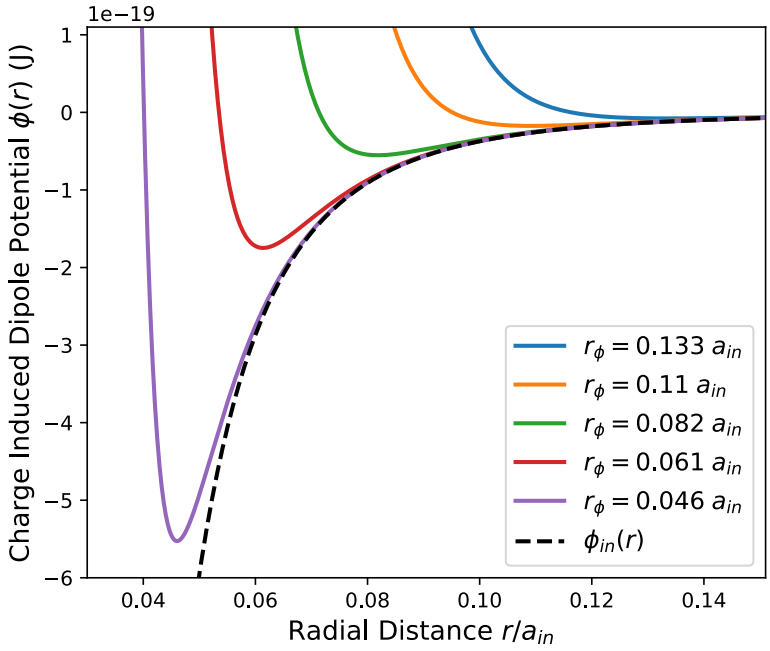

Figure A.1: Numerical charge induced dipole potential for different values of r_ϕ compared to the charge induced dipole potential.

states was more prominent. As it is shown in the distributions of minimum distances between ion-neutral and neutral-neutral pairs of particles after 1500 plasma periods in figure A.3, for $r_\phi = 0.046 a_{in}$ and a ionization fraction of 0.5, large peaks were observed corresponding to the distances r_ϕ and r_{LJ}.

As the radius of the charge induced dipole potential was increased, the population of ion-neutral and neutral-neutral bound states decreased until it was negligible for $r_\phi \approx 0.133 a_{in}$ as shown in figure A.2. The observed behaviour suggests that in order to avoid the formation of bound states an $r_\phi \approx 0.133 a$ must be used.

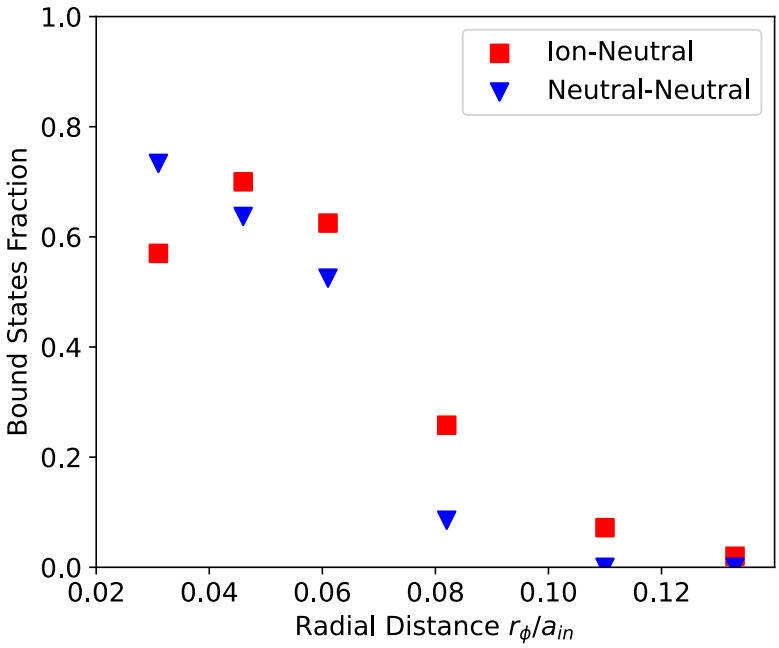

Figure A.2: Fraction of ion-neutral and neutral-neutral bound states for different r_ϕ values.

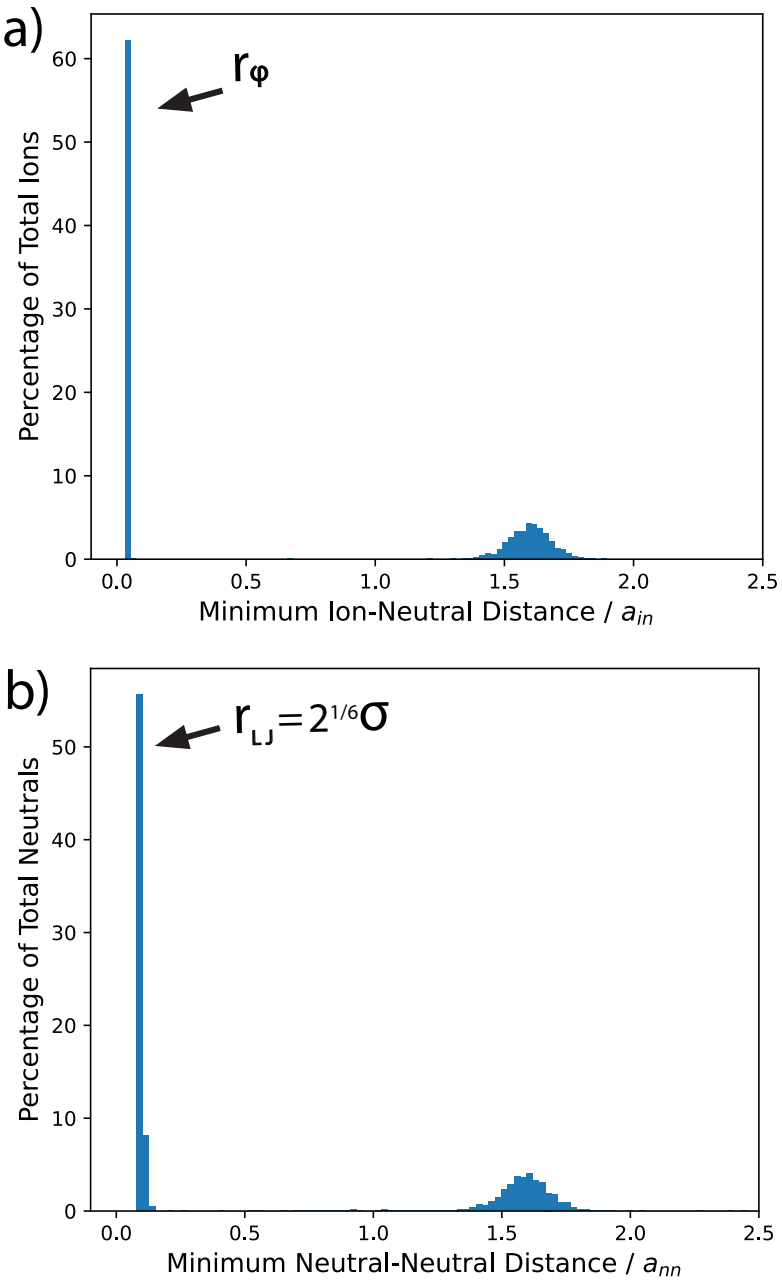

Figure A.3: a) Ion-neutral and b) neutral-neutral minimum distance distribution for $r_\phi = 0.046 a_{\text{in}}$ at an ionization fraction of 0.5.

BIBLIOGRAPHY

BIBLIOGRAPHY

[1] P. J. Bruggeman, F. Iza, and R. Brandenburg, "Foundations of atmospheric pressure non-equilibrium plasmas," *Plasma Sources Science and Technology*, vol. 26, p. 123002, nov 2017.

[2] M. D. Acciarri, C. H. Moore, and S. D. Baalrud, "Strong coulomb coupling influences ion and neutral temperatures in atmospheric pressure plasmas," *Plasma Sources Science and Technology*, 2022.

[3] A. Lo, A. Cessou, C. Lacour, B. Lecordier, P. Boubert, D. A. Xu, C. O. Laux, and P. Vervisch, "Streamer-to-spark transition initiated by a nanosecond overvoltage pulsed discharge in air," *Plasma Sources Science and Technology*, vol. 26, p. 045012, mar 2017.

[4] J. LeVan, M. D. Acciarri, and S. D. Baalrud, "Disorder-induced heating in molecular atmospheric pressure plasmas," *Submitted to PSST*, 2024.

[5] M. D. Acciarri, C. Moore, and S. D. Baalrud, "Disorder-induced heating as a mechanism for fast neutral gas heating in atmospheric pressure plasmas," *Plasma Sources Science and Technology*, vol. 33, p. 02LT02, feb 2024.

[6] N. Q. Minesi, P. B. Mariotto, E. Pannier, A. Vincent-Randonnier, G. D. Stancu, and C. O. Laux, "Kinetic mechanism and sub-ns measurements of the thermal spark in air," *Plasma Sources Science and Technology*, vol. 32, p. 044005, apr 2023.

[7] M. Domonkos, P. Tichá, J. Trejbal, and P. Demo, "Applications of cold atmospheric pressure plasma technology in medicine, agriculture and food industry," *Applied Sciences*, vol. 11, no. 11, 2021.

[8] P. J. Cullen, J. Lalor, L. Scally, D. Boehm, V. Milosavljević, P. Bourke, and K. Keener, "Translation of plasma technology from the lab to the food industry," *Plasma Processes and Polymers*, vol. 15, no. 2, p. 1700085, 2018.

[9] N. N. Misra, O. Schlüter, and P. J. Cullen, eds., *Cold plasma in food and agriculture: fundamentals and applications*. Amsterdam Boston: Elsevier/AP, Academic Press is an imprint of Elsevier, 2016. OCLC: ocn934606423.

[10] I. Adamovich, S. Agarwal, E. Ahedo, L. L. Alves, S. Baalrud, N. Babaeva, A. Bogaerts, A. Bourdon, P. J. Bruggeman, C. Canal, E. H. Choi, S. Coulombe,

Z. Donkó, D. B. Graves, S. Hamaguchi, D. Hegemann, M. Hori, H.-H. Kim, G. M. W. Kroesen, M. J. Kushner, A. Laricchiuta, X. Li, T. E. Magin, S. M. Thagard, V. Miller, A. B. Murphy, G. S. Oehrlein, N. Puac, R. M. Sankaran, S. Samukawa, M. Shiratani, M. Šimek, N. Tarasenko, K. Terashima, E. T. Jr, J. Trieschmann, S. Tsikata, M. M. Turner, I. J. van der Walt, M. C. M. van de Sanden, and T. von Woedtke, "The 2022 plasma roadmap: low temperature plasma science and technology," *Journal of Physics D: Applied Physics*, vol. 55, p. 373001, jul 2022.

[11] A. Bogaerts and G. Centi, "Plasma technology for co2 conversion: A personal perspective on prospects and gaps," *Frontiers in Energy Research*, vol. 8, 2020.

[12] A. Starikovskiy and N. Aleksandrov, "Plasma-assisted ignition and combustion," *Progress in Energy and Combustion Science*, vol. 39, no. 1, pp. 61–110, 2013.

[13] S. M. Starikovskaia, "Plasma-assisted ignition and combustion: nanosecond discharges and development of kinetic mechanisms," *Journal of Physics D: Applied Physics*, vol. 47, p. 353001, aug 2014.

[14] Z. Xiong and M. J. Kushner, "Atmospheric pressure ionization waves propagating through a flexible high aspect ratio capillary channel and impinging upon a target," *Plasma Sources Science and Technology*, vol. 21, p. 034001, apr 2012.

[15] E. Robert, V. Sarron, D. Riès, S. Dozias, M. Vandamme, and J.-M. Pouvesle, "Characterization of pulsed atmospheric-pressure plasma streams (paps) generated by a plasma gun," *Plasma Sources Science and Technology*, vol. 21, p. 034017, may 2012.

[16] T. Darny, J.-M. Pouvesle, J. Fontane, L. Joly, S. Dozias, and E. Robert, "Plasma action on helium flow in cold atmospheric pressure plasma jet experiments," *Plasma Sources Science and Technology*, vol. 26, p. 105001, sep 2017.

[17] E. C. Neyts and A. Bogaerts, "Understanding plasma catalysis through modelling and simulation—a review," *Journal of Physics D: Applied Physics*, vol. 47, p. 224010, may 2014.

[18] A. Bogaerts, X. Tu, J. C. Whitehead, G. Centi, L. Lefferts, O. Guaitella, F. Azzolina-Jury, H.-H. Kim, A. B. Murphy, W. F. Schneider, T. Nozaki, J. C. Hicks, A. Rousseau, F. Thevenet, A. Khacef, and M. Carreon, "The 2020 plasma catalysis roadmap," *Journal of Physics D: Applied Physics*, vol. 53, p. 443001, aug 2020.

[19] D. Z. Pai, D. A. Lacoste, and C. O. Laux, "Nanosecond repetitively pulsed discharges in air at atmospheric pressure—the spark regime," *Plasma Sources Science and Technology*, vol. 19, p. 065015, nov 2010.

[20] D. L. Rusterholtz, D. A. Lacoste, G. D. Stancu, D. Z. Pai, and C. O. Laux, "Ultrafast heating and oxygen dissociation in atmospheric pressure air by nanosecond repetitively pulsed discharges," *Journal of Physics D: Applied Physics*, vol. 46, p. 464010, oct 2013.

[21] N. A. Popov, "Fast gas heating in a nitrogen–oxygen discharge plasma: I. kinetic mechanism," *Journal of Physics D: Applied Physics*, vol. 44, p. 285201, jun 2011.

[22] N. A. Popov, "Pulsed nanosecond discharge in air at high specific deposited energy: fast gas heating and active particle production," *Plasma Sources Science and Technology*, vol. 25, p. 044003, may 2016.

[23] E. I. Mintoussov, S. J. Pendleton, F. G. Gerbault, N. A. Popov, and S. M. Starikovskaia, "Fast gas heating in nitrogen–oxygen discharge plasma: II. energy exchange in the afterglow of a volume nanosecond discharge at moderate pressures," *Journal of Physics D: Applied Physics*, vol. 44, p. 285202, jun 2011.

[24] Y. Yue, V. S. S. K. Kondeti, N. Sadeghi, and P. J. Bruggeman, "Plasma dynamics, instabilities and oh generation in a pulsed atmospheric pressure plasma with liquid cathode: a diagnostic study," *Plasma Sources Science and Technology*, vol. 31, p. 025008, feb 2022.

[25] L. Cheng, N. Barleon, B. Cuenot, O. Vermorel, and A. Bourdon, "Plasma assisted combustion of methane-air mixtures: Validation and reduction," *Combustion and Flame*, vol. 240, p. 111990, 2022.

[26] N. Minesi, S. Stepanyan, P. Mariotto, G. D. Stancu, and C. O. Laux, "Fully ionized nanosecond discharges in air: the thermal spark," *Plasma Sources Science and Technology*, vol. 29, p. 085003, aug 2020.

[27] P. K. Chu and X. Lu, eds., *Low Temperature Plasma Technology: Methods and Applications*. CRC Press, 1st ed., 2013.

[28] C. Tendero, C. Tixier, P. Tristant, J. Desmaison, and P. Leprince, "Atmospheric pressure plasmas: A review," *Spectrochimica Acta Part B: Atomic Spectroscopy*, vol. 61, no. 1, pp. 2–30, 2006.

[29] X. Lu, P. J. Bruggeman, S. Reuter, G. Naidis, A. Bogaerts, M. Laroussi, M. Keidar, E. Robert, J.-M. Pouvesle, D. Liu, and K. K. Ostrikov, "Grand challenges in low temperature plasmas," *Frontiers in Physics*, vol. 10, 2022.

[30] K.-D. Becker, U. Kogelschatz, K. H. Schoenbach, and R. J. Barker, eds., *Non-Equilibrium Air Plasmas at Atmospheric Pressure*. London: Routledge, 2005.

[31] N. Popov and S. Starikovskaia, "Relaxation of electronic excitation in nitrogen/oxygen and fuel/air mixtures: fast gas heating in plasma-assisted ignition and flame stabilization," *Progress in Energy and Combustion Science*, vol. 91, p. 100928, 2022.

[32] R. M. van der Horst, T. Verreycken, E. M. van Veldhuizen, and P. J. Bruggeman, "Time-resolved optical emission spectroscopy of nanosecond pulsed discharges in atmospheric-pressure n2 and n2/h2o mixtures," *Journal of Physics D: Applied Physics*, vol. 45, p. 345201, aug 2012.

[33] A. Lo, A. Cessou, and P. Vervisch, "Space and time analysis of the nanosecond scale discharges in atmospheric pressure air: Ii. energy transfers during the post-discharge," *Journal of Physics D: Applied Physics*, vol. 47, p. 115202, feb 2014.

[34] S. B. Leonov, I. V. Adamovich, and V. R. Soloviev, "Dynamics of near-surface electric discharges and mechanisms of their interaction with the airflow," *Plasma Sources Science and Technology*, vol. 25, p. 063001, nov 2016.

[35] M. Samimy, N. Webb, and A. Esfahani, "Reinventing the wheel: excitation of flow instabilities for active flow control using plasma actuators," *Journal of Physics D: Applied Physics*, vol. 52, p. 354002, jul 2019.

[36] I. V. Adamovich, "Three-dimensional analytic model of vibrational energy transfer in molecule-molecule collisions," *AIAA Journal*, vol. 39, no. 10, pp. 1916–1925, 2001.

[37] V. Guerra, A. T. del Caz, C. D. Pintassilgo, and L. L. Alves, "Modelling n2-o2 plasmas: volume and surface kinetics," *Plasma Sources Science and Technology*, vol. 28, p. 073001, jul 2019.

[38] R. Ono and T. Oda, "Measurement of gas temperature and OH density in the afterglow of pulsed positive corona discharge," *Journal of Physics D: Applied Physics*, vol. 41, p. 035204, jan 2008.

[39] G. J. M. Hagelaar and L. C. Pitchford, "Solving the boltzmann equation to obtain electron transport coefficients and rate coefficients for fluid models," *Plasma Sources Science and Technology*, vol. 14, p. 722, oct 2005.

[40] D. P. Breden, *Simulations of atmospheric pressure plasma discharges*. PhD thesis, University of Texas at Austin, 2013.

[41] F. Tochikubo and A. Komuro, "Review of numerical simulation of atmospheric-pressure non-equilibrium plasmas: streamer discharges and glow discharges," *Japanese Journal of Applied Physics*, vol. 60, p. 040501, mar 2021.

[42] M. A. Lieberman and A. J. Lichtenberg, *Principles of Plasma Discharges and Material Processing*. Hoboken, New Jersey: Wiley, 2nd ed., 2005.

[43] J. P. Verboncoeur, "Particle simulation of plasmas: review and advances," *Plasma Physics and Controlled Fusion*, vol. 47, p. A231, apr 2005.

[44] C. K. Birdsall and A. B. Langdon, "Plasma physics via computer simulation," 2018.

[45] R. W. Hockney and J. W. Eastwood, *Computer simulation using particles*. Hilger, 1989.

[46] D. Barnes and L. Chacón, "Finite spatial-grid effects in energy-conserving particle-in-cell algorithms," *Computer Physics Communications*, vol. 258, p. 107560, 2021.

[47] Z. D. Maximilian Klich, Sebastian Wilczek and R. P. Brinkmann, "Simulation and modeling of radio-frequency atmospheric pressure plasmas in the non-neutral regime," *Plasma Sources Science and Technology*, vol. 31, p. 045003, 2022.

[48] T. M. Zoltan Donko, B. Hartmann, "edupic: An educational particle-in-cell code for radio-frequency discharges," *Plasma Sources Science and Technology*, vol. 30, p. 015007, 2021.

[49] T. N. O. Chanrion, "A pic-mcc code for simulation of streamer propagation in air," *Journal of Computational Physics*, vol. 227, pp. 7222–7245, 2008.

[50] R. A. Vladimir Kolobov, "Electrostatic pic with adaptive cartesian mesh," *Journal of Physics: Conference Series*, vol. 719, p. 012020, 2016.

[51] J. Teunissen and U. Ebert, "3d pic-mcc simulations of discharge inception around a sharp anode in nitrogen/oxygen mixtures," *Plasma Sources Science and Technology*, vol. 25, p. 044005, jun 2016.

[52] S. D. Baalrud and J. Daligault, "Mean force kinetic theory: A convergent kinetic theory for weakly and strongly coupled plasmas," *Physics of Plasmas*, vol. 26, no. 8, p. 082106, 2019.

[53] S. D. Baalrud, "Transport coefficients in strongly coupled plasmas," *Physics of Plasmas*, vol. 19, p. 030701, 03 2012.

[54] S. D. Baalrud and J. Daligault, "Modified enskog kinetic theory for strongly coupled plasmas," *Phys. Rev. E*, vol. 91, p. 063107, Jun 2015.

[55] S. D. Baalrud and J. Daligault, "Effective potential kinetic theory for strongly coupled plasmas," *AIP Conference Proceedings*, vol. 1786, p. 130001, 11 2016.

[56] M. A. Lieberman and A. J. Lichtenberg, *Atomic Collisions*, ch. 3, pp. 43–85. John Wiley 'I&' Sons, Ltd, 2005.

[57] B. Scheiner and S. D. Baalrud, "Mean force kinetic theory applied to self-diffusion in supercritical lennard-jones fluids," *The Journal of Chemical Physics*, vol. 152, no. 17, p. 174102, 2020.

[58] J. Daligault, "Diffusion in ionic mixtures across coupling regimes," *Phys. Rev. Lett.*, vol. 108, p. 225004, May 2012.

[59] D. Gericke and M. Murillo, "Disorder-induced heating of ultracold plasmas," *Contributions to Plasma Physics*, vol. 43, no. 5-6, pp. 298–301, 2003.

[60] T. C. Killian and S. L. Rolston, "Ultracold neutral plasmas," *Physics Today*, vol. 63, no. 3, pp. 46–51, 2010.

[61] T. Pohl, T. Pattard, and J. M. Rost, "Relaxation to nonequilibrium in expanding ultracold neutral plasmas," *Phys. Rev. Lett.*, vol. 94, p. 205003, May 2005.

[62] S. G. Kuzmin and T. M. O'Neil, "Numerical simulation of ultracold plasmas," *Physics of Plasmas*, vol. 9, no. 9, pp. 3743–3751, 2002.

[63] M. D. G. Evans, J. M. Bergthorson, and S. Coulombe, "Actuation of a lean-premixed flame by diffuse non-equilibrium nanosecond-pulsed plasma at atmospheric pressure," *Journal of Applied Physics*, vol. 122, no. 17, p. 173305, 2017.

[64] M. S. Bak, H. Do, M. G. Mungal, and M. A. Cappelli, "Plasma-assisted stabilization of laminar premixed methane/air flames around the lean flammability limit," *Combustion and Flame*, vol. 159, no. 10, pp. 3128–3137, 2012.

[65] J. Li, B. Lei, J. Wang, B. Xu, S. Ran, Y. Wang, T. Zhang, J. Tang, W. Zhao, and Y. Duan, "Atmospheric diffuse plasma jet formation from positive-pseudo-streamer and negative pulseless glow discharges," *Communications Physics*, vol. 4, p. 64, Mar 2021.

[66] J. Tang, W. Jiang, J. Li, Y. Wang, W. Zhao, and Y. Duan, "Observation and interpretation of energy efficient, diffuse direct current glow discharge at atmospheric pressure," *Applied Physics Letters*, vol. 107, no. 8, p. 083505, 2015.

[67] A. Bogaerts, A. Berthelot, S. Heijkers, S. Kolev, R. Snoeckx, S. Sun, G. Trenchev, K. V. Laer, and W. Wang, "Co2 conversion by plasma technology: insights from modeling the plasma chemistry and plasma reactor design," *Plasma Sources Science and Technology*, vol. 26, p. 063001, may 2017.

[68] A. V. Phelps, "The diffusion of charged particles in collisional plasmas - free and ambipolar diffusion at low and moderate pressures," *Journal of Research of the National Institute of Standards and Technology; (USA)*, vol. 95, 8 1990.

[69] D. Breden, L. L. Raja, C. A. Idicheria, P. M. Najt, and S. Mahadevan, "A numerical study of high-pressure non-equilibrium streamers for combustion ignition application," *Journal of Applied Physics*, vol. 114, no. 8, p. 083302, 2013.

[70] D. Breden and L. Raja, "Simulations of nanosecond pulsed plasmas in supersonic flows for combustion applications," *AIAA Journal*, vol. 50, no. 3, pp. 647–658, 2012.

[71] X. Lu, G. Naidis, M. Laroussi, S. Reuter, D. Graves, and K. Ostrikov, "Reactive species in non-equilibrium atmospheric-pressure plasmas: Generation, transport, and biological effects," *Physics Reports*, vol. 630, pp. 1–84, 2016. Reactive species in non-equilibrium atmospheric-pressure plasmas: Generation, transport, and biological effects.

[72] N. Q. Minesi, V. P. Blanchard, E. Pannier, G. D. Stancu, and C. O. Laux, "Plasma-assisted combustion with nanosecond discharges. i: Discharge effects characterization in the burnt gases of a lean flame," *Plasma Sources Science and Technology*, vol. 31, p. 045029, may 2022.

[73] Z. Donko and N. Dyatko, "First-principles particle simulation and boltzmann equation analysis of negative differential conductivity and transient negative mobility effects in xenon*," *Eur. Phys. J. D*, vol. 70, p. 135, 2016.

[74] D. Frenkel and B. Smit, "Chapter 6 - molecular dynamics in various ensembles," in *Understanding Molecular Simulation (Second Edition)* (D. Frenkel and B. Smit, eds.), pp. 139–163, San Diego: Academic Press, second edition ed., 2002.

[75] A. P. Thompson, H. M. Aktulga, R. Berger, D. S. Bolintineanu, W. M. Brown, P. S. Crozier, P. J. in 't Veld, A. Kohlmeyer, S. G. Moore, T. D. Nguyen, R. Shan, M. J. Stevens, J. Tranchida, C. Trott, and S. J. Plimpton, "LAMMPS - a flexible simulation tool for particle-based materials modeling at the atomic, meso, and continuum scales," *Comp. Phys. Comm.*, vol. 271, p. 108171, 2022.

[76] M. Matsumoto and T. Nishimura, "Mersenne twister: A 623-dimensionally equidistributed uniform pseudo-random number generator," *ACM Trans. Model. Comput. Simul.*, vol. 8, p. 3–30, jan 1998.

[77] H. Abe, N. Sakairi, R. Itatani, and H. Okuda, "High-order spline interpolations in the particle simulation," *Journal of Computational Physics*, vol. 63, no. 2, pp. 247–267, 1986.

[78] D. Rapp and P. Englander-Golden, "Total Cross Sections for Ionization and Attachment in Gases by Electron Impact. I. Positive Ionization," *The Journal of Chemical Physics*, vol. 43, pp. 1464–1479, 05 2004.

[79] M. Baus and J.-P. Hansen, "Statistical mechanics of simple coulomb systems," *Physics Reports*, vol. 59, no. 1, pp. 1–94, 1980.

[80] T. Killian, T. Pattard, T. Pohl, and J. Rost, "Ultracold neutral plasmas," *Physics Reports*, vol. 449, no. 4, pp. 77–130, 2007.

[81] S. G. Kuzmin and T. M. O'Neil, "Numerical simulation of ultracold plasmas: How rapid intrinsic heating limits the development of correlation," *Phys. Rev. Lett.*, vol. 88, p. 065003, Jan 2002.

[82] S. K. Tiwari, N. R. Shaffer, and S. D. Baalrud, "Thermodynamic state variables in quasiequilibrium ultracold neutral plasma," *Phys. Rev. E*, vol. 95, p. 043204, Apr 2017.

[83] J. H. Ferziger and H. G. Kaper, "Mathematical theory of transport processes in gases," *American Journal of Physics*, vol. 41, no. 4, pp. 601–603, 1973.

[84] A. Fierro, E. Barnat, C. Moore, M. Hopkins, and P. Clem, "Kinetic simulation of a low-pressure helium discharge with comparison to experimental measurements," *Plasma Sources Science and Technology*, vol. 28, p. 055012, may 2019.

[85] D. R. Lide, *CRC handbook of chemistry and physics*, vol. 85. CRC press, 2004.

[86] D. A. McQuarrie and J. D. Simon, *Physical chemistry: a molecular approach*, vol. 1. University science books Sausalito, CA, 1997.

[87] W. Yang, Q. Zhou, Q. Sun, Z. Dong, and E. Yan, "Vibrational–translational relaxation in nitrogen discharge plasmas: Master equation modeling and Landau–Teller model revisited," *AIP Advances*, vol. 10, no. 10, p. 105311, 2020.

[88] M. Baus and J.-P. Hansen, "Statistical mechanics of simple coulomb systems," *Physics Reports*, vol. 59, no. 1, pp. 1–94, 1980.

[89] M. N. Glukhovtsev and S. Laiter, "Thermochemistry of tetrazete and tetraazatetrahedrane: A high-level computational study," *The Journal of Physical Chemistry*, vol. 100, no. 5, pp. 1569–1577, 1996.

[90] L. C. Pitchford and A. V. Phelps, "Comparative calculations of electron-swarm properties in n_2 at moderate $\frac{E}{N}$ values," *Phys. Rev. A*, vol. 25, pp. 540–554, Jan 1982.

[91] N. Minesi, P. Mariotto, E. Pannier, G. D. Stancu, and C. O. Laux, "The role of excited electronic states in ambient air ionization by a nanosecond discharge," *Plasma Sources Science and Technology*, vol. 30, p. 035008, mar 2021.

[92] D. C. Cartwright, A. Chutjian, S. Trajmar, and W. Williams, "Electron impact excitation of the electronic states of n_2. i. differential cross sections at incident energies from 10 to 50 ev," *Phys. Rev. A*, vol. 16, pp. 1013–1040, Sep 1977.

[93] J. Bacri and A. Medani, "Electron diatomic molecule weighted total cross section calculation: Iii. main inelastic processes for n2 and n+2," *Physica B+C*, vol. 112, no. 1, pp. 101–118, 1982.

[94] L. M. Isola, B. J. Gómez, and V. Guerra, "Determination of the electron temperature and density in the negative glow of a nitrogen pulsed discharge using optical emission spectroscopy," *Journal of Physics D: Applied Physics*, vol. 43, p. 015202, dec 2009.

[95] Y. Itikawa, "Cross Sections for Electron Collisions with Nitrogen Molecules," *Journal of Physical and Chemical Reference Data*, vol. 35, pp. 31–53, 12 2005.

[96] P. C. Cosby, "Electron-impact dissociation of nitrogen," *The Journal of Chemical Physics*, vol. 98, pp. 9544–9553, 06 1993.

[97] A. Lo, A. Cessou, P. Boubert, and P. Vervisch, "Space and time analysis of the nanosecond scale discharges in atmospheric pressure air: I. gas temperature and vibrational distribution function of n2 and o2," *Journal of Physics D: Applied Physics*, vol. 47, p. 115201, feb 2014.

[98] Y. Wang, O. Zatsarinny, and K. Bartschat, "b-spline r-matrix-with-pseudostates calculations for electron-impact excitation and ionization of nitrogen," *Phys. Rev. A*, vol. 89, p. 062714, Jun 2014.

[99] C. J. Ciccarino and D. W. Savin, "Electron-impact ionization of atomic nitrogen," *Journal of Thermophysics and Heat Transfer*, vol. 33, no. 1, pp. 154–162, 2019.

[100] A. Y. S. S M Starikovskaia and D. V. Zatsepin, "Hydrogen oxidation in a stoichiometric hydrogen-air mixture in the fast ionization wave," *Combustion Theory and Modelling*, vol. 5, no. 1, pp. 97–129, 2001.

[101] N. R. Shaffer, S. D. Baalrud, and J. Daligault, "Effective potential theory for diffusion in binary ionic mixtures," *Phys. Rev. E*, vol. 95, p. 013206, Jan 2017.

[102] S. Chapman, T. Cowling, D. Burnett, and C. Cercignani, *The Mathematical Theory of Non-uniform Gases: An Account of the Kinetic Theory of Viscosity, Thermal Conduction and Diffusion in Gases*. Cambridge Mathematical Library, Cambridge University Press, 1990.

[103] S. Stephan, M. Thol, J. Vrabec, and H. Hasse, "Thermophysical properties of the lennard-jones fluid: Database and data assessment," *Journal of Chemical Information and Modeling*, vol. 59, no. 10, pp. 4248–4265, 2019. PMID: 31609113.

[104] S. D. Baalrud and J. Daligault, "Effective potential theory for transport coefficients across coupling regimes," *Phys. Rev. Lett.*, vol. 110, p. 235001, Jun 2013.

[105] J. Daligault, K. O. Rasmussen, and S. D. Baalrud, "Determination of the shear viscosity of the one-component plasma," *Phys. Rev. E*, vol. 90, p. 033105, Sep 2014.

[106] B. Scheiner and S. D. Baalrud, "Testing thermal conductivity models with equilibrium molecular dynamics simulations of the one-component plasma," *Phys. Rev. E*, vol. 100, p. 043206, Oct 2019.

[107] B. Scheiner and S. D. Baalrud, "Mean force kinetic theory applied to self-diffusion in supercritical lennard-jones fluids," *The Journal of Chemical Physics*, vol. 152, no. 17, p. 174102, 2020.

[108] J.-P. Hansen and I. R. McDonald, "Chapter 2 - statistical mechanics," in *Theory of Simple Liquids (Fourth Edition)* (J.-P. Hansen and I. R. McDonald, eds.), pp. 13–59, Oxford: Academic Press, fourth edition ed., 2013.

[109] N. R. Shaffer, S. K. Tiwari, and S. D. Baalrud, "Pair correlation functions of strongly coupled two-temperature plasma," *Physics of Plasmas*, vol. 24, 08 2017. 092703.

[110] S. D. Baalrud and J. Daligault, "Modified enskog kinetic theory for strongly coupled plasmas," *Phys. Rev. E*, vol. 91, p. 063107, Jun 2015.

[111] *Some Accurate Theoretical Results: Sections 6.5 – 6.6*, ch. 6, pp. 325–381. John Wiley 'I&' Sons, Ltd, 1988.

[112] F. W. Lampe and G. G. Hess, "Specific reaction rate of the second-order formation of ar2+," *Journal of the American Chemical Society*, vol. 86, no. 14, pp. 2952–2953, 1964.

[113] A. Zhang, R. Scarcelli, T. Wallner, D. Breden, A. Karpatne, L. L. Raja, I. Ekoto, and B. Wolk, "Numerical investigation of nanosecond pulsed discharge in air at above-atmospheric pressures," *Journal of Physics D: Applied Physics*, vol. 51, p. 345201, jul 2018.

[114] M. D. Acciarri, C. Moore, and S. D. Baalrud, "Influence of strong coulomb coupling on diffusion in atmospheric pressure plasmas," *Plasma Sources Science and Technology*, vol. 32, p. 115004, nov 2023.

[115] G. Chen, L. Chacón, and D. Barnes, "An energy- and charge-conserving, implicit, electrostatic particle-in-cell algorithm," *Journal of Computational Physics*, vol. 230, no. 18, pp. 7018–7036, 2011.

[116] S. Markidis and G. Lapenta, "The energy conserving particle-in-cell method," *Journal of Computational Physics*, vol. 230, no. 18, pp. 7037–7052, 2011.

[117] W. T. Taitano, D. A. Knoll, L. Chacón, and G. Chen, "Development of a consistent and stable fully implicit moment method for vlasov–ampère particle in cell (pic) system," *SIAM Journal on Scientific Computing*, vol. 35, no. 5, pp. S126–S149, 2013.

[118] G. Chen and L. Chacón, "An energy- and charge-conserving, nonlinearly implicit, electromagnetic 1d-3v vlasov–darwin particle-in-cell algorithm," *Computer Physics Communications*, vol. 185, no. 10, pp. 2391–2402, 2014.

[119] G. Chen and L. Chacón, "A multi-dimensional, energy- and charge-conserving, nonlinearly implicit, electromagnetic vlasov–darwin particle-in-cell algorithm," *Computer Physics Communications*, vol. 197, pp. 73–87, 2015.

[120] D. Knoll and D. Keyes, "Jacobian-free newton–krylov methods: a survey of approaches and applications," *Journal of Computational Physics*, vol. 193, no. 2, pp. 357–397, 2004.

[121] S. Ichimaru, *Statistical Plasma Physics: Basic Principles*. CRC Press, May 2018.

[122] M. D. Acciarri, C. H. Moore, B. Lucas, and S. D. Baalrud, "When should pic simulations be applied to atmospheric pressure plasmas? impact of correlation heating," *Plasma Sources Science and Technology*, 2023.

[123] K.-D. Weltmann and T. von Woedtke, "Plasma medicine—current state of research and medical application," *Plasma Physics and Controlled Fusion*, vol. 59, p. 014031, nov 2016.